

*Armenian
Journal
of Physics*

vol. 11, issue 4

PROCEEDINGS

of the International Conference on

*“Microwave & THz Technologies and
Wireless Communications”*

IRPhE' 2018

September 19-21, Aghveran, Armenia

ISSN: 1829-1171

PROCEEDINGS

of the International Conference on

*“Microwave & THz Technologies and Wireless
Communications”*

IRPhE' 2018

September 19-21, Aghveran, Armenia

Conference Chairs:

Arsen Hakhoumian, (Dr.Sc., Ass. Member NAS RA, IRPhE, Armenia)

Tigran Zakaryan (Dr. CEO IRPhE, Armenia)

Content

1. Advances in high-speed microwave photonic signal processing, R. Minasian------(169-174)
2. Visualization of electromagnetic fields and thermal distribution by the thermo-elastic optical indicator microscope, Zh. Baghdasaryan, A. Babajanyan, L. Odabashyan, H.Lee, B.Friedman, K. Lee------(175-179)
3. Bessel beam radial slot antenna, Arsen Hakhoumian, Omid Mahmoodian------(180-187)
4. Estimation of phase noise impact on coherence length in FM-CW radars with voltage controlled oscillators, A. Hakhoumian, A. Makaryan, N. Poghosyan, T. Zakaryan------(188-190)
5. Frequency conversion in the ferromagnet at low magnetic bias fields, T. Yezekyan, A. Makaryan, V. Tadevosyan------(191-195)
6. Millimeter-wave component characterization with vector network analyzer, P. Baybakov (196-199)
7. Digital Beamforming for OFDM Radar, D. Nersisyan, A. Hakhoumian, G. Mkrtchyan, T. Manukyan------(200-203)
8. The microstrip phased array antenna of centimeter waves range, M.V. Markosyan, V.H. Avetisyan, A.K. Aharonyan, R.A. Davtyan------(204-208)
9. To problem of designing of the landing radars, S.B. Makarov, M.V. Markosyan, V.H. Avetisyan, A.K. Aharonyan, H.G. Martirosyan, R.A. Davtyan------(209-213)
10. Glucose aqueous solution sensing by modified Hilbert shaped microwave sensor, L. Odabashyan, A. Babajanyan, Zh. Baghdasaryan, B. Friedman, K. Lee------(214-222)
11. Investigation of detection of electro-magnetic radiation in the plasma at the constant electric field, G. Gulakyan, A. Makaryan, R. Miroyan------(223-226)
12. A device for measuring body bio-impedance with combined various physical affects, S. Martirosyan, A. Ghulyan, N. Yezakyan, N. Mkrtchyan, T. Lazaryan------(227-230)
13. Power analog trigger Schmitt, S. Martirosyan, J. Torikyan------(231-234)
14. An alternative expression of the Poynting vector operating in a confined region of evanescent waves: natural function in the method of single expression, H.V. Baghdasaryan, T.M. Knyazyan, T.T. Hovhannisyan, A.V. Daryan, M. Marciniak--(235-240)
15. Plasmonic nanoparticles arrangements for biosensing, H. Parsamyan, T. Yezekyan, H. Haroyan------(241-245)
16. The dynamics of instability development in spatially separated electron beam- plasma system, E. Rostomyan------(246-251)

17. Fano Resonance in coupled semicylindrical, H.Haroyan, T.Yezekyan, H.Parsamyan,
A.Ninoyan------(252-256)
18. Effect of absorption on the efficiency of THz radiation generation in a nonlinear
crystal placed into a waveguide, A.Nikoghosyan, R. Martirosyan, A. Hakhoumian, A.
Makaryan, V.Tadevosyan, G.N. Goltsman, S.V. Antipov------(257-262)
19. Efficient ultrashort THz pulse generation in LiNbO₃, ZnTe, GaSe and DAST crystals,
A.S.Nikoghosyan, R. M. Martirosyan, A. A. Hakhoumian------(263-268)
20. Compact transcapacitance model for short-channel FinFETs, A.Yesayan------(269-272)
21. On a Validity Criterion for the Born Approximation, L. B. Hovakimian------(273-277)
22. Single-layer amorphous carbon anti-reflective coatings obtained by pulsed laser
deposition method, Lenrik Matevosyan, G. Pluzyan, K. Avjyan, G. Dabaghyan------(278-279)
23. Advanced modulation and coding challenges on the way to 400G and terabit Ethernet,
Dmitry Titov------(280-283)
24. Power Domain Non-orthogonal Multiple Access (PD-NOMA) technique for 5G
networks, H. Haroyan, G. Hovsepian, S. Sargsyan------(284-287)
25. OFDM Radar Signal Processing, G. Mkrtchyan, A. Hakhoumian, D. Nersisyan,
T.Manukyan------(288-291)
26. Novel Approach to Wireless Communications Software Development Performance
and Productivity Evaluation – SAFe based, F. Muhammad, C. Cilliers------(292-302)
27. Content-Aware Cross Layer Optimization for IMT-Advanced Systems, M. Johal,
G.Markarian, A. Awang Md Isa, Y. Dasril------(303-308)
28. Analysis of BE and rtPS QoS in WiFi Network, J.Sultan, G.Markarian, Ph.Benachour--(309-321)

Advances in High-Speed Microwave Photonic Signal Processing

(Proceedings of the Int. Conference on “ Microwave and THz Technologies and Wireless comm.”)

R. A. Minasian

*School of Electrical and Information Engineering, University of Sydney, NSW, 2006, Australia
Fellow, IEEE, Fellow, OSA*

Received 15 November 2018

Abstract: Photonic signal processing offers a new powerful paradigm for processing high speed signals, due to its inherent advantages of wide bandwidth and immunity to electromagnetic interference. Recently there has been a strong drive to realise photonic integrated circuits using Silicon Photonics. This paper describes recent advances in integrated microwave photonic signal processing and sensing. These include optical single sideband modulators that can remove the effects of dispersion in wideband microwave photonic links, optical vector network analysers with high resolution, broadband tunable filters, multi-function processors, and integrated photonic sensors using optical micro-ring resonators that demonstrate extremely high sensitivity. These microwave photonic processors provide new capabilities for the realisation of high-performance signal processing and sensing.

Keywords: Photonic signal, photonic integrated circuits, single sideband modulator.

1. Introduction

Microwave photonics offers the prospect of overcoming a range of challenging problems in the processing of signals [1]. Its intrinsic advantages of high time-bandwidth product and immunity to electromagnetic interference (EMI) have led to diverse applications in the microwave and sensing fields [2]-[4]. Photonic signal processing leverages the advantages of the optical domain to benefit from the wide bandwidth, low loss, and natural EMI immunity that photonics offers. Recently there has been a strong drive to realise photonic integrated circuits using Silicon Photonics. This is particularly attractive because it enables a CMOS-compatible fabrication that enables the integration of combined photonic and electronic functions on one chip. It also makes possible a cost-effective implementation with reduced footprint, power and weight.

Recent advances in integrated microwave photonic signal processing and sensing are presented. These include optical single sideband modulators that can remove the effects of dispersion in wideband microwave photonic links, optical vector network analysers with high resolution, broadband tunable filters, multi-function processors, and integrated photonic sensors using optical micro-ring resonators that demonstrate extremely high sensitivity. These microwave photonic processors provide new capabilities for the realisation of high-performance signal processing and sensing.

2. Integrated Micro-Ring Single-Sideband Modulation

An important function that is required in many microwave photonic applications is the ability to generate optical single sideband (OSSB) modulation. OSSB is a technique that can overcome dispersion problems in radio-over-fibre systems that use simple antenna remote units, central office equipment sharing, and multiple wideband wireless services [5]. The OSSB scheme has also been widely used in optical vector network analyzers as it provides direct mapping between the optical and electrical domain [6]. Currently, there is a strong drive to realise silicon photonic

on-chip signal processors to provide a more cost effective, robust and compact solution for wide ranging applications. Ring resonator structures have been of great research interest in integrated photonics as they are not only compact but exhibit excellent performance.

A novel OSSB technique that has the capability to operate over a wideband range and at high RF frequencies to millimeter waves, is based on a simple silicon-on-insulator (SOI) dual-ring structure that exhibits weak electromagnetically induced transparency (EIT)-like behaviour [7]. The notch filter comprises a simple configuration of just two ring resonators with a ring circumference offset where the dual rings are separated by a bridging waveguide with a fixed length. It exhibits a weak EIT-like property at the through port and behaves like a notch filter with steep transition and high rejection ratio. Fig. 1(a) shows the scanning electron microscope (SEM) image of the double ring weak EIT notch filter fabricated on a silicon-on-insulator (SOI) wafer via ePIXfab, which comprises two micro-ring resonators having the design parameters that the length of the first and second rings are 57309 nm and 57313 nm respectively, and a waveguide length (L_d) having a value of 18327 nm in order to achieve the weak EIT effect. The height of the silicon core waveguide is 220 nm and the waveguide width is 450 nm for both the bus and racetracks. The filter features steep slope transitions and wide bandwidth in comparison with other double ring resonator structures of the same footprint size. The falling and rising edge slopes of the measured filter were calculated to be around 174.30 dB/nm and 171.07 dB/nm, respectively, showing excellent optical spectral component selection. Fig. 1(b) shows the optical sideband ratio of the generated OSSB signal at an RF frequency of 20 GHz measured using the high resolution optical spectrum analyzer.

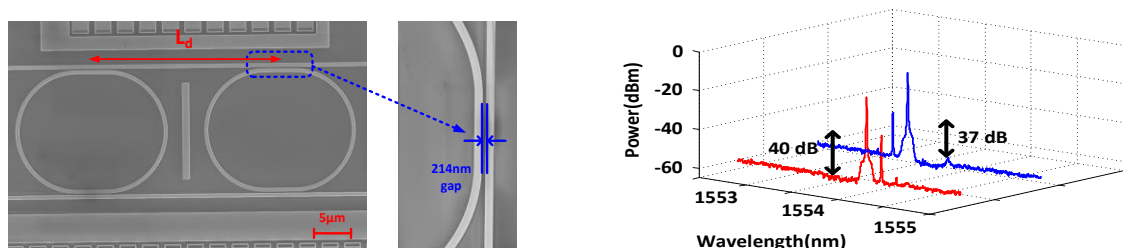


Fig. 1: Fabricated EIT notch filter and measured OSBB: (a) top-view SEM image of the fabricated SOI double ring weak EIT notch filter, (b) measured OSSB at 20 GHz where the blue line represents the upper sideband suppression of the left edge while the red line represents the lower sideband suppression of the right edge of the fabricated double ring weak EIT notch filter.

Fig. 2 experimentally demonstrates how the described OSSB modulator eliminates dispersion degradations in a microwave optical transmission link. It can be seen that the deep 30 dB dispersion-induced power fading generated with optical double sideband (ODSB) modulation is nearly eliminated, enabling a nearly constant RF response with just ± 1.25 dB ripple over a 30 GHz range when using the weak EIT-like notch filter optical single sideband (OSSB).

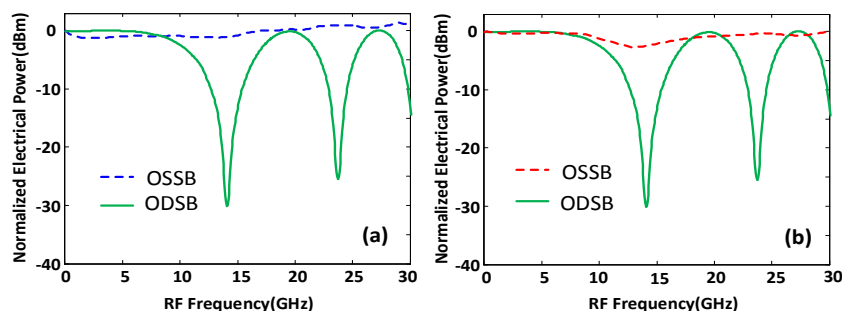


Fig. 2: Elimination of dispersion degradations in transmission: comparison between OSSB system with (a) upper sideband suppression (blue dashed line) (b) lower sideband suppression (red dashed line), and ODSB.

3. Tunable Single-Passband Microwave Photonic Filter

The ability of microwave photonic signal processing to realize filters that exhibit an extremely wide tunable RF range is a particular advantage that transcends the abilities of electronic RF filters. A particularly effective technique to realize single passband microwave photonic filters (SPMPF) is based on the concept of optical-to-RF mapping using phase-modulation to intensity-modulation conversion to translate the spectral response of an optical filter to the bandpass response of the microwave filter. The structure of a novel photonic integrated structure that can realize a widely tunable SPMPF which has a very good filter shape factor and which achieves shape-invariance during tuning is shown in Fig. 3(a) [8]. It is based on an integrated optical double notch filter using a cascaded pair of microring resonators, which produce two notches having slightly different stopband widths and centre frequencies.

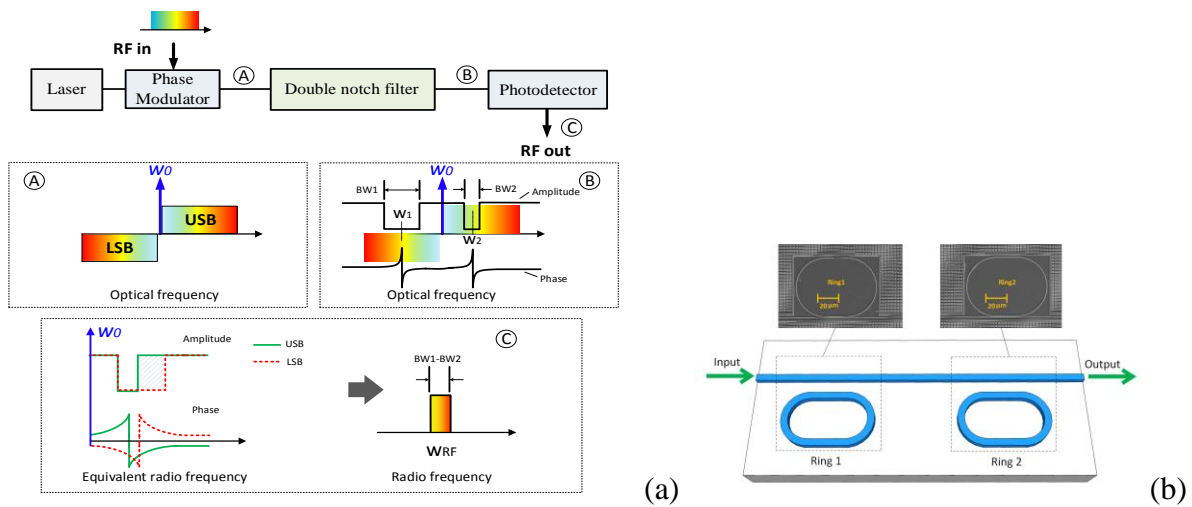


Fig. 3: (a) Schematic and operating principle of the single passband microwave photonic filter based on optical double notch filter. (b) Schematic diagram of the optical double notch filter.

The operating principle is based on phase to intensity modulation conversion, wherein the optical notch filters break the anti-phase symmetry of the modulation sidebands. The RF filter bandwidth is determined by the bandwidth difference of the two optical notch filters, not by their absolute individual bandwidths. This eliminates the need for narrow-band notch filters. The integrated optical double notch filter using a cascaded pair of non-identical microring resonators having slightly different stopband widths and centre frequencies is shown in Fig. 3(b).

The filter can be tuned by tuning the centre the frequencies of micro-resonators, while centred on the optical carrier, which can be done using integrated microheaters may be used. Fig. 4 shows the measured tuning response of the filter. The filter response is single-passband and it demonstrates 6-17 GHz tuning with shape-invariance.

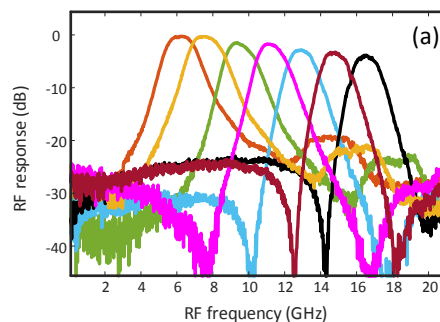


Fig. 4: Measured tuning response of the filter.

4. Multi-Function Signal Processing

There is a strong drive to realize compound signal processing functions that can be implemented together, and also to realize integrated silicon photonics. Silicon photonics is particularly attractive as it has the important advantage of integration compatibility with electronics for the drive interfaces on the same chip. For example general purpose and programmable signal processors capable of synthesizing a multitude of on-demand signal processing tasks have been reported for compact programmable RF-photonic filters using silicon photonics integrated waveguide mesh processors that enable multiple functionalities to be selected [9]. In addition, new system configurations have been realized that are capable of performing a distributed variety of compound functionalities such as individually controlled, cascaded microwave photonic bandpass filter and phase shifter functions within one subsystem. This utilizes a silicon photonics on-chip phase shifter based on single all-pass microring resonator [10], enabling the execution of multiple cascaded signal processing functions, while providing a separate control for each function.

5. Microwave Photonics Based Sensor

Optical sensors for monitoring the physical environment have important advantages including immunity to electromagnetic interference, inertness in chemical and biological applications, compactness, light-weight, and ability to operate in harsh environments. Techniques based on microwave photonics, in which the wavelength shift of the optical sensor is converted directly into the variation of an RF frequency signal are particularly attractive [11]. This is based on using an optoelectronic oscillator (OEO) [12] whose microwave oscillation frequency is determined by the resonant wavelength of the optical device that is employed for sensing. This method effectively translates the optical domain measurement into an electrical spectrum measurement, thus enabling a significantly higher frequency resolution that makes possible the achievement of a very high measurement resolution. Moreover, a much faster interrogation speed is also enabled since the microwave frequency can readily be measured by a digital signal processor (DSP) with high speed and high resolution.

An OEO-based optical sensor that is based on an integrated microwave photonic filter comprising a photonic micro-ring resonator is shown in Fig. 5 [13], where the integrated micro-ring resonator functions as a sensing probe element.

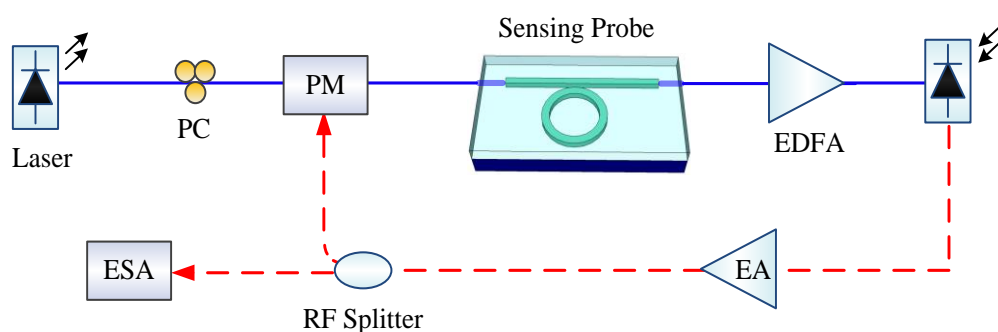


Fig. 5: Structure of the integrated OEO based temperature sensor. PM: phase modulator; EDFA: Erbium doped fiber amplifier; EA: electronic amplifier; PC: polarization controller; ESA: electrical spectrum analyser.

The micro-ring resonator essentially generates a microwave photonic filter whose center frequency corresponds to the location of the optical notch filter relative to the carrier. As an application, the target measurand was chosen to be temperature, where an easily integrated optical notch filter is employed as a sensor probe whose resonant wavelength is sensitive to temperature variations owing to the thermo-optic effect that changes the refractive index [14], thus resulting in a filtered RF signal output of the OEO whose frequency has a one-to-one correspondence to the temperature. Fig. 6 shows the experimental results.

Fig. 6(a) shows the OEO output is an almost pure electrical signal at 14.3 GHz at a temperature of 24.78 °C. The inset of Fig. 6(a) shows the zoomed in response which illustrates a narrowband signal with a linewidth of just 0.1 MHz. The next most dominant mode is located at around 4.9 MHz away from the peak oscillation mode and shows a mode suppression of around 30.6 dB. The temperature sensing performance was measured by changing the temperature of the nano-chip sensor from 24.27 °C to 25.29 °C. Fig. 6(b) shows the superimposed spectra of the generated microwave frequencies at different temperature points. As the temperature increases, the signal is shifted to a higher frequency. A linear relationship is seen between the temperature change and RF frequency shift, as shown in the linear fit in Fig. 6(c). The results demonstrate the ability to obtain extremely sensitive performance to small temperature variations with an achieved ultra-high sensitivity of 7.7GHz/°C.

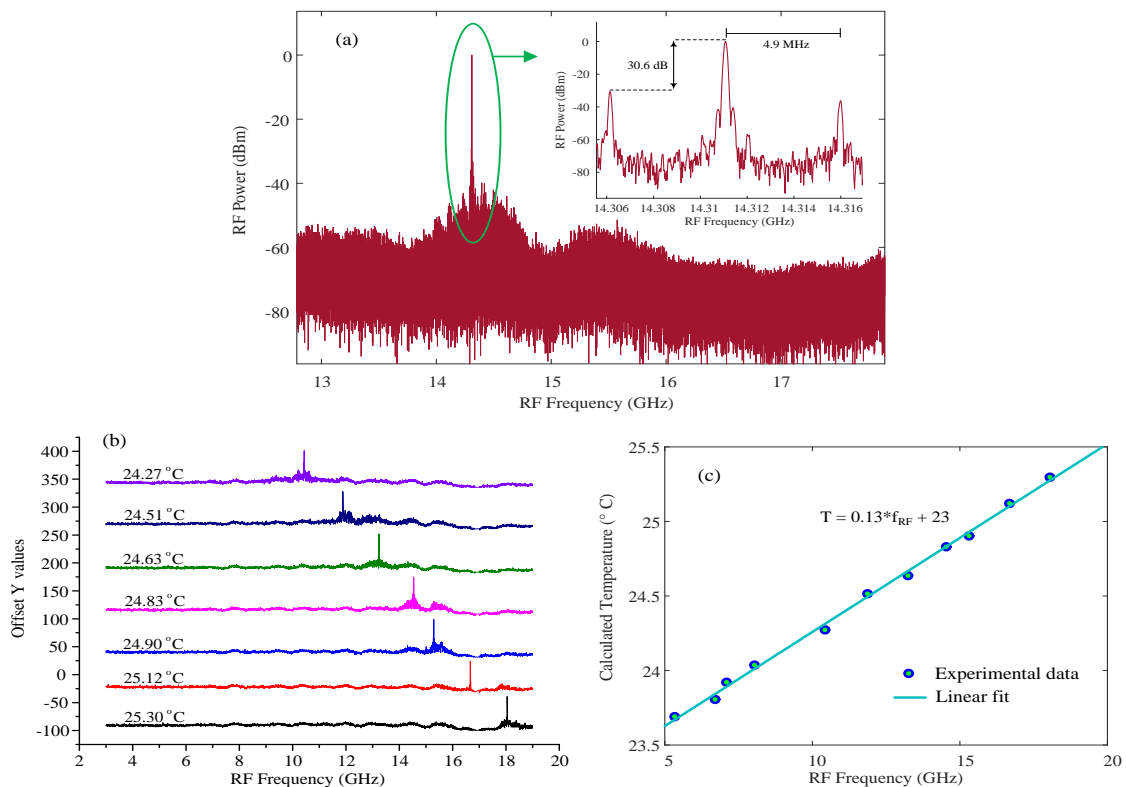


Fig. 6: Experimental results (a) Measured RF response at 24.78°C. Inset: Zoomed-in response of the RF oscillation mode. (b) Measured OEO RF oscillation frequency shift with temperature variations (c) Measured oscillation frequency shift as a function of the temperature.

6. Conclusion

Photonic signal processing offers the advantages of high time-bandwidth product capabilities to overcome inherent electronic limitations. A key benefit for wideband systems is that the entire RF/mm-wave spectrum constitutes only a small fraction of the carrier optical frequency. This opens the way to realize tunability over extremely wide microwave frequency ranges, and the ability to achieve ultra-wideband operation with wide instantaneous bandwidth and EMI immunity to provide connectivity with in-built signal conditioning.

Recent new methods in wideband signal processing have been presented. These include optical single sideband modulators that can remove the effects of dispersion in wideband microwave photonic links, optical vector network analysers with high resolution, broadband tunable filters, multi-function processors, and integrated photonic sensors using optical micro-ring resonators that demonstrate extremely high sensitivity. These processors provide new capabilities for realizing high-performance and high-resolution signal processing.

7. Acknowledgments

This work was supported by the Australian Research Council. Thanks are extended to X. Yi, L. Li, S. Song, S. Chew, P. Bian and L. Nguyen for their valuable contributions to this work.

References

- [1] R.A. Minasian, "Ultra-wideband and adaptive photonic signal processing of microwave signals", *IEEE Journal of Quantum Electronics, Invited Paper*, Focus Issue on Microwave Photonics, Vol. 52, No. 1, Article#: 0600813, 2016.
- [2] Minasian, R.A., "Photonic signal processing of microwave signals", *IEEE Trans. Microwave Theory Tech., Invited Paper*, vol. 54, pp. 832-846, 2006.
- [3] Yao, J. P., "Microwave photonics", *IEEE J. Lightwave Technol.*, vol. 27, pp. 314-335, 2009.
- [4] Minasian, R. A., Chan E. H. W., and Yi, X. "Microwave photonic signal processing", *Optics Express*, vol. 21, No. 19, pp. 22918-22936, 2013.
- [5] Waterhouse R., and Novak, D., "Microwave photonics for 5G mobile wireless systems," *IEEE Microwave Mag.*, vol. 16, no. 8, pp. 84-92, Sept. 2015.
- [6] Tang, Z., Pan, S., Yao, J., "A high resolution optical vector network analyzer based on a wideband and wavelength-tunable optical single-sideband modulator", *Optics Express*, 20, 6555-6560, (2012).
- [7] Chew, S. X., Yi, X., Song, S., Li, L., Bian, P., Nguyen, L., and Minasian, R.A., "Silicon-on-insulator dual-ring notch filter for optical sideband suppression and spectral characterization", *J. Lightw. Technol.*, Vol. 34, No. 20, pp. 4705-4714, 2016.
- [8] S. Song, S. X. Chew, X. Yi, L. Nguyen, and R. A. Minasian, "Tunable single-passband microwave photonic filter based on integrated optical double notch filter", *IEEE/OSA J. Lightwave Technol.*, Special Issue on Microwave Photonics, Vol. 36, No. 19, pp. 4557-4564, Oct. (2018).
- [9] Pérez, D., Gasulla, I., Crudgington, L., Thomson, D.J., Khokhar, A.Z., Li, Ke, Cao, Wei, Mashanovich, G.Z., Capmany, J., "Compact programmable RF-photonic filters using integrated waveguide mesh processors", Int. Conf. on Transparent Optical Networks ICTON 2017, Paper Tu.C5.3, 2017.
- [10] Chew, S. X., Nguyen, L., Yi, X., Song, S., Li, L., Bian, P., and Minasian, R. A., "Distributed optical signal processing for microwave photonics subsystems", *Optics Express*, Vol. 24, No. 5, pp. 4730-4739, (2016).
- [11] J. Yao, "Optoelectronic oscillator for high speed and high resolution optical sensing", *J. Lightw. Technol.*, 2016.
- [12] X. S. Yao and L. Maleki, "Optoelectronic microwave oscillator", *J. Opt. Soc. Am.* B13, vol. 13, no. 8, pp. 1725-1735, Aug. 1996.
- [13] S.X. Chew, X. Yi, W. Yang, C. Wu, L. Li, L. Nguyen and R.A. Minasian, "Optoelectronic oscillator based sensor using an on-chip sensing probe", *IEEE Photonics Journal*, Vol. 9, No. 2, 5500809, (2017).
- [14] G. D. Kim, H. S. Lee, C. H. Park, S. S. Lee, B. T. Lim, H. K. Bae, and W. G. Lee, "Silicon photonic temperature sensor employing a ring resonator manufactured using a standard CMOS process", *Opt. Express*, vol.18, no. 21, pp. 22215-22221, Oct 2010.

Visualization of Microwave Heating for mesh-Patterned Indium-tin-Oxide by a Thermo-Elastic Optical Indicator Microscope

(Proceedings of the Int. Conference on “ Microwave and THz Technologies and Wireless comm.”)

Zh. Baghdasaryan^{1,2}, A. Babajanyan², L. Odabashyan², H. Lee¹, B. Friedman³, K. Lee¹

¹Department of Physics, Sogang University, Seoul 121-742, Korea

²Department of Radiophysics, Yerevan State University, Yerevan 0025, Armenia

³Department of Physics, Sam Houston State University, Huntsville, Texas 77341, USA

Received 15 November 2018

Abstract: This review highlights advances toward non-destructive thermo-elastic optical indicator microscopy visualization system, with a particular focus placed on the structural type of the optical indicator. We present the electromagnetic field interaction with a thin electrical conductive layer of mesh-patterned ITO which is used as an optical indicator. Depending on the mesh-pattern orientation and electromagnetic field polarization, the microwave heating mechanism and field distribution are different. Visualization was made with a 12 GHz microwave signal and 35 dBm maximum power.

Keywords: Microwave heating, mesh-patterned ITO, thermo-elastic microscopy

1. Introduction

Transparent conductive oxide (TCO) is one of the most important and widely studied classes of advanced applied materials, with applications such as liquid crystal displays (LCD), organic light emitting diodes (OLED), solar cells and touch screens. It is an essential component in modern optoelectronic devices [1-3]. In Particular, Indium-tin-oxide (ITO) is still the dominant material for transparent conductive electrodes (TCEs) due to high optical transparency together with low sheet resistance [1].

In recent years, there is a great need for fabricating optoelectronic devices with mechanical flexibility due to the replacement of the traditional glass substrates with polymer materials. As important components of flexible electronic devices, electrodes that are transparent, have high electrical conductivity, and display favorable physical stability, such as high flexibility are required. One of the ways to increase the flexibility of a material is the mesh-patterning technique [4,5]. Results indicate that the proposed mesh patterned ITO electrode has a high potential for flexible electronic devices [6,7].

In modern technology non-destructive visualization is an important industrial requirement. Compared with conventional methods of visualization the thermo-elastic optical indicator microscope (TEOIM) [8] visualization system has great potential and advantages, including high sensitivity fast inspection time and spatial resolution. Conventional visualization methods based on a scanning probe technique include eddy current probe microscopy [9], scanning probe microwave microscopy [10], and conducting tip atomic microscopy [11]. The listed methods are still applicable but they have slow measurement process, non-practical equipment, and setup have to configure. The non-scanning probe methods, such as microwave thermography method [12] requires an infrared camera and knowledge of the basic principles of thermography based on the detection of infrared irradiation. In the TEOIM system, the working principle is detecting visible polarized light, which makes the measurement simple.

In this paper, we investigate the phenomenon of microwave heating in the mesh-patterned ITO conductive layer and show the images of heat distribution for different structural types of ITO. The measurements show that the microwave heating mechanism depends on the orientation of the mesh-pattern and the electromagnetic wave polarization.

2. Materials and methods

The experimental setup and measurement principle are shown in Fig. 1. The optical indicator (OI) was the glass substrate coated by a 100nm ITO thin film for the heat absorption. A microwave signal was generated by a synthesized sweeper (HP83620A) at the frequency 12GHz by 0dBm power and then amplified up to 35dBm by a power amplifier (ZVE – W – 183+). The generated microwave signal was transmitted by a rectangular waveguide (10.16mm × 22.86mm aperture) and interacts with the ITO thin absorbing layer placed in front of the waveguide. 12GHz was chosen as an optimal frequency in accordance with the oscillator model (WR90, TE mod). In order to decrease the noise level and increase the reflection of light, we provided a 1mm ceramic plate between the rectangular waveguide and the OI. With this configuration, we have a uniform and monochrome view in a visible area of the camera.

The TEOIM setup is based on the polarized light microscope system [8]. Light was emitted by the light emitting diode (LED; $\lambda = 530\text{nm}$). The polarization state of the incident light is modulated into circular polarization by a sheet polarizer (90°) and a $\lambda/4$ wave-plate (45°) (Fig. 1). The incident circular polarized light is reflected from the OI and passes through a second linear polarizer (analyzer) (0° and 45°), and light was finally recorded by a CCD camera ($1024\text{px} \times 768\text{px}$).

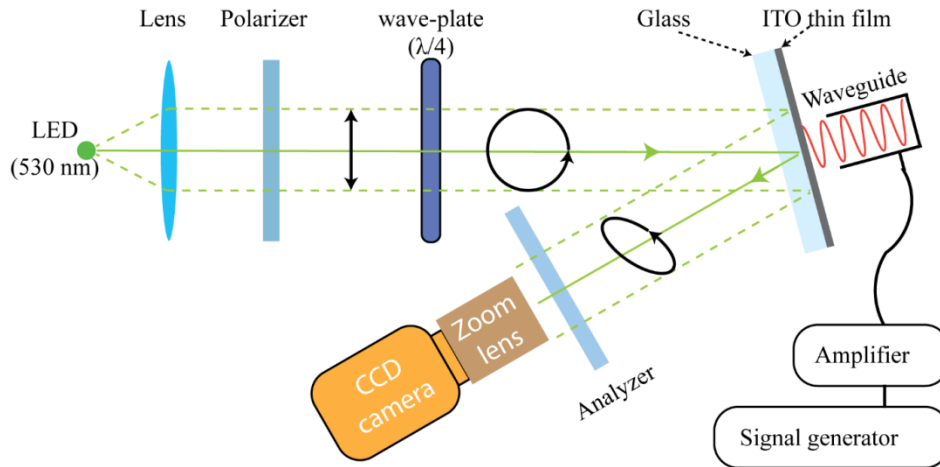


Figure 1. Schematic illustration of visualization system.

When the microwave signal is applied the conductive layer of OI heats up. After being reflected, the circularly polarized incident light changes to an elliptically polarized state due to the photoelastic effect of the glass substrate caused by thermal stress [13]. We detected the linear birefringent (LB) distribution images by choosing the analyzer orientation to be 0° or 45° . By solving the inverse problem of the mechanical stress formation, one can calculate the initial heat distribution causing those deformations:

$$q = C \left(\frac{\partial^2 \beta_1}{\partial x^2} - \frac{\partial^2 \beta_1}{\partial y^2} + 2 \frac{\partial^2 \beta_2}{\partial x \partial y} \right), \quad (1)$$

where, q is the heat source density, C is a constant parameter related to physical properties of the OI, and the wavelength of the light source, β_1 and β_2 is the linear birefringence distribution image related to the normal and shear stresses of the OI, respectively. The calculated heat distribution in our experiment will correspond to the absorbed microwave power by the ITO [14].

Mesh patterned ITO coated glass with different structural types of conductive thin layers was made for visualization. Structures were patterned by the laser ablation technique. Figure 2 (a), (e), (i), and (n) are an optical image of optical indicators. The geometries of patterned ITO are shown in Fig. 2(b), (f), (k), and (o). Sample S1 is ITO coated glass with a uniform conductive layer. Sample S2 has only one conductive line with 1mm width. S3 and S4 are arrays of conductive lines where lines of the S3 indicator are not connected but in the case of S4 the lines are connected after every 4mm . The width of the conductive lines is 0.14mm and the distance between the lines is 0.06mm .

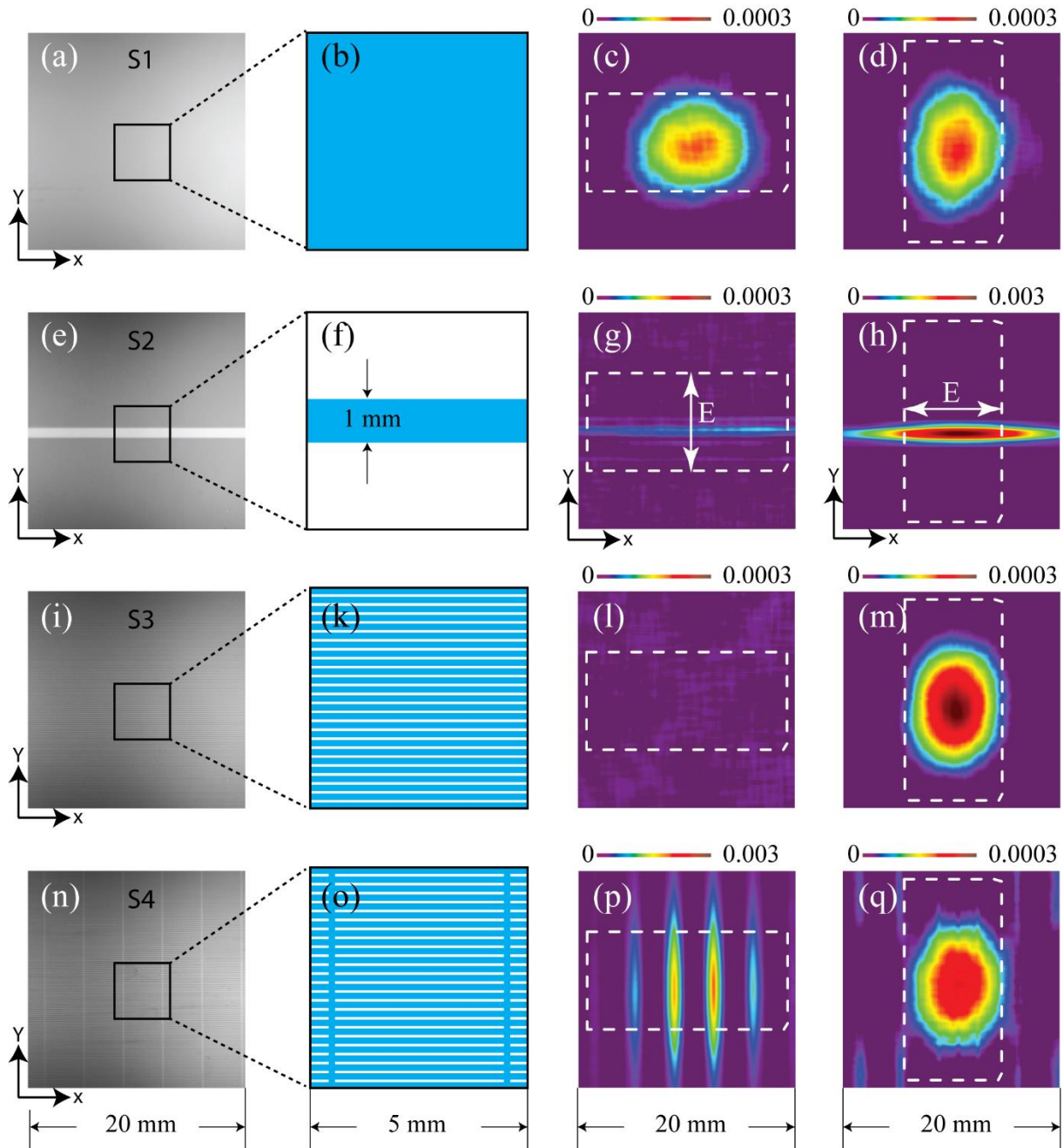


Figure 2.(a), (e), (i), and (n) The optical image of indicators with (b) (f) (k) (o) structural type, respectively. Thermal distributions in sample when the direction of alternating electric field coincides with (c) (g) (l) (p) y-axis, and (d) (h) (m) (q) x-axis. Dashed white rectangles show the orientation of the waveguide.

3. Results and discussion

ITO coated glass has been placed in the front of a rectangular wave guide to explore the microwave heating behavior of a thin conductive film. The microwave heating process can be divided into volumetric heating (i.e., dielectric loss heating) and surface heating (i.e., eddy current heating) [12]. For conductive materials, like metals and carbon fiber composites, microwave heating is dominated by eddy current heating. Since ITO is electrically conductive, the principle microwave heating is eddy current heating. Energy is radiated to the thin, conductive surface by microwaves, an alternating electric field is generated, and then induced surface currents are excited from the alternating electric field resulting in an alternating magnetic field. Next, a vortex electric field is generated by this alternating magnetic field; the vortex electric field promotes the movement of electrons which will generate Joule heat inside the metallic layer. Finally, the conductive material is heated by Joule heat as shown in Fig. 2 (c) and (d). These two images are the results of microwave heating distribution in the S1 sample. Since the S1 sample has a uniform conductive surface, in both cases, detecting the heat distribution is possible, when the electric field is perpendicular and parallel to the x -axis, respectively. Sample S2 contain only one conductive thin line with a width of 1mm . In this case, when the conductive line and electric field polarization are perpendicular to each other, the ITO line is not heated by the microwave (Fig 2 (g)). Fig. 2 (h) shows the microwave heat distribution in one conductive line, where alternating electric field polarization and the direction of the ITO line are coinciding. The intensity scale was normalized with a different range of value. The maximum value of the intensity scale is about ten times higher. It means that the line strongly heats up when the area of the conductive surface is smaller and the microwave field is localized on the conductive line. For the S3 sample results are predictable. S3 contains an array of conductive lines. Again, the surface is not heated when the conductive direction is perpendicular to the direction of E-field polarization (Fig. 2 (l)). The pattern of microwave heat distribution is detectable when the directions of the conductive lines coincide with the E-field (Fig. 2 (m)). Unlike S3, all conductive lines in S4 are connected. The distances between connector lines are 4mm . For the configuration as in Fig. 2 (p) the connector lines are strongly heated up by the microwave. This configuration is comparable with the result of Fig. 2 (h) when E-field direction coincides with ITO conductive line. For these two images intensity scales were normalized in the same range. Figure 2(q) is similar to the Fig. 2 (m) with small noises caused by the connector lines. In conclusion, when the non-conductive direction is parallel to the electric field polarization, visualization did not show a heat distribution result: mesh-patterned ITO is almost not heated in this case.

4. Conclusion

The basic principle of microwave heating for the mesh-patterned ITO was discussed. We visualized the heat distribution in the ITO by anon-contact and non-destructive TEOIM visualization technique. According to experimental results, we found out that the microwave heating distribution is strongly changed depending on the orientation of mesh-pattern and electromagnetic field polarization. TEOIM exhibits great potential, including high resolution, high sensitivity and fast inspection for investigation of symmetric structural materials. This technique can be an important tool for the testing and analysis of material properties.

Acknowledgments

This work was supported by a Sogang University Research Grant (201519064), Basic Science Research Program through the National Research Foundation of Korea (2015R1D1A1A02061824 and 2009-0093822), and by a Scientific Research Grant through the State Committee of Science of Ministry of Education and Science of Armenia (18T-1C114).

References

- [1] Peiyun Yi, Chengpeng Zhang, Linfa Peng, Xinmin Lai, "Flexible silver-mesh electrodes with moth-eye nanostructures for transmittance enhancement by double-sided roll-to-roll nanoimprint lithography," *RSC Adv.*, vol. 7, no. 77, pp. 48835-48840, Oct. 2017.
- [2] Bastian Waduge Naveen Harindu Hemasiri, Jae-Kwan Kim, Ji-Myon Lee, "Fabrication of highly conductive graphene/ITO transparent bi-film through CVD and organic additives-free sol-gel techniques," *Sci. Rep.*, vol. 7, no. 17868, pp. 1-12, Dec. 2017.
- [3] Ki-Hun Ok, Jiwan Kim, So-Ra Park, Youngmin Kim, Chan-Jae Lee, Sung-Jei Hong, Min-GiKwak, Namsu Kim, Chul Jong Han, Jong-Woong Kim, "Ultra-thin and smooth transparent electrode for flexible and leakage-free organic light-emitting diodes," *Sci. Rep.*, vol. 5, no. 9464, pp. 1-8, Mar. 2015.
- [4] Dong-Ju Kim, Hyo-Joong Kim, Ki-Won Seo, Ki-Hyun Kim, Tae-Wong Kim, Han-Ki Kim, "Indium-free, highly transparent, flexible $\text{Cu}_2\text{O}/\text{Cu}/\text{Cu}_2\text{O}$ mesh electrodes for flexible touch screen panels," *Sci. Rep.*, vol. 5, no. 16838, pp. 1-10, Nov. 2015.
- [5] Xiaopeng Bai, Sen Lin, Haolun Wang, Yi Zong, Haiyang Wang, Ziyun Huang, Donglai Li, Chang Wang, Hui Wu, "Room-temperature processing of silver submicron fiber mesh for flexible electronics," *Flexible Electronics*, vol. 2, no. 3, pp. 1-7, Jan. 2018.
- [6] Zhi-nong Yu, Jian-jian Zhao, Fan Xia, Ze-jiang Lin, Dong-puZhang, JianLeng, WeiXue, "Enhanced electrical stability of flexible indium tin oxide films prepared on stripe SiO_2 buffer layer-coated polymer substrates by magnetron sputtering," *Applied Surface Science*, vol. 257, no. 11, pp. 4807-4810, Mar. 2011.
- [7] Kosuke Sakamoto, Hiroyuki Kuwae, Naofumi Kobayashi, Atsuki Nobori, Shuichi Shoji, Jun Mizuno, "Highly flexible transparent electrodes based on mesh-patterned rigid indium tin oxide," *Sci. Rep.*, vol. 8, no. 2825, pp. 1-8, Feb. 2018.
- [8] Hanju Lee, Shant Arakelyan, Barry Friedman, Kiejin Lee, "Temperature and microwave near field imaging by thermo-elastic optical indicator microscopy," *Sci. Rep.*, vol. 6, no. 39696, pp. 1-11, Dec. 2016.
- [9] Hironori Tohmyoh, Shoho Ishikawa, Mikio Muraoka, "Nonocontact evaluation of the electrical conductivity of thin metallic films by eddy current microscopy," *Surf. Interface Anal.*, vol. 44, no. 9, pp. 1294-1298, Apr. 2012.
- [10] Bi-Yi Wu, Xin-Qing Sheng, Rene Fabregas, Yang Hao, "Full-wave modeling of broadband near field scanning microwave microscopy," *Sci. Rep.*, vol. 7, no. 16064, pp. 1-10, Nov. 2017.
- [11] Nalladega, Vijayaraghava, Design and Development of Scanning Eddy Current Force Microscopy for Characterization of Electrical, Magnetic and Ferroelectric Properties with Nanometer Resolution, Dayton, Ohio: University of Dayton, 2009.
- [12] Hong Zhang, Ruizhen Yang, Yunze He, Ali Foudazi, Liang Cheng, Guiyun Tian, "A Review of Microwave Thermography Nondestructive Testing and Evaluation," *Sensors*, vol. 17, no. 5, pp. 1-33, May. 2017.
- [13] ShantArakelyana, Hanju Lee, YeonghunJeong, Arsen Babajanyan, Barry Friedman, Kiejin Lee, "Direct imaging of the SSD and USB memory drives heating by thermo-elastic optical indicator microscopy," *Case Studies in Thermal Engineering*, vol. 10, pp. 407-412, Sep. 2017.
- [14] ShantArakelyana, Hanju Lee, Kiejin Lee, Arsen Babajanyan, Barry Friedman, "Detecting defects in sub-skin-depth metallic layers by a thermo-elastic sensor," 2017 IEEE SENSORS, Glasgow, UK, 2017, pp. 1-3.

Bessel Beam Radial Slot Antenna

(Proceedings of the Int. Conference on “ Microwave and THz Technologies and Wireless comm.”)

O.Mahmoodian , A.Hakhoumian

Institute of Radiophysics and Electronics, Alikhanian Brothers str . 1.0203 Ashtarak, Armenia

Received 15 November 2018

Abstract: The resonance type radial slot antenna as a high efficiency Bessel beam launcher was designed and investigated in wide band of operation frequencies. The analytical method to determine resonant frequencies of short-circuit radial line was evaluated and applied to calculation of the resonant frequencies of the radial resonators with different modes number, dielectric permittivity and sizes. The experimental results are in good agreement with calculation once. The expression for E and H are obtained and applied to the calculation of both electric and magnetic fields distributions. The impedance, voltage and current of radial line are investigated and related diagrams of intended modes are plotted. The circular slots are located on the top plate of radial line and are excited by the radially inward traveling transverse electromagnetic (TEM) mode in the upper part of line. The slots are arrayed on top plate which they can couple with the radial current flowing over the line to produce a radially polarized broadside beam. The position of these radiating slots is estimated from the maximum values of current distribution of line. It was founded that the observe at the distance up to 70λ .

Keywords: Radial slot antenna, circular antenna array, radially polarized.

1. Introduction

Recently, an increasing interest of generation of Bessel beams has arisen in microwave and millimeter applications. In optics and acoustics there is several methods to lanching Bessel beams, but in microwaves and millimeter waves only a few works have been recently done. In order to generate and lanching Bessel beams for microwave, radial line slot array antennas (RLSA) for satellite application and circular antenna array (CAA) for WiFi are Good examples[6]. Another main application of this type of antenna is direct broadcasting from a satellite (DBS) using $12GHz$ band which has become in commercial use in Japan[8]. In this study we proposed the broadband radial slot antenna which is the multi operational frequency antenna which can also be used for generation of Bessel beams. The structure of radial line is simple but it is the nonuniform transmission line which it's impedance vary with the radius of line.

2. Radial line theory

Radial line is composed of a parallel conductive plates and its dielectric counterpart that will generate transverse Electro Magnetic (TEM) waves and are guided radially away from source when the source is exciting the central hole of the plate Fig 1. The wave under consideration has no field variation either circumferentially or axially. The component E_z having no variation in the Z direction corresponds to a total voltage $E_z d$ between plates. The component H_θ corresponds to the total radial current $2\pi r H_\theta$, outward in one plate and inward in other [1].

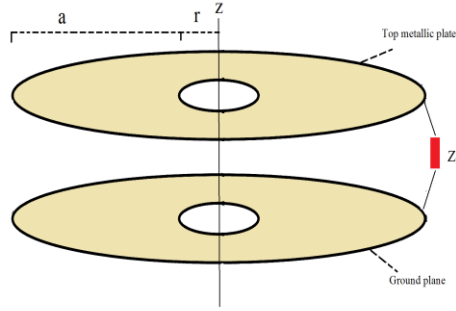


Figure 1: schematic of short circuit Radial transmission line

Among any types of electromagnetic waves which can propagate in such medium (line), we consider only such, waves which satisfied the following condition and it depends only on the radius r , $\partial/\partial\theta = \partial/\partial z = 0$ [2]. The general solution of Helmholtz equation is:

$$\xi(z) = A_1 e^{-ik_z z} + A_2 e^{ik_z z}. \quad (1)$$

and the scalar Helmholtz equation of radial waveguide is

$$\frac{1}{r} \frac{\partial}{\partial r} \left(r \frac{\partial \Psi}{\partial r} \right) \frac{1}{r^2} \frac{\partial^2 \Psi}{\partial \theta^2} + k_c^2 \Psi = 0 \quad (2)$$

if we put $z=0$ in (1), then $\xi(z) = A$ and equation 2, for the function Ψ can be written as:

$$\frac{1}{r} \frac{\partial}{\partial r} \left(r \frac{\partial \Psi}{\partial r} \right) + k^2 \Psi = 0 \quad (3)$$

So in this case $k_c^2 = k^2 - k_z^2 = k^2$.

Since $k_c = (\gamma^2 + k^2)^{1/2}$ and $\gamma = 0$ then $k_c = \omega \sqrt{\mu \epsilon}$ and resulting

$$\Psi = A_1 H_0^{(1)}(kr) + A_2 H_0^{(2)}(kr), \quad (4)$$

where $H_m^1(x), H_m^2(x)$ are Hankel functions of the first and the second kind of order m .

The first term of equation 4, defines a traveling wave Propagating to the transmission line axis and the second term presents the reflected wave from the axis of the traveling wave. The electromagnetic field of this wave can be describe as follow

$$E_z = BH_0^{(2)}(kr), H_\theta = -i\omega\epsilon A_2 \partial H_0^{(2)}(kr) / \partial r = I_{z_0}^{-1} BH_1^{(2)}(kr) \quad (5)$$

where $B = K^2 A_2$.

The remained components of the field are equal to zero, where $kr \gg 1$,

$$\frac{E_z}{H_\theta} = \frac{Z_0 H_0^{(2)}(kr)}{I H_1^{(2)}(kr)} = Z_0 \frac{e^{i(kr - \pi/4)}}{ie^{-i(kr - \pi/4 - \pi/2)}} = -Z_0$$

Therefore, the line extends in a radial cylindrical homogeneous (uniform).
The voltage and current of line can be written as follow

$$V_r = -\int_0^d \mathbf{E}_z(r) dz = -BdH_0^{(2)}(kr) \quad (6)$$

$$I(r) = -2\pi r H_\theta(r) = -2\pi i r Z_0^{-1} B H_1^{(2)}(kr) \quad (7)$$

The characteristic impedance of the radial line is presented as

$$Z_b(r) = d \frac{Z_0}{2\pi r} \frac{H_0^{(2)}(kr)}{-iH_1^{(2)}(kr)}. \quad (8)$$

Thus, the radial line is irregular and its characteristic impedance depends on the radius r , Where $kr \gg 1$:

$$Z_n(r) = Z_0 \frac{d}{2\pi r} \quad (9)$$

Z_b is inversely proportional to the radius r [2].

Radial wave in such transmission line is limited to a perfectly conducting cylindrical surface $r = a$.

$$\Psi(a) = A_1 H_0^1(ka) + A_2 H_0^2(ka) = 0 \quad (10)$$

We put A_1 in A_2 and find

$$\Psi(r) = B \left[H_0^1(kr) H_0^1(ka) - H_0^2(kr) H_0^2(ka) \right] \quad (11)$$

where $B = A_2 / H_0^{(2)}(ka)$.

$$\Psi(r) = C \left[J_0(kr) N_0(ka) - J_0(ka) N_0(kr) \right] \quad (12)$$

This expression determines the electromagnetic field of a standing wave

$$E_z = D \left[J_0(kr) N_0(ka) - J_0(ka) N_0(kr) \right]. \quad (13)$$

$$H_\theta = iZ_0^{-1} D \left[J_1(kr) N_0(ka) - J_0(ka) N_1(kr) \right], \quad (14)$$

where r is any radius of radial line from center (feed point) until the edge of line and a is the constant radius of radial line where the boundary condition of line according to 13, can be considered as follow:

$E_z = 0$ on $r > 0$ and so close to zero,

$E_z = 0$ on $r = a$.

3. Resonant frequency of radial line

The radial line discontinuities have been considered completely by Whinnery [1] and by Bracewell [5]. Radial line can be use as a resonator in any modes, but no any more practical works are done on it. Only e few approximation methods exist about radial line resonator and determination of its resonance frequency. In this paper we tried to calculate the resonance frequencies of short- circuit radial line for different modes. According to formula (13) which is suggested by Gerigorev, resonance frequency occurs when the value of E_z equals zero. This expression shows that the value of E field is the function of r and depends to the first and second kind of Bessel function of zero order $J_0(kr)N_0(kr)$ respectively. For $r = 0$, the second kind of Bessel function is infinity results infinity value of H_θ that means the impedance of feed is not finite , therefore we use a coaxial line as a probe feed in the central hole of radial line, where the radius of hole is equals to the radius of inner conductor of coax line or Transformer. By changing the r for different frequencies when E_z becomes zero both resonant frequency and radius of radial can be determined. The same work have been done by D.C. Stinson [3] as follow equation:

$$[J_0(ka)N_0(kb) - J_0(kb)N_0(ka)] = 0 \tag{15}$$

Which is the equation whose roots determine the resonance frequencies of coaxial resonator [4]. In order to estimate the resonance frequencies of radial resonator fed by coaxial cable, which a is the diameter of inner conductor of coax (feed point) and b is the radius of radial line [3], [4] as is presented in (Fig. 2).

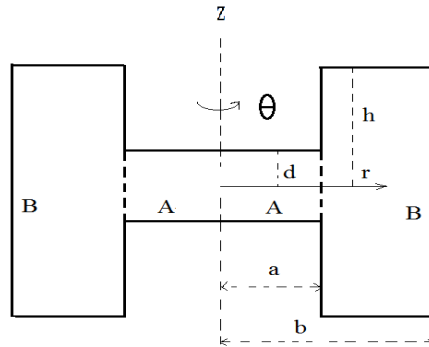


Figure2 :The schematic view of radial transmission line.

Region (A) introduces the inner conductor of coax and region (B) indicates the radial resonator. In order to calculate resonance frequency and the size of radial (b) for any shorted radial resonator we can do as follow:
 For any intended resonance frequency, by foreseeing the related dielectric constant and suitable coax we can calculate b as the radial radius. If the radius of radial (b) is fixed we can calculate E_z in any frequencies which the magnitude of E_z in both points, $r = a$ and $r = b$ equals zero. For first mode, the electric field within the center of radial fed by coax ($r = a$) and also in the edge of radial ($r = b$) equals zero. For any fixed radial size (b), we are able to calculate the related resonance frequency. In general for both methods we select the radius of radial a and then we calculate the E_z in different frequencies.

Another simple approximation to determine resonance frequency is using Bessel function of the first kind of order zero $J_n(kr)$. Therefore, for $n = 0$,

$$J_0(kr) = 0 \text{ when } kr = 2.404; 5.52; 8.653; 11.791; \dots$$

$$\text{or } J_0\left(r \frac{2\pi}{\lambda_0} \sqrt{\varepsilon}\right) = 0.$$

4. Position of circular radial slots and emission

Radial line slot antenna consist of a parallel disk of metal placed above and separated from another such disk and which slots are located on upper metallic plate to get uniform amplitude and phase [7]. Circular radiating elements are located on antenna which allow electromagnetic energy to free up. Slots are designed to couple with currents on the top plate, so the magnetic field in the upper plate determines an excitation coefficient of a slot [8]. Emission of slots occurs when the magnetic field is maximum. Changes in the amount of electric current in the radial line at different radii by Formula [7] can be plotted so that the maximum points represent the appropriate radius for inserting the slots. At the resonant frequency at each point where the electric field is zero, the magnetic field and electric current are maximized. Slots separated one guided wavelength to the other in order to get the radial polarization.

5. Measurement

The prototype of antenna is shown in Fig. 3. Radial line is performed by 1.5mm high substrate which dielectric constant is 2.17. The radius of radial line is 44mm and radiating gaps are located in 10.1mm and 32.6mm distance from the center of radial line and the width of slots is about 1mm. The measurements include:

- A. The resonance frequency and VSWR of line for multi-modes which is shown in Fig. 4.
- B. The diagram of electric and magnetic fields, voltage and current of radial line at 9GHz which E diagram shows the resonance frequency and current maximum amplitudes presents the position of the first and second slots of antenna.
- C. The radiation pattern of antenna at 8.85GHz. Antenna under test moves 40centimeter to the right and left in different distances from the source antenna (Fig 6) and radiation pattern of antenna reflected by parabolic reflector (Fig 7), which the gain is measured in decibel.

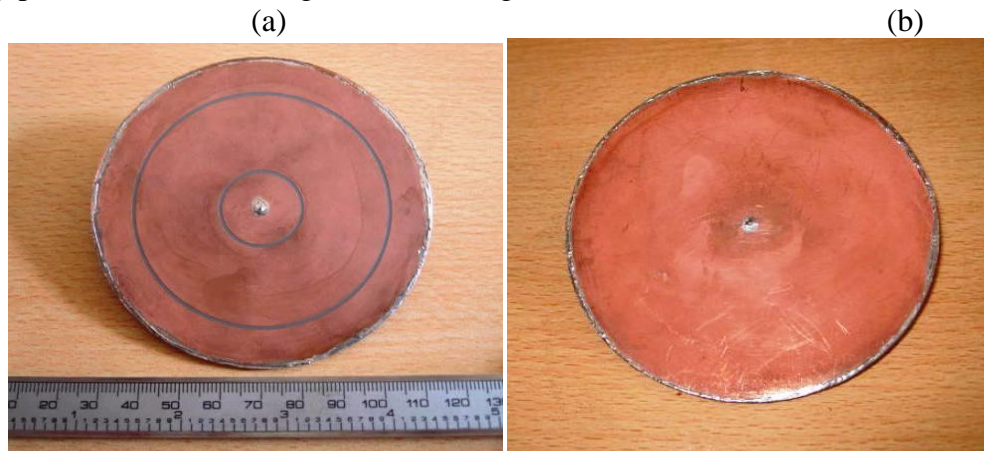
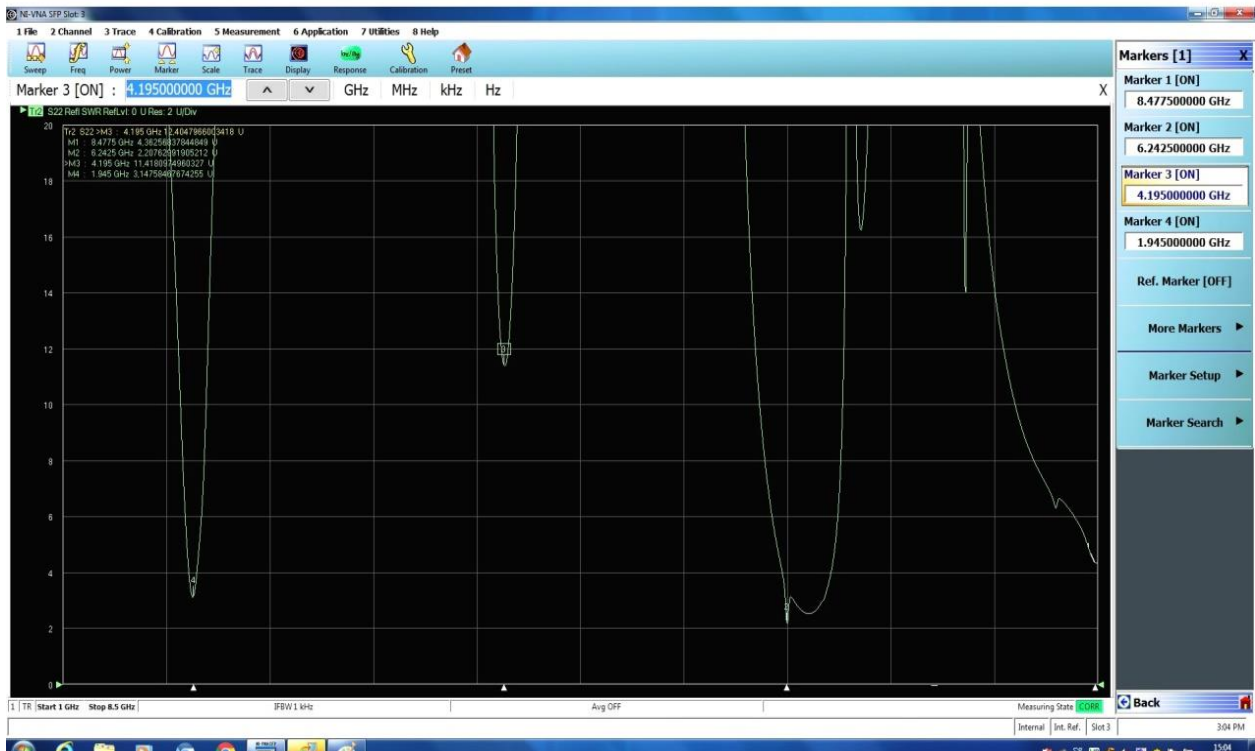


Figure 3: (a) Short circuit Bessel beam slot antenna, (b) Radial line resonator.

Radial antenna radius(b)(mm)	44
Feed probe radius(a)(mm)	0.3
Dielectric constant	2.17
Radial thickness(h)(mm)	1.5
Number of modes	4
Number of slots	2
Slots radius (mm)	10.1 , 32.6

Table1:Antenna specification



Calculated Resonance frequency(GHz)	Practical resonance Frequency(GHz)	VSWR
2	1.945	3.14
4.3	4.195	11.47
6.65	6.242	2.2
9	8.477	4.3

Figure 4:The resonance frequencies for 1th to 4th modes with related VSWR

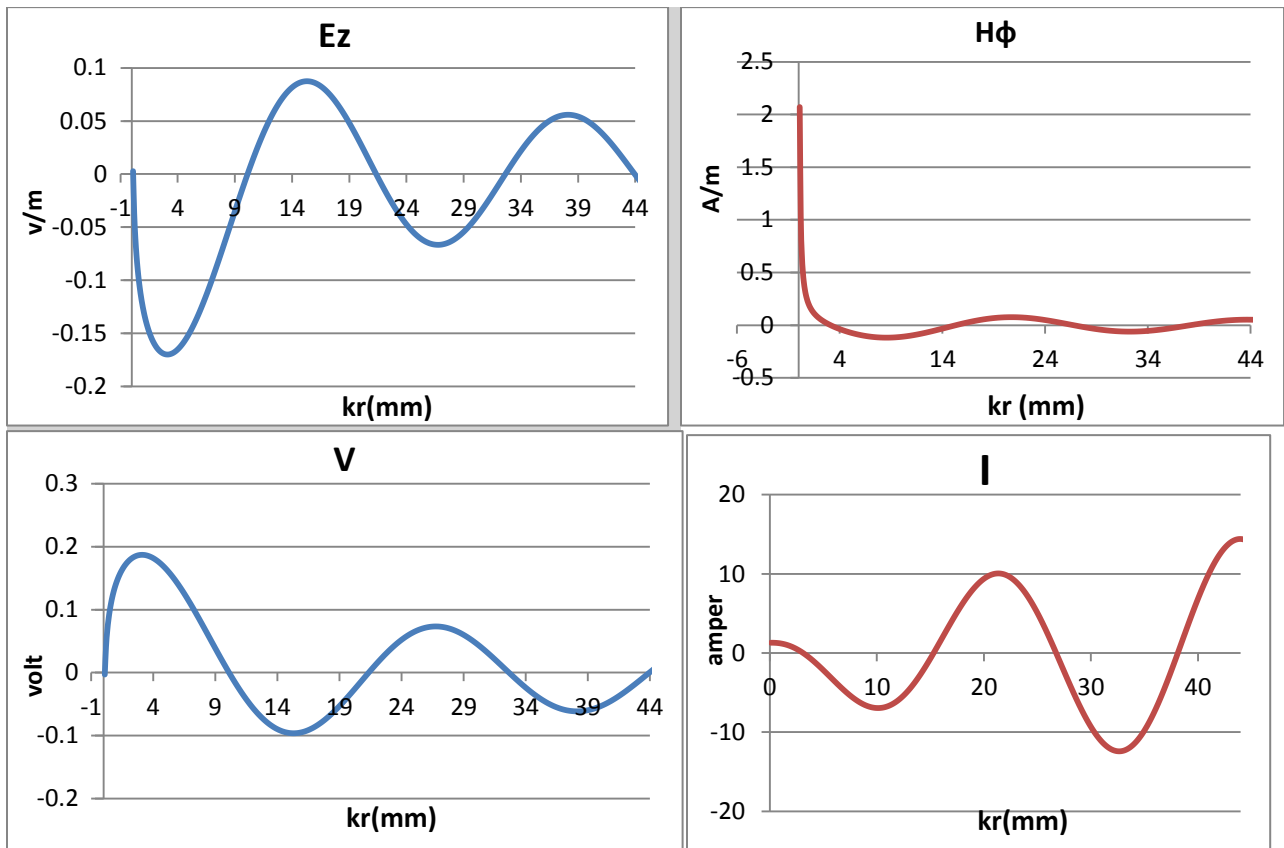


Figure 5: Diagram of E and H fields, voltage and current of resonator of 44 mm radii for 9GHz operation frequency.

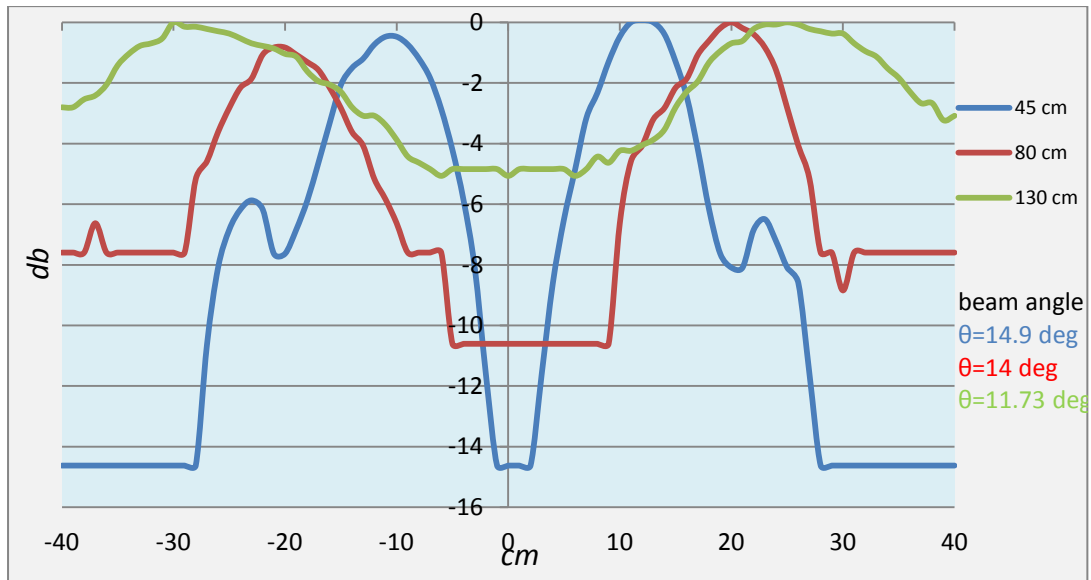


Figure 6: The directivity of antenna at 8.85 GHz for three different distance from source.

6. Conclusion

This paper presents the design of resonance Bessel beam radial slot antenna. The resonance radius of line and its resonance frequencies for different modes, measured and obtaining good results. The position of slots is measured according to the maximum value of current distribution of radial line. The Antenna far field radiation pattern is plotted for different distances from the source and presenting the good results. As we expected the far field directivity of Antenna is in the form of the Bessel function.

References

- [1] Simon Ramo, John R. Whinnery, Theodore Van Duzer: "Fields and waves in communication electronics", 3rd edition, pp.464-468, 1993, USA.
- [2] A.D. Grigorev: Electrodynamic and microwave technology, pp.115- 116, 1990
- [3] D.C. Stinson: Resonant Frequencies of Higher-Order Modes in Radial Resonator, IRE Transactions on Microwave Theory and Techniques, pp.18-23, 1955.
- [4] H.B. Dwight: "Table of roots for natural frequencies in coaxial type cavities", Jour. Math. Phys, vol.27, pp.84-89: April 1948.
- [5] R.N. Bracewell: ".Step Discontinuities in Disk Transmission lines, 1954.
- [6] Teddy Purnamirza, Donny Kristanto, and Imran M. Bin Ibrahim: A design of Compact Radial Line Slot Array (RLSA) Antennas for Wi-Fi Market Needs, Progress in Electromagnetic letters, vol.64, 21-28, 2016.
- [7]. Manuel Sierra-Castaner, Manuel Sierra-Perez, Maria Vera-Isasa and Jose Luis Fernandez-Jambrina: Low-Cost Monopulse Radial Line Slot Antenna, IEEE Transactions on Antennas and propagation, vol. 51, no. 2, pp.256-263: february 2003.
- [8]. Makoto Ando, , Kimio Sakurai, Naohisa Goto, , Kunitaka Ahmum, and Yoshiharu Ito: A Radial Line Slot Antenna for 12 GHz Satellite TV Reception, IEEE Transactions on Antennas and propagation, vol, AP-33, no. 12, pp.1347-1353: December 1985.

Estimation of Phase Noise Impact on Coherence Length in FM-CW Radars With Voltage Controlled Oscillators

(Proceedings of the Int. Conference on “Microwave and THz Technologies and Wireless comm.”)

A.A. Hakhoumian¹, A.H. Makaryan², N.G. Poghosyan¹, T.V. Zakaryan^{1*}

¹*Institute of Radiophysics and Electronics, Armenian National Academy of Sciences*

Alikhanian 1, Ashtarak, 0203, Armenia

²*Yerevan State University, A. Manoogian 1, Yerevan, 0025, Armenia*

*E-mail: tigr@irphe.am

Received 15 November 2018

Abstract: In this paper we analyze phase noise “propagation” within FM-CW radar originated from voltage controlled oscillator (VCO), which is of great importance from the viewpoint of effective moving target indication (MTI).

Keywords: Phase noise, voltage controlled oscillators, homodyne receiver, power spectrum density.

1. Introduction

Generally, circuit and device noise can perturb both the amplitude and phase of oscillator’s signal. Because usually amplitude fluctuations are greatly attenuated, the phase noise generally dominates [1-3]. In radars with VCOs in use, the stability and noisy spectrum of tuning voltage is of great interest. Obviously, noisy spectrum of tuning voltage is somehow transformed into another phase spectrum at the output terminal of VCO. In other words, VCO operates like a “noise transformer”. Much noise we apply to the tuning terminal, more phase noise we have at output terminal. The purpose of this paper is to estimate the coherence time of Doppler type homodyne receiver due to VCO’s phase noise.

2. Transformation of frequency noise into phase noise

Let’s assume we have Doppler homodyne receiver and the power spectrum density (PSD) of phase noise of oscillator is $L_1(\omega)$. The PSD of the reflected signal hence will be [4]

$$L(\omega) = 2L_1(\omega)(1 - \cos \omega t_0) = 4L_1(\omega) \sin^2 \frac{\omega t_0}{2} \quad (1)$$

where t_0 is time delay of reflected signal, and ω is cyclic frequency offset. Instantaneous frequency of the system can be presented as

$$\Omega(t) = \omega_0 + \omega_1(t), \quad (2)$$

where $\omega_1(t)$ is a noisy component of the frequency. In order to determine Doppler shift (beating frequency) we need to estimate the spectrum of frequency noise. So, instantaneous phase of oscillator is expressed as

$$\varphi(t) = \int_{-\infty}^t \Omega(t) dt. \quad (3)$$

Substituting (2) into (3) we have

$$\varphi(t) = \varphi_0 + \omega_0 t + \int_{-\infty}^t \omega_1(t) dt . \quad (4)$$

If the PSD of frequency noise $L_1^\omega(\omega)$ is already known, hence according to the integration property of Fourier transform, the PSD of phase noise $L_1(\omega)$ in stationary case will be

$$L_1(\omega) = \frac{L_1^\omega(\omega)}{\omega^2} . \quad (5)$$

Collecting all (5), (2) and (1) it is easy to obtain

$$L(\omega) = 4 \frac{L_1^\omega(\omega)}{\omega^2} \sin^2 \frac{\omega t_0}{2} = t_0^2 L_1^\omega(\omega) \sin^2 c^2 \frac{\omega t_0}{2} , \quad (6)$$

where $\text{sinc} x = \frac{\sin x}{x}$ is non-normalized cardinal sine function.

By definition, the coherence time is defined as the width of equi-area rectangular having the height equal to the maximum value of correlation function (Fig. 1)

$$\tau_{coh} = \frac{1}{R_0} \int_0^\infty R(\tau) d\tau , \quad (7)$$

where $R(\tau)$ is correlation function.

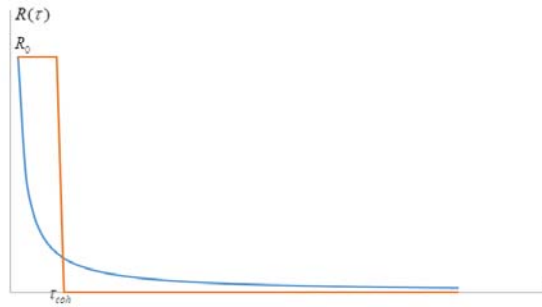


Fig. 1. Definition of coherence time

According to Wiener-Khinchin theorem

$$R(\tau) = \frac{1}{2\pi} \int_0^\infty L(\omega) e^{-i\omega\tau} d\omega . \quad (8)$$

Let's assume $L_1^\omega(\omega)$ is like white Gaussian noise

$$L_1^\omega(\omega) = L_0^\omega . \quad (9)$$

Substituting (6) and (9) into (8) and taking into account the duality property of Fourier transform finally we have for correlation function

$$R(\tau) = \frac{1}{2\pi} \int_0^\infty t_0^2 L_1^\omega(\omega) \sin c^2 \frac{\omega t_0}{2} e^{-i\omega\tau} d\omega = 4\pi t_0 L_0^\omega \text{tri}(\tau / t_0), \quad (10)$$

where $\text{tri}(x)$ is normalized symmetric triangle function.

Then substituting (10) into (7) we obtain

$$R_0 = R(\tau = 0) = 4\pi t_0 L_0^\omega, \quad (11)$$

$$\tau_{coh} = \int_0^\infty \text{tri}(\tau / t_0) d\tau = \frac{t_0}{2}. \quad (12)$$

Taking into account (6) and (9), the velocity of “phase drift” σ^2 can be expressed as

$$\sigma^2 = \frac{1}{2\pi} \int_0^\infty L(\omega) d\omega = \frac{L_0^\omega t_0}{\pi} \int_0^\infty \sin c^2(x) dx = L_0^\omega \frac{t_0}{2}, \quad (13)$$

and for absolute “phase drift” φ_{drift} we find from (12)

$$\varphi_{drift} = \sigma^2 \tau_{coh} = \frac{L_0^\omega t_0^2}{4}. \quad (14)$$

3. Conclusion

The criterion at which the sufficient “phase drift” results to coherency breaking in the system [5], can be expressed as

$$\varphi_{drift} \sim \pi, \quad (15)$$

or for maximum “unbroken” coherent time delay finally we obtain

$$t_0 \sim \sqrt{\frac{4\pi}{L_0^\omega}}. \quad (16)$$

Hence, the coherent time delay inversely depends on the square root of power spectrum density of generator’s frequency noise.

References

- [1]. M. Skolnik, Introduction to Radar Systems, 3rd ed. (McGraw-Hill, New York, 2001)
- [2]. V. Carotenuto *et al.*, IEEE Radar Conf., Arlington VA, 10-15 May (2015), 0274.
- [3]. T. Lee *et al.*, Solid State Circuits **35** (2000) 326.
- [4]. A. Hakhoumian *et al.*, Electromagnetic Waves and Electronic Systems **16** (2011) 43 (in Russian).
- [5]. G. Stroke, An Introduction to Coherent Optics and Holography, (Academic Press, New York, 1966).

Frequency Conversion in The Ferromagnet at Low Magnetic Bias Fields

(Proceedings of the Int. Conference “Microwave and THz Technologies and Wireless comm.)

T. Yezekyan, A. Makaryan*, V. Tadevosyan

Radiophysics and Electronics Dept., Yerevan State University, Yerevan, Alex Manoogyan str. 1, 0025 Armenia

E-mail: armenm@ysu.com

Received 15 November 2018

Abstract: The detection and second harmonic generation of microwave radiation in a ferromagnetic material at low magnetic bias fields was experimentally obtained at room temperature. On certain conditions, under the influence of the microwave signal, the magnetic moment of the magnetized ferrite performs nonlinear oscillations, which results the frequency conversion. The dependence of the converted signal on the magnetizing field was measured for different forms of the magnetization curve. It was shown that the conversion efficiency strongly depends on the shape of the magnetization curve of the ferromagnetic sample, as well as on the magnitude of the bias magnetic field. The results of this study may find applications for the registration and frequency conversion of radiation, for information data recording etc.

Keywords: Low magnetic bias field, nonlinear oscillations, ferromagnetic resonance, magnetic moment.

1. Introduction

The properties of ferromagnetic materials in the microwave fields were studied extensively at the beginning of the last century, after the experimental detection of ferromagnetic resonance.

The behavior of the magnetic moment in a magnetic field is described by the Landau-Lifshitz equation, which is significantly nonlinear. For the first time, the nonlinear phenomena in ferromagnetic materials in the microwave region were discovered by Bloembergen and Damon [1]. Later, numerous letters were published regarding the generation, detection, frequency conversion and amplification of microwave radiation using ferromagnetic materials (see for example [2, 3]).

These nonlinear phenomena occur only in the presence of a component of the microwave field perpendicular to the orientation of the constant magnetization of the ferromagnet. Phenomena occur at any amplitude of the microwave field, but, being a quadratic effect, they are clearly manifesting only at sufficiently large fields. Nevertheless, according to the Landau-Lifshitz equation, in the case of a parallel orientation of the alternating magnetic field with respect to the magnetic moment, no interaction between the microwave signal and the ferrite can occur.

However, there are many publications, where the changes of the magnetic moment of ferromagnetic sample was demonstrated under the influence of a linearly polarized electromagnetic radiation [4-8].

In [4] a mechanism is proposed to explain the nonlinear interaction of electromagnetic radiation with a magnetized ferromagnetic. The experimental results presented in [4-6] (the dependence of the amplitude of the detected signal on the angle of the laser polarization, polarity reversal, as well as the presence of the detected signal maximums), are in good agreement with the proposed mechanism of occurrence of non-linearity. However, it is generally considered that the abovementioned phenomena cannot be related to a magnetic nonlinearity of ferromagnetic, because in the optical region, magnetic permeability of ferromagnetic materials is practically equal to one. Therefore, the interpretation of the ultrafast magneto-optical response of ferromagnetic materials is still the subject of discussions.

In the present work, the detection and frequency doubling of the low-power microwave radiation in a magnetized ferromagnetic material is obtained, when the magnetic field of the

microwave radiation is collinear to the magnetization vector of the ferromagnetic material. The dependence of the conversion efficiency on the parameters of the microwave signal and on the characteristics of the ferromagnetic sample was investigated.

2. Experimental setup and results of measurement

The block diagram of the experimental setup is shown in Fig. 1.

From the microwave generator 1 (VSG25A) modulated RF signal was fed to the primary coil wound around the investigated ferromagnetic sample 2 (see. Fig. 1). As a non-linear ferromagnetic sample, a low-frequency Nickel-Manganese ferrite with rectangular shape by dimensions of $2.8 \times 5.6 \times 8 \text{ mm}^3$ was used.

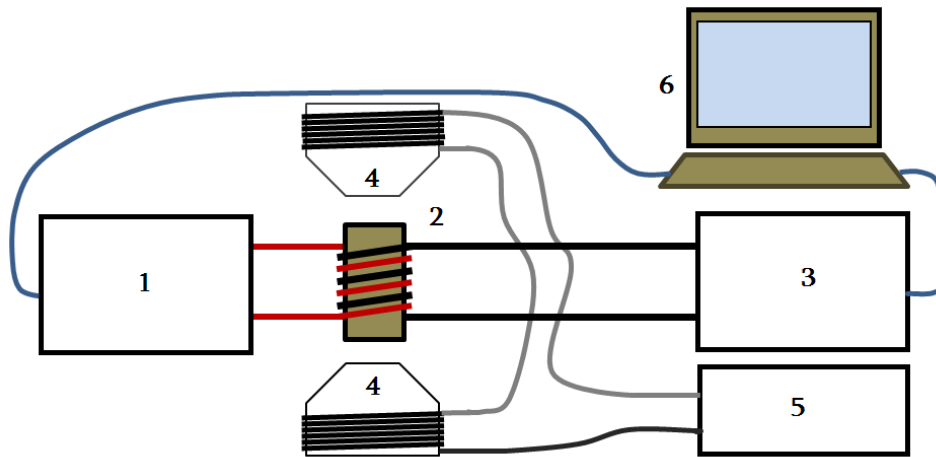


Fig. 1. The block diagram of experimental setup: 1-the microwave generator VSG25A, 2-low-frequency Nickel-Manganese ferrite, 3- USB-SA124B spectrum analyzer, 4-electromagnet, 5-controlled DC power supply, 6-PC

To obtain an effective transformation, it is necessary to magnetize the ferrite sample with a bias magnetic field, where the nonlinearity is maximal. For the magnetization of ferromagnetic sample, it was placed in a magnetic field of the controlled electromagnet 4.

In such configuration of the ferromagnetic sample and electromagnet, the magnetic field of microwave radiation proves to be parallel to the constant magnetizing field.

As was shown in [5, 6], one of the important characteristics of magnetic materials, which can be used for the estimations of nonlinear properties of materials, is the static magnetization curve. The magnetization curve can take various forms, depending on the composition, size and shape of the sample, as well as on the magnetic properties of the medium.

Therefore, we measured the static magnetization curve for the sample used in the experiments, which is completely described by the differential magnetic permeability of the sample:

$$\mu'(H_0) = (dBv / dH) |_{H=H_0} \quad (1)$$

The shape of the magnetization curve of our sample is shown in Fig. 2a.

For registration of the detected signal (change in the average value of the magnetic moment of the sample under the influence of the microwave field, $\nu = \nu_{\text{mod}}$) and the signal at the double frequency ($\nu = 2\nu_0$), the secondary coil was also wound on the same ferrite sample, as shown in Fig. 1.

The signal on the secondary coil was detected by a USB-SA124B spectrum analyzer connected to a PC.

Measurements were made both in the sweep mode (sweep range is 0.5-2.5 GHz) and for a separate, fixed frequencies. It should be noted that the detection had non-resonant character and any features over the entire range of the microwave generator (0.5-2.5 GHz) were not obtained.

In Fig.2. along with the magnetization curve, the dependence of the magnitude of the detected signal (with the carrier frequency of the input microwave signal $\nu_0 = 1.5 \text{ GHz}$, and modulation frequency $\nu_{\text{mod}} = 120 \text{ kHz}$) on the bias magnetic field is shown (Fig. 2b). As expected, the maximal value of the detected signal is obtained when the bias magnetic field is $H \approx 50 \text{ Oe}$; this is the region where the changes of slope of the magnetization curve of the ferromagnetic sample are most rapid. A similar dependence on the magnetic field bias was also obtained for the magnitude of the second harmonic.

Reversing the direction of the external magnetic field, leads to the reversal of the sign of the detected signal.

We measured the magnitudes of both the detected signal and the second harmonic of the signal, depending on the power of the main microwave signal ($\nu_0 = 1.5 \text{ GHz}$), results are presented in Fig. 3.

The corresponding spectra of the signals (both the detected and the second harmonic), measured by the USB-SA124B spectrum analyzer, are presented in Fig. 4a and 4b, respectively.

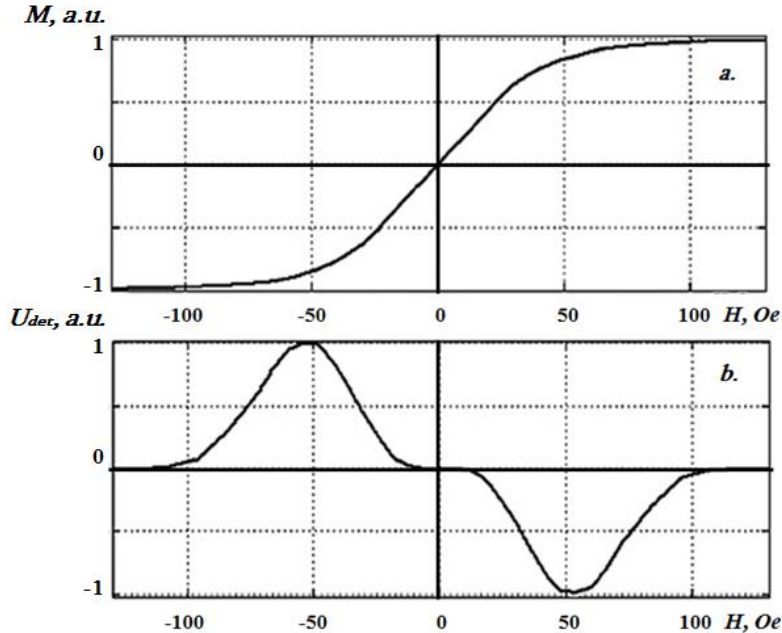


Fig. 2. a -The shape of the magnetization curve of Nickel-Manganese ferrite sample, b-The dependence of detected signal magnitude on bias magnetic field.

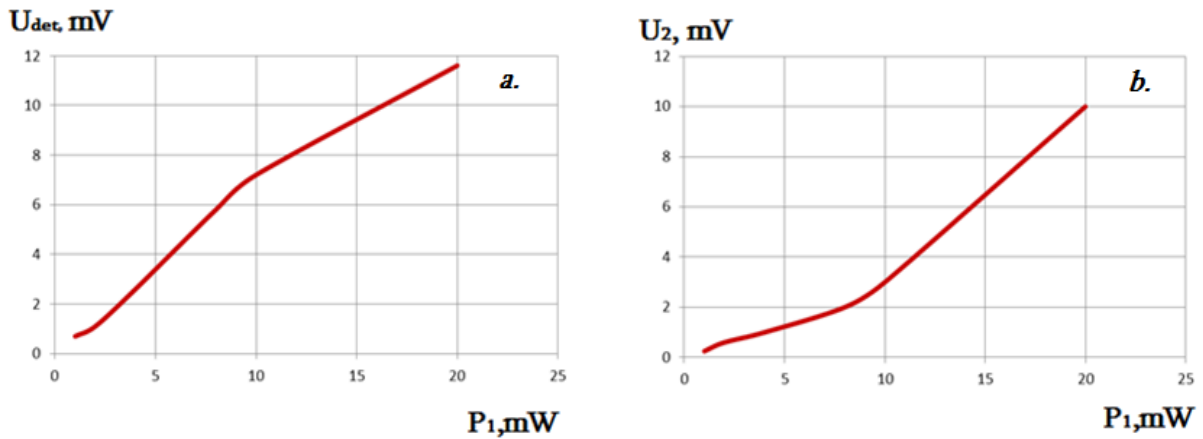


Fig. 3. The magnitudes of obtained signals depend on the power of the main microwave signal ($\nu_0=1.5$ GHz, $\nu_{mod} = 120$ kHz): *a*-detected signal ($\nu_{det} = 120$ kHz), *b* - second harmonic ($\nu=3$ GHz).

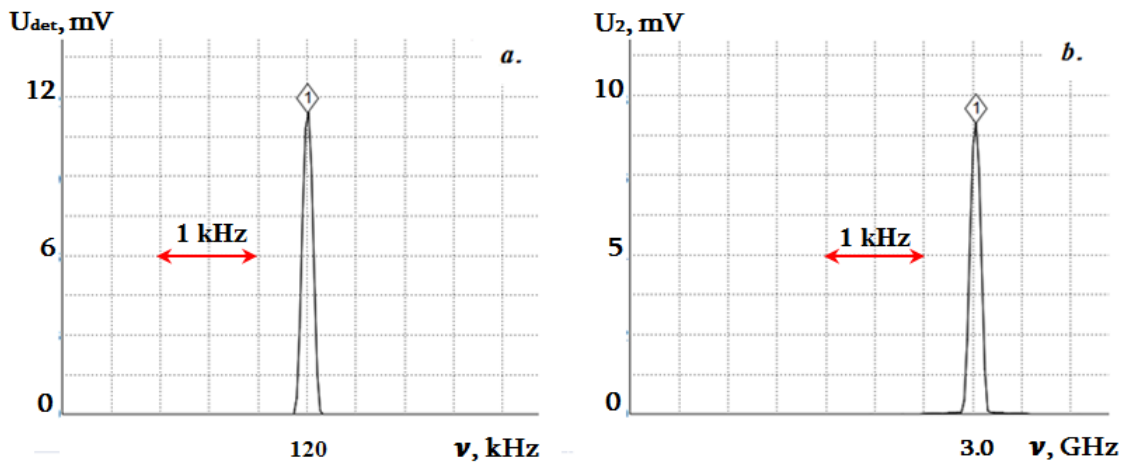


Fig. 3. *a*-The spectrum of detected signal, *b*-The spectrum of second harmonic signal.

3. Discussion and conclusions

Summarizing, the detection and frequency doubling of microwave radiation in the low-frequency ferrite at room temperature was experimentally obtained.

In [1-3] the nonlinear phenomena of ferrites are the result of a ferromagnetic resonance and manifest themselves only when the constant (magnetizing) H_0 and alternating (microwave) H_{\sim} magnetic fields are mutually perpendicular.

However, our studies have shown that nonlinear interactions in the ferromagnet can also occur at the collinear arrangement of H_0 and H_{\sim} , which is impossible according to the Landau-Lifshitz equation. The measurement results show that the magnitudes of the detected signal as well as the signal on the doubled frequency significantly depends on the bias magnetic field H_0 and the shape of the magnetization curve. This means that the magnetic moment, in addition to the damped precession, also oscillates at the frequency of the alternating magnetic field. However, the amplitude of oscillations of magnetic moment in the sample depends on the slope of the magnetization curve (on the differential magnetic permeability μ') at a given value of the bias

magnetic field. Consequently, at the certain values of the bias magnetic field, the magnetic moment in the ferromagnetic sample will perform nonlinear oscillations.

In the region of the quadratic nonlinearity of the magnetization curve, a low-frequency component, which is proportional to the power of the microwave signal, and the second harmonic of the microwave signal will appear in the spectrum of oscillations of the magnetic moment.

Comparison of the measurement results shows that the magnitude and sign of the detected signal, as well as the magnitude of the second harmonic signal correlate well with static curves of differential magnetic permeability.

In conclusion, we suppose that the results obtained can find practical applications in the detection and frequency conversion of electromagnetic radiation, in recording, information processing and storing etc.

References

- [1] N. Bloembergen, R.W. Damon, Relaxation Effects in Ferromagnetic Resonance. Phys. Rev. (1952) Vol. 85. P.699.
- [2] Ed. by A. G. Gurevich (1961) Ferrites in Nonlinear SHF Devices. Collection of Articles (Inostr. Liter., Moscow) [in Russian].
- [3] Ed. by A. L. Mikaelian (1963) Nonlinear Properties of Ferrites in SHF Fields. Collection of Articles (Inostr. Liter., Moscow) [in Russian].
- [4] R.M. Martirosian, A.H. Makaryan, V.M. Mekhitarian, V.R. Tadevosyan Optical Detection in a Ferromagnet. JETP Letters. (2014) Vol. 99. No. 8. P.435-440.
- [5] R. Martirosian, A. Makaryan, V. Mekhitarian, V. Tadevosyan, F. Nazari, A. Julfayan, Magneto-Nonlinear Materials for Detection of Electromagnetic Radiation, Physical Bases of Instrumentation. 2016. Vol. 5. No. 1(18). P. 88–97. [in Russian].
- [6] D. Bagdasaryan, A. Hakhoumian, R. Martirosian, A. Makaryan, V. Tadevosyan, Farokh Nazari, A. Julfayan, Ferromagnetic Detector of infrared radiation. International Conference on Microwave and THz Technologies, photonics and Wireless communications, IRPhE' 2016, May 4-6 (2016), Yerevan, Armenia, P.TH-11.
- [7] A.V. Kimel, A. Kirilyuk, F. Hansteen, R.V. Pisarev, Th. Rasing Nonthermal optical control of magnetism and ultrafast laser-induced spin dynamics in solids. J. Phys.: Condens. Matter. (2007) T.19. P.043201 (1-24).
- [8] A.B.-A. Baranga, R. Battesti, M. Fouche, C. Rizzo, G.L.J.A. Rikken, Observation of the Inverse Cotton-Mouton Effect, <hal-00518059v2> (2010).

Millimeter-Wave Component Characterization With Vector Network Analyzer

(Proceedings of the Int. Conference on “ Microwave and THz Technologies and Wireless comm.”)

P. Baybakov

Keysight Technologies, Moscow, Russia

Received 15 November 2018

Abstract: The N5291A measurement solution for mmwave network analysis is a distributed system composed of a vector network analyzer (VNA), a test set controller, and frequency extenders. A distributed system is made up of separate components that communicate together to act as one system. The frequency extenders interface with the device under test (DUT) and are the only pieces of the system that operate at mmwave frequencies. This allows us to test mmwave devices without having to completely rebuild VNAs to handle higher frequencies. The frequency extenders connect to a test set controller, which interfaces with the test set of the VNA. This gives the VNA a new maximum frequency of 120 GHz so it can test modern mmwave devices.

Keywords: Vector network analyzer, frequency extenders, single-connection .

1. Introduction

The adoption of millimeter wave have evolved significantly over the years and can be placed into 2 major application spaces:

The commercial application space:

The earliest commercial applications of millimeter wave have been in Wireless Gigabit communication systems example of this would be 60GHz wireless HDMI.

Then in around early 2010 we saw the start of millimeter waves frequencies adoption for automotive radar applications at 77GHz . This started with the initial implementation of park assist and collision avoidance radar and evolved now to applications of multi-channel radar systems for autonomous vehicle control.

More recently there has been a significant drive for more data and faster wireless communications systems. This has driven the wireless communication markets to utilize the $60-90\text{GHz}$ frequencies for $5G$ applications.

Aerospace and defense:

This industry has for a very long time lead the application of millimeter wave frequencies for several of their solution needs. The millimeter wave band has always offered them the secure satellite and ground communication systems.

Secure communication systems demand for complex encryption of large amounts of data and millimeter wave frequencies worked well for them. This has driven development of ultra-wideband military communication solutions that use millimeter wave frequencies.

As environmental phenomena challenged the use of optical/thermal imaging for EW system. There has been increase in the need of EM field imaging methods at millimeter wave bands. These Doppler radar imaging systems have driven the need for the A/D RADAR systems to take advantage of millimeter wave frequencies.

Finally, we have security imaging, which is one place we all are familiar with where the application of millimeter wave is used.

All these applications present unique challenges in their testing and application. Error sources such as cable losses, connector repeatability, and phase shifts that might have been mostly negligible at radio frequencies are amplified at higher frequencies. High-end vector network analyzers typically have maximum frequencies of 67GHz , so many of these applications require testing beyond the limits of most hardware.

The most convenient solution is a VNA with a single-connection/multiple-measurement (SCMM) architecture. As implemented in the Keysight PNA-X network analyzers, you can measure passive or active devices with one set of connections: S-parameters, noise figure, gain compression, THD, IMD, and more. For even greater measurement versatility, the SCMM capability supports the spectrum analysis measurement application. The measurement solution for mmwave network analysis is a distributed system composed of a vector network analyzer (VNA), a test set controller, and frequency extenders. Keysight's distributed solution is based on the *N5295AX03* modular frequency extension. The *N5295AX03* can be added to an existing compatible network analyzer (PNA or PNA-X with a maximum frequency of 26.5GHz or higher), reducing the cost of test by upgrading instead of replacing. The frequency extenders connect to the *N5292A* test set controller, which interfaces with the test set of the VNA.

The frequency extenders up-convert the 26.5GHz output from the test set to test devices at

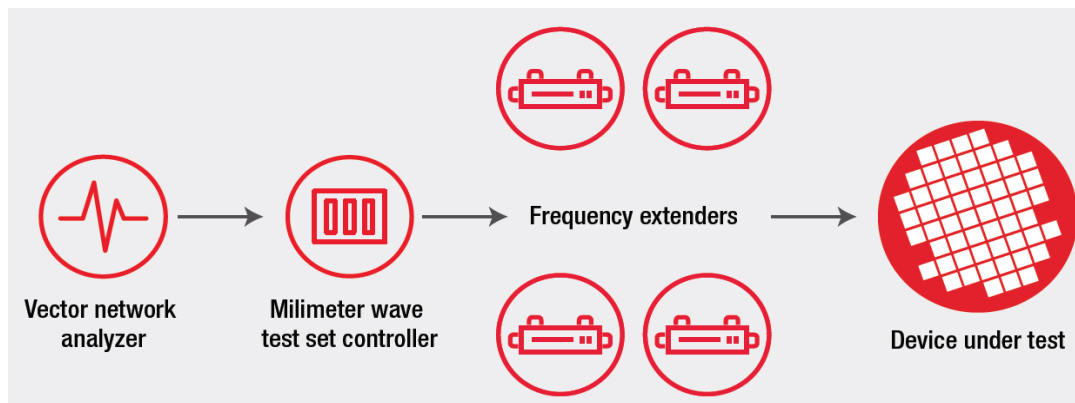


Figure 1: High level block diagram of the mmwave VNA system



Figure 2: N5291A mmwave measurement system

millimeter-wave frequencies. The block diagram of the *N5295AX03* frequency extender shows the conversion circuitry. There are three multiplier chains available, which can mix the RF input

to produce frequencies as high as 120GHz. This frequency is well within the millimeter range and provides accurate characterization of cutting-edge millimeter-wave devices.

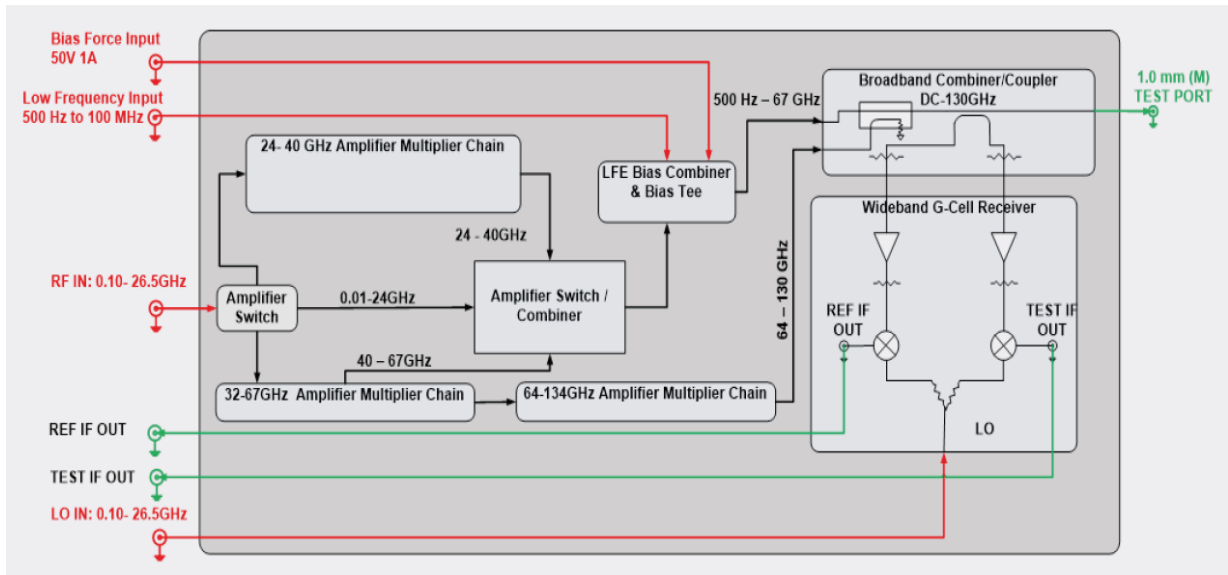


Figure 3: N5295AX03 frequency extender block diagram

The test set controller amplifies the network analyzer’s local oscillator (LO) signal to drive the frequency extenders’ mixers across their entire frequency range. The controllers also error correct and condition the frequency extender output to be at the IF of the VNA. The controller simplifies the measurement setup by providing RF, LO, and intermediate frequency (IF) signals to the frequency extenders over a single cable.

To test monolithic microwave integrated circuits (MMICs), which contain many components that operate in different frequency ranges, one should have a measurement system enabling measurements from low frequencies to mmwaves. This is implemented in VNA low-frequency extension test set, allowing measurement down to 900Hz.

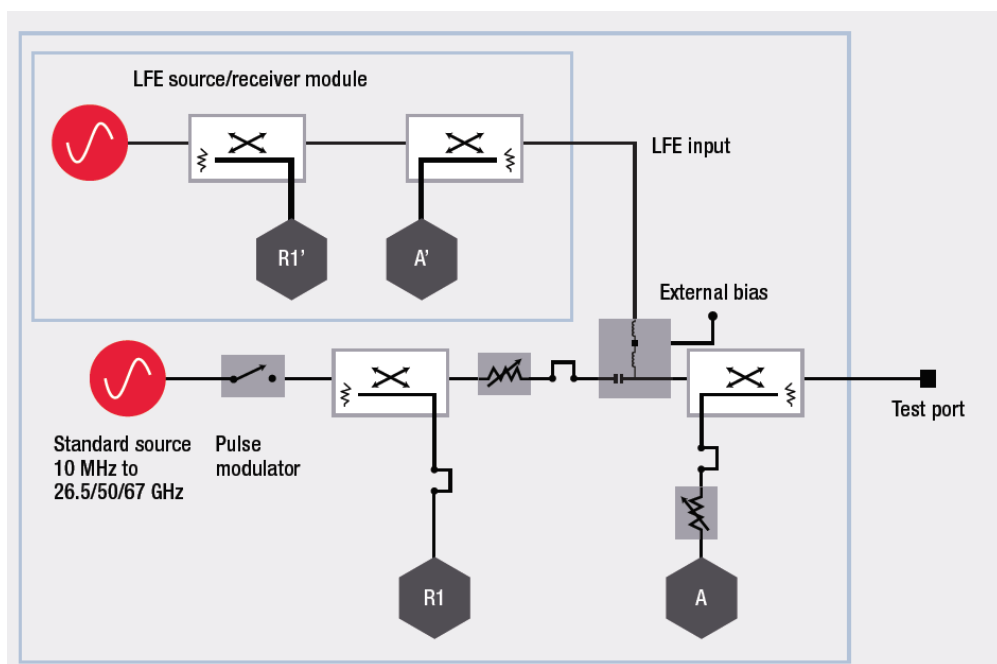


Figure 4: LFE implementation

2. Conclusion

The single-connection/multiple-measurements (SCMM) distributed architecture VNA measurement system allows to confidently characterize and optimize new-generation mmwave devices.

The key advantages are:

1. Single sweep, traceable measurements with minimum measurement uncertainty from 900Hz to 120GHz due to standardized 1 mm coaxial connector.
2. Typical dynamic range $>110\text{dB}$ up to 110GHz , $>100\text{dB}$ up to 120GHz .
3. Temperature stability due to separate frequency extension modules with convection cooling.

References

- [1] Keysight Technologies, "How can distributed architecture help mmwave network analysis?", white paper, May 2018
- [2] Keysight Technologies, "Achieving metrology-grade results at millimeter-wave frequencies", application note, June 2018

Digital Beamforming For OFDM 3D Radar

(Proceedings of the Int. Conference on “ Microwave and THz Technologies and Wireless comm.”)

D. Nersisyan,^{1,2} A. Hakhoumian¹, G. Mkrtchyan^{1,2}, T. Manukyan^{1,2}

¹ Institute of Radiophysics and Electronics, Alikhanian Brothers str. 1, 0203 Ashtarak, Armenia

² YEA Engineering, Engineering City, Bagrevand 21/1, Nor Nork, 0062 Yerevan Armenia

Received 15 November 2018

Abstract: Digital beamforming allows to analyze the all beams simultaneously. The implementation of digital signal processing for this challenge we used the FPGA, because the FPGAs can proceed parallel processing. We have created the 8 beams and 3 modes for 3D OFDM Radar. The mode names are Normal, Offset and Mono, which are used for different Radar applications. For DBF (Digital Beam Formation) we have used 4 antennas and each of that has 5 rectangular patch elements. The type of feeding for these antennas is serial. To achieve better side lobe level the rectangular patch sizes are modified by Dolph-Chebichev function. The receiver antenna array beam-width in azimuth plane is 25° and in elevation plane is 60°.

Keywords: Digital beamforming, directional transmission, discrete phase shifter.

1. Introduction

The beamforming is the signal processing technique which used for directional transmission or reception. It's changes the input signal phase for every antenna which force to move the beam direction. There is two methods of Beamforming that are realized for modern Radars.



There is two methods of Beamforming that are realized for modern Radars.

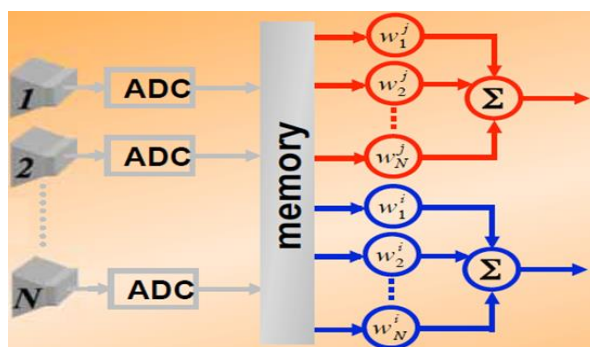
1) First method is the analog Beamforming (Figure1):

In this case the signal phase controlled by discrete phase shifters. This technic has a lot of disadvantages. It cannot reach fast scanning rate because the beam formation proceed by the serial way. Antenna array feeding line becomes massy, which cause to the complexity. The phase shifters with good accuracy is so expensive and that increase the system cost, additionally, they adds the noises in RF tract, which cause to loss of information.

The phase shifters with good accuracy is so expensive and that increase the system cost, additionally, they adds the noises in RF tract, which cause to loss of information.

Figure 1: Analog Beamforming

2) Second method is the digital Beamforming (Figure 2):



This technique performs the space filtering by using the DSP. In this case, the signal processing is realizing in digital world and that means we can use the parallel signal processing and scan all beam positions simultaneously. In the analog beamforming, we had discrete beam positions but in this technic, the DSP allows to change the input signal phases continuously.

Figure 2: Digital Beamforming

In the Radar systems we have the strongly fixed time period to scan elevation and azimuth. The energy equation is:

$$E = Pt$$

where E is energy, P is power, t is time.

Front this equation clearly shown that we can win in the energy by decreasing the processing time.

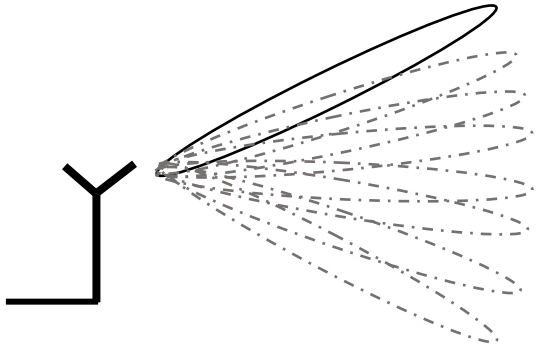


Figure 4: Serial processing

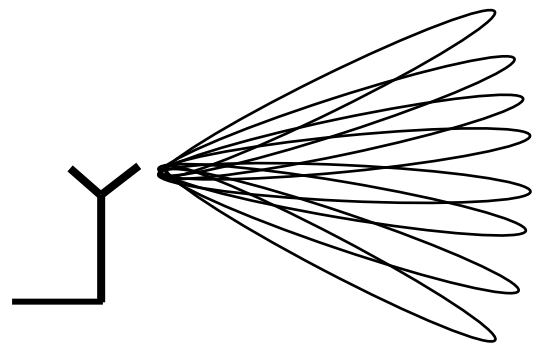


Figure 3: Parallel processing

In the Figure 3 and 4 shown the serial and parallel beamforming implementation visualization.

2. Implementation

The digital beamforming techniques have implemented for small RADAR prototype. Practically there is need to create several Tx beams which are shown in the Figure 6. The Tx beam is wide and has a fan-shaped pattern. This type of radiation pattern build by using antenna array Figure 5. The antenna spacing is larger then wavelength size.

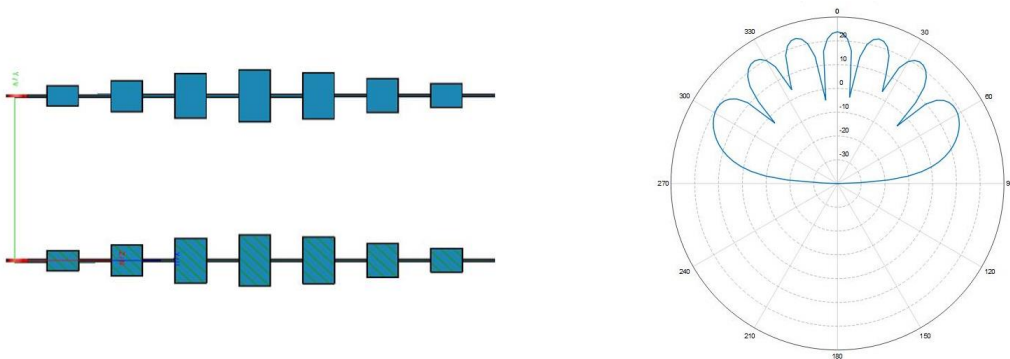


Figure 5: Transmitter antenna and radiation pattern

With phase shifters has an opportunity to change radiation pattern form and get different modes. First mode is the Normal mode. This is the default operational mode. Second mode is the High elevation mode. This mode used to detect close and high objects. The third mode cold Long-range mode. The radiation pattern mainly concentrated on front to detect the targets, which are far from RADAR.

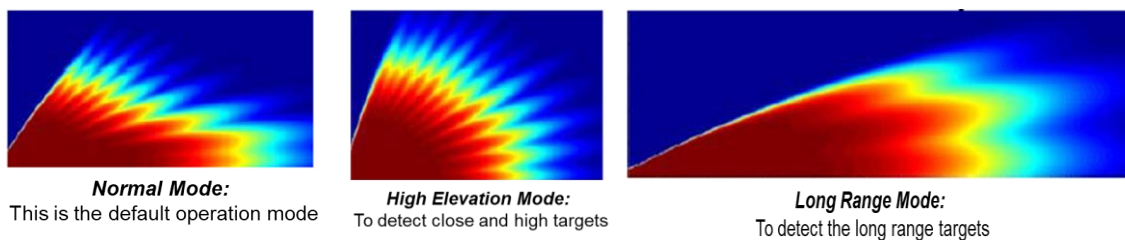


Figure 6: Three implemented modes for 3D OFDM Radar

Receiver part consist of 4 antenna array lines. By using Dolph-Chebyshev function for element size, the side lobe level increases. With this way the main lobe level become expressed, and scanning process getting easy. The total gain is 20DBi, radiation pattern size in E and H plane approximately equal to 26 and 13 degrees (Figure 7).

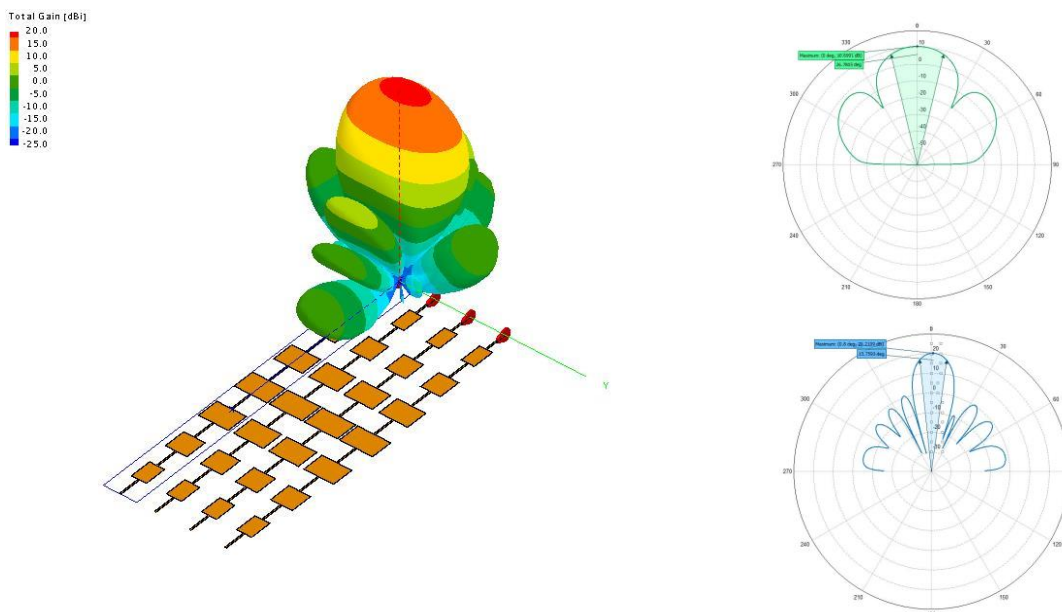


Figure 7: Receiver antenna radiation pattern

In the Receiver side, we have created 3 modes. First mode is the “Normal Mode”. In this mode beams distributed equal in whole field of view. Second mode is called “Offset Mode”. This mode was developed to concentrate beams in one sector of filed of view to achieve more accuracy. Third mode is most valuable mod and called “Mono Mode”. This mode used for elevation high accuracy measurements and target tracking.

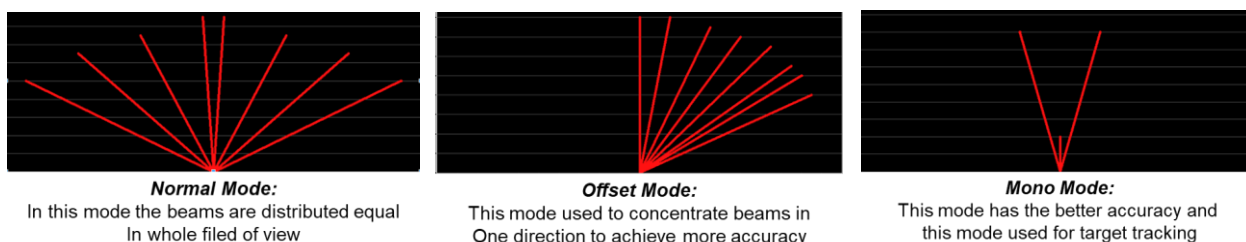


Figure 8: Receiver antenna Modes

3. Conclusion

- Based on digital Beamforming different type of antenna operation modes has been implemented which allows to use that in different Radar applications.
- Digital Beamforming well suitable for OFDM signals because the both of them based on matrix DSP.

References

- [1] T.S. Rappaport, A. Annamalai, R.M. Buehrer, W.H. Tranter, "Wireless communications: past events and a future perspective," IEEE Communications Magazine, vol. 40, no. 5, pp. 148-161, May 2002.
- [2] N. Levanon, "Multifrequency radar signals," IEEE 2000 International Radar Conference, pp. 683-688, May 2000.
- [3] M. Engels (Ed.), "Wireless OFDM systems: How to make them work?," Kluwer Academic Publishers, Boston, 2002.
- [4] N. Levanon, "Multifrequency complementary phase-coded radar signal," IEE Proceedings Radar, Sonar and Navigation, vol. 147, no. 6, pp. 276-284, Dec. 2000.
- [5] N. Levanon, "Multifrequency Signal Structure for Radar Systems," U.S. Patent 6 392 588, May 21, 2002.
- [6] B.J. Donnet, I.D. Longstaff, "Combining MIMO Radar with OFDM Communications," European Radar Conference EuRAD 2006, pp. 37-40, Sept. 2006.

The Microstrip Phased Array Antenna in The Centimeter Waves Range

(Proceedings of the Int. Conference on “ Microwave and THz Technologies and Wireless comm.”)

M.V. Markosyan^{1,2}, V.H. Avetisyan^{1,2}, A.K. Aharonyan^{1,2}, R.A. Davtyan²

¹ Yerevan Telecommunication Institute, Dzorapi str. 26, 0015 Yerevan, Armenia

² Russian-Armenian University, H. Emin str. 123, 0051 Yerevan, Armenia

Received 15 November 2018

Abstract: In this paper a module of linear array antenna for a circular view with a single excitation point is proposed. With his module the structure of the phased array working in the range 8.9-9.1 GHz and consisting of 16 sub arrays was organized. The design of the phased array allows reducing the number of receiver and transceiver modules of the system and lowering the cost price, since one module provides the operational functionality of 16 transmitting and receiving elements. This makes it possible to simplify the lattice design, which leads to a reduction in the cost of the system. Such flat antenna arrays are used in survey terrestrial radars, in onboard radars with a synthetic aperture for monitoring the earth's surface.

Keywords: phased array antenna, survey terrestrial radar, synthetic aperture, rectangular stripline resonator.

1. Introduction

The appearance of microstrip antenna devices is caused by the need for lightweight, thin, comfortable and cheap antenna devices. Any microstrip antenna device is a thin dielectric sheet with a thin copper coating on both sides. On one side are made radiating element, circuits of feed, control and matching. The other metal side of the antenna board serves as a screen. Such flat antenna arrays are used in surveillance ground radars and on-board radars with synthesized aperture for earth's surface monitoring [7–9].

In this article, we propose a linear array for a circular scan with a single driving point. Such arrays are used as emitters of flat arrays, perpendicular to the line of emitters in a linear array. This allows you to simplify the design of the array, which leads to the array price cheap.

In this regard, to ensure high accuracy, you need to have a sufficiently narrow beam (in the horizontal plane), compared to the vertical plane. For implementation of the given array, have been carried out the researching with the follow initial data (the data were identified and improved by analyzing the parameters of similar radar): The operating bandwidth is 8.9–9.15GHz, array beam width on the horizontal plane is 1.5° , array beam width on the vertical plane is 20° , array gain factor is 32dB, side lobes level in the horizontal plane is $< -19dB$.

2. Theoretical calculations for the linear array implementation

As a radiator in this linear array, a rectangular stripline resonator is used (Fig. 1). The substrate material is RO4360G2, with $\epsilon_r = 6.4$, dielectric width is 0.813mm.

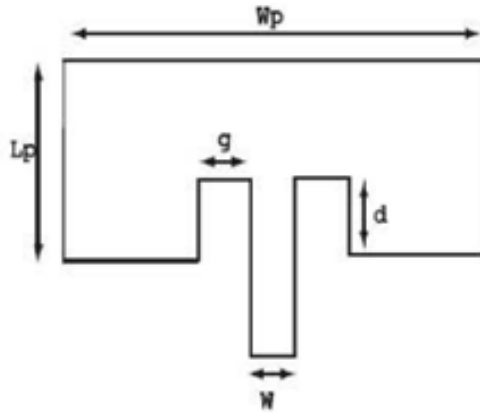


Fig.1 Geometrical view of resonator

Determination of the parameters of this resonator at a central frequency of $9GHz$ is carried out as follows.

The length of the resonator is determined by the formula:

$$L = \frac{c_0}{2f_r \sqrt{\epsilon_{reff}}} - 2\Delta L$$

where c_0 – light speed, f_r – resonance frequency, ϵ_{reff} – effective dielectric constant, ΔL – length correction. And the width of the resonator is determined by the formula:

$$W = \frac{c_0}{2f_r} \sqrt{\frac{2}{\epsilon_r + 1}}$$

where ϵ_r – substrate dielectric constant [1]. As a result of the calculations, we have the resonator length $L = 8mm$ and width $W = 6mm$.

In the next step, the theoretical distance between two elements of the given array is determined according to the formula

$$dx(y) = \frac{\lambda}{1 + |\sin \theta|} = 19mm .$$

Taking into account the initial data by the width of the DP(directional pattern) of the array in two planes, we obtain the number of elements along the horizontal plane $N_x = 64$, and along the vertical plane $N_y = 4$. Accordingly, the length of the array by the horizontal direction will be $L_x = N_x * 19 = 1300mm$, and by the vertical $L_y = N_y * 19 = 1300mm$. Then, the questions of the given array radiating elements power supply organization are considered [1,2]. For the radiating elements supply was chosen the tees circuit. This circuit allows feed a large number of radiating elements of the array from one point. The use of this circuit leads to the array design cheaper and simplified, which in turn will simplify the systems where it will be used [3].

Two-channel power dividers (tees) are used for junction (summing) of microwave signals (Fig. 2).

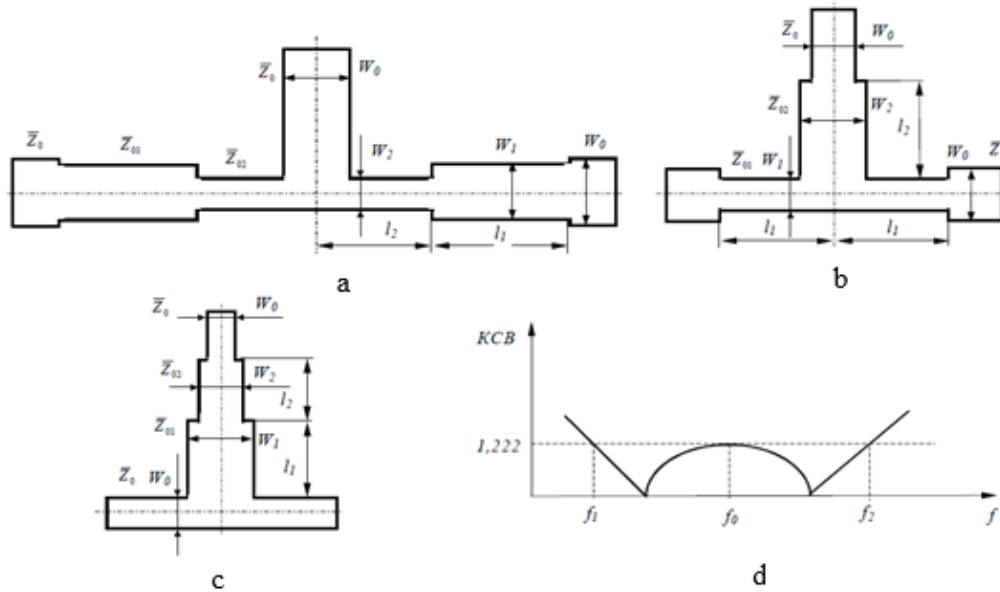


Fig. 2. Types of broadband tees having a two-stage crossing:

- (a) - with two-stage matching transformers in the output shoulders;
- (b) - with matching transformers in the input and output shoulders;
- (c) - with two-stage matching transformers in the input shoulder;
- (d) - frequency response of two-stage tee

The main electrical characteristic of the unit is the frequency response of the SWR from the shoulders. Allowable maximum level of SWR_{MAX} in the operating range with the required ceiling of the boundary frequencies is $k = \frac{f_0}{f_1}$. The calculation of the power divider is carried out as follows.

The first step is to determine the material of ϵ and h substrate thickness. Then, is set the wave resistance of the path Z_0 ; the band center of the operating range $f_0 = \sqrt{f_1 f_2}$; he boundary frequencies of the working band f_1 d f_2 the maximum allowed value of the standing-wave ratio of the divider shoulders in the SWR_{MAX} range; contact ratio of the working band k . Then, is determined the number of matching steps of the n divider; wave resistance of matching stages Z_i ; the geometric dimensions of the divider structure ($W_i; l_i$).

3. Numerical simulation of a linear array in the 8.9-9.15GHz range

Based on the input requirements of our task, it is advisable to divide the linear array into subarray, which will be powered from one point (Fig. 3). In this case, a numerical simulation of this subarray was performed using the CADFEKO program [4].

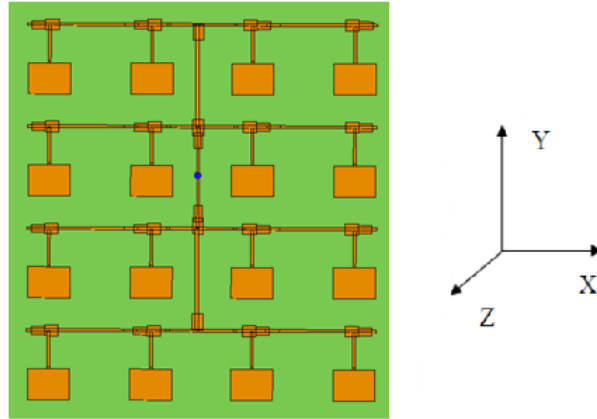


Fig.3. General view of subarray in CADFEKO interface

The result of subarray's directional pattern simulation in the horizontal and vertical planes, accordingly are shown below.

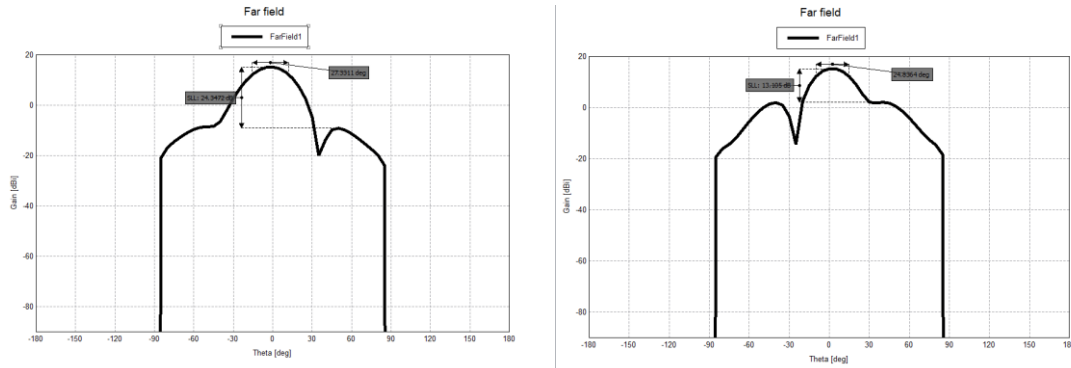


Fig.4: The simulation DP in the horizontal and vertical planes accordingly

After researching the results of array simulation, the production of module was carried out. (Fig.5).

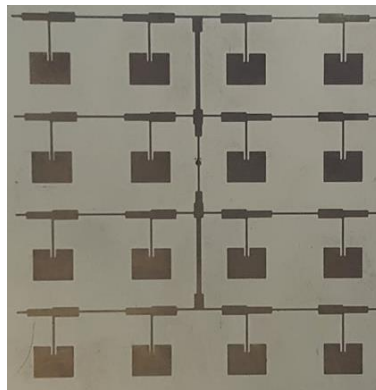


Fig.5. General view of the manufactured module

After the module production the actual measurement of the parameters of this subarray was carried out. In fig. the DP of the subarray is shown on the horizontal and vertical planes (Fig.6).

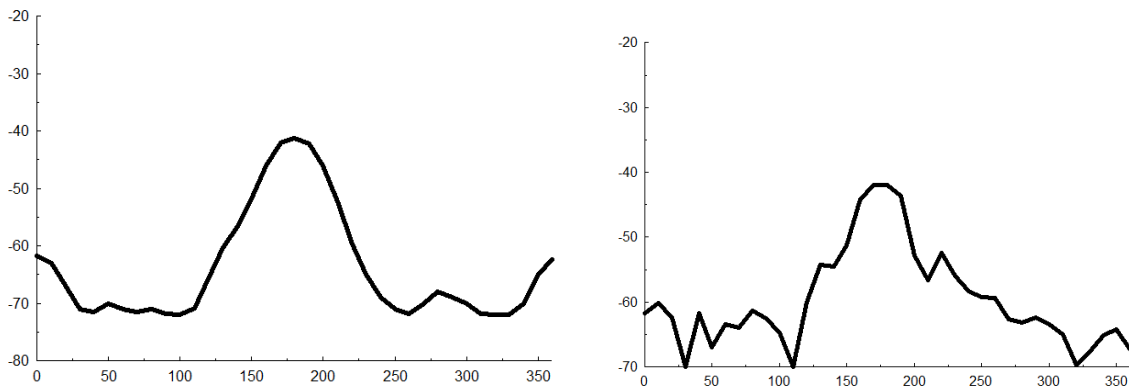


Fig.6. The DP of the subarray on the horizontal and vertical planes respectively

Researching the measurement results, we have deduced that the gain factor of subarray is $11.5dB$, and the width of the DP in two planes is about 25° .

In generally the given results repeat the results deduced by computer simulation. The results of modeling of array consisting of 16 subarrays was carried out and is given below.

Fig. 6 shows the obtained result of the array DP modeling consisting of 16 subarrays in the vertical and horizontal planes respectively.

References

- [1] M.I. Skolnik _A. Radar handcook, second edition, San Francisco, California, 1990.
- [2] O.G. Vendik, M.D. Parnes, Antennas with electrical scanning, 2001.
- [3] I.S. Kovaleva , Design and calculation of strip devices , Soviet radio , 1974.
- [4] <http://www.feko.com>

To Problem of Designing of The Landing Radars

(Proceedings of the Int. Conference on “ Microwave and THz Technologies and Wireless comm.”)

S.B. Makarov¹, M.V. Markosyan^{2,3}, V.H. Avetisyan^{2,3}, A.K. Aharonyan^{2,3},
H.G. Martirosyan², R.A. Davtyan²

¹ St. Petersburg Polytechnic University, Polytechnicheskaya str. 29, 195251 Saint Petersburg, Russia

² Yerevan Telecommunication Institute, Dzorapi str. 26, 0015 Yerevan, Armenia

³ Russian-Armenian University, H. Emin str. 123, 0051 Yerevan, Armenia

Received 15 November 2018

Abstract: Two structural diagrams for the designing of landing radars are compared. The first diagram of radar construction is based on the use of a single receiving-transmitting phased array antenna that forms a scanning four-beam directional pattern in receive mode and narrow probing beam in transmission mode. The second diagram is the radar with separated receiving and transmitting antenna systems. The phased array antenna is also used as the receiving antenna system. A separate transmitting antenna system consists of a set of separate radiating units, each of which sequentially irradiates its section of the radar coverage area by switching of the transmitter to a choosing unit. The process of searching of an aircraft and measuring its angular coordinates, range and speed in a particular area section of the radar coverage is synchronized with the switching of the microwave probing transmitter signal to the unit which irradiates this section.

Keywords: Landing radar, transmitting antenna system, single receiving-transmitting antenna.

1. Introduction

Landing radars are an integral part of the radar equipment of any airport. They operate in the centimeter wavelength range ($\lambda \approx 3.2\text{cm}$), and the angle radar coverage of such radars is about $30^\circ \dots 35^\circ$ by course (azimuth) and is $10^\circ \dots 12^\circ$ for the glide path (elevation). The range of the landing radar usually does not exceed 30km . The dispatcher's radar, also of the centimeter wavelength range, operates in the interval of $30 \dots 50\text{km}$ from the airport, and the surveillance radar of the meter wavelength range operates in the area of $50 \dots 80\text{km}$. The first provides monitoring of the air situation and the implementation of operational control of aircraft (AC), and the second is used for continuous monitoring of the overall air situation. The reliability of the AC landing in a large degree depends on the characteristics of the landing radar. These are its resolution, the measurement accuracy of the speed, the range and the angular coordinates of the AC, which ultimately are determined the degree of the tracking alignment of the AC and its tracking to the airport runway. On the other hand, the operation speed of the radar determines the speed of data updating about of the air situation in the operation area of radar and the traffic capacity of an airport. The requirement to the extended precision of determining of the AS angular coordinates is satisfied by using the high-precision monopulse method [1], and the radar high speed operation is provided by electronic scanning of beams of the phased antenna array (PhA), which is used in the radar antenna system [2]. However, the reliability of the radar and its manufacture cost bring about the question of choosing of the radar designing structure.

The purpose of given work are the discussion and comparison of two structural schemes for the radar designing and the estimation of their some parameters. The first scheme is designing for the radar with a single receiving-transmitting PhA and the second scheme is – for the radar with the separate receiving and transmitting antenna systems.

2. The landing radars with single combined phased array antenna

The block diagram of that landing radar is shown in fig. 1. The radar has the combined PhA, which is a single receiving-transmitting antenna. In receiving operation mode of the radar, the monopulse method is used for determining of the AC angular coordinates. In the radar transmission mode, the control voltage generator supply the radar transmitter by the group of voltages, which are intended for the formation of probe pulses. Another group of control voltages supply the variable phase shifters and attenuators in the paths of the PhA component antennas for forming of scanning probe beam.

In the PhA reception mode, those phase shifters and attenuators receive the corresponding voltages from the generator for formation of a scanning four-lobe directional pattern (DP). The transition of the PhA from the one operation mode to another is carried out by another group of the generator control voltages which supply the switches in the paths of the PhA component antennas.

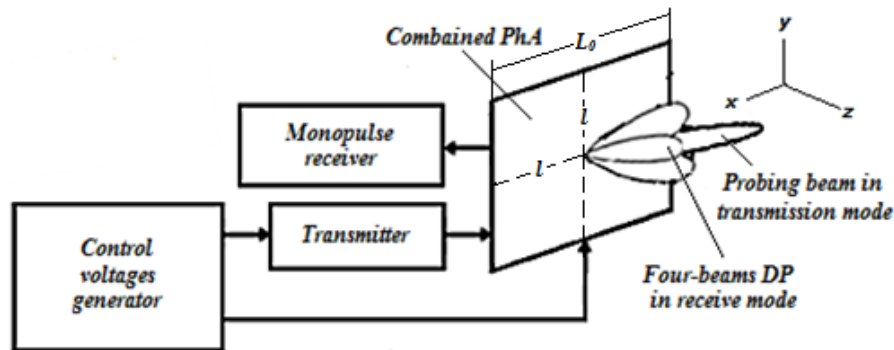


Fig. 1. Block diagram of landing radar with single combined PhA

The two needle-shaped beams of the receiving four-lobe DP, which determine the AC course, are spaced in the horizontal plane and are intersected in the radar boresight at $-3dB$ level. Those two beams scan synchronously and coupled in the angle interval $\pm 17,5^\circ$ by course and $\pm 6^\circ$ y glide path. Two other beams of the receiving four-lobed DP in the vertical plane, scan synchronously in the same way and determine the glide path of the AC. For determination of AC course and glide path with an accuracy less than a tenth of a degree, the width $2\theta_{0,5}$ of those needle-shaped beams should be $2\theta_{0,5} \leq 1,5^\circ$ at the level $(-3dB)$ [3]. Such PhA can be represented as a sheet with 4 sections $L_0 = 2l$ (e fig. 1), where each of them forms one needle-shaped beam which simultaneously scans with the other three simultaneously formed beams. Taking into account the operating wavelength

$\lambda \approx 3.2\text{cm}$, $2\theta_{0,5} \approx 1,3^\circ$ and efficiency coefficient of PhA $\eta = 0.8$, we will do some estimates by the following relationships [4]

$$(2\theta_{0,5})_{x,y} \approx 57,3 \times 0,888 \lambda / l_{x,y} \quad (1)$$

$$G = \eta D = \frac{\eta 4\pi l_x l_y}{\lambda^2} \quad (2)$$

where $l_x = l_y = l$: the linear size of each section of the sheet, D – directivity coefficient of one section, G – its gain factor. The estimates show that each section of the PhA should have an aperture equal to $l^2 \approx 1,25 \times 1,25 \text{m}^2$ and $G \approx 15340 (41,86 \text{ dB})$ Taking into account the four-lobed structure of the receiving DP, the PhA will have aperture equals to $L_0^2 \approx 2,5 \times 2,5 \text{m}^2$ and the gain factor equals to $G_0 \approx 30680 (44,86 \text{ dB})$ Assuming that the four-lobed DP is swinging by the course in limits $\pm 17,5^\circ$ in the radar coverage area without arising of diffraction maximum, we choose the ratio of the wavelength λ to the distance d_x between component antennas equals to $\lambda / d_x \approx 0,75$ [4]), that is $d_x \approx 2,4 \text{cm}$. The number n_x of component antennas along a horizontal in each section of the sheet is defined as $n_x \approx l / d_x = 1,25 / 0,024 = 52$ and accordingly in PhA as $N_x = 104$ Similarly, assuming that the four-lobed DP is swinging by the glide path in limits $\pm 6^\circ$ in the radar coverage area without arising of diffraction maximum, we choose the ratio $\lambda / d_y \approx 0,84$. we will have: $d_y \approx 2,7 \text{cm}$ the number n_y of component antennas along a vertical in each section of the sheet is $n_y \approx l / d_y = 1,25 / 0,027 = 46$ and accordingly, in PhA $N_y = 92$ The total number N of component antennas (radiators) will be equal to $N = N_x \times N_y \approx 9568$ This means, that we have the presence of corresponding huge number of switching elements, phase shifters, etc. in the paths of the radiators.

3. The landing radars with separate receiving and transmitting antenna system

Block diagram of such landing radar is shown on fig. 2 [5]. The receiving antenna system consists of the PhA operating only in the receiving mode and forming the above described four-lobed DP for providing high-precision monopulse method of measuring of the AC angular coordinates. It is clear, that at the same requirements to the determination accuracies of the AC course and glide path and the same requirements to swinging of the four-lobed DP within the same radar coverage angular area, the receiving PhA will have the same aperture $2,5 \times 2,5 \text{m}^2$ gain factor $G_0 = 30680 (44,86 \text{ dB})$ and the same number of component antennas $N \approx 9568$ as estimated above. In turn, this means that the receiving PhA will have the same number of variable phase shifters and attenuators contained in the paths of the component antennas. However, the receiving PhA as opposed to the transceiver PhA of the previous circuit, does not contain switching elements for the operation mode changing. Notes, that the number of such elements is more and amounts to a round sum in monetary unit.

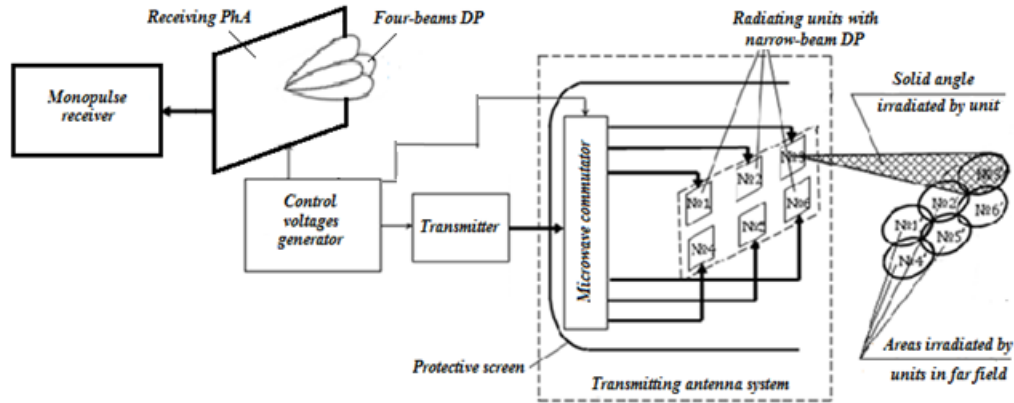


Fig. 2. Block diagram of landing radar with separate receiving and separate transmitting antenna systems

The transmitting part of the antenna system consists of a microwave commutator and a double-row set of identical radiating units, for example, as narrow-beam horns. Each row should have five units, but for simplifying of the Fig.2, each row has 3 horns as shown in the given figure. Each of these 10 horns has the DP lobe width about $6^{\circ} \dots 7^{\circ}$. The axes of the horns are located relative to each other by such manner that the irradiated angular solid sectors of the horns are partially superimposed on each other and thereby the whole coverage area of the radar is irradiating at the series excitation of the horns. Thus, the irradiation zone of the transmitting unit is equal to the radar required coverage area. During the operation of a concrete horn, the four-lobed DP of the receiving PhA scans within the irradiated solid angle of this horn for searching of the AC and measuring its coordinates and speed. At the switching the microwave power to another horn, the receiving PhA synchronously switches to the scanning mode in another solid angle corresponding to this horn, similarly functioning already in this area. The commands are carried out by supplying of corresponding voltages from control voltages generator to the microwave commutator and the receiving PhA. Two possible diagrams of implementation of the microwave commutator with the using of the controlled balanced gas-discharge switchers or the controlled gas-discharge full-connection switchers are given in the [5]. Let us estimate some parameters of the landing radar shown in Fig. 2. However, at first note the following. As identical radiating units (see Fig. 2) with the mentioned above narrow-beam lobes of the DP, may be used the radiating PhAs of corresponding apertures, but without variable phase shifters and attenuators. Constant phase shifts between the radiators of each PhA should be chosen by such manner that the main lobes of each of the radiating PhA would irradiate that section of the radar coverage area which was irradiated by the replaceable horn. The use of such phase arrays has the advantage to obtain lower levels of the DP side lobes by using a special amplitude distribution over the sheet of each PhA. The aperture of each radiating PhA should provide a beam with $6^{\circ} \dots 7^{\circ}$ width. The calculation of such PhA with the value 0.8 of its efficiency coefficient, have carried out according to expressions (1), (2), and at choosing of $\lambda/d \approx 0,84$ (d the absence of a diffraction maximum), gives a sheet value of such a radiating PhA $-27 \times 27 \text{ cm}^2$, gain - $G_r = 716$ (28.55dB), and the number of radiators - 100. Taking into account double-row arrangement of such PhA with 5 pieces in each row, the dimensions of the radiating sheet of the whole transmitting antenna system - $(27 \text{ cm} \times 5) \times (27 \text{ cm} \times 2) = 1,35 \times 0,54 \text{ m}^2$ Now, let us

estimate the average power P_T of the radar transmitter. We assume that the operation maximum range of the radar is $D_{max} \approx 30\text{km}$ and sensitivity P_R of its receiving system is $P_R = 10^{-13}\text{W}$ (-130dBW), which is realized in the centimeter range modern radars. We also assume, that the AC has the average scattering cross section σ equal to $\sigma = 5\text{m}^2$. The gain value of the receiving antenna is assumed to be equal to that deduced above - $G_0 = 30680(44,86\text{ dB})$. The estimation of the average power P_T of the transmitter follows from the radar equation [3].

$$P_T = 64\pi^3 P_R D_{max}^4 / \sigma \lambda^2 G_0 G_T \quad (3)$$

The result is $P_T \approx 1,43\text{kW}$. At other same values included in expression (3), the power may be reduced by increasing the gain G_T of radiating PhA. However, it is necessary to note that at the same angular coverage area of radar and increasing of G_T k times, the number of PhAs in each row and in each column of the transmitting antenna system will increase in \sqrt{k} times, and linear dimensions of its sheet will increase in k times. Next, it is possible to avoid the commutation of microwave probing signal from the transmitter to the transmitting antenna system. For this, we can use the single radiating PhA which should scan its main lobe from one section of the radar coverage area to another section in accordance with the given commands. In this case, the additional number of variable phase shifters are necessary in the single radiating PhA.

Thus, the reducing of the radar realization cost requires a complex estimation taking into account both as the discussed above parameters and as much the costs of the units and blocks included in the radar.

References

- [1] A.I. Leonov, K.I. Fomichev. Monopulse radiolocation. M., Radio and communication, 1984.
- [2] G.A. Erokhin, O.V. Chernov, N.D. Kozirev, V.D. Kocherzhevski. Antenna-feeder devices and radio wave propagation. M., Hotline – Telecom, 2007.
- [3] M.I. Finkelshtein. Basics of radiolocation. M., Radio and communication, 1983.
- [4] A.L. Drabkin, V.L. Zuzenko, A.G. Kislov. Antenna-feeder devices. M., Sov.radio, 1974.
- [5] S.B. Makarov, M.V. Markosyan, V.H. Avetisyan, H.G. Martirosyan, «Landing radar with commutation of the mutually spaced irradiated sections of its coverage area», Bulletin of High Technology, vol.1, no. 3, pp. 3-7, 2017.

Glucose Aqueous Solution Sensing by Modified Hilbert Shaped Microwave Sensor

(Proceedings of the Int. Conference on “ Microwave and THz Technologies and Wireless comm.”)

L. Odabashyan^{a,b}, A. Babajanyan^b, Zh. Baghdasaryan^{a,b}, B. Friedman^c, K. Lee^{a,*}

^aDepartment of Physics, Sogang University, Seoul 121-742, Korea

^bDepartment of Radiophysics, Yerevan State University, Yerevan 0025, Armenia

^cDepartment of Physics, Sam Houston State University, Huntsville, Texas 77341, USA

*E-mail: klee@sogang.ac.kr

Received 15 November 2018

Abstract: We present a microwave sensor based on the modified first order Hilbert curve designed for detecting glucose concentration in aqueous solutions by using a real-time microwave near-field electromagnetic interaction technique. We observed S_{11} reflection parameters of the sensor at resonant frequencies depend on the glucose concentration. We could determine the glucose concentration in the 0-250 mg/dl concentration range at an operating frequency near 2.6 GHz. The measured minimum detectable signal was 0.018 dB/(mg/dl) and the measured minimum detectable concentration was 1.68 mg/dl. The simulation result for the minimum detectable signal and the minimum detectable concentration was 0.023 dB/(mg/dl) and 1.3 mg/dl, respectively. Our proposed system has excellent potential to serve as a human bloodless glucometer.

Keywords: Non-invasive; Modified Hilbert; Microwave sensor; Glucose concentration

1. Introduction

Glucose is the main calorimetric energy source for the human body, and it performs critical work in cellular metabolism [1]. However, a high concentration of glucose can be the cause of arteriosclerosis or diabetic retinopathy. In a healthy person, the pre-prandial blood glucose level is under $100\text{mg} / \text{dl}(0.1\text{wt.}\%)$, and the post-prandial blood glucose level is $140\text{mg} / \text{dl}(0.14\text{wt.}\%)$. When a person has diabetes, the post-prandial blood glucose level is greater than $200\text{mg} / \text{dl}(0.2\text{wt.}\%)$ and the pre-prandial blood glucose level is also high. In 2014, 8.5% of adults age 18 years and older had diabetes. In 2015, diabetes was the direct cause of 1.6 million deaths and in 2012 high blood glucose was the cause of another 2.2 million deaths [2]. Knowing the blood glucose concentration for patients with diabetes mellitus is crucial for maintaining it within physiological limits. Blood glucose concentration often needs to be measured several times a day [3].

Presently, the glucose sensors based on an invasive measurement technique are widely used, for example, the finger-prick glucometers which have a low price and provide high accuracy.

However, the invasive glucose sensors have a number of obvious problems such as pain, the risk of infection, tissue damage where blood is taken, etc. It is evident that a non-invasive glucometer would be of great help to achieve a better control of insulin and glucose levels. Therefore, developing the blood glucose sensors based on a non-invasive measurement technique is important for improving and facilitating patient health care [4,5]. Currently there are several types of blood glucose biosensors based on a microwave dielectric waveguide probe [6], an artificial transmission line [7], a band-stop filter [8], a microwave spiral resonator [9], a near-field microwave microprobe [10]. However, the existing devices are limited to sensing samples and trends and require further resolution improvement.

In this paper, we propose a microwave sensor based on the modified Hilbert curve of first order for determination of the D-glucose ($C_6H_{12}O_6$) concentration. The measurements are done on an aqueous solution by measuring the microwave reflection coefficient S_{11} at resonant frequencies of about $2.6GHz$. The change in reflection coefficient S_{11} is directly related to the change in the glucose concentration due to an electromagnetic interaction between the microwave sensor and the samples. We chose the concentration of glucose from $50mg/dl$ to $250mg/dl$, since this range corresponds to the concentration of glucose in human blood for both normal and diabetic patients. As a background we chose deionized (DI) water.

We also modeled the Hilbert curve sensor by using COMSOL Multiphysics software which accurately predicts response of the microwave signal. The simulated results for S parameters of the sensor in both cases, without and with material under test (MUT) were in good agreement with the obtained experimental data.

2. Design and fabrication

Figure 1 (a) and (b) shows the structural image of the sensor without and with the quartz flask, respectively. A ceramic with dielectric permittivity of about 9.2 and sizes of $20.4mm \times 40.4mm \times 1mm$ was chosen as the substrate. The both sides of ceramic substrate were coated by a thin layer (about $50\mu m$) of silver paste. The sensor was prepared by drying, laser patterning and annealing techniques. The sensor finally was soldered to the conductors.

One side of the sensor which was patterned has a shape as a modified Hilbert-shaped closed curve. The geometry of the modified Hilbert-shaped sensor is shown in Fig. 1 (c). Here h , s , and w are the width of the stripline, length of the Hilbert-shaped curve unit of the first order, and the

width of the curve, respectively. The designed parameters of the sensor are $h = 1\text{mm}$, $w = 0.1\text{mm}$ and $s = 2.6\text{mm}$.

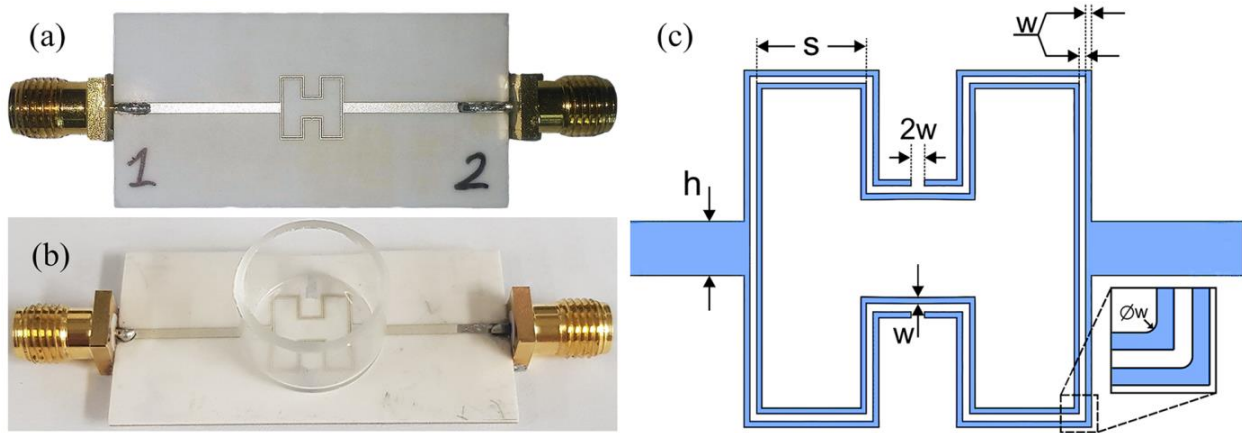


Fig. 1. The modified 1st order Hilbert-shaped fractal sensor (a) without and (b) with quartz vial. (c) The structural geometry of sensor pattern.

In experiment, we placed a quartz flask with aqueous solutions with various concentrations of D-glucose on the sensor and the response was detected by a vector network analyzer (VNA: Agilent E5071B). The dielectric constant of the quartz flask was 3.8, height was 8mm and thickness was 1mm . Outer and inner radius were 7mm and 6mm , respectively. The volume of aqueous solution was kept at $500\mu\text{l}$ during all experiments and in the simulation as well. High sensitivity can be achieved when the quartz flask is placed on the symmetric center of the Hilbert curve. The resonator was calibrated with DI water giving an S_{11} minimum of -26.84dB . The data acquisition time for glucose real-time monitoring was 0.5s and experiments were conducted at a temperature of 25°C . The microwave Hilbert-shaped sensor for detecting glucose concentration was modeled by using COMSOL simulation software. Changes of the resonant frequency f_0 and reflection coefficient S_{11} of the sensor are caused by the replacement of the MUT as a load. The geometry of the simulated model in COMSOL simulation software and near-field electromagnetic field distribution are represented in Fig. 2. The electromagnetic field intensity is concentrated around the sensing Hilbert-shaped pattern for both the electric field and the magnetic field distribution as shown in Fig. 2 (b), (c).

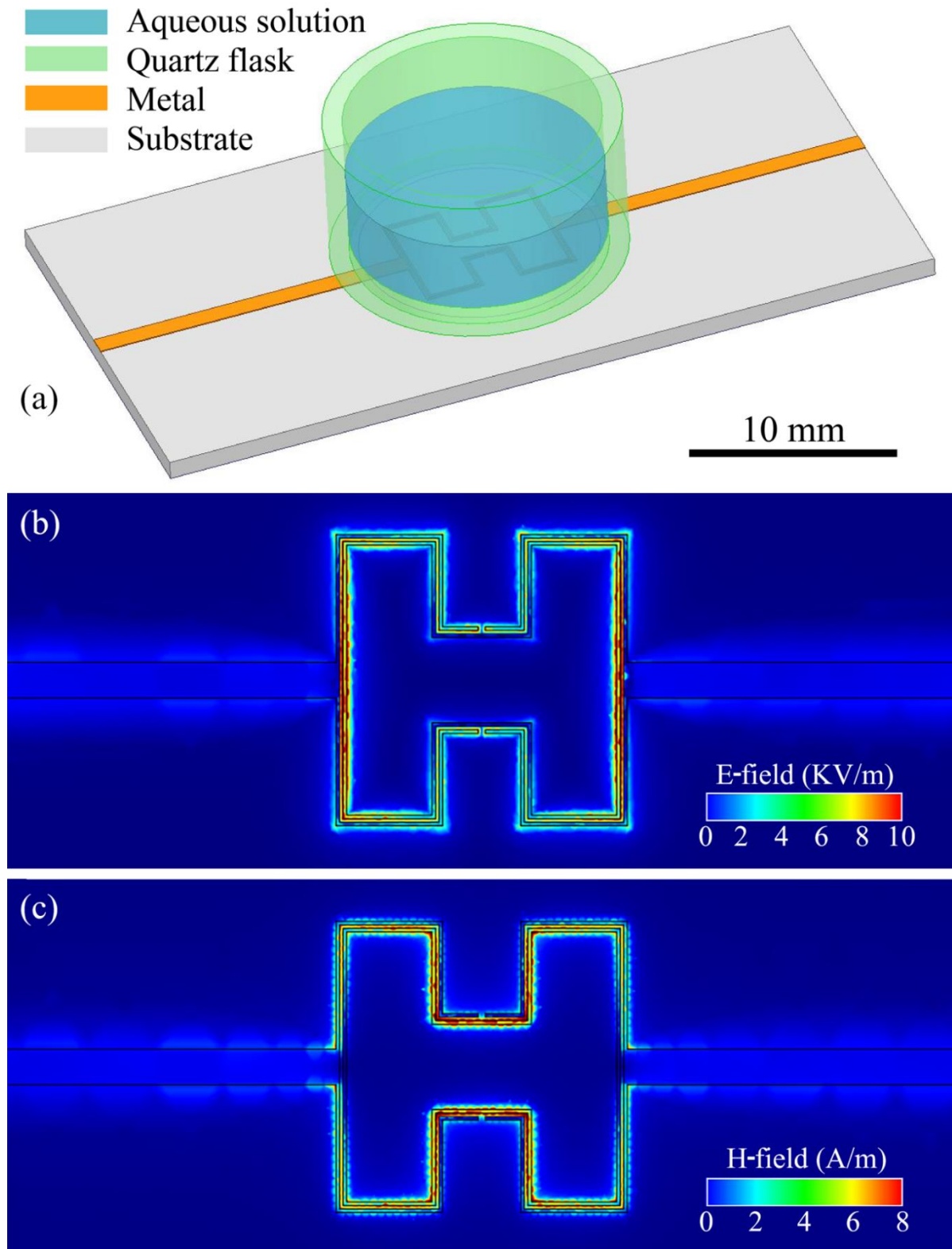


Fig. 2. (a) The geometry of the sensor simulation model in COMSOL. Simulated (b) electric and (c) magnetic near-field distribution at 3.3 GHz.

3. Theoretical background

The operational principle of sensor/MUT system is based on the shift in the microwave reflection coefficient S_{11} due to changes of the electromagnetic characteristics of the MUT, such as the dielectric permittivity and the magnetic permeability. Most biological materials have magnetic permeability close to that of free space that is not changing, thus the changes in magnetic permeability were neglected during our test [11]. The dielectric constant is a parameter that can be experimentally measured. By measuring dielectric properties of a given material, we can indirectly measure other properties of that material related to their molecular structures such as a concentration. The relative permittivity of material has complex form with $\varepsilon = \varepsilon' - j\varepsilon''$, where ε' is the real part of complex permittivity and causes electric energy storage in the material. The imaginary part of the complex permittivity ε'' caused by the conductivity characterizes the energy loss with $\tan \delta = \varepsilon'' / \varepsilon'$ when an EM signal passes through the material. The dependence of dielectric permittivity on solute glucose concentration is expressed with the molar increment δ and given by $\varepsilon_g(\omega) = [\varepsilon'_0(\omega) + c\delta'] - j[\varepsilon''_0(\omega) + c\delta'']$ where $\varepsilon_0(\omega)$ is the complex permittivity of DI water ($\varepsilon'_0(\omega) = 78.25$ and $\varepsilon''_0(\omega) = 13.3$ at 3.3GHz , 25°C), c is the concentration of glucose, $\delta = \delta' - j\delta''$ is the increase in permittivity when the glucose concentration is raised by 1 unit ($\delta' = 0.00577(\text{mg} / \text{dl})^{-1}$, $\delta'' = 0.00015(\text{mg} / \text{dl})^{-1}$) and ω is the field frequency [9,12]. The dependence of dielectric permittivity on concentration and field frequency can be understood with the Debye relaxation model. By increasing the operation frequency the real part of permittivity shows decreasing behavior and the imaginary part shows increasing behavior, whereas by increasing the glucose concentration in the solution the real part of permittivity of the solution decreases and the imaginary part increases [13].

4. Results and discussion

The (a) measured and (b) simulated reflection parameters for the designed unloaded sensor are presented in Fig 3. The resonant frequency is nearly at 3.3GHz for both simulated (3.38GHz) and measured (3.33GHz) data. The shift between measured and simulated resonant frequency of about 57MHz and about 4.7dB can be caused by port mismatching and cable losses, etc. In general, the behaviors of measured and simulated reflection parameters are in good agreement and described the testing process well. Putting the quartz vial with aqueous solution on the sensor (loaded sensor) causes the change of scattering parameters (resonant frequency,

amplitude) due change of the total impedance of the system. As was expected, S -parameters depended on the variation of the glucose concentration in the aqueous solution. Figure 4 (a) shows simulated and experimental results of microwave reflection coefficient S_{11} profiles for DI water and for D-glucose aqueous solution with glucose concentration range from $50\text{mg} / \text{dl}$ to $250\text{mg} / \text{dl}$. Both the simulated and experimental curves have the resonant minimum value of S_{11} at the frequency of about 2.6GHz (2.67GHz vs. 2.53GHz).

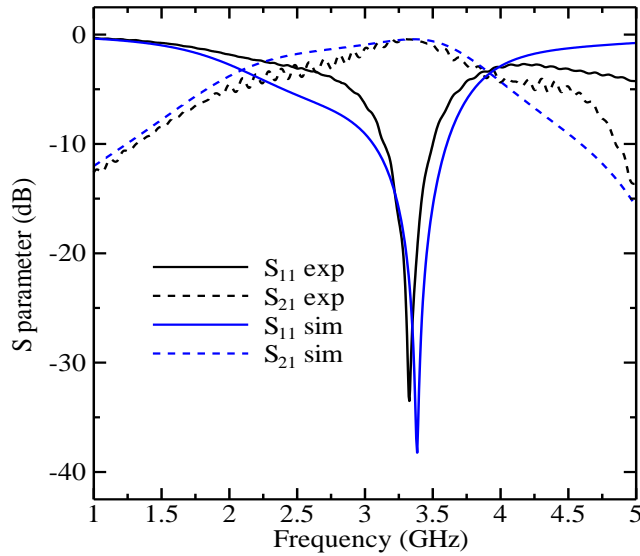


Fig. 3. The experimental and simulated reflection/transmission coefficients of the sensor.

S_{11} increased as the glucose concentration decreased as shown in Fig. 4 (b) for both simulation and experiment. The maximum difference of S_{11} parameter for sensor loaded by DI water and solution with $250\text{mg} / \text{dl}$ glucose concentration was about 5.5dB at 2.67GHz in simulation and about 4.6dB at 2.53GHz in experiment. In other cases, the difference monotonously decreases by decreasing the glucose concentration. The relationship between S_{11} and glucose concentration is linear and the S_{11} trend varies with slope of $0.023\text{dB} / (\text{mg} / \text{dl})$ in simulation and $0.018\text{dB} / (\text{mg} / \text{dl})$ in measurement. Stable linear relationships are important for detection and analyzing glucose concentrations in solution. The minimum detectable concentration c_{\min} of designed sensor defined as

$$c_{\min} = \frac{S_{11}^R}{\Delta S_{11} / \Delta c} \quad (1)$$

where Δc is the concentration variation, ΔS_{11} is the change in S_{11} corresponding to Δc , and $S_{11}^R = 0.03\text{dB}$ is the resolution of the experimental system. The minimum detectable concentration was found to be 1.3mg/dl and 1.68mg/dl for simulation and experiment, respectively (data are summarized in Table 1).

Table 1. The main operating parameters of the designed sensor.

Sensor parameter	Simulation	Measurement
Dynamic range for S_{11}	5.5 dB	4.6 dB
Resonant frequency	2.67 GHz	2.53 GHz
Sensitivity for S_{11}	0.023 dB/(mg/dl)	0.018 dB/(mg/dl)
Minimum detectable concentration	1.3 mg/dl	1.68 mg/dl

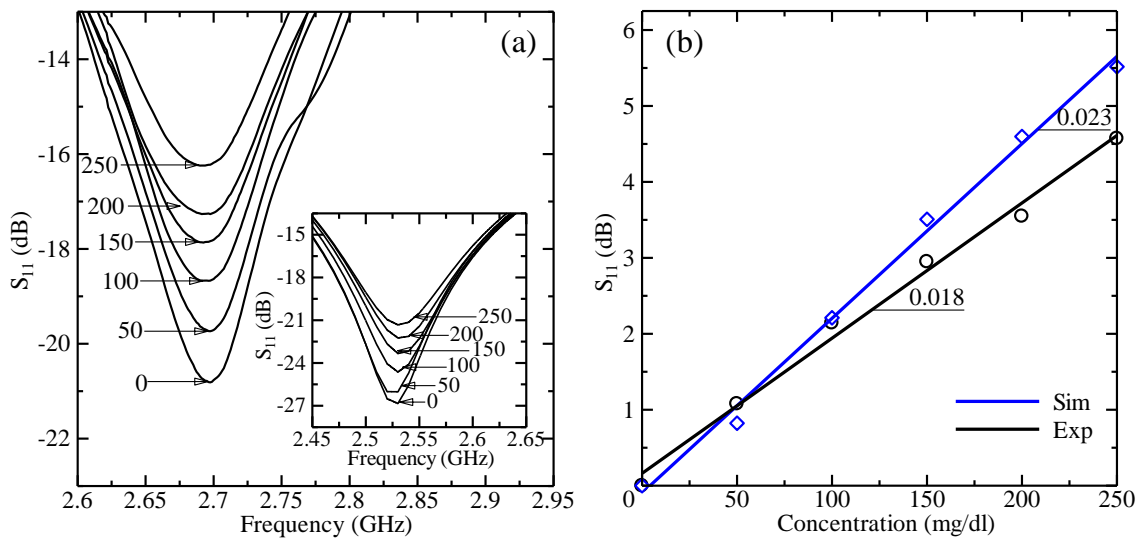


Fig. 4. (a) Simulated and measured (inset) results of microwave reflection coefficient S_{11} profile for DI water and for glucose aqueous solution with different concentrations 50-250 mg/dl for 500 μl volume. (b) The simulated and measured microwave response dependence on D-glucose concentration at the resonant frequency of about 2.67 GHz and 2.53 GHz, respectively.

We also simulated the electromagnetic field interaction between the sensor and the glucose solution, to visualize the electromagnetic field distribution during measurement. Figure 5 shows the simulated subtraction images of 250mg/dl and 0mg/dl (DI water) glucose concentrations for (a), (c) electric field and the (b), (d) magnetic field at (a), (b) sensor/MUT interface (i.e. on boundary of sensor/glucose solution) and at (c), (d) 1mm high from sensor/MUT interface (i.e.

inside of the glucose solution), respectively. When the glucose concentration increased, both electric and magnetic fields strengths increased too. Changes in electromagnetic field distribution were due to the increase in complex dielectric permittivity of glucose solution, when the concentration of glucose in solution was increased.

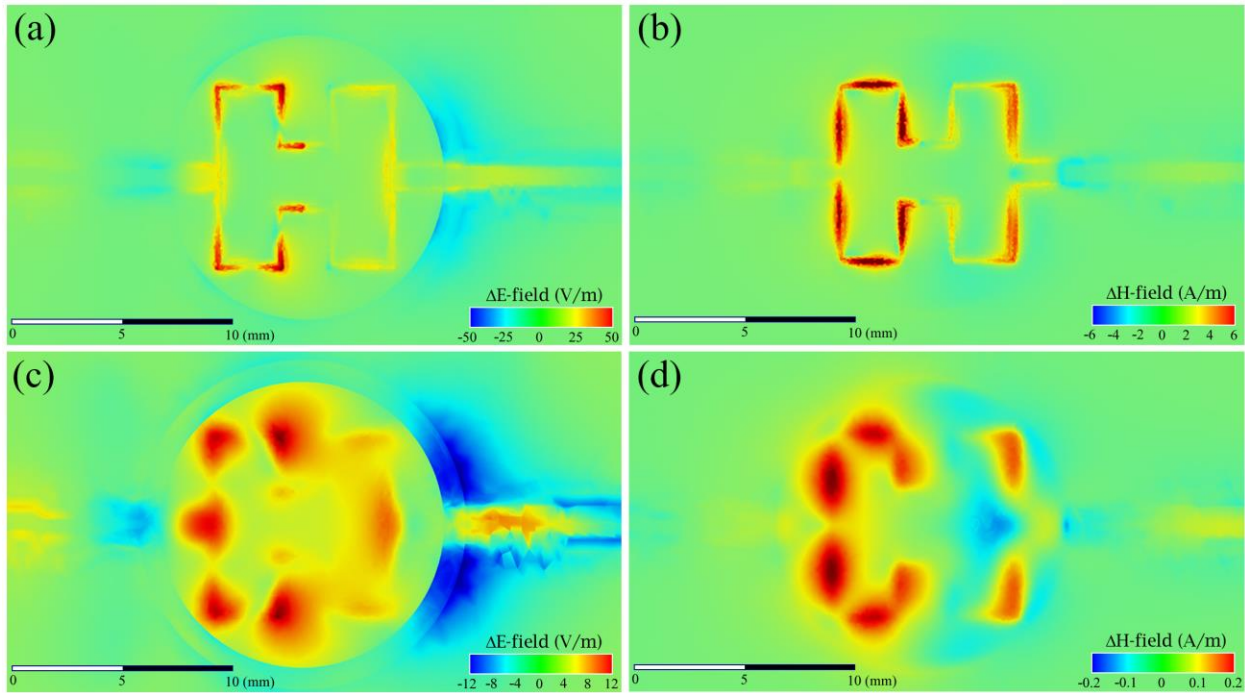


Fig. 5. The simulated subtraction image of 250 mg/dB and 0 mg/dl (DI water) MUTs for (a), (c) electric field and the (b), (d) magnetic field at (a), (b) sensor/MUT interface (i.e. on boundary of sensor/glucose solution) and (c), (d) at 1 mm distance from sensor/MUT interface (i.e. inside of the glucose solution), respectively at an operating frequency 2.67 GHz.

5. Conclusion

The microwave sensor based on modified Hilbert-shaped closed curve was designed and prepared as a non-invasive glucometer for monitoring of glucose concentrations in glucose aqueous solution. The sensor can detect the variation of glucose concentrations in aqueous solution with a non-destructive method.

The linear relationship between measured reflection coefficient S_{11} response and D-glucose concentrations at about 2.6GHz was found to be $0.018dB / (mg / dl)$. The minimum detectable resolution for glucose concentration was about $1.68mg / ml$ for $500\mu l$ MUT volume.

The results show the sensitivity and utility of sensor for glucose monitoring. Finally, it has great potential to offer a good platform for non-invasive and nondestructive measurement of human glycemia.

Acknowledgments

This work was supported by a Sogang University Research Grant (201519064), Basic Science Research Program through the National Research Foundation of Korea (2015R1D1A1A02061824 and 2009-0093822), and by a Scientific Research Grant through the State Committee of Science of Ministry of Education and Science of Armenia (18T-1C114).

References

- [1] Ashish Shendurse, Chandraprakash Khedkar, Glucose: Properties and analysis, The Encyclopedia of Food and Health, Oxford: Academic Press 3 (2016) 239-247.
- [2] World Health organization, <http://www.who.int/features/factfiles/diabetes/en/>.
- [3] M. Cusick, et al., Associations of mortality and diabetes complications in patients with type 1 and type 2 diabetes, *Diabetes Care* 28 (27) (2005) 617-625.
- [4] M. Burge, et al., Continuous glucose monitoring: The future of diabetes management, *Diabetes Spectr.* 21 (2) (2008) 112-119.
- [5] A. Rosen, et al., Applications of RF/microwaves in medicine, *IEEE Trans. Microw. Theory Tech.* 50 (3) (2012) 963-974.
- [6] Seungwan Kim, Jongchel Kim, Arsen Babajanyan, Kiejin Lee, Barry Friedman, Noncontact characterization of glucose by a waveguide microwave probe, *Current Applied Physics*, 9 (4) (2009) 856–860
- [7] Jan Vrba and David Vrba, *Radioengineering*, 24(4) (2015) 877-884
- [8] Thomas Chretiennot, David Dubuc and Katia Grenier, *Sensors*, 16 (10) (2016) 1733
- [9] H. Melikyan, et al., Non-Invasive in-vitro sensing of d-glucose in pig blood, *Med. Eng. Phys.* 34 (3) (2012) 299-304
- [10] Kiejin Lee, Arsen Babajanyan, Chongchel Kim, Seungwhan Kim, Barry Friedman, *Sensors and Actuators A: Physical*, 148 (1) (2008) 28-32.
- [11] R. Pethig, Dielectric properties of body tissues, *Clin. Phys Physiol. Meas.* 8 (1987) 5-12.
- [12] D. Lide, *Handbook of Chemistry and Physics*, CRC Press, New York, 2004.
- [13] Debye, P., *Ver. Deut. Phys. Gesell.* 15, 777; reprinted 1954 in collected papers of Peter J.W. Debye. Interscience, New York, 1913.

Investigation of Detection of Electromagnetic Radiation in The Plasma at The Constant Electric Field

(Proceedings of the Int. Conference on “Microwave and THz Technologies and Wireless comm.”)

G. Gulakyan¹, A. Makaryan², R. Miroyan²

¹Information Systems Service and Development Department, YSU Ijevan Branch, Ijevan,
Usanoghakan str. 3, 4001, Armenia

²Radiophysics and Electronics Dept., Yerevan State University, Yerevan, Alex Manoogyan
str. 1, 0025 Armenia

Received 15 November 2018

Abstract: The present paper deals on the investigation results of the detection of electromagnetic radiation in a glow discharge plasma of various gases. The voltage to the lamp is applied from a current source, providing a glow discharge in the lamp. It was shown that the detection efficiency depends strongly on the shape of the I-V characteristic of a gas-discharge lamp, as well as on the applied voltage (electric field). The different types of neon gas-discharge lamps were used as detectors. We also investigated the detection of a pulsed neodymium laser in air at an external electric field. Under the joint action of the laser pulse and the applied electric field, in the focusing region of the laser beam breakdown of air occurs. Thanks to the constant applied field, the created plasma behaves as a medium with a quadratic nonlinearity, which makes it possible to detect the electromagnetic radiation.

Keywords: Glow discharge plasma, nonlinear properties, laser-induced plasma.

1. Introduction

Gas-discharge lamps are widely used in various devices as indicators, light sources, noise sources, dischargers, etc., due to simplicity of design, reliability and low cost.

The nonlinear properties of gas-discharge devices are well known in the low-frequency region of electromagnetic waves. Their properties in the microwave and THz ranges have also been investigated by many authors (see, for example, [1–3]). Unlike nonlinear crystals, gas-discharge devices can withstand very high intensities of electromagnetic radiation, therefore, they can be successfully used as nonlinear elements for frequency conversion of high-power laser radiation.

In the last decades a lot of attention has been paid to the interaction of laser radiation with plasma, particularly, terahertz pulse generation in the laser-induced plasma from a series of noble gases, such as He, Ne, Ar, Kr, and Xe was systematically investigated [4–6]. Femtosecond laser pulses consisting of both a fundamental and its second-harmonic frequency were used for the terahertz generation [2–9]. Numerous works have appeared relating to the processes occurring in the atmospheric air under the influence of high power laser radiation. The powerful THz radiation was received from the femtosecond laser filament in air.

In gas-discharge devices, it is possible to arbitrarily increase the region of nonlinear interaction of electromagnetic wave with the plasma, thereby increasing the conversion efficiency.

We studied the features of the detection of laser radiation in a glow discharge plasma in neon gas-discharge lamps, as well as the detection of neodymium laser radiation in ambient air in the presence of an external constant electric field in present paper.

Various neon lamps with parallel electrodes were used as glow discharge detectors. The look and typical form of the I-V characteristics of the lamps used are shown respectively in Fig. 1a and 1b.

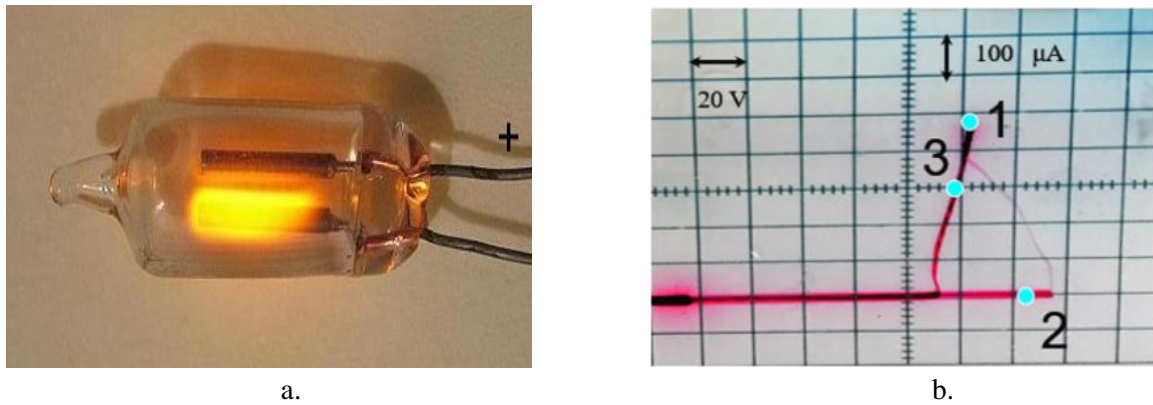


Fig. 1. a. appearance of lamp, b. typical form of the I-V characteristics

We considered different operation modes of the lamp: glow discharge mode (points 1, 2 on the I-V characteristic) and standby mode (point 3, the lamp is closed until the laser pulse appears).

The block diagram of the experimental setup is shown in Fig. 2.

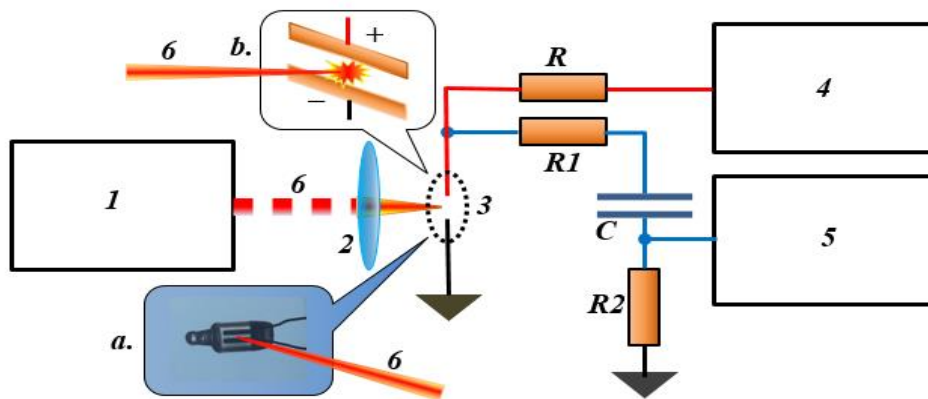


Fig. 2. 1-pulse neodymium laser, 2-lens, 3-plasma area (a. neon gas-discharge lamp, b. electrodes in ambient air), 4-adjustable high-voltage DC source, 5-oscilloscope Tektronix TDS 7102, 6-laser beam, R-ballast resistor, R1, R2, C-decoupling circuit with voltage divider.

The operating point on the I-V characteristic of the lamp was chosen by feeding a constant voltage to the gas discharge lamp 2 through the ballast resistor R. The YAG: Nd laser radiation was focused in the interelectrode region of the lamp.

The detected signal was taken from the anode of the gas-discharge lamp through a decoupling and voltage divider circuit (R1, R2, C), and was supplied to the Tektronix TDS 7102 oscilloscope.

When the distance between the side walls of the lamp exceeds the interelectrode distance L , and the operating point is selected in the region of the glow discharge (point 1 according to the I – V curve), a flat discharge is realized. Since the characteristic size of the Faraday dark space in this case does not depend on the gas pressure, the glow discharge turns out to be essentially non-uniform. If at the same time the interelectrode distance does not exceed the characteristic size of

the near-electrode layers the current-voltage characteristic of the lamp is non-linearly increasing [10]: $U \sim L^{3/2} J^{1/2}$, or $J \sim U^2$, where J is the lamp current density.

At the operating point 2, close to the threshold of a glow discharge, under the influence of electromagnetic radiation, a discharge occurs in the lamp, and because of the region of negative resistance according to the I-V curve, the operating point jumps from 2 to 3.

Oscillograms of the corresponding detected signals (change in voltage on the lamp when exposed to a laser pulse) are shown in Fig. 4.

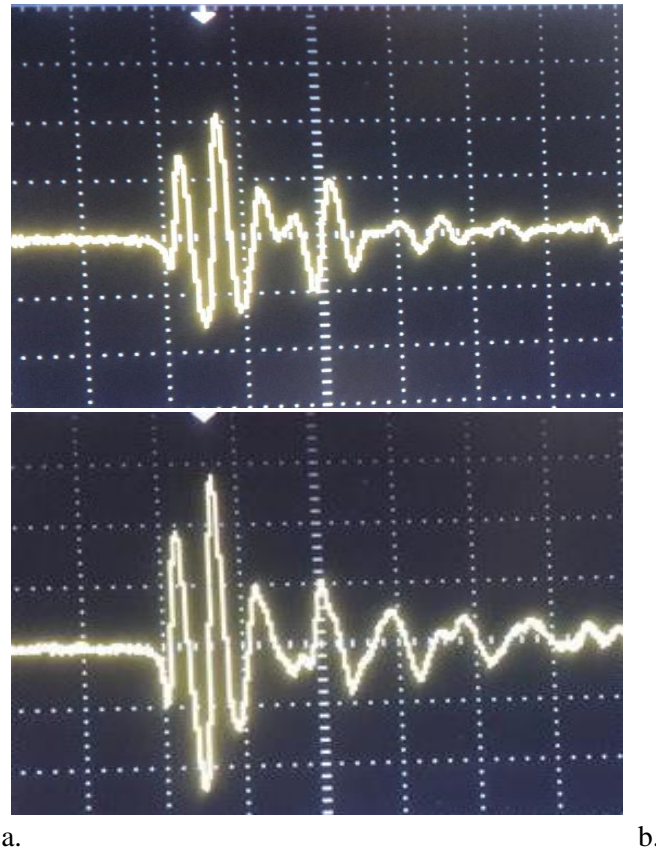


Fig. 4. Oscillograms of the detected signals: a. corresponding to the operating point 1 (see Fig. 1b), b. corresponding to the operating point 2.

The comparison shows that the detection efficiency strongly depends on the shape of the I-V curve of the gas-discharge lamp, as well as on the applied bias voltage (electric field). In the case of the choice of operating point 2 due to a sharp change in the anode current under the action of laser radiation, the detected signal is more than one and a half times stronger than the signal obtained in the first case.

The detection of a laser pulse in plasma of atmospheric air is also of interest.

In this paper, we investigated the detection of radiation from a relatively low-power pulsed neodymium laser (peak power $\sim 0.7MW$) in atmospheric air plasma. It should be noted that laser radiation with a specified power is unable to independently initiate air breakdown, however, when combined with external electrostatic and laser fields, it is possible to initiate breakdown.

The laser beam is focused on the interelectrode space by means of a short-focus lens ($d \approx 1mm$) (see Fig. 4.) with an electrostatic field of strength $E_0 \approx 2000kV/m$ (the interelectrode voltage $U_0 \approx 2kV$). With the combined effect of a laser pulse and an electrostatic

field in the region of the beam focusation, air breakdown occurs. In the case when the plane of polarization of the laser radiation coincides with the direction of the electrostatic field, a nonlinear polarization of the plasma occurs $P_{NL} \sim (E_m \cos \omega_1 t + E_0)^3$, which is responsible for the optical rectification of the laser pulse.

We measured the change in voltage on the electrodes induced by the breakdown of air in the interelectrode gap. The registration scheme is the same (see Fig. 2.). The signal magnitude was $\sim 150V$ at $R_1 = 100k\Omega, R_2 = 10k\Omega, C = 0.1\mu F$.

When the polarization plane of the laser beam is rotated by 90° , the minimum value of the electrostatic field at which air breakdown occurs increases about 1.6 times. At the same value of the laser power ($0.7MW$), the amplitude of the detection signal (change in voltage on the electrodes) also increases ($\sim 1.4times$). This is explained by the fact that due to the breakdown of air, the interelectrode resistance decreases abruptly, as a result the voltage across the electrodes drops to almost zero. Consequently, the magnitude of the detected signal depends mainly on the initial voltage on the electrodes.

In conclusion, we note that the results obtained in present work can be used to convert the frequency of laser radiation in the plasma. Particularly, they can be used to generate THz pulses in ambient air using relatively low-power femtosecond lasers that are unable to independently initiate the breakdown of air.

References

- [1] G.D. Lobov. Devices for Primary Processing of Microwave Signals, M. MEI, (1990).
- [2] Y. Chen, M. Yamaguchi, M. Wang, X. C. Zhang, Terahertz pulse generation from noble gases, Appl. Phys. Lett., 91, 251116 (2007)
- [3] A. Abramovich, N. S. Kopeika, D. Rozban, E. Farber, Inexpensive detector for terahertz imaging. Appl. Opt., 46, 7207 (2007).
- [4] V. A. Andreeva, O. G. Kosareva, N. A. Panov, D. E. Shipilo, P. M. Solyankin, M. N. Esaulkov, P. González de Alaiza Martínez, A. P. Shkurinov, V. A. Makarov, L. Bergé, and S. L. Chin, Ultrabroad Terahertz Spectrum Generation from an Air-Based Filament Plasma, Phys. Rev. Lett., 116, 063902 (2016).
- [5] A. Houard, Yi Liu, B. Prade, V. Tikhonchuk, A. Mysyrowicz. Strong Enhancement of Terahertz Radiation from Laser Filaments in Air by a Static Electric Field. Phys. Rev. Lett., 2008, 100 (25), pp.255006. <10.1103/PhysRevLett.100.255006>. <hal-00455124>
- [6] Yi Liu, A. Houard, B. Prade, A. Mysyrowicz, A. Diaw, et al.. Amplification of transition-Cherenkov terahertz radiation of femtosecond filament in air. Appl. Phys. Lett., 2008, 93 (5), pp.051108. <10.1063/1.2965612>. <hal-00458429>
- [7] T.-J. Wang, J.-F. Daigle, S. Yuan, F. Th'èberge, M. Ch'ateauneuf, J. Dubois, G. Roy, H. Zeng, and S. L. Chin, Remote generation of high-energy terahertz pulses from two-color femtosecond laser filamentation in air, Phys. Rev. A 83, 053801 (2011).
- [8] K. Y. Kim, J. H. Glowonia, A. J. Taylor and G. Rodriguez, Terahertz emission from ultrafast ionizing air in symmetry-broken laser fields, Optics Express 15, 8, 4577-4584 (2007).
- [9] J. Liu, J. Dai, S.-L. Chin and X.-C. Zhang, Broadband terahertz wave remote sensing using coherent manipulation of fluorescence from asymmetrically ionized gases, Nature Photonics 4, 627-631 (2010).
- [10] B.A. Knyazev. Low-temperature plasma and gas discharge, Novosibirsk, 2003. 290 p.

A Device For Measuring Body Bioimpedance With Combined Various Physical Affects

(Proceedings of the Int. Conference on “ Microwave and THz Technologies and Wireless comm.”)

S. G.Martirosyan¹, A. G. Ghulyan¹, N. D. Yezakyan¹, N.S.Mkrtchyan², T.H.Lazaryan²

¹ Institute of Radiophysics and Electronics, Alikhanian Brothers str. 1, 0203 Ashtarak, Armenia

² Izmirlyan Medical Center, Aharonyan str. 6, 0069 Yerevan, Armenia

Received 15 November 2018

Abstract: A biomedical device is described which is supposed to be used for the purpose of diagnosis and investigation in biomedical tissues and skin, body’s different parts. It can externally affect on the skin of human body with different types of currents (i.e. direct, alternate, pulse and so on). Many researches have been done about affecting electrical signals in human body. So, it can be to diagnose the presence of the disease in the patient with the existing results. Several medical procedures can be done by using our suggested the device: electro sleep, electro analgesia, galvanization and etc. The device measures bioimpedance of the person suspended by temperature in the different points of the skin. The affecting direction of active points can be changed. The software will be provided in the second version. Computer will help to save medical data and do long time investigations for every patient.

Keywords: Bioimpedance, transitional impedance, silver electrode , amplipulse .

1. Introduction

We must know not only affecting factor but also the reaction of the organism for that factor in diagnostic purposes. The electrical properties of the skin depend on the region structure of the skin. The best factor for that property is the bioimpedance. The impedance of tunic of body is tens to hundred $K\Omega$ in different parts of the skin [1].

The current is given from the different points of the skin using electrodes. The current finds the way where impedance is minimal. That current flows through the person and can be changed depending on the rate of blood flow.

At the point of the square of electrode it is desirable to minimize “electrode-skin” transitional impedance, which depends on the substance of the electrode, the properties of the skin, the contacting square of the electrode and med-contacting layers.

Every ‘skin-electrode’ contact (i.e. SEC) can be foreseen as electrical equivalent scheme, which has impedances and capacitors (Figure 1):

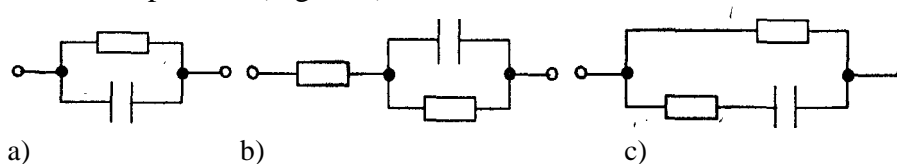


Figure 1: SEC equivalent schemes in low frequencies (a. simple scheme, b. the scheme when dealing with the layer of the skin and hypodermic nets, c. the other properties accompanied by muscular tissues [2, 3].

Let’s see the existing electrode types as they have important role in SEC node. They are divided into 3 groups:

- Metallic electrodes – they have great oxidization which is a disadvantage.
- Metal + soluble salt + that salt’s ions.
- Gas electrodes – they are porosity systems, i.e. the mixture of platinum or graphite.

Silver electrodes' advantage is that after the regulations they have minimal noise, theoretically - no noise. Two electrodes are located in different thermal conditions, however it causes small zero deviation [3].

We can do several works with the help of device from existing methods [4-7].

- Amplipulse therapy is an electrotherapy method during which the patient is exposed to alternating modulated currents of low intensity. These currents combine currents of high and low frequencies. Amplipulse therapy uses alternating sinusoidal currents of $2000-10000\text{Hz}$ frequency modulated by sinusoidal low-frequency oscillations (ranging $10-150\text{Hz}$). [6]
- General, local galvanization stimulates regulatory function of nervous and endocrine systems, normalizes secretory and motor function of digestive tract, stimulates trophic etc., in particular, increases protecting function of the skin.
- Interferential current therapy is a synergistic vibration in the human body resulting from overlaying (interference) of two independent high frequency currents. Normally the current sent via one electrode has constant frequency, while the current in the other electrode has alternating frequency. The low frequencies (up to 50Hz) cause excitation of neuromuscular structures. $50-100\text{Hz}$ currents improve tissue trophism, blood circulation; tone the muscles [7].
- Electro sleep therapy is a method of local action by impulse electric current of the corresponding parameters through electrodes and wet hydrophilic gaskets (or with the help of an electro conductive gel), contact super imposed paired, one polarity - on the skin surface of the eye sockets or the superciliary areas of the head, single, different polarity - on the skin surface of the posterior region of the patient's neck.
- Current strength - up to 10mA ; voltage - up to 18V ; pulse repetition rate - $1-160\text{Hz}$; the pulse duration is $0.2-0.5\text{ms}$; the shape of the pulse is predominantly rectangular; duty cycle - 10 [4, 5].
- Etc.

2. Device structure

We designed the first prototype of device and measuring body. The measuring body consists of silver electrode which is located in the center of cylindrical heating system and is isolated from it. The heating system insures uniform heat of the electrode environment (Figure 2).

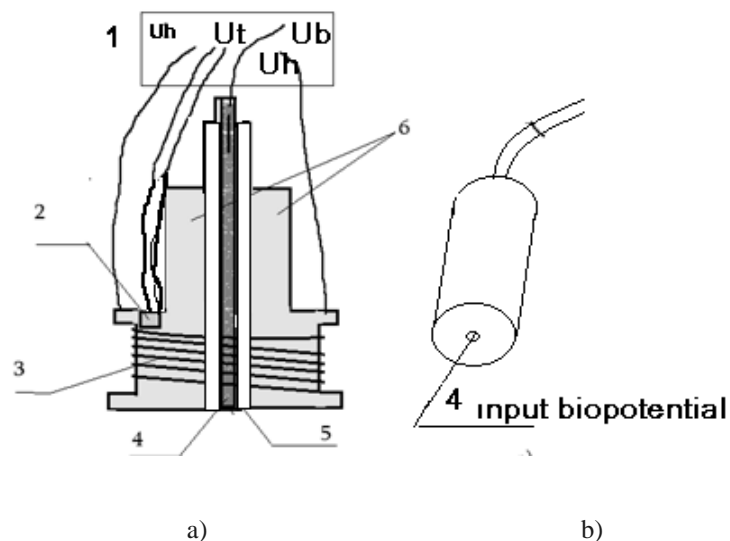


Figure 2: The internal part of measuring header (a) and general view (b)

The Measuring header has:

1. Cables which are connected to a device.
2. Semiconductor thermo sensor which insures skin environment's constant temperature watching.
3. Wrapped in nichrome wire which insures the heating of electrode.
4. Silver wire or electrode ($d = 1mm$) from which we measure bioimpedance.
5. Isolator which is isolated; 4 and 6.
6. The heating surface.

The heating doesn't support in most of devices. The physiological differences are observed in the heating process and other measuring headers can't register it. Besides the doctor has freedom to choose the direction of the affecting voltage.

Our designed device has the following structural scheme (power source scheme and its connections aren't included in the scheme for the simplicity) (Figure 3):

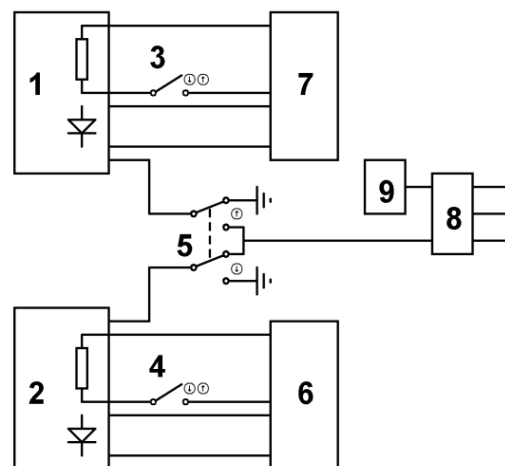


Figure 3: The structural scheme of the device

The 1 and 2 are the headers which are described above. The heating connections of electrodes are done by 3 and 4. The 5 switch defines at what moment which electrode would be the biopotential register and which the grounded. The 6 and 7 are thermo regulators. The 8 is biopotential signal amplifier. One of the inputs of amplifier is given in the 9th functional generator voltage and the other – biopotential voltage. In the output of the 8 we have constant, differential and alternative voltages of the biopotential signal.

The heating header has possibility of heating since 50° because the human body will burn above that temperature.

The device works as follows. The doctor switches on the measuring units after that the power. Now the doctor can heat the measuring units or one of it's or none (can be changed while working the device).

Now the doctor starts to do the main part. For example, the constant current is given to the patient while the latter rests. After that the mean voltage is subtracted by using potentiometer (isn't shown in the figure) and the patient is given different types of currents (constant, alternative, pulse, etc.) and the constant and differential voltages are measured in the output. The output voltages can differ by the person's age, illness and the skin's examination parts, etc.

3. Results

The surrounding electricity is everywhere in the buildings, hospitals, etc. and the person also receives 50Hz or 60Hz notch signals. So in experimental results we must identify it. It has $0.25 - 1\text{V}$ amplitude. For instance, it is small in fingers, knees, but is high in the lower part of the leg. There is no difference while heating in the low frequencies in teenager, but in elder people notch signal is small while heating.

When the frequency is 500Hz or higher, the triangle waves have spectral changes and the amplitude is over in tops. The signal is more linear when heating and has 50Hz notch signal more lower (fig. 4).

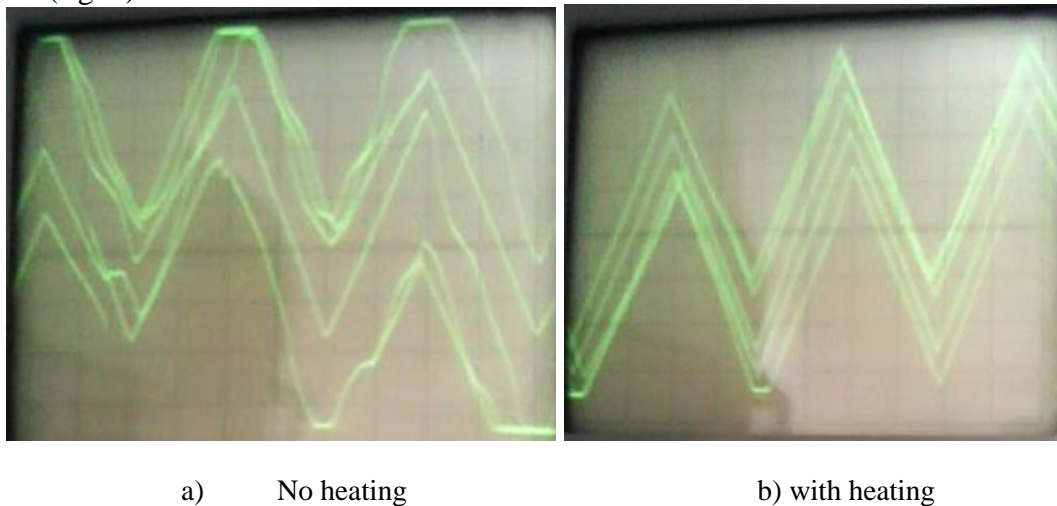


Figure 4: The output signal in the ear (500 Hz input triangle signal)

So the device can be used in medical institutions for diagnosis and investigation purposes. The device can be used as stationary system and outside the clinic as it is uses low power.

References

- [1] A.R. Livenson. Electrical safety of medical equipment / A. R. Livenson. - 2nd ed., Elaboration and add. - M.: Medicine, 1981. - 279 p.
- [2] V.I. Loshilov, L.I. Kalakutski. Biotechnical electroneurostimulation systems. - M.: MSTU, 1991. - 168 p.
- [3] John G. Webster, Medical Instrumentation: Application and Design, 4th Edition, Hoboken, NJ : John Wiley & Sons, Inc., 2010 - 713 pages.
- [4] V.G. Yasnogrodski. Electrotherapy, M.: Medicine, 1987, 240 p.
- [5] <http://www.radius.by/en/glossary/amplipulsetherapy.html>
- [6] <http://www.alfaradon.by/en/treatment/physiotherapy/galvanization-treatment/>

Power Analog of Trigger Schmitt's

(Proceedings of the Int. Conference on "Microwave and THz Technologies and Wireless comm.")

S. Martirosyan¹, J. Torikyan¹

¹ Institute of Radiophysics and Electronics, Alikhanian Brothers str. 1, 0203 Ashtarak, Armenia

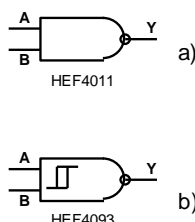
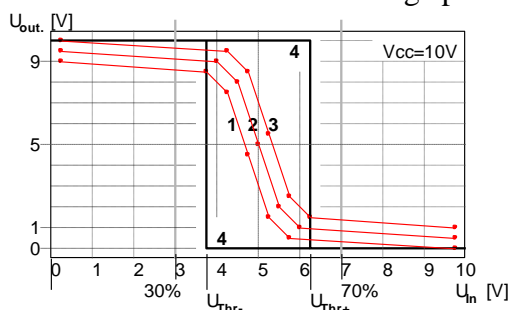
Received 15 November 2018

Abstract: Our designed electrical appliance is intended for use in managing and controlling devices as a powerful electrical coupling hub. It is a functional equivalent of the HEF4093 integrated circuit and is assembled on the basis of a modern integrated circuit (comparator) and a MOSFET transistor for power output. The input of the scheme requires digital or analog signal. At the output of the device it is possible to switch the load, which may have high currents. The transistor is protected from the short load mode. The structure of scheme allows the free choice of comparator and transistor based on the required electrical parameters. The device model has been tested on 0.5-2 amperes range.

Keywords: Schmitt's trigger, integrated circuit, logical function elements.

1. Introduction

It is known that all types of digital circuits are based on series of logical function elements: "AND", "NOT", "OR", "NAND", "NOR". The characteristics of the "input-output" dependence of the "NAND", "NOR" elements are shown in Fig. 1 where curves 1, 2, 3 are indicating possible deviations from the average position.



Functional Table		
$Y = \overline{AxB}$		
Inputs		Output
A	B	Y
L	L	H
L	H	H
H	L	H
H	H	L
H=High Logic Level		
L=Low Logic Level		

Fig. 1.

Fig. 2.

Fig.3.

The signal corresponding to the logic level "0" should be no more than 30% of the supply voltage (V_{CC}) to avoid an undefined zone in the center of the characteristic, and the signal corresponding to "1" should be at least 70%. The HEF4011 microcircuit contains 4 elements "2xNAND" and input characteristics have indicated by numbers 1, 2, 3 in Fig.1. [1].

It is also known that logical signals, which are supplied to the input of simple logic circuits, must have very short fronts in time (about 1...20ns) to ensure low consumption currents. If it is necessary to feed signals of the inputs of logic circuits with more rise and fall times with the orders of μs or ms and reduce the current consumption and 40% range of uncertainty, logic elements with a Schmitt trigger circuit at the inputs (for example, HEF4093) are used. The trigger provides the hysteresis characteristic shown in Fig.1 (curve 4), where the transition from "0" to "1" and from "1" to "0" is about 20% of V_{CC} . The symbol of the element "2xNAND" of the usual scheme is shown in Fig. 2a and the symbol based on the Schmitt trigger is on Fig. 2b. They have the same logical table of functions, as shown in Fig.3. [1, 2].

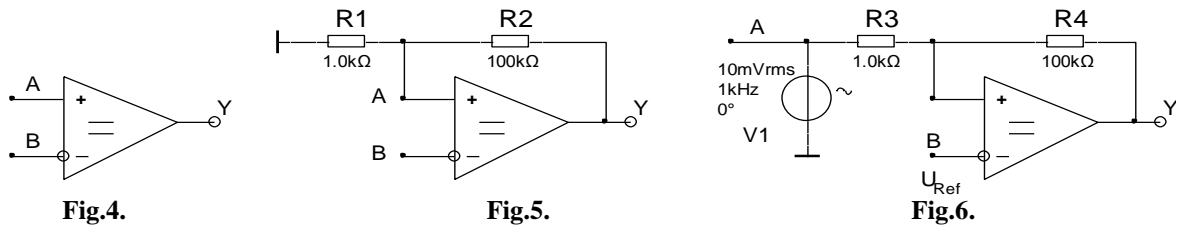
The advantage of the Schmitt trigger circuit is that we can give to its input not only digital signal, but also an analogue signal and the internal transistors are always either in the saturation or in the cut-off modes and the chip consumes very little power.

The disadvantage of the digital element as an analog converter with the input of the Schmitt trigger is that it requires a high input signal ($0.6V_{CC} \div 1V_{CC}$). Usually the supply voltage will be from 3V to 15V for such microcircuits. Therefore, using the simplest digital circuit, it can convert an analog signal, the smallest value of which can be $U_{in} = 0.6 \times 3V = 1.8V$.

2. Objective

The purpose of the work is to develop the analog of HEF4093 that performs the function “2xNAND”, with sensitivity of the order of *mV* and has an output operating current tens or hundreds of times more than the chip HEF4093.

Analog signals (starting from *mV*) can be converted to digital without prior amplification, using an integrated comparator, the symbol of which is shown in Fig.5. [3]. Such signals are obtained from various analog transducers of physical values into an electrical signal.



The comparator function is described as follows: if $U_a - U_b = \Delta U_{in} > 0$ (on the order of *mV*), then $Y = "1"$ and if $U_a - U_b = \Delta U_{in} < 0$, then $Y = "0"$. Therefore the moment of equality of two signals can be represented by a logical "0" or "1" with accuracy of the order of *mVs*. The biggest advantage of the Schmitt trigger based on the comparator is that it can send analog signals to its input, ranging from *mVs* to the supply voltage.

In Fig.5 is shown a comparator with positive feedback, performed on the R1 and R2 resistances. Due to positive feedback, a hysteresis is automatically generated. The upper threshold of the comparator is determined from the equation $U_{Thr+} = U_{out} \times R1/(R1 + R2)$, where $U_{out} = V_{CC}$. Accordingly, the lower threshold is $U_{Thr-} = U_{out} \times R1/(R1 + R2)$, where $U_{out} = 0$, or $U_{out} = V_{EE}$. The hysteresis voltage is defined by $U_{Hist} = U_{Thr+} + U_{Thr-}$.

Based on the requirements of the task, it can choose any voltage and width of the hysteresis and calculate the resistances R1, R2. In terms of application, this Schmitt trigger based on the comparator is very flexible. If in the Fig. 5 the left end of resistance R1 is used as an input and a variable signal is fed there and the input of B is for voltage U_{REF} , then the moments when the input voltage A exceeds the reference voltage can be registered with hysteresis accuracy (Fig.6) [3].

On the basis of Fig.6, was developed a “2xNAND” circuit for analog signals (Fig.7), where a high-power N-channel field-effect transistor (FET) is used as an inverter [4].

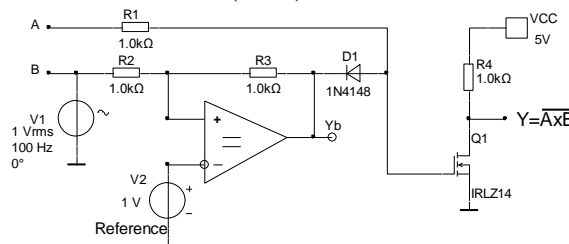


Fig.7.

Input A in the Fig.7 is intended only for a logical signal, and input B for any logical or analog signals. If necessary, it can select the desired reference voltage U_{REF} . This circuit is equivalent to a HEF4093 chip with more flexible inputs and a powerful output.

When $U_A = "1"$ and $U_B > U_{REF} + U_{Hist}$, then the output of the circuit is $Y = "0"$ (transistor Q_1 is in saturation mode). The current which pass through the load $R4$ is determined by the following equation: $I_{Load} = V_{CC} / (R4 + R_{sat})$, where R_{sat} is the internal resistance of Q_1 when it is in saturation mode. It can provide current from hundreds of mAs to several amperes by choosing the necessary transistor Q_1 .

It was designed a powerful analogue of the Schmitt trigger based on the scheme of the Fig.7 in order for using in the security and management schemes. For this purpose, the circuit in Fig.7 was supplemented with a circuit which limits the load of current on a security level. The circuit is shown in Fig.8 with a current stabilization.

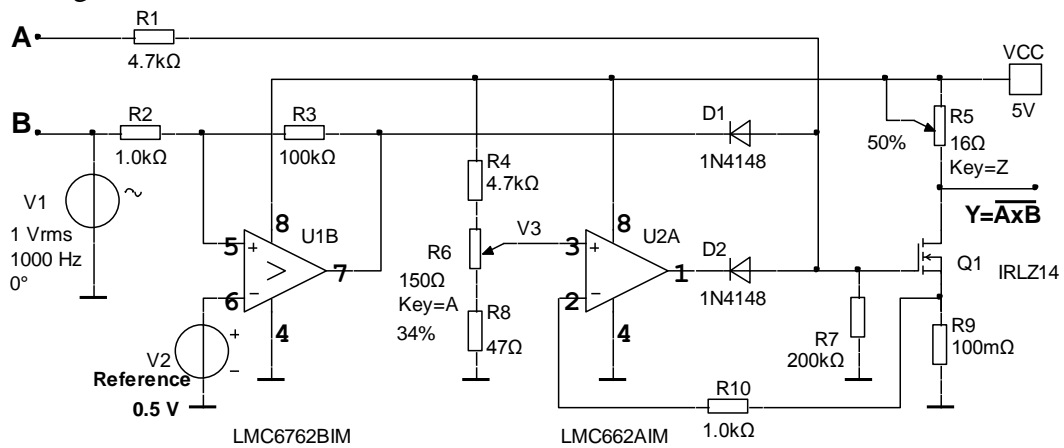


Fig. 8.

In this circuit, the resistances $R5$, R_{sat} and $R9$ pass the same current. The load current I_{Load} is determined by the following equation: $I_{Load} = V_{CC} / (R5 + R_{sat} + R9)$. If $R5$ is much greater than R_{sat} and $R9$, then $I_{Load} = V_{CC} / R5$.

In Fig.8, the circuit elements $R1, R2, R3, V2$ and $U1$ constitute the function of comparator part of the circuit [5]. The elements $R4, R6, R8, R10, D2$, operational amplifier $U2$, FET transistor Q_1 and $R9$ constitute a current stabilizer [6]. The stabilization current of the transistor is determined by the equation $I_{sat} = V_3 / R9$ [3].

3. Experiment

The model uses a powerful FET N-channel transistor IRLZ14S with parameters: allowable drain voltage 60V, direct drain current 10A, resistance in saturation mode 0.2Ω, $TO - 220$ package, power dissipation 43W.

The stabilization current is regulated by a resistor $R6$ within 0.5-2A ($V3 = 50 \dots 200mV$).

The table shows the results of the experiment at $V3=100mV$.

$R5$ [Ω]	16	12,8	11,2	9,6	8	6,4	4,8	3,2	0	0
I_{sat} [mA]	308	342	384	437	508	754	992	1030	1030	1030

The table shows that the current stabilizes at a level of 1A with $R5 \leq 4.8\Omega$ and the circuit is protected from short circuit. The power dissipated on the transistor will be

$$P_{Q_1} = V_{CC} \times I_{sat} = 5W \ll 43W .$$

Required designs of radiator, dissipation area for the $TO-220$ package easily provide the heat sink of the transistor Q_1 .

4. Conclusion

1. It was developed a powerful and full functional analogue of the HEF4093 chip with sensitivity of the order of mVs and has an operating output current from hundreds of milliamperes to several amperes.

2. It was given an example of implementation, where the resistance $R9$ and the output transistor work even in the short circuit mode, due to the small power dissipation on them.

3. This circuit design ensures continuous and uninterrupted operation of security devices, where short circuits of supply wires of remote loads often occur.

4. The power dissipated at the commutation transistor is many times smaller than the permissible power dissipation of it after entering the current stabilization mode.

References

- [1] S.Volkov "Square-wave impulse generators on MOS elements", Sofia, Moscow, Energy Publishing House 1981 (in Russian).
- [2] Datasheet Quad 2-input NAND Schmitt triggers HEF4093.
- [3] U. Tittse, K. Shenk, "Semiconductor circuitry", Moscow, "Mir", 1982(in Russian).
- [4] Datasheet Power MOSFET transistor IRLZ14S.
- [5] Datasheet Comparator LMC6762.
- [6] Datasheet Oper. Amplifier LMC662.

An Alternative Expression of The Poynting Vector Operating in a Confined Region of Evanescent Waves: Natural Function in The Method of Single Expression

(Proceedings of the Int. Conference on “ Microwave and THz Technologies and Wireless comm.”)

H.V. Baghdasaryan¹, T.M. Knyazyan¹, T.T. Hovhannisyan¹,
A.V. Daryan², M. Marciniak³

¹National Polytechnic University of Armenia, 105 Terian str., Yerevan 0009, Armenia

²Alikhanyan National Laboratory, Cosmic Ray Division, 2 Alikhanyan brothers str., Yerevan 0036, Armenia

³National Institute of Telecommunications, 1 Szachowa Street, 04-894 Warsaw, Poland

Received 15 November 2018

Abstract: An alternative expression of the Poynting vector is presented. This expression is an intrinsic function at the electromagnetic wave description in the method of single expression (MSE). The MSE does not represent solutions of the Helmholtz equation as a sum of counter-propagating waves that permits to operate with an alternative expression for the Poynting vector. At the boundary problems solution carried out numerically by the MSE spatial distributions of electric and magnetic field amplitudes and the Poynting vector are obtained. An alternative expression of the Poynting vector is applicable both in confined media of a positive product of permittivity and permeability and of a negative product, that is relevant to the region of evanescent waves. The expression of the Poynting vector in the MSE is in complete agreement with the traditional representation of the Poynting vector.

Keywords: Evanescent waves, Poynting vector, Helmholtz equation, counter-propagation waves.

1. Introduction

The well-known expression for electromagnetic energy flow is the Poynting-Heaviside vector [1-3]:

$$\vec{P} = \frac{c}{4\pi} [\vec{E} \times \vec{H}], \quad (1)$$

In media, where electromagnetic wave cannot propagate, for example: in metals and plasma at frequencies less than plasma frequency or in optics at the total internal reflection (TIR) from the boundary of two dielectric media at the overcritical angles of wave incidence the Poynting vector is identically equal to zero [1-3]. However, in thin enough layers of metals [4-6], plasma (reentry plasma [7]) or at frustrated total internal reflection (FTIR) [8, 9] an electromagnetic wave after penetration to the confined region, where no propagating waves exist, indicates some transmitted energy as the fraction of the incident wave. A relevant boundary problem solution reveals that a wave penetrates into the medium where it is transformed to the evanescent field distributions, namely, exponential decreasing and increasing amplitude distributions [9-11]. These are not propagating waves and an application of the expression (1) for this type of a confined medium is a complicate procedure. Though partial energy transmission through the confined region of evanescent waves is under scientific and technical interest for a long time, still no information regarding the energy flow distribution within this type of regions are presented in the literature up to now [9-11].

Traditional methods of boundary problems solution operate with the Poynting vector only outside of the evanescent waves region. As opposed to them in the method of single expression (MSE) [12-15] for any boundary problem solution the Poynting vector is calculated within the media under analysis. The MSE gives an unusual solution to boundary problems as it operates with the alternative expression of the Poynting vector valid in any media including confined regions of evanescent waves as well.

The aim of the current work is a presentation of the alternative expression of the Poynting vector in the MSE suitable for monitoring the power flow distribution within the confined region of evanescent waves. As an example, the boundary problem solution by using the MSE is presented for a layer of negative permittivity at the wave normal incidence.

2. The method of single expression for the normal incidence of a plane wave

The MSE is an alternative correct tool for wavelength-scale analysis of any multilayer and modulated structures comprising dielectric, semiconductor or metallic layers with loss, gain or Kerr-type non-linearity [12-15]. The sketch of the boundary problem of normal incidence of a linearly polarized plane wave on an arbitrary layer bounded by loss-less and gain-less media is presented in Fig.1.

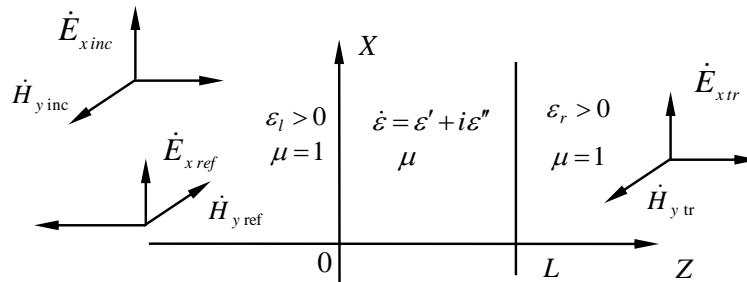


Fig. 1. Normal incidence of linearly polarized plane wave on a layer, from the left. Permittivities of surrounding loss-less and gain-less media and in the layer of thickness L are ϵ_l , ϵ_r and ϵ , correspondingly.

The description of the MSE for a plane wave normal incidence on any multilayer or modulated structure is the following. From Maxwell's equations in 1D case the following Helmholtz equation can be obtained for linearly polarized complex electric field component $\dot{E}_x(z)$ propagating along the z axis (*here and hereafter the dot above the letter indicates complexity of the value*):

$$\frac{d^2 \dot{E}_x(z)}{dz^2} + k_0^2 \dot{\epsilon}(z) \mu \cdot \dot{E}_x(z) = 0, \quad (2)$$

where $k_0 = \frac{\omega}{c} = \frac{2\pi}{\lambda_0}$ is the free space propagation constant, $\dot{\epsilon}(z) = \epsilon'(z) + i\epsilon''(z)$ is the complex permittivity of a medium, μ is the permeability.

At $\epsilon'(z) \cdot \mu > 0$, which means: either double positive ($\epsilon'(z) > 0$ and $\mu > 0$) or double negative ($\epsilon'(z) < 0$ and $\mu < 0$) medium, general solutions of the equation (2) in the traditional approach are represented as counter-propagating plane waves. In this case the relevant expression for the Poynting vector is:

$$P_z(z) = \frac{c}{8\pi} \text{Re}[\dot{E}_x(z) \times H_y^*(z)]. \quad (3)$$

At $\epsilon'(z) \cdot \mu < 0$, which means: either ($\epsilon'(z) > 0$ and $\mu < 0$) or ($\epsilon'(z) < 0$ and $\mu > 0$) in the traditional approach solutions of the equation (2) are decreasing and increasing exponential field distributions and this is a so-called region of evanescent waves. In unbounded region of evanescent waves the expression for the Poynting vector is completely imaginary value that brings to the absence of energy transfer, i.e. $P_z(z) = 0$ [1-3]. However, it is well known, it is possible to have energy transfer through a confined region of evanescent waves, i.e. $P_z(z) \neq 0$. Though the traditional expression of the Poynting vector is valid to monitor energy flow in such regions, but its application is a complicate task. The boundary problem solution by the MSE

permits to overcome this problem. The essence of the MSE is a presentation of a general solution of the Helmholtz equation for electric field component $\dot{E}_x(z)$ in the form of a single expression:

$$\dot{E}_x(z) = U(z) \cdot \exp(-iS(z)) \quad (4)$$

instead of the traditional presentation as a sum of counter-propagating waves. Here $U(z)$ and $S(z)$ are real functions describing the resulting electric field amplitude and phase, respectively. Time dependence $\exp(i\omega t)$ is assumed but suppressed throughout the analysis. The solution in the form (4) prevails upon the traditional approach of counter-propagating waves and is more general since it is not relied on the superposition principle, hence applicable for non-linear media as well. This form of solution describes all possible distributions of electric field amplitude in space, corresponding to propagating, standing or evanescent waves in a medium of a negative product of permittivity and permeability. This means that no preliminary assumptions concerning the Helmholtz equation's solution in different media are needed in the MSE.

Based on the expression (4) the Helmholtz equation (2) after separation on real and imaginary parts is reformulated to the set of first order differential equations (5) regarding the electric field amplitude $U(z)$, its spatial derivative $Y(z)$ and a quantity $\Pi_z(z)$, which is proportional to the power flow density (the Poynting vector) in a medium:

$$\begin{cases} \frac{dU(z)}{dz} = Y(z) \\ \frac{dY(z)}{dz} = \frac{\Pi_z^2(z)}{U^3(z)} - \varepsilon'(z) \cdot \mu \cdot U(z) \\ \frac{d\Pi_z(z)}{dz} = \varepsilon''(z) \cdot U^2(z) \end{cases} \quad (5)$$

here $z = k_0 z$ is the coordinate normalized on the wavelength and $\Pi_z(z) = U^2(z) \frac{dS(z)}{dz}$. The

actual value of the Poynting vector $P_z(z)$ can be obtained by multiplication of $\Pi_z(z)$ on $\frac{c}{8\pi\mu}$:

$$P_z(z) = \frac{c}{8\pi\mu} \Pi_z(z) = \frac{c}{8\pi\mu} U^2(z) \frac{dS(z)}{dz}. \quad (6)$$

The sign of $\varepsilon'(z)$ in the set of equations (5) can be taken either positive or negative describing relevant electromagnetic features of dielectric and metal (plasma), correspondingly. The sign of $\varepsilon''(z)$ indicates loss or gain in a medium.

The set of differential equations (5) is integrated numerically starting from the non-illuminated side of a layer at $(z = L)$, where only one outgoing travelling wave is supposed. The initial values for the integration are obtained from the boundary conditions of electrodynamics at the non-illuminated side of the layer (at $z = L$) as: $U(L) = E_{xtr}$, $Y(L) = 0$ and $\Pi_z(L) = \sqrt{\varepsilon_r} \cdot E_{xtr}^2 = \Pi_{ztr}$, where Π_{ztr} is proportional to the Poynting vector in the medium of permittivity ε_r beyond the layer (at $z > L$) and E_{xtr} is the amplitude of the transmitted wave. In linear problem solution the last can be taken as arbitrary.

Numerical integration of the set (5) goes step by step towards the illuminated side of the layer taking into account the actual value of the layer's permittivity for the given coordinate at each step of the integration. In the process of integration it is possible to record any variable of the set (5) in order to have full information regarding distributions of electric field amplitude, its derivative and power flow density inside and outside of the structure. From the boundary conditions of electrodynamics at the illuminated side of the structure the amplitude of incident wave E_{xinc} and the power reflection coefficient R :

$$E_{x\text{inc}} = \left| \frac{U^2(0) \cdot \sqrt{\varepsilon_l} + \Pi_z(0) + iU(0) \cdot Y(0)}{2U(0) \cdot \sqrt{\varepsilon_l}} \right|, \quad R = \left| \frac{E_{x\text{ref}}}{E_{x\text{inc}}} \right|^2 = \left| \frac{U^2(0) \cdot \sqrt{\varepsilon_l} - \Pi_z(0) - iU(0) \cdot Y(0)}{U^2(0) \cdot \sqrt{\varepsilon_l} + \Pi_z(0) + iU(0) \cdot Y(0)} \right|^2$$

are restored at the end of the calculation. Here $U(0)$ is the resultant amplitude of the electromagnetic wave, $Y(0)$ is its derivative and $\Pi_z(0)$ is proportional to the power flow density at the illuminated interface of the layer at $z=0$, $E_{x\text{ref}}$ is the amplitude of the reflected wave, ε_l is the permittivity of the medium in the front of the structure, at $z < 0$. The power flow density in the left medium (at $z < 0$) is the sum of two counter-propagating power flows, i.e. incident and reflected ones. In accordance with the energy conservation law $\Pi_z(0) = \Pi_{z\text{inc}} + \Pi_{z\text{ref}}$, where $\Pi_{z\text{inc}} = \sqrt{\varepsilon_l} \cdot E_{x\text{inc}}^2$ is proportional to the incident power flow density and $\Pi_{z\text{ref}} = -\sqrt{\varepsilon_l} \cdot E_{x\text{ref}}^2$ is proportional to the reflected power flow density. The negative sign of $\Pi_{z\text{ref}}$ is stipulated by its propagation opposite to z axis. The power transmission coefficient $T = \frac{\Pi_{z\text{tr}}}{\Pi_{z\text{inc}}} = \frac{\sqrt{\varepsilon_r} \cdot E_{x\text{tr}}^2}{\sqrt{\varepsilon_l} \cdot E_{x\text{inc}}^2}$ is defined as the ratio of the transmitted $\Pi_{z\text{tr}}$ to the incident $\Pi_{z\text{inc}}$ power flows.

3. Monitoring power flow through the confined region of evanescent waves-layer of negative permittivity

Let us consider the linearly polarized plane wave interaction with the layer of negative permittivity where evanescent waves are observed. Continuity of the traditional Poynting vector is fulfilled at the borders, while the relevant expression for the Poynting vector (6) in the MSE is calculated numerically throughout the structure without any issues regarding to the signs of permittivity $\varepsilon'(z)$, $\varepsilon''(z)$ and permeability μ .

As a specific example the MSE is applied for modelling of a plane wave incidence from the left on the layer (see Fig.1) of the thickness L of the negative real part of permittivity $\varepsilon' = -1$, at the absence of loss or gain $\varepsilon'' = 0$ and at the loss $\varepsilon'' = -0.2$ and the positive permeability $\mu = 1$. The calculation results are presented in Fig. 2. Partial transmission through the confined regions of evanescent waves is observed for thin enough layers of negative permittivity (Fig.2a,b). At the absence of loss in the layer ($\varepsilon'' = 0$) by increasing the thickness of the layer the reflectance R tends to the 1 (full reflection) and to zero transmission ($T = 0$), which is the limiting case for unbounded media of negative permittivity when the Poynting vector is zero.

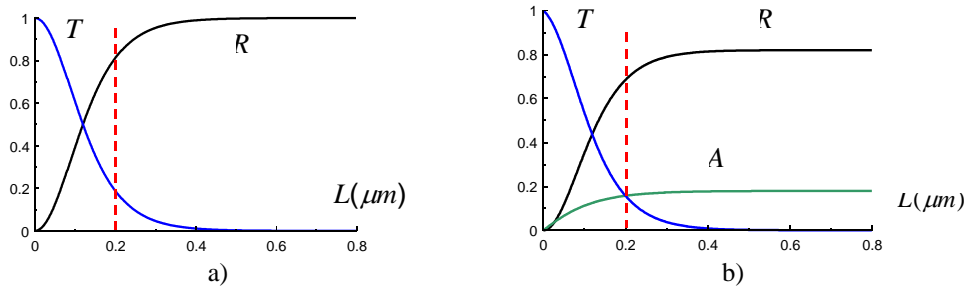


Fig.2. Reflectance R and transmittance T from the layer of negative permittivity versus its thickness L at the plane wave normal incidence; a) at $\varepsilon' = -1, \varepsilon'' = 0$, b) $\varepsilon' = -1, \varepsilon'' = -0.2$; $A = 1 - R - T$ is the loss in the layer.

$$\lambda_0 = 850 \text{ nm}.$$

At the loss ($\varepsilon'' = -0.2$) in the layer of the thickness L by an increase of its thickness the reflectance tends to the value less than 1 by the expense of loss in the layer (the curve indicated by letter A in Fig. 2b.).

To go deeply in the physics of the observed dependences it is useful to consider the layer of specific thickness, for example, of $L = 200 \text{ nm}$ (Fig.3).

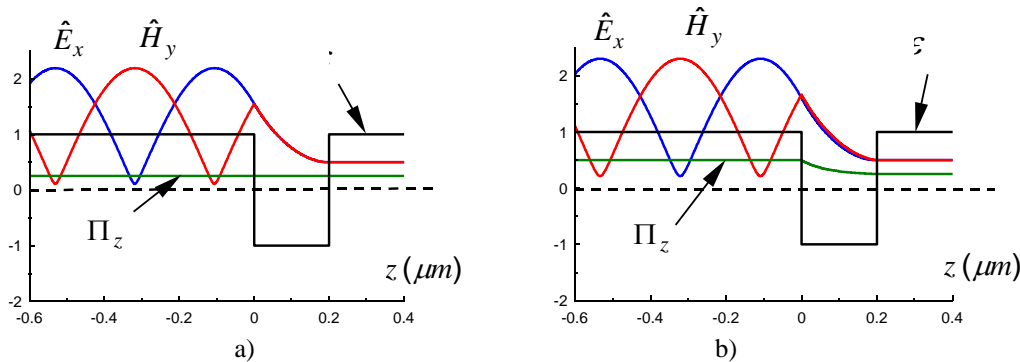


Fig.3 Distributions of electric \hat{E}_x and magnetic \hat{H}_y field amplitudes and power flow vector $\Pi_z(z)$ within and outside of the layer of the fixed thickness $L = 200 \text{ nm}$. $E_{xtr} = 0.5 \text{ ESU (CGSE)}$, $\lambda_0 = 850 \text{ nm}$, $\varepsilon_l = \varepsilon_r = 1$; a) at the absence of loss $\varepsilon'' = 0$, $R = 0.8121$, $T = 0.1879$; b) at the loss $\varepsilon'' = -0.2$, $R = 0.6856$, $T = 0.1568$, $A = 0.1576$.

A superposition of incident and reflected waves at $z < 0$ creates the region of partial standing wave (oscillating amplitudes of electric \hat{E}_x and magnetic \hat{H}_y components). Within the layer an exponential decrease of both amplitudes is observed (Fig.3a,b).

A continuity of the power flow at the boundaries is clearly observed in the modelling. At the absence of loss or gain ($\varepsilon'' = 0$) the power flow within the layer is constant and equal to the transmitted power flow (Fig. 3a). The transmitted power flow $\Pi_{ztr}(L) = \sqrt{\varepsilon_r} E_{xtr}^2$ is equal to

$$\Pi_z(L) = U^2(L) \cdot \left. \frac{dS(z)}{dk_0 z} \right|_{z=L}$$

at the output of the layer ($z = L$) and within the layer ($0 \leq z \leq L$). At the illuminated side of the structure in accordance with the energy balance law the sum of incident and reflected power flows is equal to the power flow within the layer.

At the loss in the layer ($\varepsilon'' = -0.2$) an exponential decrease of the Poynting vector in the region of evanescent waves is observed (Fig.3b). Thus, the loss in the region of evanescent waves is also possible to monitor by the MSE.

4. Conclusion

The expression of the Poynting vector (6) in the MSE is a valid alternative to the traditional one, especially useful for the region of evanescent waves and making it a unique instrument for analyzing energy flow within any media.

The MSE makes also possible to monitor power flow in the confined region of evanescent waves at electric and magnetic loss or gain by application of complex values $\hat{\varepsilon} = \varepsilon' + i\varepsilon''$ and $\hat{\mu} = \mu' + i\mu''$ [16,17] and at the plane wave oblique incidence [18-20].

5. Acknowledgment

Authors are thankful to the members of COST Actions MP 1403, MP1401 and CA16220 and the participants of IRPhE 2018 for fruitful discussions.

References

- [1] J.A. Stratton, *Electromagnetic Theory*, McGraw – Hill Book Company, Inc., 1941.
- [2] L.D. Landau and E.M. Lifshits, *Electrodynamics of Continuous Media*, 2nd ed., Oxford, England: Pergamon Press, 1984.
- [3] J.D. Jackson, *Classical Electrodynamics*, John Wiley & Sons, Inc., New York, 1962.
- [4] O.S. Heavens, *Optical Properties of Thin Solid Films*, Dover Publications Inc., N-Y, 1965.
- [5] H. V. Baghdasaryan, T. M. Knyazyan, A. A. Mankulov, G.G. Eyrarnjyan, “Numerical analysis of thin transparent film influence on reflecting and absorbing properties of metallic mirror”, in Proc. ICTON 2006, pp.213-216, Nottingham, UK, June 18-22, 2006.
- [6] R. Kotynski, H. Baghdasaryan, T. Stefaniuk, A. Pastuszczyk, M. Marciniak, A. Lavrinenko, K. Panajotov, and T. Szoplik, “Sensitivity of imaging properties of metal-dielectric layered flat lens to fabrication inaccuracies”, *Opto–Electronics Review*, vol. 18, Issue 4, pp.446–457, 2010.
- [7] L. Zheng, Q. Zhao, and X.J.Xing, “Effect of plasma on electromagnetic wave propagation and THz communication for reentry flight”, *ACES Journal*, vol. 30, No. 11, pp. 1241-1245, November 2015.
- [8] Z. Vörös and R. Johnsen, “A simple demonstration of frustrated total internal reflection”, *Am. J. Phys.* Vol.76/8, pp. 746- 749, August 2008.
- [9] L. Novotny, B. Hecht: *Principles of Nano-Optics*, Cambridge University Press, 2012.
- [10] F. de Fornel, *Evanescence Waves from Newtonian Optics to Atomic Optics*, Springer, 1997.
- [11] M. Bertolotti, C. Sibilia, A. M. Guzmán, *Evanescence Waves in Optics: An Introduction to Plasmonics*, Springer, 2017.
- [12] H.V. Baghdasaryan, *Basics of the Method of Single Expression: New Approach for Solving Boundary Problems in Classical Electrodynamics*. Monograph: Chartaraget, Yerevan, 2013, 164 pages.
- [13] H.V. Baghdasaryan, T.M. Knyazyan, “Problem of plane EM wave self-action in multilayer structure: An exact solution”, *Opt. and Quant. Electron.*, vol. 31, pp. 1059 – 1072, 1999.
- [14] H.V. Baghdasaryan, T.M. Knyazyan: Modelling of strongly nonlinear sinusoidal Bragg gratings by the method of single expression, *Opt. and Quant. Electron.*, vol. 32 (6/8), pp. 869-883, 2000.
- [15] H.V. Baghdasaryan, T.M. Knyazyan, T.T. Hovhannisyanyan, M. Marciniak, “Solution of boundary problems in intensity-dependent nano-optics and quantum mechanics by the method of single expression”, in Proc. ICTON 2017, paper Tu.B4.3, Girona, Spain, 2-6 July 2017.
- [16] H.V. Baghdasaryan, T. M. Knyazyan, “Extension of the method of single expression for analysis of materials with complex permittivity and permeability”, in Proc. ICTON 2006, pp.13-18, Nottingham, UK, 18-22 June 2006.
- [17] H.V. Baghdasaryan, T.M. Knyazyan, T.H. Baghdasaryan, B. Witzigmann, and F. Roemer, “Absorption loss influence on optical characteristics of multilayer distributed Bragg reflector: wavelength-scale analysis by the method of single expression”, *Opto–Electronics Review*, vol. 18, Issue 4, pp. 438–445, 2010.
- [18] H.V. Baghdasaryan, T.M. Knyazyan, T.H. Baghdasaryan, “Novel powerful simulation tool for wavelength-scale analysis of an oblique plane wave interaction with multilayer metamaterial structures”, in Proc. 2nd International Congress on Advanced Electromagnetic Materials in Microwaves and Optics, 3 pages, September 21-26, Pamplona, Spain, 2008.
- [19] H.V. Baghdasaryan, T.M. Knyazyan, T.H. Baghdasaryan, G.G. Eyrarnjyan, “Development of the method of single expression (MSE) for analysis of plane wave oblique incidence on multilayer structures having complex permittivity and permeability”, in Proc. ICTON 2008, Th.A1.4, pp. 250 – 254, Athens, Greece, 22-26 June 2008.
- [20] H.V. Baghdasaryan, T.M. Knyazyan, T.T. Hovhannisyanyan and M. Marciniak, “Metal-dielectric multilayer structure supporting surface plasmons: electromagnetic modelling by the method of single expression”, *Opt. and Quant. Electron.*, vol. 47, Issue 1, pp. 3-15, 2015.

Plasmonic Nanoparticles Arrangements for Biosensing

(Proceedings of the Int. Conference on “ Microwave and THz Technologies and Wireless comm.”)

H. Parsamyan, T. Yezekyan, H. Haroyan.

Yerevan State University, 1 Alex Manoogian, 0025 Yerevan, Armenia

Received 15 November 2018

Abstract: The localized surface plasmon resonance (LSPR) of gold and silver spherical and cubic nanoparticles (NP), as well as NP dimers is studied. We use numerical simulations based on finite element method to derive extinction cross sections (ECS) and LSPR wavelengths of the investigated structures. Study of the dependence of the LSPR of the cubic NPs on the different values of chamfering radius shows the red shift of the resonant wavelength while decreasing the chamfering radius. For the silver nanocube the analysis suggests three extinction peaks on ~333 nm, ~364 nm due to strong absorption and on ~400 nm due to scattering, while for gold nanocube there is only one extinction peak on ~526 nm. The diameter of the spheres and the sides of the cubes is 50 nm. According to the simulations the localized surface plasmon properties of the silver nanoparticles are much stronger and more diverse than that of corresponding gold nanoparticles. The study of nanocube and nanosphere dimers is carried out as well.

Keywords: Surface plasmon, plasmonic nanoparticles, biosensing, finite element method.

1. Introduction

The need for a fast, ultracompact, highly-sensitive, label-free and reliable devices for biosensing has provided a growing interest [1]. During the past decades, with the developing of nanotechnology the metal nanoparticles with different morphology have become of great interest due to their unique ability to interact with the incident light causing localized surface plasmon resonance (LSPR) phenomenon. The LSPR is a result of collective oscillations of the free electrons of a metal, which typically appear in the visible or near infrared for noble metals and strongly depends on the material of the particle, shape, sizes and the surrounding medium. These features allow one to use plasmonic metal NPs for study of fundamental optical processes, such as absorption, scattering and non-linear effects [2], as well as for technical applications, including drug delivery [3], cancer therapy [4], electronics, high-resolution imaging [5], surface enhanced Raman spectroscopy [6]. Moreover, the ability of NPs to interact with single small molecules with fluorescence enhancement and confine electromagnetic energy within small volumes make metal NPs good candidates for label-free chemical and biological sensing techniques offering sensitive, robust, and facile detection [7]. The sensing principle relies on the measurements of the LSPR spectral shift caused by the change of surrounding dielectric environment during a binding process. Since the nanoparticles themselves are colored, detection can often be carried out with the naked eye, yielding rapid, portable detection. In addition, the production and fabrication of nanoparticles, which contain small amounts of material, is often inexpensive.

Further advances in nanofabrication techniques led to wide investigation of NPs with various morphologies from nanocubes to more extraordinary structures, such as nanostars and nanotriangles [8-9]. A higher near-field enhancement and strong LSPR features can be achieved

in the structures containing two (dimers) or more closely spaced particles, which distance is in the order of NPs sizes. Thus, plasmonic properties of such systems can be drastically enhanced by exciting the system with a plane electromagnetic wave polarized along the interparticle axis.

This paper is focused on improvement of LSPR biosensors by using different geometries and arrangements of nanoparticles. Here, we present the numerical analysis of the LSPR of the single gold (*Au*) and silver (*Ag*) nanoparticles (NP) of spherical and cubic shapes, and for nanoparticle dimers as well. To have a LSPR in visible region, the diameter of the spheres and the sides of the cubes were chosen 50nm . The optical extinction spectra of the investigated structures are derived via a full wave electromagnetic simulation based on finite element method. Comparative analyses of the extinction cross section ECS (both absorption and scattering cross sections) of the single cubic and spherical NPs, as well as for cube-cube and sphere-sphere NP dimers were carried out.

2. Results and discussion

The first part of simulations is carried out for single silver and gold spherical and cubic NP. During all simulations the diameter of the spheres and the corner size of the cubes were set 50nm and chamfering radius was 3nm . Investigated structures are excited by a plane wave propagating along x-axis and polarized along z-axis. Fig. 1(a) shows the ECS of a single gold nanosphere (black line) and nanocube (red line).

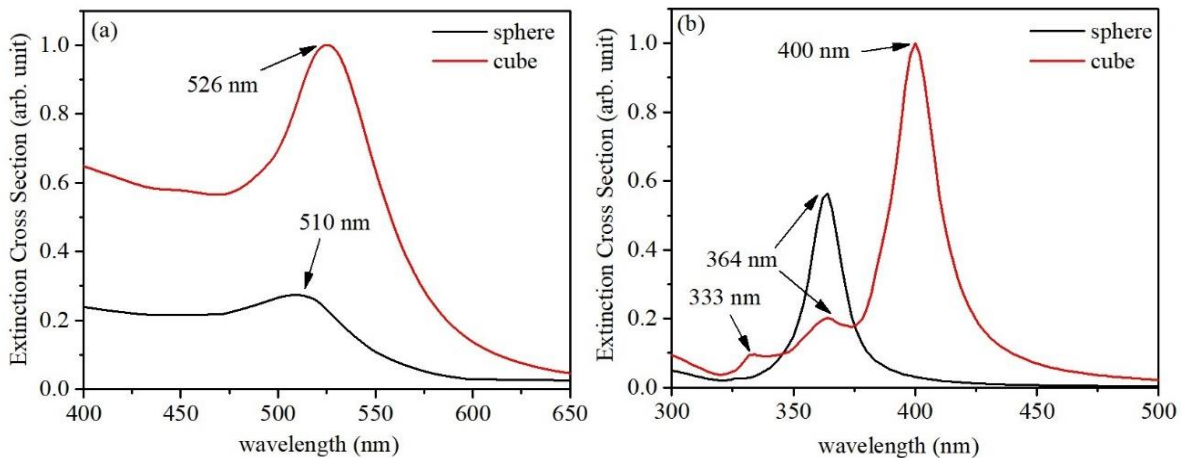


Fig. 1. The Extinction Cross Section of individual (a) gold and (b) silver sphere (black line) and cube (red line).

The extinction peak of the *Au* sphere is around 510nm , while for the cube - 526nm .

The ECS of individual silver nanosphere (black line) and nanocube (red line) are shown on the Fig. 1(b). For the sphere only one extinction peak exists on around 364nm , while for an Ag cube there are three extinction peaks: around 333nm and 364nm due to strong absorption and about 400nm due to scattering. Note that for both Au and Ag, the plasmonic properties of the cube are much stronger than those of a sphere, which appears because of sharp edges of cubes causing field enhancement around them.

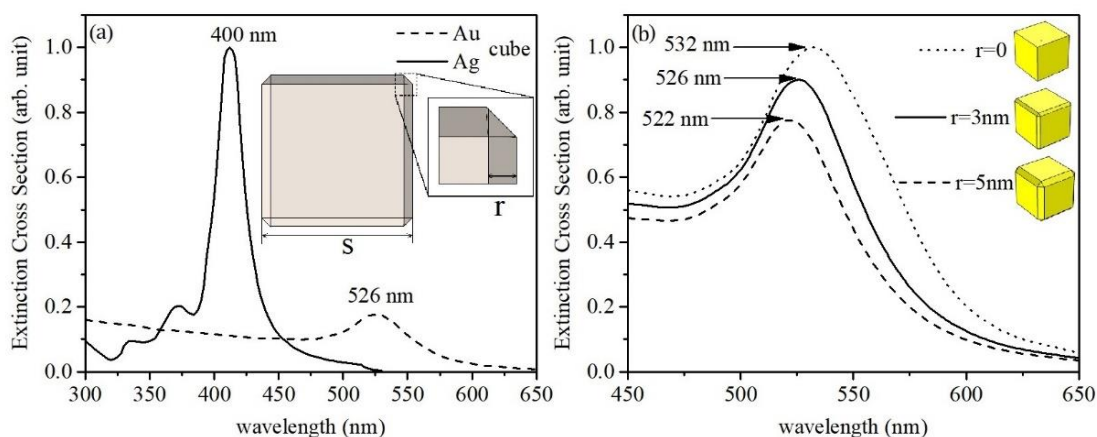


Fig. 2. The Extinction Cross Section of (a) Au (dashed line) and Ag (solid line) cube, (b) individual Au nanocube with different values of the chamfering radius of corners.

Fig. 2(a) shows the comparison of the extinction cross sections of a single Au (dashed line) and Ag (solid line) cubic nanoparticles. The inset of Fig. 2(a) shows the schematic of a single nanocube. The corners of the simulated cubes are chamfered with the radius r (see the zoomed part of Fig 2(a) and inset of Fig. 2(b)). Such morphology corresponds to the dean-flow mixing preparation technique of nanocubes [10]. One can see that the extinction of a silver cube is much higher compared to the gold one. Extinction cross sections of a single Au nanocube of different values of the chamfering radius of corners is presented on Fig. 2(b). The dashed, solid and dotted lines correspond to the chamfering radii of 5nm , 3nm and 0 (ideal cubic shape). The analysis suggests the red shift of the resonant wavelength while decreasing the chamfering radius of a cube.

The second part of simulations includes calculation of the ECS of the simplest case of NP clusters - dimers. The distance between parts of dimers is 5nm . Fig. 3(a) shows extinction cross sections of spherical (black line) and cubic (red line) Au dimers. According to simulations the LSPR of Au cubic dimer lies around 566nm , while for spherical dimers - around 528nm .

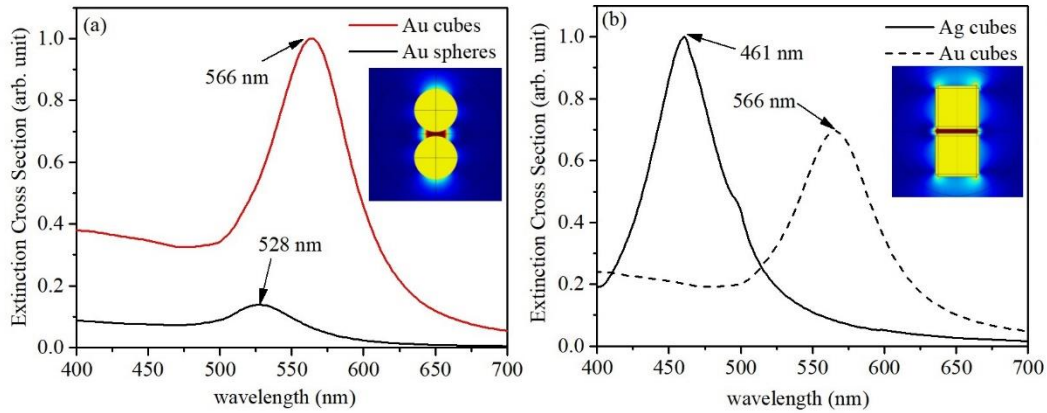


Fig. 3. The Extinction Cross Section of (a) spherical (black) and cubic (red) Au dimers, (b) cubic Ag (solid) and Au (dashed) dimers.

Fig. 3(b) presents the comparison of extinction cross sections of cubic *Au* (dashed line) and *Ag* (solid line) dimers. The resonance of the cubic *Ag* dimer lies around 461 nm. Inset images in Fig. 3(a) and (b) show the field distribution of the spherical and cubic *Au* dimers, respectively. Note, that the separation of NPs is along the polarization axis of the incident field and the main part of energy is concentrated in the interparticle region. The field distribution in the gap between cubic nanoparticles is more uniform which is better from point of view DNA origami fluorescence study. However, other field distributions are also possible by changing the operating wavelength.

3. Conclusion

In summary, the plasmonic properties of a nanocube are much stronger compared to a nanosphere for both gold and silver particles. On the other hand, the LSPR and thus, sensitivity of the system can be increased by considering nanoparticle dimers. The analysis suggests the red shift of the resonant wavelength while decreasing the chamfering radius of corners of a cube and a field enhancement in the region between parts of a dimer. The field distribution in the gap between cubic nanoparticles is more uniform, which is better from point of view DNA origami fluorescence study, while in a nanosphere dimer the field intensity is higher but distribution is nonuniform. Nonetheless, other distributions of electromagnetic field can also be achieved by considering some shift from resonant wavelengths.

4. Acknowledgments

This work was supported by the State Committee of Science of Armenia (grant No 16GE-027).

References

- [1] S. Unser, I. Bruzas, Jie He and L. Sagle, “Localized surface plasmon resonance biosensing: current challenges and approaches Sensors,” vol. 15, no 7, pp. 15684-15716, Jul. 2015.
- [2] M. Hentschel, et al, “Linear and nonlinear optical properties of hybrid metallic–dielectric plasmonic nanoantennas,” *Beilstein J Nanotechnol*, vol. 7, pp. 111–120, Jan. 2016.
- [3] I. I. Slowing, Juan L. Vivero-Escoto, Chia-Wen Wu, Victor S.-Y. Lin, “Mesoporous silica nanoparticles as controlled release drug delivery and gene transfection carriers,” *Advanced drug delivery reviews*, vol. 60, no. 11, pp. 1278-1288, Aug. 2008.
- [4] I. Brigger, C. Dubernet, P. Couvreur, “Nanoparticles in cancer therapy and diagnosis,” *Advanced drug delivery reviews*, vol. 60, pp. 24-36, Dec. 2012.
- [5] V. Amendola, et al, “Surface plasmon resonance in gold nanoparticles: a review,” *Journal of Physics: Condensed Matter*, vol. 29, no. 20, pp. 203002, Apr. 2017.
- [6] M. Jahn, et al, “Plasmonic nanostructures for surface enhanced spectroscopic methods,” *Analyst*, vol. 141, no. 3, pp. 756-793, Dec. 2015.
- [7] S. Chen, M. Svedendahl, M. Käll, L. Gunnarsson and A Dmitriev, “Ultrahigh sensitivity made simple: nanoplasmonic label-free biosensing with an extremely low limit-of-detection for bacterial and cancer diagnostics,” *Nanotechnology*, vol. 20, no. 43, pp. 434015, Oct. 2009.
- [8] T. K. Sau and C. J. Murphy, “Room temperature, high-yield synthesis of multiple shapes of gold nanoparticles in aqueous solution,” *Journal of the American Chemical Society*, vol. 126, no. 28, pp. 8648-8649, Jul. 2009.
- [9] A. S. D. S. Indrasekara, S. Meyers, S. Shubeita, L. C. Feldman, T. Gustafsson and L. Fabris, “Gold nanostar substrates for SERS-based chemical sensing in the femtomolar regime,” *Nanoscale*, vol. 6, no. 15, pp. 8891-8899, May. 2014.
- [10] M. Thiele, A. Knauer, D. Malsch, A. Csáki, Th. Henkel, J. M. Köhlerb and W. Fritzsche “Combination of microfluidic high-throughput production and parameter screening for efficient shaping of gold nanocubes using Dean-flow mixing,” *Lab on a Chip*, vol. 17, no. 8, pp. 1487-1495, May. 2017.

The Dynamics of Instability Development in Spatially Separated Beam-Plasma System

(Proceedings of the Int. Conference on “ Microwave and THz Technologies and Wireless comm.”)

E.V. Rostomyan

Institute of Radiophysics and Electronics Armenian National Academy Science

Received 15 November 2018

Abstract: The instabilities in system consisting of electron beam and spatially separated dissipative plasma is investigated in details. A study is developed that allows carrying out the investigation in general form, independently on system geometry, specific parameters, external fields etc. It only is assumed slight overlapped of the beam and the plasma fields (so-called weak beam-plasma coupling). In this case the beam-plasma interaction significantly differs from conventional case of full overlap (strong coupling). Under weak coupling the role of the beam proper oscillations becomes decisive. The instability is due to growth of the beam negative energy wave. With increase in level of dissipation the instability turns to a new, up to recently unknown type of dissipative instability.

Keywords: Spatially separated beam-plasma system, electron beam, dissipative instability.

1. Introduction

Very vast literature has grown on beam-plasma interaction since discovering of the instability of low density electron beam passing through plasma. This is largely related to the idea of design of high power sources of electromagnetic radiation based on this phenomenon. It was assumed that the sources would have many advantages as compared to well-known vacuum devices [1-2]. Further it becomes clear that spatial separation of the beam and the plasma in waveguide provides better conditions for the sources. Modern sources correspond to cylindrical waveguide with thin annular plasma and spatially separated thin annular electron beam [1-2]. In this case the operation of the sources is based on the beam interaction with the surface wave of hollow plasma cylinder. In contrary to case of strong beam-plasma coupling when the beam and the plasma fields are fully overlapped in opposite case of weak coupling the role of the beam oscillations are crucial. The beam-plasma instability becomes due to growing of the negative energy wave (NEW) of the beam. In this connection the role of all factors those lead to excitation of the NEW increases also and they should be taken into account. Among them dissipation plays most important role [3].

Present investigation considers the problem of time evolution of initial perturbation under weak beam-plasma coupling i.e. when the beam and the plasma fields are overlapped slightly (weak coupling). Developing fields are presented in form of wave train with slowly varying amplitude (SVA). It is shown that the evolution of SVA is described by partial differential equation of second order. The equation is solved and the space time structure of the field is analyzed. The solution of the equation gives very much and complete information on the instability, most of which is unavailable by other methods. The expression for the fields' evolution explicitly shows that with increase in level of dissipation the instability transforms to the new type of dissipative instability [4]

2. Statement of the problem. Dispersion relation.

From electrodynamic point of view spatially separated beam-plasma system is nothing else as multilayer structure. Traditional analytical consideration of such systems encounters certain difficulties. It leads to a very cumbersome dispersion relation (DR), which, (i) complexly depends on geometry and (ii) sharply complicates with increase in number of

layers. However, in the case of slight overlap of the beam and the plasma fields the problem may be considered by perturbation theory, based on smallness of coupling parameter. It leads to the dispersion relation (DR) [4,5]

$$D_p(\omega, k)D_b(\omega, k) = G\left(\kappa^4 \delta\epsilon_p \delta\epsilon_b\right)_{\omega=\omega_0, k=k_0} \quad (1)$$

where $D_{p,b}(\omega, k) = k_{\perp p,b}^2 - \kappa^2 \delta\epsilon_{p,b}$, $\kappa^2 = k^2 - \omega^2 / c^2$, $\delta\epsilon_p = \omega_p^2 / \omega(\omega + i\nu)$, $\delta\epsilon_b = \omega_b^2 / \gamma^3(\omega - ku)^2$, $\omega_{p,b}$ are the Langmuir frequencies of the beam and the plas and G is the small coupling coefficient [2,3]. The DR obviously shows interaction of the beam and the plasma waves. The interaction is weak. The DR (1) is carried out based actually on single assumption: weak beam-plasma coupling. It leads to following equation for determination of the growth rates (GR) of developing instabilities. The instability is due to interaction of NEW with plasma wave. The GR attains its maximum in resonance of NEW with plasma wave Resonance of this type (wave-wave) named Collective Cherenkov resonance [6]. The equation for GR is

$$(x' + i\nu / (2\gamma^2 ku))x' = -G\sqrt{\alpha} / 4\gamma^3 \quad (2)$$

where x' is the deviation from the exact expression of NEW. In absence of dissipation the growth rate of instability caused by NEW growth is

$$\delta_{NEW}^{(\nu=0)} = (ku / 2\gamma) \sqrt{(G/\gamma)\sqrt{\alpha}} \quad (3)$$

Dissipation exhibits itself as additional factor that intensifies growth of the NEBW. Equation (2) gives following expression for the growth rate upon arbitrary level of the dissipation [6].

$$\delta(\lambda) = \delta_{NEW}^{(\nu=0)} f(\lambda) \quad f(\lambda) = \sqrt{1 + \lambda^2 / 4} - \lambda / 2 \quad \lambda = (1 / 2\gamma^2) (\nu / \delta_{NEW}^{(\nu=0)}) \quad (4)$$

The expression (4) obviously shows the growth rate upon increasing in level of dissipation. In limit of strong dissipation $\lambda \rightarrow \infty$, it presents maximal growth rate of the new type of dissipative instability, shown up in [6] (It also follows from (2) by neglecting first term in parentheses)

$$\delta_{NEW}^{(\nu \rightarrow \infty)} = (G\sqrt{\alpha} / 2\gamma) (ku)^2 / \nu \equiv 2\gamma^2 (\delta_{NEW}^{(\nu=0)})^2 / \nu \quad (5)$$

3. The space-time evolution of the instability and its transition to dissipative type.

Now our aim is based on the DR (1) to solve the problem of initial pulse time evolution [7]. Let an instant $t=0$ in point $z=0$ a perturbation arises and the instability begins developing. We present developing fields form wave train of following type

$$E(z, t) = E_0(z, t) \exp\{-i\omega_0 t + ik_0 z\} \quad (6)$$

where ω_0 and k_0 satisfy the conditions $D_b(\omega, k)=0$ and $D_p(\omega, k)=0$. We also assume that the amplitude $E_0(z, t)$ is slowly varying as compared to ω_0 and k_0 i.e.

$$|\partial E_0 / \partial t| \ll \omega_0 E_0; \quad |\partial E_0 \partial z| \ll k_0 E_0 \quad (7)$$

The behavior e slowly varying amplitude (SVA) $E_0(z, t)$ is actually governed by the DR. To derive the equation for SVA we recall that the fields vary near ω_0 and k_0 and use formal substitutions

$$\omega \rightarrow \omega_0 + i \frac{\partial}{\partial t}; \quad k \rightarrow k_0 - i \frac{\partial}{\partial z} \quad (8)$$

Expanding the DR (1) in power series near ω_0 and k_0 one can obtain following equation for SVA

$$\left(\frac{\partial}{\partial t} + v_b \frac{\partial}{\partial z} \right) \left(\frac{\partial}{\partial t} + v_p \frac{\partial}{\partial z} + v^* \right) E_0(z, t) = \delta_0^2 E_0(z, t) \quad (9)$$

where $v_{p,b}$ are group velocities of the plasma wave and the NEW of the beam respectively, $v_b > v_p$, $\delta_0 \equiv \delta_{\text{NEW}}^{(v=0)}$ and $v^* = \text{Im } D_p \left(\partial D_p / \partial \omega \right)^{-1}$ is proportional to collision frequency $v^* = \text{const} \cdot \nu$.

The equation may be solved by using Fourier transformation with respect to coordinate z and Laplace transformation with respect to time t . Corresponding inverse transformation

$$E_0(z, t) = \frac{1}{(2\pi)^2} \int_{C(\omega)} d\omega \int_{-\infty}^{\infty} dk \exp(-i\omega t + ikz) \frac{J(\omega, k)}{(\omega - ku)(\omega - kv_0 + i\nu) + \delta_0^2} \quad (10)$$

gives needed result. Here the function $J(\omega, k)$ is determined by initial conditions. Its specific form of this function is not essential for following. In (10) $C(\omega)$ is the contour of integration over ω . It is a straight line that lies in the upper half plane of the complex plane $\omega = \text{Re } \omega + i \text{Im } \omega$ and passes above all singularities of the integrand. Thus, the problem has been reduced to the integration in (10). For convenience we transform the integration variables to another pair $\omega, k \rightarrow \omega, \omega' = \omega - ku$. We carry out the first integration (over ω) by residue method, but the second – by steepest descend method. As a result we have the expression for SVA

$$E_0(z, t) = - \frac{J_0}{2\sqrt{\pi}} \frac{\exp \chi_v^{(ss)}(z, t)}{(v_b - v_p)^{1/2} \delta_0^{1/2} (v_b t - z)^{1/2}} \quad (11)$$

$$\chi_v^{(ss)} = \frac{2\delta_0}{v_b - v_p} \sqrt{(z - v_p t)(v_b t - z)} - \nu \frac{v_b t - z}{v_b - v_p} :$$

$$J_0 = J(\omega = \omega(\omega_s'), \omega' = \omega_s').$$

4. Analyses of the dynamics

At first glance we have arrived to complicate expression. However, the expression (11) lends itself to simple analysis. The analysis gives many information on the instability and its dynamics: its convective character, growth rates (spatial and temporal), velocities of unstable

perturbations, influence dissipation on it. This information composes overall picture of the instability and dynamics its development. The structure of (11) explicitly shows that the space distribution and development dynamics of the fields is given mainly by the factor

$$\sim \exp \chi_v^{(ss)} \tag{12}$$

The analysis of the expression for $\chi_v^{(ss)}$ shows that the front of induced waveform moves at beam velocity v_b , but the back edge – at velocity v_p , (see curve 1 in Fig 2) i.e. velocities v of unstable perturbation vary through the range $v_p \leq v \leq v_b$. This explicitly shows the convective character of the instability only by determination and without reference on complicate rules. The expression $\frac{\partial}{\partial z} \chi_v^{(ss)} = 0$ gives the place and velocity of the peak. In absence of dissipation it moves at average velocity $z_{pk} = v_{pk}t$ and places at the middle of induced waveform at all instants $v_{pk} = (v_b + v_p)/2$. Developing waveform is fully symmetric with respect to its peak at all instants. Substitution of the peak coordinate into $\chi_v^{(ss)}$ gives the field value in the peak. It exponentially increases and the growth rate is equal to $\delta_0 \equiv \delta_{NEW}^{(v=0)}$ (3). The well-known initial problem gives the same maximal growth rate but it cannot specify place, where the most intensive growth occurs. The coincidence to the results of initial problem testifies presented approach: its initial assumptions, mathematics and results. It may appear that this way of analysis is a bit more complicate. However, it must be admitted that along with growth rates we have obtained much additional information. The information obviously clarifies the picture of the instability development and makes it realistic. The results of the boundary problem also follow from the expression for $\chi_v^{(ss)}$ (see below). One can easily see the merits of presented approach. In a fixed point z the field first increases up to value $E_0 \sim \exp \delta_0 z / (v_p v_b)^{1/2}$.

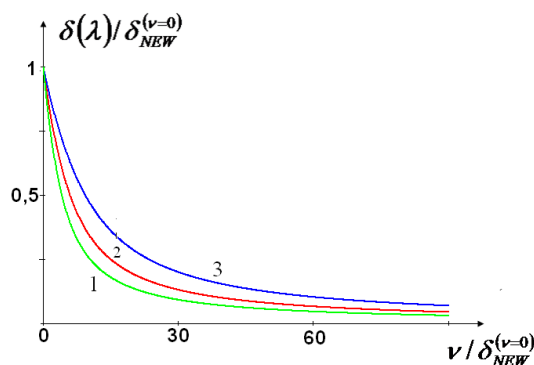


Fig 1. Dependence of the growth rate on dissipation (see (4))

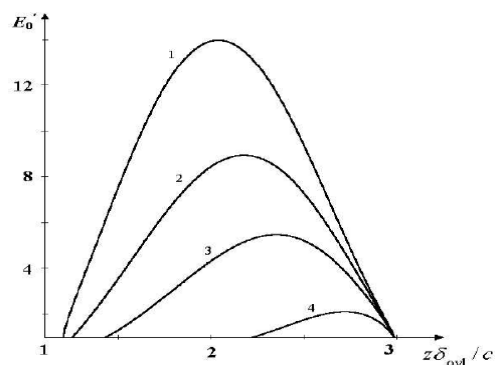


Fig 2. Shapes of the waveform vs longitudinal coordinate at fixed instant $t = 3/\delta_0$ for various values of parameter $k = \nu/\delta_0$, $k_1 = 0, k_2 = 1, k_3 = 2, k_4 = 4$

This maximum is attained at the instant $t = z/v_a$ where $v_a = 2v_p v_b / (v_p + v_b)$. Then field falls off and at the time $t \geq z/v_p$ the train passes given point. The velocity v_a is the group velocity of the resonant wave upon amplification calculated by DR (8). The exponent $\delta_0 / (v_p v_b)^{1/2}$ in (28) coincides to solution of the boundary problem and is the maximal spatial growth rate. This coincidence once more actually justifies all steps of presented approach. Dissipation changes described dynamics of induced waveform. Growth rate in the peak as well as growth rates of all perturbations falls down. Dissipation suppresses slow perturbations. The threshold velocity is

$$V_{th}^{(ss)} = (\lambda v_b + v_p) / (1 + \lambda); \quad \lambda = v^2 / 4\delta_0^2 \quad (13)$$

The wave train shortens. Only high velocity perturbations (at velocities in the range $V_{th} < v < v_b$) develop.

The expression for $\chi_v^{(ss)}$ gives not only the maximal growth rates (spatial and temporal). It also gives growth rate of perturbations moving at given velocity v . Substitution of $z = vt$ leads to $E_0 \sim \exp \Gamma_0(v)t$ where

$$\Gamma_0(v) = 2\delta_{ovl} \frac{\sqrt{(u-v)(v-v_0)}}{u-v_0} \quad (14)$$

For given velocity the dependence of the growth rates on the dissipation level takes following form

$$\Gamma_0(v) \rightarrow \Gamma_v(v) = 2\delta_{ovl} \frac{\sqrt{(u-v)(v-v_0)}}{u-v_0} - v \frac{v_b t - z}{v_b - v_p} \quad (15)$$

The dynamics of the peak in presence of dissipation may be obtained by analyzing the equation for peak accounting for dissipation. It takes following form

$$(z - v_{pk}t)^2 - \lambda(v_b t - z)(z - v_p t) = 0 \quad (16)$$

The solution of this equation actually presents the peak's movement depending on level of dissipation

$$z_{pk} = v_{go}t \left\{ 1 + \sqrt{\frac{\lambda}{1+\lambda} \left(1 - \frac{v_b v_0}{w_{go}^2} \right)} \right\} \quad (17)$$

This expression shows that actually the peak shifts to the front of developing waveform. This is a result of suppression of slow perturbations. Substitution of z_{pk} into $\chi_v^{(ss)}$ gives the maximal growth rate under arbitrary level of dissipation

$$E_0(z = z_m, t) \sim \exp(\delta_0 t \cdot f(\lambda)), \quad (18)$$

where the function $f(x)$ coincides to that presented in (4). Accordingly, in limit of high level dissipation the new type of dissipative instability develops and we have $E \sim \exp \delta_{NEBW}^{v \rightarrow \infty} t$,

where $\delta_{NEBW}^{v \rightarrow \infty}$ is given by (5). This obviously show gradual transition between two type instabilities those develop in spatially separated beam-plasma system. The shapes of induced waveform for various level of dissipation are plotted in Fig.2, while the dependence of maximal growth rate on dissipation level is plotted on Fig 1.

References

- [1] M. V. Kuzelev A. A. Rukhadze. *Plasma Phys Report* v. 26, p.231, 2000
- [2] M. V. Kuzelev, A. A. Rukhadze, P. S. Strelkov. *Plasma Microwave electronics*. Publ House of MSTU after Bauman, 2002 (in Russian).
- [3] E.V. Rostomyan. *The behavior of streaming instability in dissipative plasma*. Lambert Academic Publishing 2018.
- [4] E.V. Rostomyan. *J Plasma Phys* **v.78** (5), 531, (2012).
- [5] E.V. Rostomyan. In“*Plasma Physics. Basic Fundamentals and Modern Applications*”InTechOpen Publishing 2018
- [6] M.V.Kuzelev, A.A.Rukhadze. *Plasma Free Electron Lasers*. Edition frontier, Paris,1995.
- [7] Bers in *Basics of Plasma Physics* edited by M. N. Rosenbluth and R. Z. Sagdeev North Holland, Amsterdam, 1983, v. 1, p. 451.

Fano Resonance in Coupled Semicylindrical Microresonators

(Proceedings of the Int. Conference on “ Microwave and THz Technologies and Wireless comm.”)

H. Haroyan, T.Yezekyan, H. Parsamyan, A. Ninoyan

Yerevan State University, Alex Manoogian str. 1, 0025, Yerevan, Armenia

Received 15 November 2018

Abstract: A system of two, coupled semicylindrical microresonator with relatively simple excitation by a plane wave is studied and Fano resonance was obtained there. The resonator is formed on the base of a dielectric/metal/dielectric structure, where the wave energy penetrates into the resonator through a thin metal layer and is stored in a semicylindrical dielectric with high permittivity. The proposed microresonator combines the steep dispersion of the Fano resonance profile and compactness of the semicylindrical system. The control of evanescence coupling between two resonators is realized by varying the distance between resonators. Numerical analysis is carried out to investigate the process of tuning the system under the conditions of Fano resonance and further control over the coupling.

Keywords: Fano resonance, semi-cylindrical, microresonators, evanescence coupling.

1. Introduction

Efficient and low-loss optical coupling to high quality (Q) factor Whispering Gallery Mode (WGM) microresonators [1] is important for a wide range of applications include frequency [2,3] and soliton mode-locked microcombs [4–8], bio and nano-particle sensors [9–11], cavity optomechanical oscillators [12], Raman lasers [13], and quantum optical devices [14,15]. Usually, to achieve phase-matched and mode-matched evanescent wave efficient coupling, it is necessary to use a host material of resonator with relatively low refractive index compared to those of standard waveguide coupling materials. In addition, fiber tapers as unclad waveguides are quite brittle and applicable only for resonators, refractive index of which is close to the refractive index of fiber. Hence, for waveguide coupling regime it requires tens or hundreds micrometer diameters of coupling region to achieve effective phase-matching. At the same time, for Biosensing purposes, binding of single virions is observed from discrete changes in the resonance frequency of a WGM excited in a microcavity. It is shown, that the magnitude of the discrete wavelength-shifted signal can be sufficiently enhanced by reducing the microsphere size [9,16]. On the other hand, the effective control of the light wave as a rule is realized using materials with a large refractive index.

Recent developments have greatly improved the sensitivity of optical sensors based on metal nanoparticle arrays and single nanoparticles. This kind of sensors is used for biosensing purposes that is to detect molecular binding events and changes in molecular conformation. The device is based on biological, or bioinspired receptor unit with unique specificities toward corresponding analytes. These analytes are often of biological origin like DNAs of bacteria or viruses, or proteins which are generated from the immune system (antibodies, antigens) of infected or contaminated living organisms. Still, one of many other challenges in biosensor development is the sensitivity.

Meanwhile, since its discovery, the asymmetric Fano resonance has been a characteristic feature of interacting quantum systems. Recently, the Fano resonance has been found in plasmonic nanoparticles, photonic crystals, and electromagnetic metamaterials and there are several papers on the use of that effect for biosensors.

In one of our previous works, we proposed a simple system consisting of a semicylindrical microresonator, which can be used as a biosensor [16]. In the present paper, our aim is to combine the steep dispersion of the Fano resonance profile and compactness of the semicylindrical system to obtain a more sensitive device due to a high Q -factor.

Here we propose a structure, which consists of two coupled semicylinders with different radii (it is necessary for having different resonant conditions) placed on a metal thin layer; an incident plane wave is used to excite the resonators (see Fig.1). The main advantage of this structure is the easy coupling method with an incident plane wave. The resonator system combines properties of a Fabry-Perot resonator, where the input of wave energy is carried through mirrors, and a cylindrical resonator, where

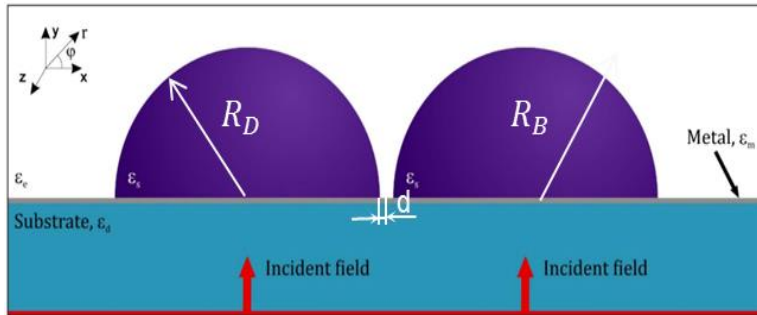


Fig. 1. The cross section of the structure of coupled semicylindrical microresonators with different radii. $\epsilon_s = 2.25$, $\epsilon_e = 1$ are dielectric permittivities of the substrate (SiO₂ Silica) and the surrounding medium (Air), respectively. As a metal and semicylinder medium Ag and GaAs (ϵ_s) were used correspondingly.

Whispering-gallery modes with azimuthal m and radial l mode numbers are formed. Here, the possibility of simple input and output of radiation is combined with the possibility of using the unique properties of an evanescent wave on the cylindrical surface of a dielectric. The control of evanescent coupling between two resonators is realized by varying the distance between resonators.

Fano resonance is a type of resonant scattering phenomenon that gives rise to an asymmetric line-shape and it occurs when a discrete quantum state interferes with a continuum band of states. The nature of the asymmetry was established with the theory of configuration interaction by Fano in 1961 [17].

The microscopic origin of the Fano resonance arises from the constructive and destructive interference of a narrow discrete resonance with a broad spectral line or continuum.

Classical analogy of Fano resonance has been also investigated in the case of two coupled damped oscillators with a driving force applied to one of them [18]. The characteristic equations of motion for this system have the following forms:

The characteristic equations of motion for this system have the following forms:

$$\begin{aligned} \ddot{x}_1 + \gamma_1 \dot{x}_1 + \omega_1^2 x_1 + \nu_{12} x_2 &= a \cdot e^{i\omega t} \\ \ddot{x}_2 + \gamma_2 \dot{x}_2 + \omega_2^2 x_2 + \nu_{12} x_1 &= 0 \end{aligned} \quad (1)$$

where ω_1 and ω_2 are natural frequencies (eigenmodes) of the oscillators in the absence of damping (defined by the mass and the spring constant), γ is a frictional parameter, ν_{12} is a coupling coefficient, and ω is a frequency of the external force. If the coupling parameter is weak ($\omega_1^2 - \omega_2^2 \gg \nu_{12}$), then the eigenmodes of the coupled system can be written as

$$\tilde{\omega}_1^2 \approx \omega_1^2 - \frac{\nu_{12}}{\omega_2^2 - \omega_1^2}, \quad \tilde{\omega}_2^2 \approx \omega_2^2 + \frac{\nu_{12}}{\omega_2^2 - \omega_1^2}, \quad (2)$$

Similarly with a mechanical oscillator the equation can be applied also for electromagnetic oscillators or resonators, where ω_1 and ω_2 are resonant frequencies, γ is a losses parameter

and ω is a frequency of the external field. Let's for clarity to name the resonator which excites by external field as "Bright", and the second one "Dark".

2. Results and discussion

Numerical analysis based on finite element method is carried out for demonstrating Fano resonance for two coupled semicylindrical resonators. Since we are consider Fano resonance as a way for improving sensing features of system our investigations are focused on achieving of higher quality Q factor due to sharpness of resonant curve and demonstration non-symmetrical behavior of resonant curves owing to Fano effect in coupled system. First of all to achieve our goal we are studied distributions of the electric field E_z component amplitudes in single resonator for particular mode to have a reference point (see Fig.1). The values of the parameters are chosen as: $\varepsilon_d = 2.25$; $\varepsilon_e = 1$; $R = 1.5 \mu\text{m}$ and $h = 80\text{nm}$; the values of ε_m (as a metal we use silver) and ε_s (as a semiconductor we use $GaAs$) have been chosen according to Ref. [19] and [20], respectively. The Q -factor of the resonator was determined by the equation $Q \approx \lambda p / \Delta\lambda$, where λp and $\Delta\lambda$ are the peak wavelength and the full width at half-maximum, respectively, for considered parameters $Q \approx 7600$. In our previous work we determine conditions when radiation from the curved boundary is negligible, and the Q -factor of resonator is mainly determined by the radiation from metal layer and Joule's losses. For chosen parameters the curve radius that is the radius of semicylinder can be take started from $R \approx 1 \mu\text{m}$ where radiation from the curved boundary can be neglected.

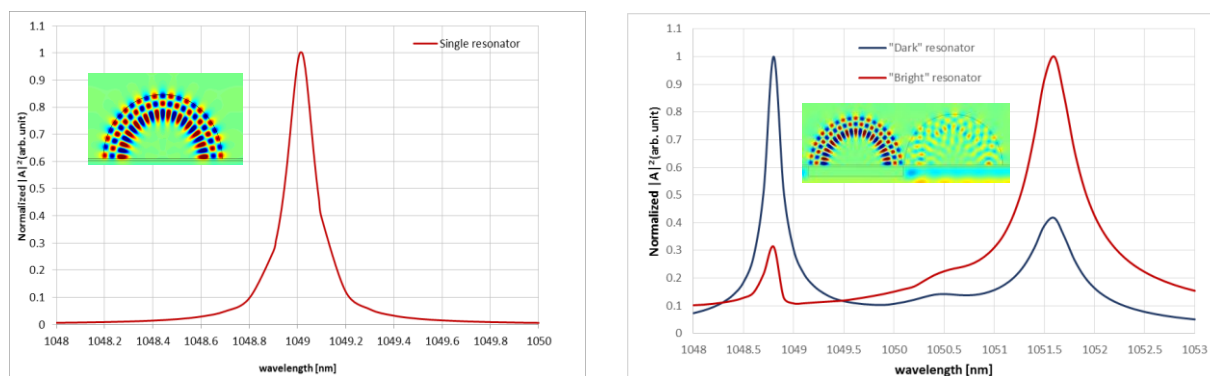


Fig.2. Electrical field E_z component normalized amplitude vs. wavelength for coupled resonators.

After the second "Bright" resonator with different radius $R = 1.6 \mu\text{m}$ is placed near the existing resonator, the distance between resonators $d = 80\text{nm}$. To prevent the penetration of external field into resonator and therefore excitation of "Dark" resonator the metal layer thickness is widened (see Fig.2). As it can see from Fig.2 the resonant wavelength of resonator with $R = 1.5 \mu\text{m}$ is shifted from $\lambda_0 = 1049.01 \text{ nm}$ to $\lambda_0 = 1048.8 \text{ nm}$ and resonant curve became more sharper hence the Q factor higher $Q = 12000$, which is 1.58 times bigger. It is noticeable that asymmetrical resonant behavior of electric field vs. excitation wavelength is also seen, which is another proof of Fano resonance existence. It's useful to note that obtained results are expectable within classical interpretation of Fano resonance presented in [18]. However it should be mentioned that at the same time the square of electric field amplitude of single resonator is about 4 times higher.

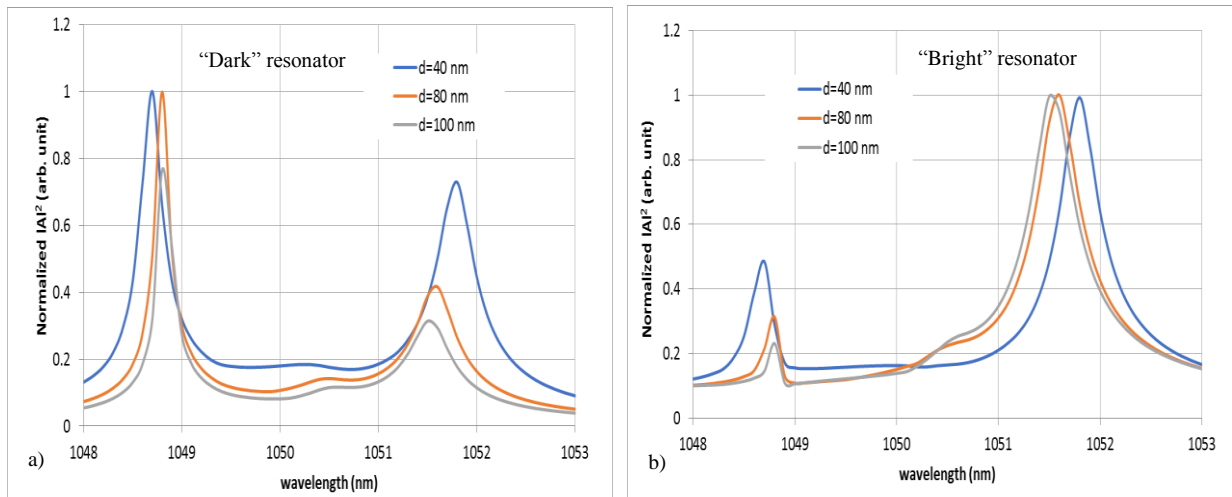


Fig.3. Electrical field E_z component normalized amplitude vs. wavelength a) in “Dark” and b) in “Bright” resonators, for different d distances between resonators.

To control the coupling coefficient the distance d between resonators is varied and resonant curves are obtained (see Fig.3). As seen from Fig.3 a) within investigated wavelength range there are two resonant peaks instead of one as for single resonator. Moreover, the main resonant curve near the 1049nm is shifted and sharpened, the second resonant peak arisen due to field penetration from “Bright” resonator which resonant wavelength is near to 1051nm . It is clear, as closer resonators as higher coupling and influences of “Bright” resonator onto “Dark” one, hence higher the second peak value, which brings to the widening of main resonant curve. On the other hand, the bigger distance between resonators the lower main resonant peak since the “Dark” resonator excites from “Bright” one. Therefore there is an optimal distance to obtain sharper resonant curve with reasonable strength of field inside the resonator, for chosen parameters this distance is about $d \approx 80\text{nm}$.

From Fig.3 b) follows the existence of second asymmetrical resonant curve of “Bright” resonator at the resonant wavelengths as for “Dark” one, the bigger distance the smaller second asymmetric peak due to weak coupling. It is also worth to mention that with increasing d distance the resonant peaks getting closer together.

3. Conclusion

In summary, a system of two, coupled semicylindrical microresonator with relatively simple excitation by a plane wave is studied and Fano resonance is demonstrated. The resonator is formed on the base of a dielectric/metal/dielectric structure, where the wave energy penetrates into the resonator through a thin metal layer and is stored in a semicylindrical dielectric with high permittivity. Resonators system combines properties of Fabry-Perot resonator, where the input of wave energy is carried through mirrors, and cylindrical resonator, where Whispering-gallery modes with azimuthal and radial modes are formed. The control of evanescence coupling between two resonators is realized by varying the distance between resonators. Due to the coupling the resonant curve became more sharper hence the Q factor is 1.58 times bigger in comparison with single resonator with same parameters. The obtained results substantiate the practical value of the proposed system as an acceptable way to improve the sensing characteristics of this type of microresonator.

Acknowledgments

This work was partially supported by the State Committee of Science of Armenia (grant No 16GE-027).

References

- [1]. K. J. Vahala, "Optical microcavities," *Nature* 424, pp. 839–846, 2003.
- [2]. P. Del’Haye, A. Schliesser, O. Arcizet, T. Wilken, R. Holzwarth, and T. J. Kippenberg, "Optical frequency comb generation from a monolithic microresonator," *Nature* 450, pp. 1214–1217, 2007.
- [3]. T. J. Kippenberg, R. Holzwarth, and S. A. Diddams, "Microresonator-Based Optical Frequency Combs," *Science* 332, pp. 555–559, 2011.
- [4]. T. Herr, V. Brasch, J. D. Jost, C. Y. Wang, N. M. Kondratiev, M. L. Gorodetsky, and T. J. Kippenberg, "Temporal solitons in optical microresonators," *Nat. Photonics* 8, pp. 145–152, 2014.
- [5]. X. Yi, Q.-F. Yang, K. Y. Yang, M.-G. Suh, and K. Vahala, "Soliton frequency comb at microwave rates in a high-Q silica microresonator," *Optica* 2, 1078, 2015.
- [6]. V. Brasch, M. Geiselmann, T. Herr, G. Lihachev, M. H. P. Pfeiffer, M. L. Gorodetsky, and T. J. Kippenberg, "Photonic chip-based optical frequency comb using soliton Cherenkov radiation," *Science* 351, pp. 357–360, 2016.
- [7]. C. Joshi, J. K. Jang, K. Luke, X. Ji, S. A. Miller, A. Klenner, Y. Okawachi, M. Lipson, and A. L. Gaeta, "Thermally controlled comb generation and soliton modelocking in microresonators," *Opt. Lett.* 41, 2565, 2016.
- [8]. P.-H. Wang, J. A. Jaramillo-Villegas, Y. Xuan, X. Xue, C. Bao, D. E. Leaird, M. Qi, and A. M. Weiner, "Intracavity characterization of micro-comb generation in the single-soliton regime," *Opt. Express* 24, 10890, 2016.
- [9]. F. Vollmer and S. Arnold, "Whispering-gallery-mode biosensing: label-free detection down to single molecules," *Nat. Methods* 5, pp. 591–596, 2008.
- [10]. T. Lu, H. Lee, T. Chen, S. Herchak, J.-H. Kim, S. E. Fraser, R. C. Flagan, and K. Vahala, "High sensitivity nanoparticle detection using optical microcavities," *Proc. Natl. Acad. Sci.* 108, pp. 5976–5979, 2011.
- [11]. F. Vollmer and L. Yang, "Label-free detection with high-Q microcavities: a review of biosensing mechanisms for integrated devices," *Nanophotonics* 1, 2012.
- [12]. T. J. Kippenberg and K. J. Vahala, "Cavity Optomechanics: Back-Action at the Mesoscale," *Science* 321, pp. 1172–1176, 2008.
- [13]. S. M. Spillane, T. J. Kippenberg, and K. J. Vahala, "Ultralow-threshold Raman laser using a spherical dielectric microcavity," *Nature* 415, pp. 621–623, 2002.
- [14]. T. Aoki, B. Dayan, E. Wilcut, W. P. Bowen, A. S. Parkins, T. J. Kippenberg, K. J. Vahala, and H. J. Kimble, "Observation of strong coupling between one atom and a monolithic microresonator," *Nature* 443, pp. 671–674, 2006.
- [15]. H. J. Kimble, "The quantum internet," *Nature* 453, pp. 1023–1030, 2008.
- [16]. F. Vollmer, S. Arnold, and D. Keng, "Single virus detection from the reactive shift of a whispering-gallery mode," *Proc. Natl. Acad. Sci.* 105, 20701–20704, 2008.
- [17]. U. Fano, "Effects of Configuration Interaction on Intensities and Phase Shifts", *Phys. Rev.* 124, pp. 1866–1878, 1961.
- [18]. Joe, Y. S. et al. "Classical analogy of Fano resonances", *Physica Scripta*, 74(2), 259, 2006.
- [19]. P. B. Johnson and R. W. Christy, "Optical Constants of the Noble Metals," *Phys. Rev. B* 6, pp. 4370–4379, 1972.
- [20]. Skauli, P. S. Kuo, K. L. Vodopyanov, T. J. Pinguet, O. Levi, L. A. Eyres, J. S. Harris, M. M. Fejer, B. Gerard, L. Becouarn, and E. Lallier, "Improved dispersion relations for GaAs and applications to nonlinear optics," *J. Appl. Phys.* 94, pp. 6447–6455, 2003.

Effect of Absorption on The Efficiency of THz Radiation Generation in a Nonlinear Crystal Placed Into a Waveguide

(Proceedings of the Int. Conference on “ Microwave and THz Technologies and Wireless comm.”)

A.S. Nikoghosyan¹, R.M. Martirosyan¹, A.A. Hakhoumian², A.H. Makaryan¹,
V.R.Tadevosyan¹, G.N. Goltsman³, S.V. Antipov³

¹Yerevan State University, Alex Manoogian str. 1, 0025 Yerevan, Armenia

²Institute of Radiophysics and Electronics, Alikhanian Brothers str. 1, 0203 Ashtarak, Armenia

³Moscow State Pedagogical University, Moscow, 119571, Russia

Received 15 November 2018

Abstract: The effect of THz radiation absorption on the efficiency of generation of coherent THz radiation in a nonlinear optical crystal placed into a metal rectangular waveguide is studied. The efficiency of the nonlinear conversion of optical laser radiation to the THz band is also a function of the phase-matching (PM) condition inside the nonlinear crystal. The method of partial filling of a metal waveguide with a nonlinear optical crystal is used to ensure phase matching. Phase matching was obtained by the proper choice of the thickness of the nonlinear crystal, namely the degree of partial filling of the waveguide. We have studied the THz radiation attenuation caused by the losses in both the metal walls of the waveguide and in the crystal, taking into account the dimension of the cross section of the waveguide, the degree of partial filling and its dielectric constant.

Keywords: Nonlinear crystal, phase-matching, femtosecond laser, single-layer reflection.

1. Introduction

Waveguides containing dielectric inserts find applications in many waveguide components [1]. It has been shown that the method of measuring the absorption of a dielectric, which partially fills a waveguide, is 50 times more sensitive than the traditional method of single-layer reflection [2]. Efficient generation of ultra-short THz pulses in a nonlinear crystal, partially filling a rectangular waveguide, using pico- or femtosecond laser pulses was proposed and performed in [3-5]. The generation of the THz pulse is based on the mixing of the spectral components of a femtosecond optical laser pulse in a nonlinear crystal (optical rectification method). The method of partial filling of a metal waveguide with a nonlinear optical crystal was used to ensure phase matching (PM).

The influence of THz radiation absorption on the efficiency of generation of coherent THz radiation in a nonlinear optical crystal placed into a metal rectangular waveguide (Fig.1) is presented here. The efficiency of the nonlinear conversion of optical laser radiation to the THz range is also a function of the PM condition in the nonlinear crystal, i.e of the equality of the group velocity of the optical pulse and of the phase velocity of the THz pulse at the difference frequency. Phase matching was obtained by the proper choice of the thickness of the nonlinear crystal, namely the degree of partial filling of the cross section of the waveguide.

The THz radiation attenuation caused by the losses both in the metal walls of the waveguide and in the crystal was calculated taking into account the dimensions of the cross section of the waveguide, the thickness of the crystal (the degree of partial filling) and its dielectric constant. DAST, $LiNbO_3$ and $ZnTe$ crystals were studied due to their high efficiency of conversion of optical radiation into the THz range. These crystals have a high second-order nonlinear susceptibility and various dielectric constants for which the condition PM is satisfied.

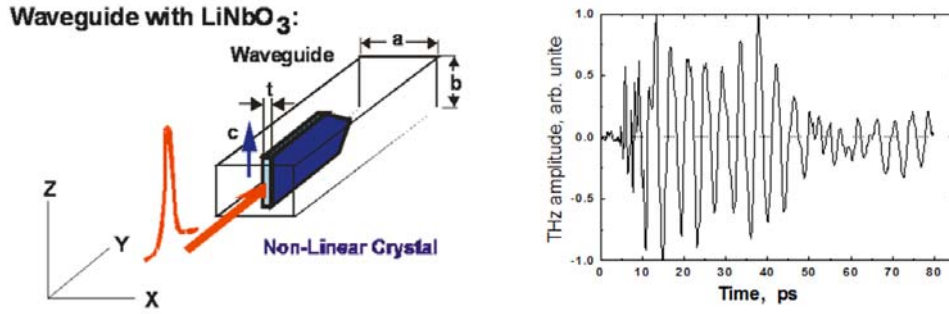


Fig.1. Nonlinear crystal LiNbO₃ in a metal rectangular waveguide (a), THz pulse (b)

2. THz radiation attenuation caused by the losses in the metal walls of the waveguide and in the crystal

The attenuation coefficient in the metal walls of a waveguide partially filled by a nonlinear crystal is determined from expression (1):

$$\alpha_m = m \frac{a}{b} \left\{ \left(\frac{\epsilon_0 \mu_0}{m^2} - 1 \right) \frac{1}{R_1} \left[R_2 + 2 \frac{b}{a} \left(\frac{\cos \beta t}{\sin \alpha d} \right)^2 \right] + 1 \right\} \frac{R_s}{a Z_0}, \quad (1)$$

where

$$R_1 = \frac{2t}{a} \left(1 + \frac{\sin 2\beta t}{2\beta t} \right) + \left(1 - \frac{2t}{a} \right) \left(\frac{\cos \beta t}{\sin \alpha d} \right)^2 \left(1 - \frac{\sin 2\alpha d}{2\alpha d} \right),$$

$$R_2 = \frac{2t}{a} \left(\frac{\beta}{\alpha} \right)^2 \left(1 - \frac{\sin 2\beta t}{2\beta t} \right) + \left(1 - \frac{2t}{a} \right) \left(\frac{\cos \beta t}{\sin \alpha d} \right)^2 \left(1 + \frac{\sin 2\alpha d}{2\alpha d} \right),$$

$$R_3 = \sqrt{\omega \mu / 2 \sigma},$$

$m = \lambda / \lambda_{wG}$ is the deceleration factor of an electromagnetic wave, λ is the wavelength in a free space, λ_{wG} is the wavelength in the waveguide, a and b are the width and height, respectively, of the rectangular waveguide, d is the distance from the narrow wall of the waveguide to the crystal, $2t$ is the thickness of the crystal, $\alpha = 2\pi / \lambda \sqrt{\epsilon_0 \mu_0 - m^2}$; $\beta = 2\pi / \lambda \sqrt{\epsilon \mu - m^2}$ and $Z_0 = \sqrt{\mu_0 / \epsilon_0} = 377 \Omega$ is the impedance of the free space, σ is conductivity of waveguide walls. The attenuation determination was performed for various crystal fillings $2t/a$. Nonlinear crystals DAST ($\epsilon = 5.2$); ZnTe ($\epsilon = 10.1$); LiNbO₃ ($\epsilon = 26.5$) were investigated, with different dielectric constant and high figures of merit (FOMs [6]) used for generation of THz pulse. The losses in an empty waveguide depend on the ratio of the width of the waveguide to its height and are minimal when $a/b = 2$. In expression (2) the values of $a = 2.4 \text{ mm}$, $b = 1.2 \text{ mm}$ are substituted. It should be noted that in the case of a small dielectric permittivity (DAST ($\epsilon = 5.1$)) and partial filling, there are cases when the losses in the metal walls are comparable to the losses in the walls of an unfilled metal waveguide.

Figure 2 shows that for a DAST crystal with a low dielectric constant, in the case of $2t/a \leq 0.15$ and $a/\lambda > 0.65$, the loss in the metal wall is comparable to the loss in the empty waveguide, that is, the waveguide does not distort the pulse in the frequency range of waves of the main type. In addition, in the case of a thin crystal with a low dielectric permittivity, attenuation can be weaker than in an unfilled waveguide for a/λ from 0.4 to 0.8. In a partially filled waveguide, this effect is due to the decrease of the cut-off frequency.

In the case of a high dielectric constant of the crystal, the losses in the waveguide walls are higher, and the attenuation depends more on the degree of filling with a crystal, $2t$, than on ratio of a/λ , i.e. the frequency.

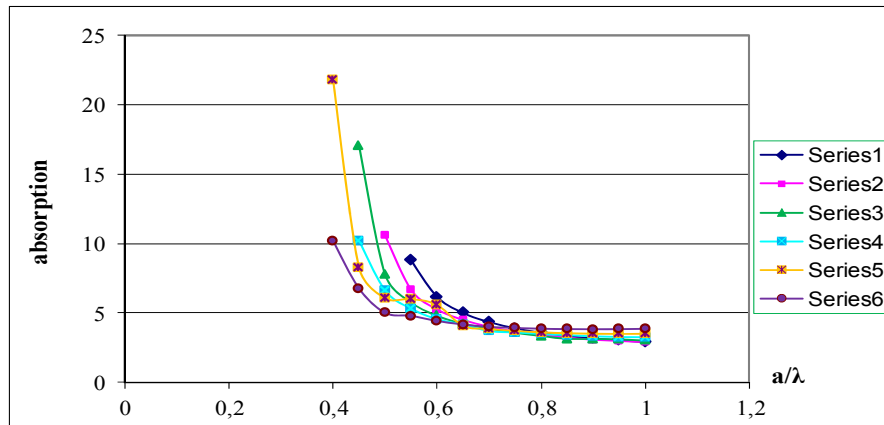


Fig.2. Attenuation in a metallic waveguide partially filled with a DAST crystal, $\epsilon^e = 5.2$, for $2t/a = 0$ (Series1); $2t/a = 0.025$ (Series2); $2t/a = 0.05$ (Series3); $2t/a = 0.075$ (Series4); $2t/a = 0.1$ (Series5); $2t/a = 0.15$ (Series6).

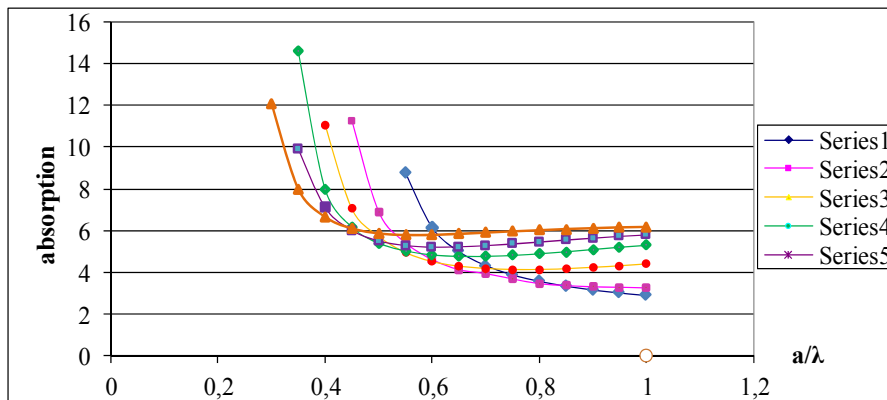


Fig.3. Attenuation in a metallic waveguide partially filled with a ZnTe crystal, $\epsilon^e = 10.1$, for $t/a = 0$ (Series1); $2t/a = 0.025$ (Series2); $2t/a = 0.05$ (Series3); $2t/a = 0.075$ (Series4); $2t/a = 0.1$ (Series5); $2t/a = 0.15$ (Series6); $a = 2.4$ mm.

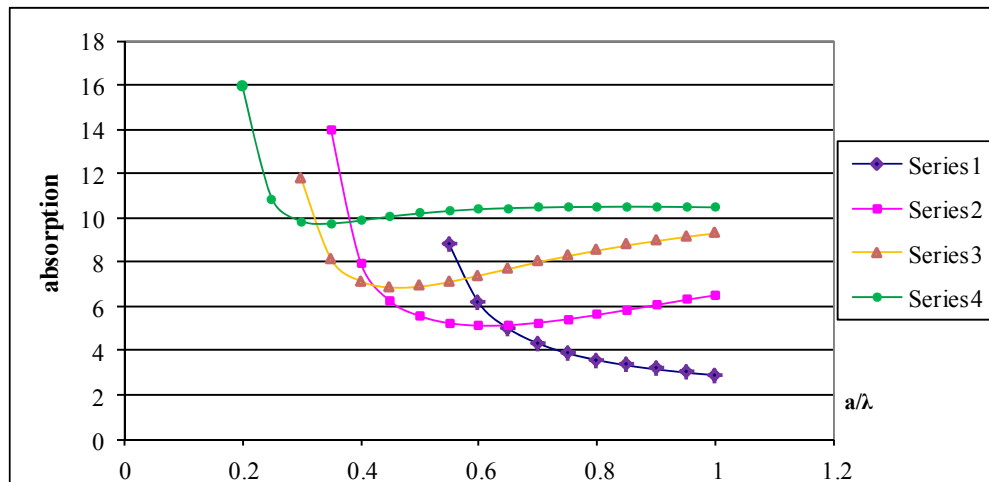


Fig.4. Attenuation in a metallic waveguide partially filled with a $LiNbO_3$ crystal, $\epsilon^e = 26.5$, for $2t/a = 0$ (Series1); $2t/a = 0.025$ (Series2); $2t/a = 0.05$ (Series3); $2t/a = 0.15$ (Series4).

The attenuation in the walls of a waveguide with a $LiNbO_3$ crystal is less than in an empty waveguide in the wavelength range of $0.5 < a/\lambda < 0.65$. Thus, THz pulses or waves can be generated in a narrow frequency range with an attenuation less than that in an empty waveguide. In this frequency band, the pulse will not be attenuated and broadened in a waveguide.

The attenuation due to losses in a crystal, partially filling a waveguide, was determined from the expression (2)

$$\alpha_d = \epsilon \frac{\pi a}{m \lambda R_1} \frac{1}{a} \frac{2t}{a} \left(1 + \frac{\sin 2\beta t}{2\beta t} \right) / \frac{a}{tg \delta}, \quad (2)$$

where $tg \delta = \epsilon''/\epsilon'$. The attenuation constant shown in Fig. 5 is $\alpha = \alpha_d \cdot tg \delta / a$, (α_d in units of Np/m). The figure illustrates that the attenuation of THz pulses increases with the degree of filling of the given cross-section of a waveguide.

The obtained data mean that a threefold reduction of the attenuation of a given frequency is possible if a partially filled waveguide is used instead of a completely filled one. Reducing the attenuation in turn allows the use of crystals of greater length than in the case of complete filling of the waveguide. This results in a double effect. The partially filled waveguide makes it possible to ensure the condition of phase matching as well as reduces the loss of THz radiation due to absorption in the generating crystal. This cannot be achieved by other methods providing phase matching, when a non-linear crystal is located in a free space where the attenuation coefficient is a constant value. Thus, a waveguide partially filled with a nonlinear crystal, will ensure efficient generation of THz radiation due to phase matching and less absorption in the crystal.

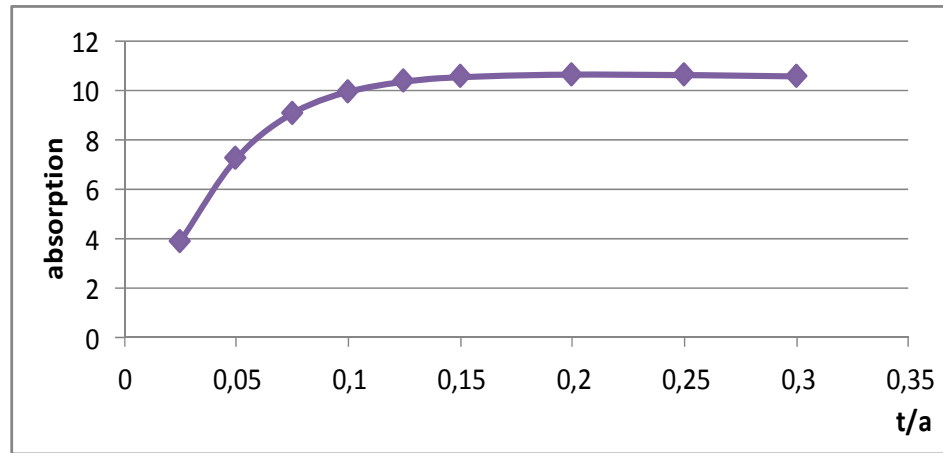


Fig.5. Attenuation constant in the waveguide partially filled with a LiNbO_3 crystal for $2t/a$ varying in (0; 1) interval.

3. Conclusion

Generation efficiency in the process of converting the frequency of ultrashort laser pulses to the THz range depends on the fulfillment of the phase matching condition as well as on the losses ($\alpha_s = \alpha_m + \alpha_d$) at a given crystal length. DAST , LiNbO_3 and ZnTe crystals were studied due to the high efficiency of conversion of optical radiation to THz range in a waveguide partially filled with one of these crystals.

It is shown that the attenuation of THz pulses increases with the degree of filling of the given cross-section of a waveguide by crystal (Fig.5). However, in the case of a small dielectric permittivity and partial filling, the losses in the metal walls are comparable to the losses in the walls of an unfilled metal waveguide. Moreover, in the case of a thin crystal with low dielectric permittivity, attenuation can be weaker than that in an unfilled waveguide. In a partially filled waveguide, this phenomenon occurs because of the decrease of the cut-off frequency, which is more obvious when the waveguide is completely filled with a crystal. In the case of a high dielectric permittivity of the crystal, the losses in the walls of the waveguide are observed to be higher, which is more due to the degree of filling with the crystal than due to the ratio of a/λ , i.e. from the frequency. In all crystals, minimum attenuation is observed for a certain frequency band.

Acknowledgments

This work was supported by the Ministry of Education and Science of Russian Federation, under contract №14.583.21.0069, RFMEFI58317X0069

References

- [1] W. Schlosser and H. G. Unger, "Partially filled Waveguides and surface waveguides of rectangular cross-section", in *Advances in Microwaves*, L. Young ed., vol.1, Academic Press, 1966.
- [2] G. Gallot, S. P. Jamison, R. W. McGowan, and D. Grischkowsky, "Terahertz waveguides", *J. Opt. Soc. Am. B*, vol. 17, pp. 851- 863, 2000.
- [3] A. S. Nikoghosyan, "USP Generation in the Millimeter and Centimeter Bands in a waveguide Partially Filled with a Nonlinear Crystal", *Kvantovaya Elektronika*, Moscow, vol. 15, no.5, pp. 969-971, 1988.
- [4] E. M. Laziev, A. S. Nikoghosyan, "Phase Synchronism and Ultrashort SHF Pulses Generation in Waveguides", *SPIE, Mode-Locked Lasers and Ultrafast Phenomena*, vol. 1842, pp. 113-118, 1991.
- [5] A. S. Nikoghosyan, R. M. Martirosyan, A. A. Hakhoumian, J. M. Chamberlain, R. A. Dudley, N. N. Zinov'ev, "Generation of THz Radiation in Waveguide Partially Loaded with Nonlinear Crystal", *Electromagnetic waves and Electronic Systems*, vol. 11, N4, pp. 47- 55, 2006.
- [6] J. Hebling, Ka-Lo Yeh, M. C. Hoffmann, B. Bartal, and K. A. Nelson, "Generation of high-power terahertz pulses by tilted-pulse-front excitation and their application possibilities", *A. J. Opt. Soc. Am. B*, vol. 25, N7/July 2008.

Efficient Ultrashort THz Pulse Generation in LiNbO₃, ZnTe, GaSe and DAST Crystals

(Proceedings of the Int. Conference on “ Microwave and THz Technologies and Wireless comm.”)

A. S. Nikoghosyan¹, R. M. Martirosyan^{1,2}, A. A. Hakhoumian³.

¹*Yerevan State University, Alex Manoogian str. 1, 0025 Yerevan, Armenia*

²*National Academy of Sciences of the Republic of Armenia, 24/5, Marshall Baghramian Ave., 0019 Yerevan, Republic of Armenia*

³*Institute of Radiophysics and Electronics, Alikhanian Brothers str. 1, 0203 Ashtarak, Armenia*

Received 15 November 2018

Abstract: The value of the generated terahertz power limits the major specifications of the THz coherent techniques in imaging and tomography. We report on the effective generation pulse of THz radiation in a nonlinear crystals partially filling the cross section of the rectangular waveguide. The generation of terahertz (THz) radiation in the band 0.1-3 THz via optical rectification of femtosecond laser pulses in LiNbO₃, ZnTe, DAST, GaSe nonlinear optical crystals are presented, as well as the results of the numerical calculations for phase-matching.

Keywords: THz radiation, nonlinear crystal, optical rectification, phase-matching.

1. Introduction

Due to the achievements of nonlinear optics, in particular nonlinear frequency conversion of femtosecond optical laser pulses in the terahertz (THz) range and the development of THz sources and detectors, interest in effective waveguide [1] has grown considerably.

In the frequency range 0.1–10THz, a free electron lasers (FELs) have the highest average power, $\sim 10^{-1} - 10W$ (or $100\mu J$ of energy), but their disadvantage is that they cost much and are very large in size, i.e. are inaccessible for the scientists of many countries. Optically pumped molecular lasers (THz power up to $30mW$), klystrons, backward-wave oscillator (BWOs with $P \sim 10^{-3}W$), optical rectification ($P \sim 10^{-3}W$), difference frequency generators, Schottky and Gunn diodes, photomixers ($100mW$ (pulsed)), photoconducting antennas ($P_{THz} \sim 80\mu W$) generate less power than FEL do. However, modern advances in the development of THz detectors make it possible to use highly sensitive and high-speed receivers to compensate for the low power of THz source.

The value of the generated terahertz power limits the major specifications of the THz coherent techniques in THz-TDS systems, imaging and tomography. Photoconductive antenna and frequency conversion in nonlinear crystals (optical rectification) are two of the most common sources of broadband THz pulses for use in research, THz-TDS and other applications. Nowadays, optical rectification of femtosecond laser pulses is one of the most promising methods for generation of high-energy THz pulses [2-4]. The advantages of the optical rectification method are the possibility for phase matching to increase the THz radiation power, a wide spectral band of THz pulse, absence of generation threshold, linear polarization of the THz field strength, simplicity, and diversity of possible applications.

Efficient generation of ultra-short THz pulses, by optical rectification, in a nonlinear crystal, partially filling a rectangular waveguide, using pico- or femtosecond optical laser pulses was proposed and performed in [5-6]. The efficiency of the nonlinear conversion of optical laser radiation to the THz range depends on the condition of phase matching (PM) in the nonlinear crystal, i.e. of the equality of the group velocity of the optical pulse and of the phase velocity of the THz pulse at the difference frequency. Phase matching was obtained by the proper choice of the thickness of the nonlinear crystal, namely the degree of partial filling of the waveguide.

This paper presents the experimental spectra of THz pulse, having been generated in DAST, ZnTe, LiNbO₃ crystals located in a free space (the case of phase-mismatch) as well as the results of the crystals thickness numerical calculations made to ensure phase-matching when the crystal partially fills the cross section of the waveguide. DAST, GaSe, LiNbO₃ and ZnTe crystals were studied due to their high figures of merit (FOMs [7]) as FOM provides high efficiency of conversion of optical radiation into the THz range at PM. Two figures of merit of the nonlinear crystal used for optical rectification [7] are defined as

$$FOM_w = \frac{d_{eff}^2 L^2}{n_{opt}^2 n_{THz}}, \quad (1)$$

$$FOM_s = \frac{4d_{eff}^2}{n_{opt}^2 n_{THz} \alpha_{THz}}. \quad (2)$$

FOM_w (if $\alpha_{THz} < 5cm^{-1}$) and FOM_s (if $\alpha_{THz} > 5cm^{-1}$) are the measure of the energy conversion efficiencies at optical rectification in a weakly and a strongly absorbing crystals, respectively.

2. The effective generation of terahertz radiation in the band 0.1-2.5THz

LiNbO₃, DAST and ZnTe nonlinear optical crystals mounted in a free space have been used in our experiments. The optical excitation of a broadband THz pulse was performed using 200 fs pulses from a Ti-Sapphire laser ($\lambda = 800nm$), [6]. The experimental setup for generation and detection of THz pulses is shown in Fig.1. The generation of the THz pulse is based on the mixing of the spectral components of a femtosecond optical laser pulse in a nonlinear crystal (optical rectification method), [2-7].

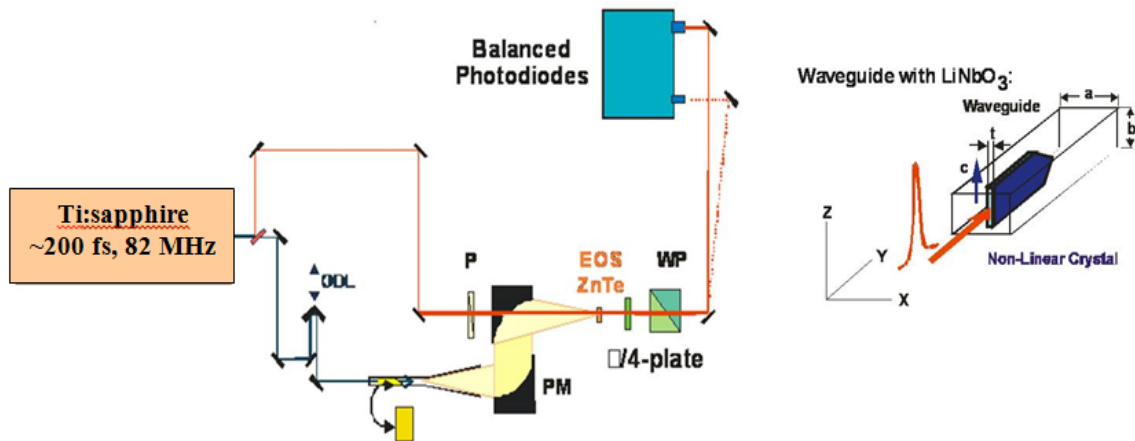


Fig.1. A simplified scheme showing the experimental instrumentation used to generate and detect THz pulses. The inset on the right shows a non-linear LiNbO₃ crystal in the waveguide and the excitation geometry.

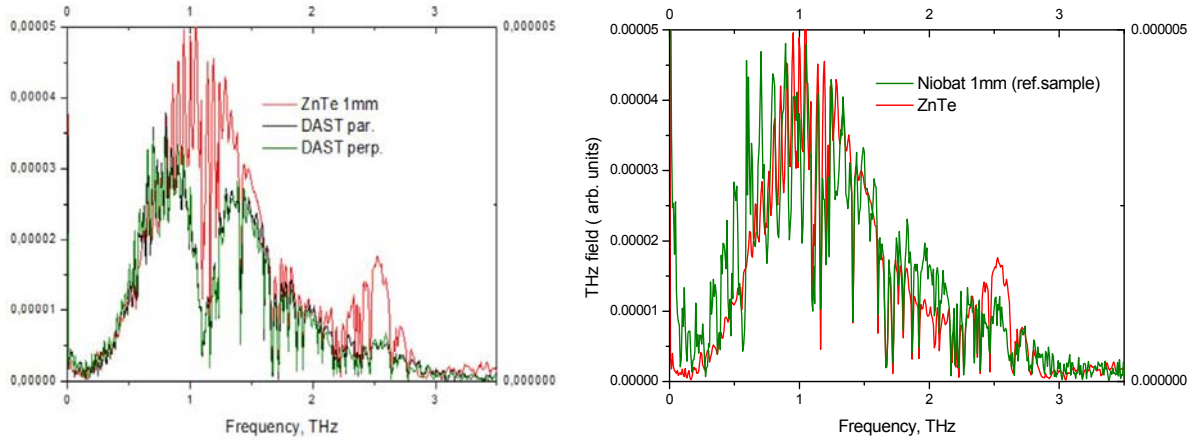


Fig.2. Spectra of THz pulses generated in LiNbO_3 , ZnTe , DAST crystals.

The spectra of the THz pulses having been generated in LiNbO_3 , ZnTe , DAST crystals, acquired after fast Fourier transform of the time-domain THz waveform, are illustrated in Figure 2. The maximum spectral density of the THz radiation in the frequency range from 0.1 to 3 THz is observed at 997 GHz, 1.04 THz, 802 GHz for LiNbO_3 , ZnTe and DAST crystals, respectively. The registration of the spectrum to up to 3 THz is due to the fact that a 1 mm-thick ZnTe crystal was used for coherent detection, which is the optimal crystal for the pump wavelength of 800 nm, i.e., within the tuning range of the widely used Ti: sapphire femtosecond lasers. By the selection of the optical pump wavelength (λ_{opt}) between 700 and 1600 nm in organic DAST crystal [8] were obtained several maxima in the spectral range between 0.4 and 6.7 THz, with an optimum at 2 THz generated with 1500 nm laser pulses. For example, at $\lambda_{opt} = 710 \text{ nm}$, two spectral density maxima have been observed at about of 600 GHz and 1.4 THz. Two spectral density maxima are observed at 802 GHz and 1.4 THz in our case as well, at a pump wavelength of 800 nm. In the case of a DAST crystal, the spectral density minima within the THz field at 1.3 THz and 3 THz (Fig. 2) are due to the maximum absorption coefficient for these frequencies. [8].

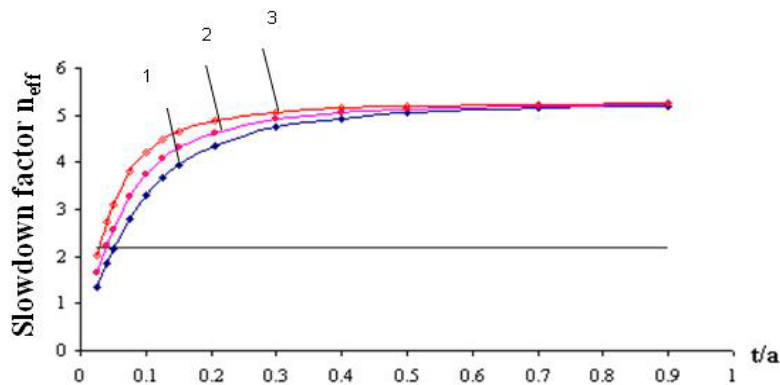


Fig.3. Slow-down factor n_{eff} of difference frequency radiation depending on t/a for LiNbO_3 , when $\epsilon_{DFR}^e = 28$, $n^e(f_{DFR}) = 5.291$, $n^e(0.8 \mu\text{m}) = 2.1745$. Curve 1 - $k_2 = a/\lambda = 0.5$; curve 2 - $k_2 = 0.65$; curve 3 - $k_2 = 0.9$.

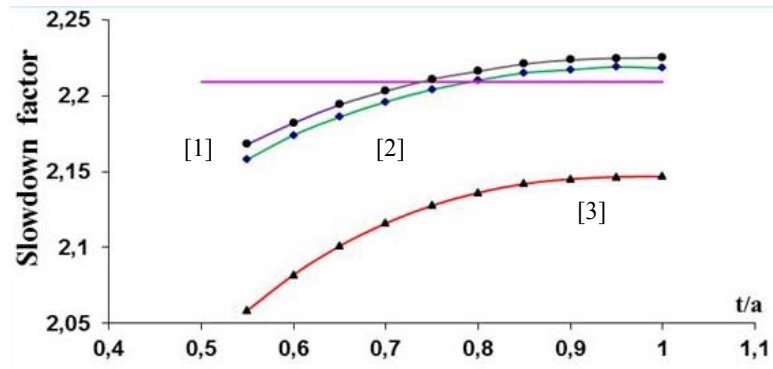


Fig.4. DFR slowdown factor n_{eff} versus t/a for DAST, $\epsilon(\lambda_{\text{DFR}}) = 5.2$, $a/\lambda = 1; 0.95; 0.65$;

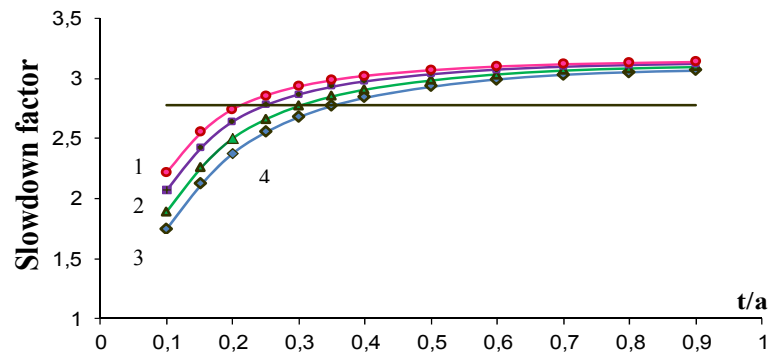


Fig.5. Calculated dependences of DFR slowing-down factors n_{eff} for ZnTe, $\epsilon(\lambda_{\text{DFR}}) = 10.1$, in given a/λ .
1 - $a/\lambda=1$; 2 - $a/\lambda=0.85$; 3 - $a/\lambda=0.7$; 4 - $a/\lambda=0.6$.

In the case of collinear interaction of optical and THz waves in a crystal, the crystal thickness required for PM is determined by the dependence of $n_{\text{eff}}(\lambda_{\text{THz}}) = c/v(\lambda_{\text{THz}})$ on $k_1 = t/a$ and $k_2 = a/\lambda_{\text{THz}}$ for a given value of the dielectric susceptibility of the THz wave, $\epsilon(\lambda_{\text{THz}})$, from dispersive transcendental equations [6]. The calculated values of n_{eff} as functions of k_1 (crystal thickness $t = ak_1$) and some of k_2 values in the frequency band of the fundamental mode of the H_{10} type of the waveguide, are shown in Fig.2 - 6. In the case of a thin crystal ($k_2 < 0.2$), n_{eff} quickly grows and tends to the value of the refractive index n_{THz} of the wave of the crystal placed in a free space. The line parallel to the k_1 axis, having the value $n_{\text{eff}} = n(\lambda_{\text{opt}})$ [5], intersects the family of curves $n_{\text{eff}} = f(t/a)$ at the points defining $k_1 = t/a$ or the thickness of the crystals for which the phase matching condition is satisfied. Thus the crystal acts as a nonlinear frequency converter, and the waveguide + crystal structure acts as a device that changes the phase velocity of the THz wave to the value of the group velocity of the laser pulse.

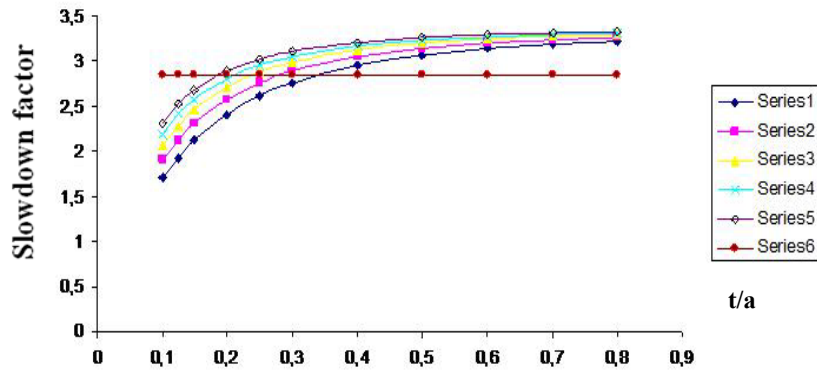


Fig.6. DFR slowdown factor versus t/a for GaSe, $\epsilon(\lambda_{\text{THz}}) = 11.5$, $a/\lambda = 0.5$ Series 1; $a/\lambda = 0.6$ Series 2; $a/\lambda = 0.7$ Series 3; $a/\lambda = 0.8$ Series 4; $a/\lambda = 0.9$ Series 5.

3. Conclusion

Optical excitation of broadband THz pulse was performed using 200 fs pulses from a Ti-Sapphire laser ($\lambda = 800\text{nm}$). DAST, GaSe, LiNbO₃ and ZnTe crystals were studied due to the high efficiency of conversion of optical radiation to THz range by OR. The crystals were located in a free space - the case of phase-mismatch. Frequencies in the range 0.1–3THz are obtained.

The results of numerical calculations show that it is possible to provide phase matching of nonlinear polarization waves and THz wave by choosing the degree of filling of the cross section of the waveguide with one of these crystals. This method allows to increase the nonlinear conversion efficiency of ultra-short laser pulses in the GHz–THz range. The results of experiments with a LiNbO₃ crystal show that the DFR intensity increases by an order of magnitude as compared with the case with no phase matching [6]. These results show a technique for the generation of high-power, broadband, high-repetition-rate THz pulses in a waveguide partially filled with a nonlinear crystal. The results can be used for creating effective THz broadband active waveguide systems or frequency scanning antenna.

Acknowledgments

This work was supported by the Ministry of Education and Science of Russian Federation, under contract №14.583.21.0069, RFMEFI58317X0069.

References

- [1] V Berger and C Sirtori, “ Nonlinear phase matching in THz semiconductor waveguides”, *Semiconductor Science and Technology*, vol.19, pp. 964–970, 2004.
- [2] S.-W. Huang, E. Granados, W. R. Huang, K.-H. Hong, L. E. Z. Zapata and F. X. Kärtner, “High conversion efficiency, high energy THz pulses by optical rectification in cryogenically cooled lithium niobate”, http://bibpubdb1.desy.de/record/147176/files/THz_final.pdf.
- [3] J. Xu, B. Globisch, C. Hofer, N. Lilienfein, T. Butler, N. Karpowicz, and I. Pupeza, “Three-octave terahertz pulses from optical rectification of 20 fs, 1 μ m, 78 MHz pulses in GaP”, *J. Phys. B: Atomic. Mol. Opt. Phys.*, vol.51, 154002 (5pp), 2018, <https://doi.org/10.1088/1361-6455/aacfe7>
- [4] J. A. Fulop, L. Palfalvi, G. Almasi, and J. Hebling, “Design of high-energy terahertz sources based on optical rectification”, *OPTICS EXPRESS*, vol. 18, No. 12, pp. 123117-12327, June 2010.
- [5] E. M. Laziev, A. S. Nikoghosyan, “Phase Synchronism and Ultrashort SHF Pulses Generation in Waveguides”, *SPIE, Mode-Locked Lasers and Ultrafast Phenomena*, vol. 1842, pp. 113-118, 1991.
- [6] A. S. Nikoghosyan, R. M. Martirosyan, A. A. Hakhoumian, J. M. Chamberlain, R. A. Dudley, N. N. Zinov'ev, “Generation of THz Radiation in Waveguide Partially Loaded with Nonlinear Crystal”, *Electromagnetic waves and Electronic Systems*, vol. 11, N4, pp. 47- 55, 2006.
- [7] J. Hebling, A. G. Stepanov, G. Almási, B. Bartal, and J. Kuhl, “Tunable THz pulse generation by optical rectification of ultrashort laser pulses with tilted pulse fronts,” *Appl. Phys. B*, vol. 78, pp. 593–599, 2004.
- [8] A. Schneider, M. Neis, M. Stillhart, B. Ruiz, R. U. A. Khan, and P. Günter, “Generation of terahertz pulses through optical rectification in organic DAST crystals: theory and experiment”, *J. Opt. Soc. Am. B*, vol. 23, No. 9, pp 1822-1835, 2006.

Compact Transcapacitance Model for Short-Channel DG FinFETs

(Proceedings of the Int. Conference on “Microwave and THz Technologies and Wireless comm.”)

Ashkhen Yesayan

Institute of Radiophysics and Electronics, Alikhanian Brothers str. 1, 0203 Ashtarak, Armenia

Received 15 November 2018

Abstract: A compact capacitance model is developed accounting for small-geometry effects in FinFETs. While decreasing the channel length, the transcapacitance model becomes very sensitive to all short channel effects, both in moderate and strong inversion regimes. In addition, for short channel devices, we need to take into account the inter-electrode capacitive coupling in the subthreshold regime, which is not significant for long channel devices. The quantum mechanical effects, which are very significant for thin Fins, are included in the model. The effect of mobility degradation on C-V characteristics is also demonstrated. The model was validated with numerical 3D Atlas simulations and a good accuracy of the model has been demonstrated in all operating regimes.

Keywords: MOSFET, short-channel devices, trans-capacitance, threshold voltage roll-off.

1. Introduction

During the last decade multi-gate MOSFETs become very popular and replace conventional MOSFETs for sub 100 nm CMOS technology [1]. The key factors that limit how far a multi-gate MOSFET can be scaled come from short-channel effects such as threshold voltage roll-off, drain-induced barrier lowering, velocity saturation. The choice of undoped channel is preferable for these devices because of the dopant fluctuation and associated improvement in mobility. Among the great variety of FinFETs the DG FinFET is recognized as the most stable to short channel effects. The progress in compact modeling of multi-gate MOSFET/FinFET is critically important for performing circuit simulations. Among the great variety of published works on this subject the outstanding is charge based compact model based on EKV formalism developed for long channel undoped DG MOSFET [2], which was further extended to short channels [3]. The above mentioned short channel model is based on the exact solution of potential profile along the channel [4] and is fully physics based, thus has no limitations for geometrical parameters of DG FinFET. The another advantage of this model is that it is fully explicit which is important for its implementation in hardware language. The static model developed in [3] includes all short channel effects including velocity saturation effect which is modeled by adopting the channel length modulation concept. However in the development of quasi-static model the velocity saturation effect was not included, instead the constant mobility was considered. In this work, the transcapacitance model including mobility degradation effect for short channel DG-FinFET will be discussed. The presented analytical model will be validated with 3D Atlas simulations.

2. Capacitances model for short channel DG FinFET

The trans-capacitance model we used here is based on the channel charge partition proposed by Ward [5]. Transcapacitances are defined as $C_{ij} = \pm dQ_i/dV_j$ where i, j are standing for gate, source and drain terminals and Q_i is the charge corresponding to the i -th terminal. Expressions for transcapacitances for DG FinFET were derived in [3, 6], considering constant mobility model. Here emphases will be done on quasi static effects arising from channel length reduction. The quantum mechanical effects are included in the model as it was discussed in [3]: where the

structural confinement is modeled as a shift of threshold voltage, and quantum correction to surface potential in high electric fields is accounted as an effective oxide capacitance.

a) Inter-electrode capacitive coupling

For short channel devices, we need to take into account the inter-electrode capacitive coupling [7]. According to Gauss' law, the inter-electrode coupling charge is given by the perpendicular electric field terminating on the chosen electrode. In our model, the normal electric field to the gates in subthreshold regime is calculated from the potential profile introduced in [4]. The inter-electrode coupling charge per channel length is calculated from Gauss' law and then by integrating it over the channel length, we compute the total gate charge. Then corresponding capacitances are calculated as charge derivatives to corresponding terminal voltages. It is worth to note that in sub-threshold regime inter-electrode capacitive coupling has no dependence on terminal voltages and depends only on device geometry. The calculations show that the inter-electrode charge coupling respectively on the drain and source electrodes are:

$$C_{dg_in} = C_{sg_in} = C_{gg_in} / 2.$$

We can assume that C_{gg_in} is concentrated in a part of the channel length that we define as:

$$L_p = \frac{C_{gg_in}}{2HC_{ox}}.$$

Thus, to calculate the terminal mobile charge in moderate and inversion regimes and the capacitance associated with it, we should replace L by $(L - L_p)$.

From comparison with TCAD simulations we have seen that in the saturation region the coupling charge associated with the high transverse electric field near the drain has a significant influence on $C - V$ characteristics in saturation regime. This charge can be calculated from the first-order derivative of potential in this region. By neglecting the mobile charge in saturation region, the potential profile can be derived from Laplace equation. This capacitance (let's define it as C_{gg_in2}) depends on terminal voltages, it is significant in saturation region and vanishes in linear region, thus we add it in the model only in equation of L_p :

$$L_p = \frac{C_{gg_in} + C_{gg_in2}}{2HC_{ox}}.$$

The table below demonstrates the significans of inter-electrode capacitive coupling for differend channel lengths, by the means of L_p/L ratio. Calculation have been done for $V_g = 0.6V$ and $V_d = 1V$.

Channel length L (nm)	L_p/L
20	0.347
50	0.145
100	0.074
1000	0.007

b) Mobility degradation effect

The mobility dependence on the longitudinal electric field becomes significant while shrinking the channel length. In the development of static model, the mobility degradation in high electric field is modeled by the means of channel length modulation [3]. However, in the development of quasi-static model the mobility dependence on longitudinal electric field should

be accurately accounted while calculating charge derivatives. The mobility dependence on the longitudinal electric field can be presented as:

$$\mu_{eff} = -\frac{\mu_{\perp}}{1 + E_{\parallel} / E_c},$$

where $E_c = \frac{V_{sat}}{\mu_{\perp}}$ is the electric field at velocity saturation (V_{sat} is the carrier velocity saturation),

$E_{\parallel} = \frac{dV}{dx}$ is the longitudinal electric field, μ_{\perp} is the transverse effective mobility and is modeled

by Mathias's rule. The transverse mobility reduction is due to scattering on acoustic and optical phonons and on surface roughness. The transverse mobility degradation becomes significant for thin body FinFETs. The dependence of mobility on longitudinal electric field is included in transcapacitance model as it was described in [8].

3. Discussion and model validation

The developed capacitance model for short channel DG FinFETs has been compared with 3D Atlas simulations. The mobility model used in Atlas simulations is the CVT model. The following parameters have been used for simulations: the side gate oxide thickness is equal to 1.5nm , the top gate oxide thickness is of 50nm , the silicon Fin doping is $N_a = 5 \cdot 10^{14} \text{cm}^{-3}$, the source and drain regions doping is $N_d = 5 \cdot 10^{21} \text{cm}^{-3}$. The Fin height that we simulated is $1\mu\text{m}$.

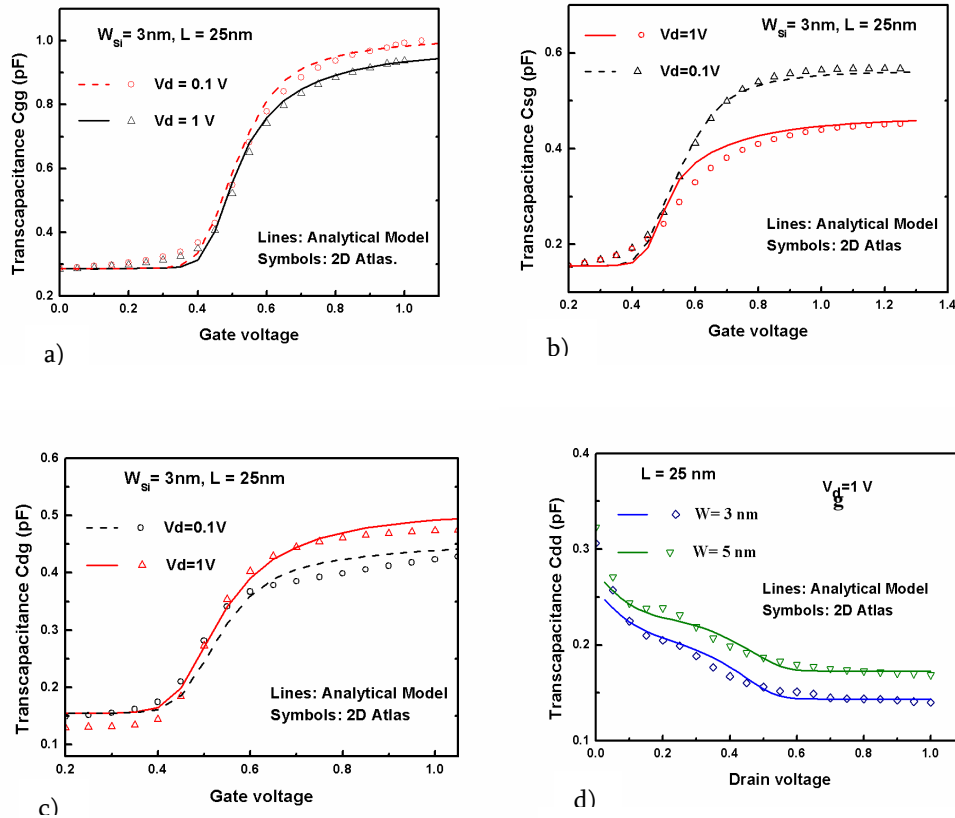


Fig. 1. Transcapacitances C_{gg} , C_{sg} , C_{dg} , C_{dd} obtained from model and simulations are respectively illustrated in figures a), b), c) and d).

Fig. 1 illustrates transcapacitances calculated from the model and Atlas simulations for an ultra-scaled device with channel length 25nm , and Fin thickness 3nm . From the good agreement of the model with 3D simulations, it is clear that mobility model is well interpreted in the model. The effect of mobility degradation on $C(V)$ characteristics especially is evident at saturation regime. This can be seen while comparing, e.g. the gate to gate transcapacitance C_{gg} shown in Fig. 1 a), and plots of C_{gg} presented in [3], where constant mobility was considered. Inter-electrode capacitive coupling near the drain at saturation regime is responsible for the specific curvature of C_{dd} plots in linear region (see Fig. 1 d)). The drain charge is very sensitive to all the effects in saturation region. The term C_{gg_in2} included in expression of L_p shapes the curvature of these plots and is significant only for short channel FinFETs.

4. Conclusion

The mobility degradation effect has been introduced in the transcapacitance model for short channel DG FinFET. The extended model preserves the accuracy of previously developed model and is fully physics based. The presented analytical calculations have been validated with 3D Silvaco Atlas simulations as the reasonable replacement of experimental data.

Acknowledgment

The numerical simulations 3D ATLAS, presented in this paper, have been performed during COMON project: FP7-IAPP-218255 at InESS, University of Strasbourg.

Reference

- [1] Tech. rep., International technology roadmap for semiconductor (ITRS). 2009.
- [2] J.-M. Sallese, F. Kruppenacher, F. Pregaldiny, C. Lallement, A. Roy, C. Enz, "A design oriented charge-based current model for symmetric DG MOSFET and its correlation with the EKV formalism," *Solid-State Electron*, vol. 49 no. 3, pp. 485–489. 2005.
- [3] A Yesayan, F Prégaldiny, N Chevillon, C Lallement, JM Sallese, "Physics-based compact model for ultra-scaled FinFETs," *Solid-State Electronics*, vol. 62, no1, pp. 165-173, 2011.
- [4] Liang X, Taur Y. A 2-D analytical solution for SCEs in DG MOSFETs. *IEEE Trans Electron Dev* 2004;51(9):1385–91.
- [5] Ward D, Dutton R. A charge-oriented model for MOS transistor capacitances. *IEEE J Solid-State Circ* 1978;13(5):703–8.
- [6] Tang M. Etude et modélisation compacte du transistor FinFET. Ph.D. Thesis, University of Strasbourg; December 2009.
- [7] Borli H, Vinkenens K, Fjeldly T. Physics-based capacitance modeling of short-channel double-gate MOSFETs. *Phys Status Solidi (c)* 2008;5(12):3643–6.
- [8] Arora N. MOSFET models for VLSI circuit simulation. New York: Theory and Practice, Springer-Verlag; 1993, ISBN:3-211-82395-6.

On a Validity Criterion for the Born Approximation

(Proceedings of the Int. Conference on “Microwave and THz Technologies and Wireless commun.”)

L. B. Hovakimian

Institute of Radiophysics and Electronics of NAS RA, 0203 Ashtarak, Armenia

Received 15 November 2018

Abstract: In this presentation a validity criterion for the Born approximation is examined for elastic scattering on a finite range radially symmetric potential in multidimensional space. Our analysis utilizes the transformation properties of the radial Schrödinger equation for S waves. The analytic structure of criterion is found to yield the corresponding results for low dimensional cases in a rather natural way. Some peculiarities of perturbative scattering in $2+\Omega$ dimensions are brought out.

Keywords: Born approximation, validity criterion, multidimensional space.

1. Introduction

The Born approximation [1] is a valuable computational scheme often used in studies of forward and inverse scattering problems in quantum mechanics [2-4] and cross-disciplinary fields (see, e. g., [5-8]). For the Schrödinger collision problem involving a radially symmetric potential [$U(\mathbf{r})=U(r)$] in three space dimensions ($D=3$), a widely accepted criterion for the validity of the Born approximation is described by the expression [3, 4]

$$\gamma_B(k, D=3) = \left| \frac{2m}{\hbar^2} \int_0^\infty r e^{ikr} \left(\frac{\sin kr}{kr} \right) U(r) dr \right| \ll 1, \quad (1)$$

where m is the mass of the particle propagating with the de Broglie wavelength $\lambda = 2\pi/k$ and collision energy $E = \hbar^2 k^2 / 2m$. In the short-wavelength limit,

$$\Theta \sim \frac{\lambda}{a} \ll 1,$$

when the scattered intensity is essentially concentrated within a narrow forward cone [2] of angular width Θ , the inequality (1) produces the restrictive relation [2, 3],

$$1 \gg \gamma_B(k, D=3) = \frac{I}{ka} \sim I\Theta \propto k^{-1}, \quad ka \gg 1, \quad (2)$$

$$I \sim \frac{ma^2}{\hbar^2} |U_0|,$$

in which U_0 is the characteristic strength of the potential with influence range a . A look at the scaling relation in (2) shows that at high incident energies (fast collisions) the leading term of γ_B is controlled by the forward cone angle $\Theta \propto \lambda$.

In this contribution, a procedure is described for examining the progenitor of the validity criterion (1) in D spatial dimensions [9-16]. Our treatment proceeds along heuristic lines and utilizes the D -dependent transformation properties of the radial Schrödinger equation. Since the information about the orbital angular momentum of the scattered particle is not represented in Eq. (1), we will specifically deal here with the case of collisions in the S wave channel.

2. Heuristic considerations

We begin our analysis by noting that for an S wave particle interacting with a central force field in D space dimensions the radial wave function, $\Phi(r)$, satisfies the differential equation [10-13,15,16],

$$\left[\frac{d^2}{dr^2} + \frac{D-1}{r} \frac{d}{dr} - q(r) + k^2 \right] \Phi(r) = 0, \quad (3)$$

in which

$$q(r) = \frac{2m}{\hbar^2} U(r)$$

is the reduced potential. One may reorganize Eq. (3) to make it look like a radial wave equation for a particle in three space dimensions by eliminating the first-order derivative term through the ansatz [12, 13,15,16],

$$\Phi(r) = r^{-(D-1)/2} \phi(r). \quad (4)$$

Insertion of (4) into (3) leads to Sturm-Liouville equation,

$$\left[\frac{d^2}{dr^2} - \frac{l(l+1)}{r^2} - q(r) + k^2 \right] \phi(r) = 0, \quad (5)$$

where the D -dependent object, $l = l(D)$, determines the properties of the centrifugal barrier (or centripetal potential well) and is given by

$$l = \frac{D-3}{2}. \quad (6)$$

According to Eqs. (3)–(6), the S wave problem in continuous radial D dimensions [12, 13] becomes equivalent [12, 15] to familiar l -wave problem [2–4] in the three-dimensional configuration space.

Taking advantage of this equivalence, we may proceed further by using the fact that in the l -th partial wave channel the radial (outgoing wave) Green's function associated with (5) behaves as [17],

$$G_0^+(r, r', l, k) = \frac{i\pi}{2} \sqrt{rr'} \begin{cases} J_{l+1/2}(kr) H_{l+1/2}^{(1)}(kr'), & r \leq r', \\ H_{l+1/2}^{(1)}(kr) J_{l+1/2}(kr'), & r' \leq r, \end{cases} \quad (7)$$

where $J_\nu(z)$ is the Bessel function and $H_\nu^{(1)}(z)$ is the Hankel function of the first kind. A careful examination of Eq. (7) reveals that the fundamental structure of the integrand appearing in Eq. (1) can be interpreted in the following physically transparent way,

$$re^{ikr} \left(\frac{\sin kr}{kr} \right) = G_0^+(r, r' = r, l = 0, k), \quad (8a)$$

with important supplementary information provided by

$$r = G_0^+(r, r' = r, l = 0, k = 0), \quad (8b)$$

$$\frac{r}{2l+1} = G_0^+(r, r' = r, l, k = 0), \quad l > -1/2. \quad (8c)$$

By relying on such an *interpretation* and employing Eq. (6), we arrive at the conclusion that the multidimensional analogue of the validity criterion (1) is given by inequality

$$\gamma_B(k, D) = \left| \int_0^\infty G_0^+(r, r' = r, l = l(D), k) q(r) dr \right| \ll 1. \quad (9)$$

This formula demonstrates explicitly how the k -dependent features of perturbative scattering in a central field of force become correlated with continuously changing radial dimensions. In particular, one may clearly see from Eqs. (6), (8c) and (9) that in the limit of vanishing incident energy [18] the object $\gamma_B(k \rightarrow 0, D)$ can exhibit non-divergent character when the condition $D > 2$ is fulfilled. At this juncture, it is necessary to emphasize the following: the Born perturbation expansion [1] has been extensively studied for more than 90 years, and the bibliography accumulated in this area of research is vast. It is therefore not unreasonable to presume that our heuristically constructed D -sensitive form (9) might have been enunciated in some earlier publication(s). However, up to this moment we have not been able to spot an appropriate reference to this issue. Let us remark that it is also possible to incorporate particle's grand orbital angular momentum [10,15,16] into the mathematical structure of the inequality (9) via straightforward generalization [19] of considerations presented herein.

3. Different faces of $\gamma_B(k, D)$

It is a simple matter to verify that for the familiar three-dimensional case ($l = 0$) the expression (9) obviously agrees with Eq. (1), as it should. For the case of two-dimensional potential scattering ($l = -1/2$), the construction (9) also automatically reproduces the analytic structure of the corresponding criterion [20],

$$\gamma_B(k, D = 2) = \left| \frac{\pi m}{\hbar^2} \int_0^\infty r J_0(kr) H_0^{(1)}(kr) U(r) dr \right| \ll 1.$$

In one dimension ($l = -1$, $r = |x|$, $U(-x) = U(x)$), Eq. (9) reorganizes into

$$\gamma_B(k, D=1) = \left| \frac{2m}{\hbar^2} \int_0^\infty r e^{ikr} \left(\frac{\cos kr}{kr} \right) U(r) dr \right| \ll 1, \quad (10)$$

and shows, in its own manner, how the Born approximation is destined to fail [2] in the long-wavelength limit $k \rightarrow 0$. We may also mention, for the sake of completeness, that if the one-dimensional potential is globally attractive and shallow [21],

$$\int_{-\infty}^{\infty} U(x) dx < 0, \quad I \ll 1,$$

then the threshold condition,

$$\gamma_B(k = i\kappa, D=1) = 1, \quad \kappa a \ll 1, \quad (11)$$

rigorously gives in an alternative and succinct way the asymptotic expression [2, 21] for the eigenenergy $E_0 < 0$ of the weakly bound state:

$$\kappa = \left| \frac{2m}{\hbar^2} \int_0^\infty U(r) dr \right| \sim \frac{I}{a}, \quad |E_0| = \frac{\hbar^2 \kappa^2}{2m} = \frac{m}{2\hbar^2} \left(\int_{-\infty}^{\infty} U(x) dx \right)^2 \ll |U_0|.$$

An additional facet of the Born approximation scattering event [9, 11, 12, 14] can be unraveled by examining the γ_B -versus- D behavior in $D = 2 + \Omega$ dimensions. Working from Eq. (9), we obtain in the short-wavelength domain a restrictive relation,

$$1 \gg \gamma_B = \frac{I}{\Omega}, \quad \Omega \gg ka \gg 1, \quad (12)$$

which is clearly *anomalous* from the standpoint of the customary scaling relation (2). The principal inference to be drawn from (12) is that in extra [16, 22] dimensions ($1 \gg \Theta \gg \Omega^{-1}$) the leading term of γ_B is *no more* under control of such basic parameter [2] of wave-mechanical scattering theory as cone angle Θ . It is quite remarkable that the specific wave vector window originating in (12) becomes heavenly wide in the asymptotic limit of infinite ($\Omega \rightarrow \infty$) dimensions [11, 13]. One may notice, at the same time, that this peculiar window disappears from stage (becomes *invisible*) when a transition is made to the opposite extreme, $\Omega \rightarrow ka \rightarrow 1$ (i.e., $D \rightarrow 3$). Under such transition, γ_B of (12) descends to three-dimensional world and exhibits the familiar structure of Born's constraint for slow ($\Theta \sim 1$) collisions [2, 3],

$$1 \gg \gamma_B(k \sim a^{-1}, D=3) \sim I.$$

References

- [1] M. Born, “Quantenmechanik der Stoßvorgänge”, *ZS. f. Phys.* 38, 803 (1926).
- [2] L. D. Landau and E. M. Lifshitz, *Quantum Mechanics*. Oxford: Pergamon, 1977.
- [3] G. S. Sahakyan and E.V. Chubaryan, *Quantum Mechanics*. Yerevan: Yerevan State University Press, 2009.
- [4] D. I. Blokhintsev, *Quantum Mechanics*. Springer, 2012.
- [5] S. M. Rytov, *Introduction to Statistical Radiophysics*. Moscow: Nauka, 1966.
- [6] M. Cheney and B. Borden, *Fundamentals of Radar Imaging*. Philadelphia: Siam, 2009.
- [7] J. Li, X. Wang, and T. Wang, “On the validity of Born approximation”, *Prog. Electromagn. Res.* 107, 219 (2010).
- [8] D. Tajik, A. D. Pitcher and N. K. Nikolova, “Comparative study of the Rytov and Born approximations in quantitative microwave holography”, *Prog. Electromagn. Res. B* 79, 1 (2017).
- [9] R. Aaron and A. Klein, “Convergence of the Born expansion”, *J. Math. Phys.* 1, 131 (1960).
- [10] I. Adawi, “Scattering of waves in many dimensions”, *J. Math. Phys.* 12, 358 (1971).
- [11] D. Wyler, N. Rivier, and H. L. Frisch, “Hard-sphere fluid in infinite dimensions”, *Phys. Rev. A* 36, 2422 (1987).
- [12] S. M. Apenko, “Weakly bound states in $2 + \varepsilon$ dimensions”, *J. Phys. A* 31, 1553 (1998).
- [13] M. M. Nieto, “Existence of bound states in continuous $0 < D < \infty$ dimensions”, *Phys. Lett. A* 293, 10 (2002).
- [14] L. B. Hovakimian, “Optical theorem in N dimensions”, *Phys. Rev. A* 72, 064701 (2005).
- [15] W.-Q. Zhao, “Relation between dimension and angular momentum for radially symmetric potential in N -dimensional space”, *Commun. Theor. Phys.* 46, 429 (2006).
- [16] S.-H. Dong, *Wave Equations in Higher Dimensions*. New York: Springer, 2011.
- [17] G. F. Drukarev, *Collisions of Electrons with Atoms and Molecules*. Springer, 2012.
- [18] I.Ya. Pomeranchuk, “Remark on the scattering of zero-energy particles”, *Collected Works*, vol.1, Moscow: Nauka, 1972, pp. 341-342 [in Russian].
- [19] L. B. Hovakimian, unpublished work.
- [20] M. A. Ruvinskii, “Elastic scattering of nonlocalized Mott excitons by dislocations”, *Sov. Phys.– Solid State* 5, 1240 (1963), see also Z. Li et al., “Cluster scattering in two-dimensional electron gas investigated by Born approximation and partial-wave methods”, *Physica E* 43, 543 (2010).
- [21] P. Zhevandrov and A. Merzon, “Shallow potential wells for the Schrödinger equation and water waves”, *Morfismos* 6, 1 (2002).
- [22] P. Ehrenfest, “Welche Rolle spielt die Dimensionalität des Raumes in den Grundgesetzen der Physik?”, *Ann. Phys. (Leipzig)* 61, 440 (1920).

Single-Layer Amorphous Carbon Anti-Reflective Coatings Obtained by The Pulsed Laser Deposition Method

(Proceedings of the Int. Conference on “Microwave and THz Technologies and Wireless comm.”)

L. Matevosyan¹, G. Pluzyan¹, K. Avjyan^{1*}, G. Dabaghyan².

¹ Institute of Radiophysics and Electronics, Alikhanian Brothers str. 1, 0203 Ashtarak, Armenia

² Institute of Information and Telecommunication Technologies and Electronics
(National Polytechnic University of Armenia), Teryan str. 105, Yerevan, Armenia

* E-mail: avjyan@gmail.com

Received 15 November 2018

Abstract: Single-layer a-C anti-reflective coatings on the Si and GaAs substrates were obtained by using a Q-switched nanosecond pulsed laser deposition method. It is established that single-layer a-C coatings effectively reduce the high reflection of substrates (on average to 5 % for Si and 8 % for GaAs in 400-750 nm wave range). Used by us technology for fabrication of a-C anti-reflective coatings is very simple (excludes high-energy implantation, high-temperature diffusion and deposition processes) and applied for the first time.

Keywords: Pulsed laser deposition, anti-reflective coating, amorphous carbon, photosensitive structures.

1. Introduction

It's obvious that suppression of visible light reflection from material surfaces is an important for various applications such as photosensitive structures, solar cells, flat-panel displays, etc. Therefore, attention to the design of technologies and novel materials for anti-reflective coatings (ARC) is in demand. As an alternative approach, further investigations in this field led to the use of metasurfaces (two-dimensional structures) as an intermediate layer for visible light ARC. In particular, were developed an ARC design based on a 10nm thick layer of silver nanodiscs (effective refractive index less than 1.0), which enabled strong suppression of reflection from the underlying substrate [1]. But we adhere to the opinion that single-layer ARC is more practical in the case of amorphous carbon ($a-C$) film, since it consists of only one element, which has an ability of broaden variation of refractive index and band-gap depending on technological conditions of fabrication. We continued the investigation of application possibilities of $a-C$ film as a visible light single-layer ARC. The pulsed laser deposition (PLD) technique was chosen as a fabrication technology, since ta-C films with high (up to 85%) sp^3 bonds were obtained earlier by using of this technology [2-4]. Si and GaAs were used as a substrate.

Up to date have not been reported about application of PLD for fabrication of visible light ARC based on a-C film. Primarily it caused by low band-gap of PLD-produced $a-C$ films. At second, there are not comprehensive and trusted experimental studies of the refractive index and sp^3/sp^2 hybridization ratio of C for nano-sized ($\leq 100nm$) films. And, at third, PLD is not recognized as an industry technology. Although practically all materials needed for functional electronics are obtained by this technology, the wide application of this method in production of electronic components is limited due to the difficulty of obtaining films with required qualities on relatively large areas. There are a few successful applications of PLD from which promising are broad band ($1-6\mu m$) infrared detector based on $(p)InSb-(n)CdTe$ lattice matched heterojunction [5] and an α -particle sensitive $a-C/n-Si$ heterostructure [6]. PLD is still an alternative technology as yet.

2. Experimental part and results

a-C films were deposited onto factory quality polished *Si* and *GaAs* substrates (400nm thickness) at room temperature by ablation of graphite target in the vacuum. The deposition unit consists of a *Q*-switched YAG: *Nd3+* laser (1.064μm wavelength, 30ns pulse duration, laser energy - 0.35J per pulse, repetition rate - 1Hz) and a vacuum chamber with residual gas pressure $2 \cdot 10^{-5}$ tor. AR properties of fabricated coating were studied from reflectance spectra on thin-film measurement system Filmetrics F20 at the normal incident of light. Thicknesses of film (0.28nm per pulse) were determined on profiler Mitutoyo SurfTest SJ-410.

Based on the studies of optical reflection spectra, it is established that single-layer *a-C* coatings effectively reduce the high reflection of substrates (on average to 5% for *Si* and 8% for *GaAs* in 400nm–750nm wave range. The reflection minimum (0.086%) on the *Si* substrate is observed at a wavelength $\lambda_0 = 575\text{nm}$ (fig. 1a; *a-C* film thickness - 71nm). This value is 0.84% at a wavelength $\lambda_0 = 516.22\text{nm}$ for a *GaAs* substrate coated with the 65nm thickness of *a-C* film (fig. 1b).

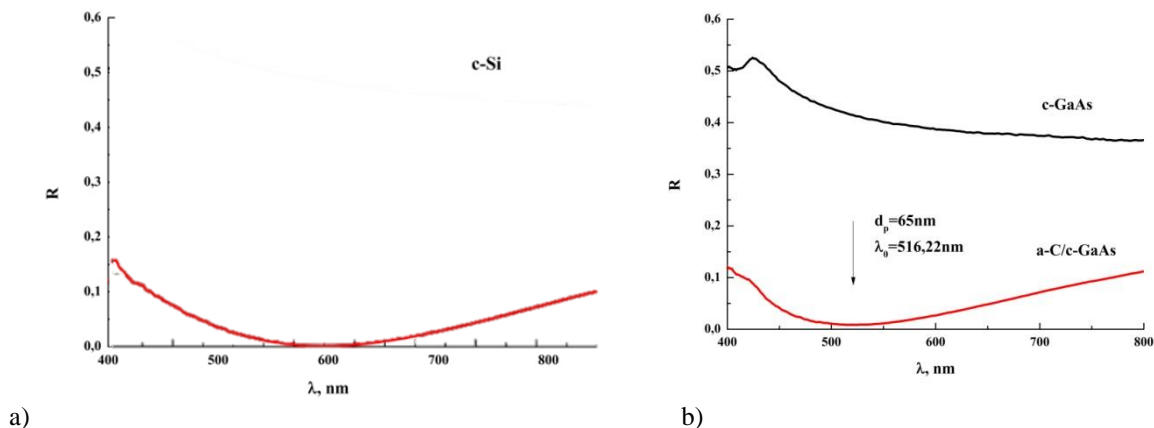


Fig. 1. *a-C* ARC on a) *Si* and b) *GaAs*.

Used by us PLD technology for fabrication of *a-C* anti-reflective coatings is very simple (excludes high-energy implantation, high-temperature diffusion and deposition processes) and applied for the first time.

References

- [1] H. Yasuda, R. Matsuno, N. Koito, H. Hosoda, T. Tani, and M. Naya, “Anti-reflective coating for visible light using a silver nanodisc metasurface with a refractive index of less than 1.0”. *Appl. Phys. Lett.*, vol. 111, pp. 231105, 2017.
- [2] G. Reibe, S. Weibmantel, D. Rost, “Preparation of super-hard coatings by pulsed laser deposition,” *Appl. Phys. A*, vol. 79, pp. 1275–1278, 2004.
- [3] Y. Miyajima, S.J. Henley, G. Adamopoulos, V. Stolojan, et al, “Pulsed laser deposited tetrahedral amorphous carbon with high sp³ fractions and low optical bandgaps,” *Journal of Applied Physics*, vol.105, pp. 073521, 2009.
- [4] B Schultrich, Carbon Film Deposition with ns Lasers. In: Tetrahedrally Bonded Amorphous Carbon Films I. Springer Series in Materials Science, vol 263. Springer, Berlin, Heidelberg, 2018.
- [5] L.A. Matevosyan, K.E. Avjyan, S.G. Petrosyan, A.V. Margaryan, “Photoelectrical properties of (p)InSb–(n)CdTe heterojunction,” *USPEKHI PRIKLADNOI FIZIKI (ADVANCES IN APPLIED PHYSICS)*, Vol. 2, No. 4, p. 403, 2014.
- [6] K.E. Avjyan L.A. Matevosyan K.S. Ohanyan L.G. Petrosyan, “An *a-C/n-Si* heterostructure as an ionizing radiation detector”, *Instruments and Experimental Techniques*, Vol. 59, No. 1, pp. 60-62, 2016.

Advanced Modulation and Coding Challenges on The Way to 400G and Terabit Ethernet

(Proceedings of the Int. Conference on “ Microwave and THz Technologies and Wireless comm.”)

D. Titov¹

¹ Keysight Technologies, Moscow, Russia

Received 15 November 2018

Abstract: The most common modulation scheme for 100GE today is NRZ modulation. 100GE is achieved by using 4 lanes of 25 gigabit per second (Gb/s) NRZ modulated signals. Theoretically, reaching 400GE speeds with NRZ is possible by applying these same concepts using 8 lanes of 56 Gb/s signaling. However, as speeds of NRZ designs increase above 28 Gb/s, channel loss of the transmission medium becomes a limiting factor. PAM4 signals use 4 amplitude levels with logical bits 00, 01, 10 and 11 to represent a symbol. However, PAM4 designs are far more susceptible to noise since four signal levels are packed into an amplitude swing of two. Therefore, the signal to noise ratio (SNR) is lower and analyzing noise from transceiver designs needs to account for channel return loss, as well as noise from the test instrumentation. PAM4 will use forward error correction (FEC) to account for this.

Keywords: NRZ modulation, two-state transmission system, maximum of error free data.

1. Introduction

Modern world is a world of devices which are exchanging data between themselves. The amount of data sent is also increasing dramatically as more and more high and ultra-high-quality video formats become available. To provide the speed and throughput for such number of devices exchanging such vast amount of data existing infrastructure is not enough, so we need a revolution in the way we transmit this data. So, as we see, the main driver of new technology revolution is the amount of information to be transferred as fast as it could be.

One of the main generators of data are IoT devices, which are almost everywhere and the number of them is already more than the number of people living on Earth and seems to reach 50 billion on 2020. There are these main IoT branches: smart home, wearables, smart city, industrial automation, smart energy, connected cars and medical devices.

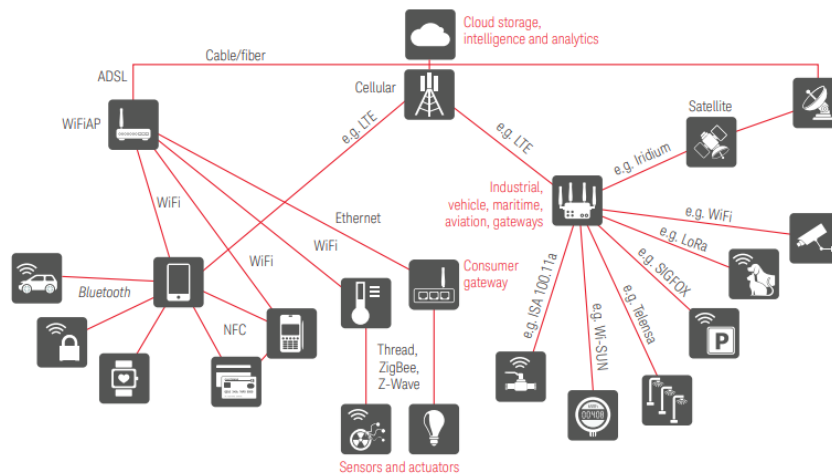


Figure 1. Communication standards for connected devices

Connected devices have a lot of ways to communicate: from very close NFC smart cards up through mid-range wi-fi to very long-range satellite standards. As the demands for transmitting/receiving speed, range quality and security and device operating time vary from application to application, there is no unifying standard to be preferred among others. But as we see on Fig. 1, sooner or later the data is transferred to a data center via optical fiber and that's where new technology revolution starts.

2. Accelerating from 100GE to 400GE

The most common modulation scheme for 100GE today is NRZ modulation. 100G Ethernet uses 4×25 gigabit per second ($Gbit/s$) or $10 \times 10Gbit/s$ NRZ modulated signals. NRZ is a two-state transmission system (also referred to as two-level pulse amplitude modulation or PAM2) where a logical "1" is represented by positive voltage, and "0" is represented by an equivalent (generally) negative voltage. 100GE is achieved by using 4 lanes of 25 gigabit per second (Gb/s) NRZ modulated signals. Theoretically, reaching 400GE speeds with NRZ is possible by applying these same concepts using 8 lanes of $56Gb/s$ signaling. However, as speeds of NRZ designs increase above $28Gb/s$, channel loss of the transmission medium becomes a limiting factor. According to the Shannon Hartley theorem, there is a theoretical maximum amount of error free data over a specified channel bandwidth in the presence of noise. As such, either the channel bandwidth or the number of signal levels must be increased to improve the data rate or channel capacity. Therefore, new multilevel signal modulation techniques are needed. PAM4 signals use 4 amplitude levels with logical bits 00, 01, 10 and 11 to represent a symbol. The number of symbols transmitted per second (baud rate) is half the number of bits transmitted per second. For example, a data rate of 28 gigabaud (GBaud) means there are 56 gigabits of data transmitted per second. This is double the data rate (throughput) in the same bandwidth compared to 28 GBaud NRZ, which is essentially $28Gb/s$, since one bit represents one symbol. However, PAM4 designs are far more susceptible to noise since four signal levels are packed into an amplitude swing of two. Therefore, the signal to noise ratio (SNR) is lower and analyzing noise from transceiver designs needs to account for channel return loss, as well as noise from the test instrumentation. PAM4 will use forward error correction (FEC) to account for this. FEC is an advanced coding technique that sends the required information to correct errors through the link along with the payload data. FEC introduces new test challenges that must be considered in physical layer testing of PAM4 signals. To facilitate the error correction capability, PAM4 encoding can also be done using Gray coding pattern. Gray code, also referred to as reflected binary code, is a coding pattern where successive symbols differ by one binary bit. In the case of PAM4 bit sequences defined above, the Gray code representation for the same symbols would be 00, 01, 11 and 10 for the levels 0, 1, 2 and 3 respectively. Gray coding is recommended by the Institute of Electrical and Electronics Engineers (IEEE) and Optical Internetworking Forum (OIF) standards to encode bits onto a PAM4 signal.

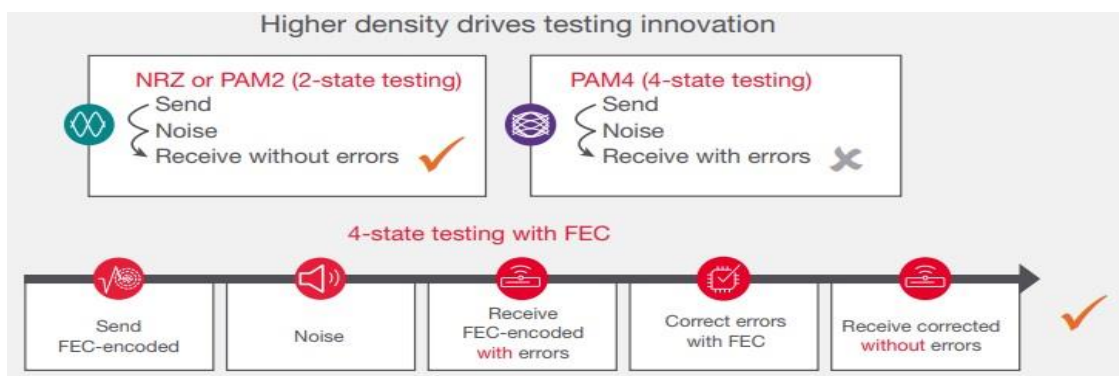


Figure 2. Testing with and without FEC

Reed Solomon (RS) coding operates on a block of data with a fixed size known as a symbol. These are grouped together into a frame. It is important to note that the “symbol” and “symbol error rate” terms which appear in data center networking standards using PAM4 are referring to the RS symbols, and not the PAM4 symbols. The Reed Solomon encoding and decoding work on binary data, before and after the Gray coding conversion from binary to PAM4 and back. [1].

When we talk about test implications of FEC, there are three main considerations: coding gain, burst errors and striping. Coding gain is a figure of the robustness of the error correction code. Pros are that higher coding gain allows the correction of higher number of errors. The tradeoffs are that higher coding gain require sending more overhead, it increases the amount of logics required for coding and decoding and it increases latency. But as higher speed serial data links using PAM-4 have a higher native error rate than those using NRZ line coding, a FEC with higher coding gain is required. A given coding gain in an RS system can correct up to a defined maximum number of errors in a code word. Once this number is exceeded, the entire code word cannot be decoded, and all the data is lost. This event is referred to as a frame loss and these can be counted as frame loss ratio (FLR) similarly to bit error ratio (BER). BER is the measure of the percentage of bits received with errors, due to noise or interference, divided by the number of bits transmitted. Therefore, FLR is the measure of the percentage of frames not delivered, divided by the number of frames sent.

Note that a “burst” in this context is not necessarily consecutive bits. The errors could be interspersed with correct data bits and would still result in a frame loss if the maximum number of correctable bits for the FEC code being used is exceeded. Error bursts can originate in the receiver end of the link, or anywhere within the link where the data is retimed without FEC decode and re-encoded, such as the passthrough mode in optical modules.

Striping the data rotates the individual data streams through all the available lanes in the link in a round robin fashion. Though striping doesn’t increase the computed coding gain, it effectively increases the gain when error bursts occur. [1]

3. Other challenges on a way to 400GE and beyond

The remaining challenges on a way to 600GE and even 1TE are the quality and interoperability of transceivers. The nature of pluggable modules necessitates that any new transceiver technology must be thoroughly tested to comply with specifications to ensure seamless compatibility before it is inserted into the network. Compliance tests (for optical, electrical and channel parts) are set to ensure that a receiver will operate with a worst-case transmitter and visa versa. The fundamental test for these network elements is the bit error ratio, demonstrating reliable operation in digital data transmission systems and networks. The basic principle is simple: the known transmitted bits are compared with the received bits over a transmission link including the device under test. The bit errors are counted and compared with the total number of bits to give the bit error ratio (BER). The applied test data signal can be degraded with defined stress parameters, like transmission line loss, horizontal and vertical distortion to emulate worst-case operation scenarios at which the device under test must successfully demonstrate error free data transmission. Obviously, this test is of fundamental importance for receiving network elements, due to the manifold impairments occurring on optical transmission lines. Therefore, all optical transmission standards define such stressed receiver sensitivity based on a BER measurement. The basic test methods and setups are usually very similar. However, the test conditions, the stress parameters or methods of stress generation vary from standard to standard, depending on the application area, transmission medium, data rate or data protocol.

Advanced modulation, such as PAM4, will enable data center operators to reach 400GE speeds. However, the cost of next generation optical transceivers then becomes the major contributor to the cost of data centers transitioning to 400GE. With software simulation, it is possible to pinpoint problems early in the design cycle and avoid costly manufacturing issues later. So, once 400GE transceivers reach the manufacturing phase, real time analysis and monitoring of process, test and equipment data can drive manufacturing improvements and efficiencies, mitigating risks of failure and down time.

Manufacturers of optical transceivers are faced with increasing challenges to their businesses, particularly how to reduce product cost. Pressures to reduce cost as data rates rise means manufacturing engineering managers and their engineers must be more creative in how to reduce costs before their competitors do. Traditional methods of eliminating tests or trying to make tests run faster may not be feasible, may not yield the intended benefit or may provide results that don't agree well with their customer's measurements. The use of parallel testing promises huge improvements, but more innovation is needed.

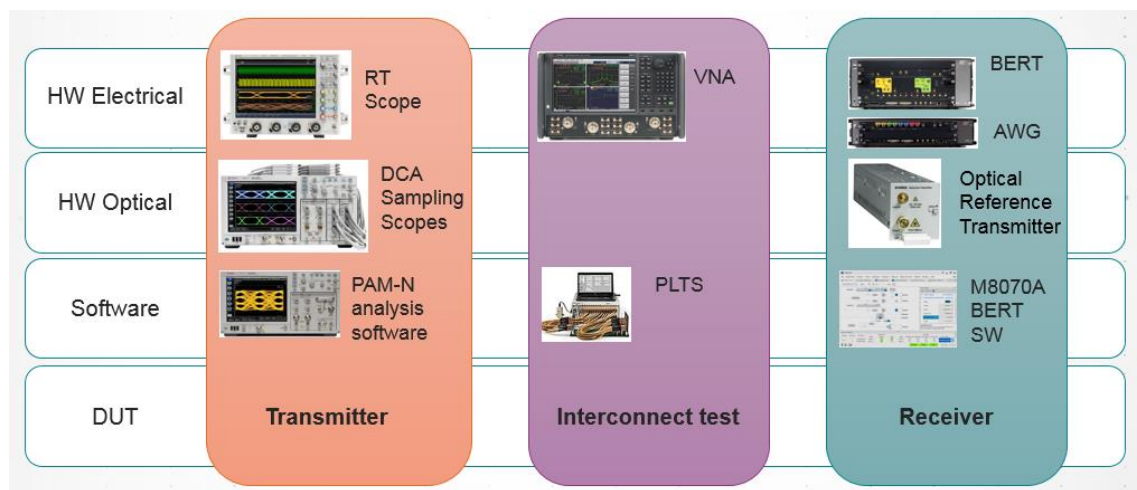


Figure 3. Keysight solutions for transceivers testing

Keysight Technologies is a unique company offering a complete set of solutions for transceiver testing. From real-time and sampling scopes to metrology-grade vector network analyzers and BERTs with the help of software for automated compliance testing Keysight solutions help the companies all over the world to achieve their goals faster, reduce costs and shorten time-to-market.

4. Conclusion

To achieve new technology revolution and accelerate from 100GE to 400GE and beyond, new technologies, such as PAM-4 with FEC must be implemented. Increased coding gain and striping are used to make the system more robust and less susceptible to errors. To achieve the level of quality and interoperability, desired by the new generation of data centers, transceivers must be thoroughly tested for compliance before entering the market. Keysight Technologies is in a unique position as it is the only company providing the complete set of solutions for transceivers testing.

References

- [1] Keysight Technologies, "Accelerating from 100GE to 400GE in the Data Center. Advanced Modulation and Coding Challenges" White paper. <http://literature.cdn.keysight.com/litweb/pdf/5992-3021EN.pdf>, 2018.

Power Domain Non-orthogonal Multiple Access (PD-NOMA) Technique For 5G Networks

(Proceedings of the Int. Conference on “ Microwave and THz Technologies and Wireless comm.”)

H. Haroyan¹, G. Hovsepyan¹, S. Sargsyan².

¹Yerevan State University, 1 Alex Manoogian, 0025 Yerevan, Armenia

²Institute of Radiophysics and Electronics, Alikhanian Brothers str. 1, 0203 Ashtarak, Armenia

Received 15 November 2018

Abstract: The possibility of applying non-orthogonal multiple access technology with compound modulation scheme for future 5G networks to improve the overall spectral and spatial efficiency is investigated. Calculation method of channel capacity for Power Division Non-orthogonal Multiple Access (PD-NOMA) with combined spatial modulation (SM) and amplitude phase modulation schemes is developed. Throughputs of PD-NOMA and Frequency Division Multiple Access (FDMA) techniques are compared. Numerical calculations and simulation show that in some scenarios the total capacity in the case of using PD-NOMA is about 1.6 times higher as for FDMA multiplexing technique.

Keywords: Non-orthogonal multiple access, 5G networks, channel capacity, spectral and spatial efficient.

1. Introduction

With the growing demands for high data rate, the use of millimeter-wave bands for next generation wireless communication network such as the fifth generation (5G) mobile systems attracts much attention of researchers. 5G promises a major change in mobility and, although not just ‘built’ for Internet of Things (IoT), it is heralded as a major driver of the growth of IoT [1]. The number of users in future generation cellular networks (e.g., 5G) is expected to increase dramatically.

One driving force of this increase in users is likely to be the continued deployment of the IoT which will consist of large numbers of connected devices. The rapid growth in connected users necessitates new technologies which improve spectral efficiency (SE) and allow for this additional traffic in the network.

There is an expected explosion in the number of users which will be connected to future wireless networks with the continued expansion of the Internet of Things. New technologies are needed in order to keep up with this connectivity demand. Therefore, the existing OFDM technology may not be well suited for the transmission of the data of some 5G applications. Hence, several alternatives non-orthogonal multiple access (NOMA) have been proposed and will be considered for the 5G physical layer [2].

One of the most promising techniques is power domain non-orthogonal multiple access which takes advantage of users having different received power levels, either through power control or naturally occurring in the network, in order to separate the users. Power domain non-orthogonal multiple access (PD-NOMA) is used with successive interference cancellation (SIC) in order to cancel higher power signals, which are decoded first, before decoding the other users.

The idea is to allow at least one UE to be separated from the other UEs in the power domain at the receiver. This allows for the UEs to completely share the time and frequency resources. Fig. 1 shows working scheme of PD-NOMA and block diagram. One of the attractive features of PD-NOMA is that it can be used in combination with UL multiuser multi-input multi-output (MU-MIMO) schemes in order to further overload resources. This can be achieved in the uplink (UL) by using power control to have one UE transmit at a higher power level than the other UEs using the same resources (see Fig.1. a)). At the base station the UE with much higher received power is then decoded first by treating the other UEs as noise. After being decoded the user’s signal is then canceled from the original received signal using SIC. The remaining users are then decoded.

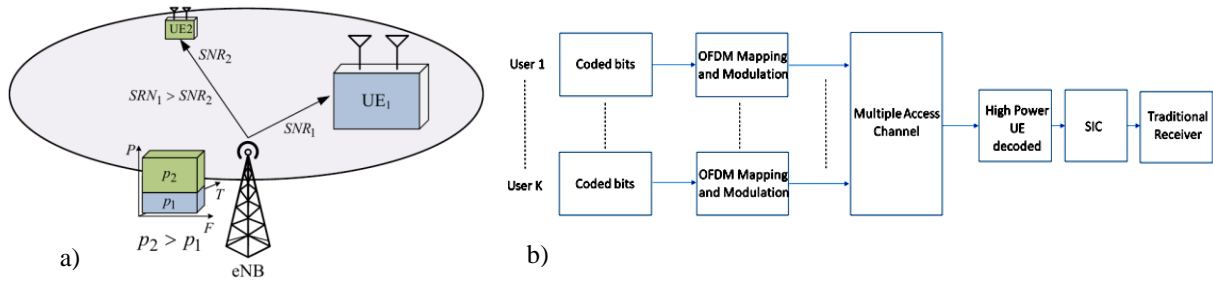


Fig.1. a) Principle of PD-NOMA scheme in the case of two users, b) Block diagram of PD-NOMA.

2. Results and discussion

The calculation of throughput in the case of noisy channel is calculated based on Shannon's law. In the case of frequency division (FD) the total capacity will be the sum of separate channels capacities

$$C_{tot} = \sum_k^K C_k \quad (1)$$

there the C_k is the k -th channel capacity estimated by

$$C_k^{FD} = F_k \cdot \log_2 \left(1 + \frac{\alpha_k P_k}{N_k} \right), \quad 1 \leq k \leq K \quad (2)$$

In the case of FD the frequency band F is divided into F_k sub-bands. Inter-channel interference is negligible if multiplexing is orthogonal and there are only AWGN noise. However, then multiplexing is non-orthogonal like PD-NOMA the inter-channel interference is arises and with existing AWGN noise decrease the system SNR. Hence, for PD-NOMA the total capacity should be calculated by slightly different relation there the existence and influences of neighboring channel is taken into account (K -is the users/channels quantity):

$$C_k^{PD} = \begin{cases} F \cdot \log_2 \left(1 + \frac{\alpha_k P_k}{\alpha_k \cdot \sum_{i=k+1}^K P_i + N_k} \right), & 1 \leq k < K \\ F \cdot \log_2 \left(1 + \frac{\alpha_k P_k}{N_k} \right), & k=K \end{cases} \quad (3)$$

Based on eqs. (1) and (2) the total throughput is calculated for different scenarios. It is interesting to compare total throughputs of FD and PD-NOMA multiplexing techniques in different conditions. Let's consider two scenarios with 2 and 3 users. The users located in different distances from NB, hence according to PD-NOMA principle they have different powers: in the case of two users we choose: $P_2/P_1 = 1/4$, and for three users: $P_3/P_2/P_1 = 1/4/16$ (see Fig.2 a,b)).

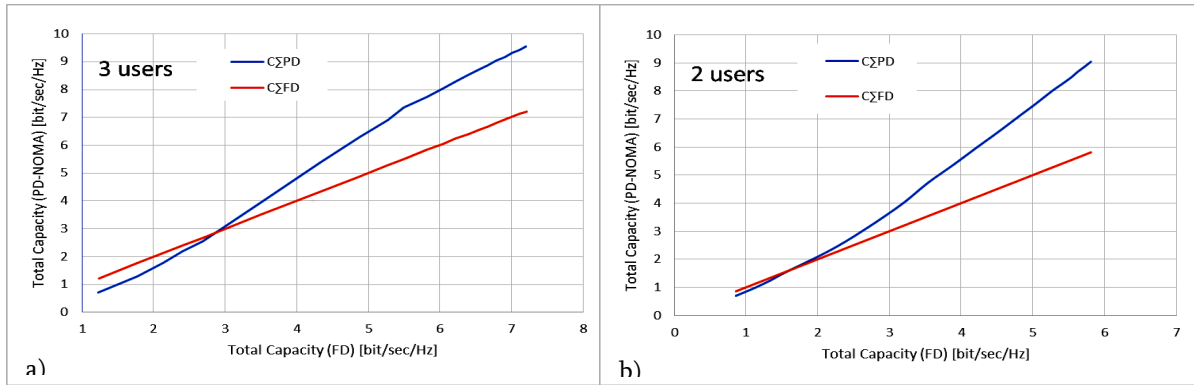


Fig.2. a, b) The total capacities of PD-NOMA vs. total capacities of FDMA in the case of 3 and 2 users correspondingly.

As the modulations have been chosen: QPSK for the farthest user from NB (according to PD-NOMA technique with the highest power), 16QAM for the second one, and 32QAM for the nearest user. As can be seen from Fig.2. the gain in total capacity of PD-NOMA compared to FD is different for different number of users. For instance, in the case of 3 users the gain is started from 2.8 bit/sec/Hz while for 2 users -1.6 bit/sec/Hz . It is worth to mention, the gain is higher for higher capacities which is expectable, but to obtain a higher channel capacity the higher order of modulation must be applied which brings to the more sensitivity to the noise level and complexity of SIC receiver. The comparison of Fig.2 a) and b) shows that with increasing the quantity of users capacity gain decreases. It should be also noticed that the bigger differences between powers of users the higher gain is expectable, but it brings to the high Peak-to-Average Power Ratio (PAPR) especially if users number is high. This fact is the main drawback of PD-NOMA technique.

It is also interesting to clarify how total throughput depends on total power (the sum of powers for different users) of users in both multiplexing scenarios (see Fig.3).

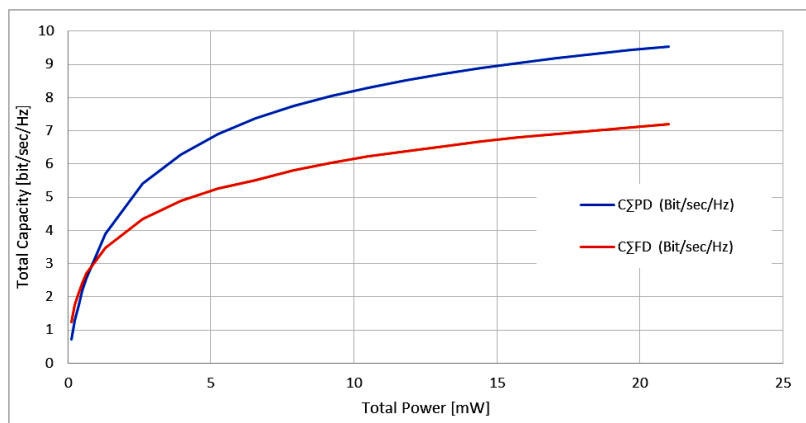


Fig.3 Total capacity dependence on total power for PD-NOMA and FDMA techniques.

As follows from Fig.3 the gain in total capacity if PD-NOMA is higher as bigger total power. But it is also clear that the total power increasing is not so profitable from point of view energy efficiency.

3. Conclusion

Non-orthogonal power division multiple access technology is studied and compared with traditional orthogonal frequency division multiple access technique. The advantages of PD-NOMA with introducing self-interference cancellation (SIC) algorithm in the receiver side in the case of 2 and 3 users is demonstrated. The total throughput of PD-NOMA in some scenarios is higher in comparison with traditional orthogonal multiplexing. It is turned out that with increasing the quantity of users' capacity gain decreases. It is also important that the higher gain is expectable if differences between powers of users are bigger, meanwhile it brings to the high Peak-to-Average Power Ratio (PAPR) especially if users' number is high. This fact from our point of view the main drawback of PD-NOMA technique.

Acknowledgments

This work was supported by the ISTC Joint Research Grant Program.

References

- [1] Mattern, Friedemann; Floerkemeier, Christian. "From the Internet of Computers to the Internet of Things" ETH Zurich. Retrieved 23 October 2016.
- [2] A. Benjebbour, Y. Saito, Y. Kishiyama, A. Li, A. Harada, and T. Nakamura, "Concept and Practical Considerations of Non-orthogonal Multiple Access (NOMA) for Future Radio Access", ISPACS 2013.
- [3] Piamontese A., Modenini A., Colavolpe G., Alagha N. Improving the spectral efficiency of nonlinear satellite systems through time-frequency packing and advanced processing. *IEEE Transactions on Communications*; 61, pp. 3404-3412, 2013.
- [4] H. Haroyan, G. Harutyunyan, T. Harutyunyan, S. Sargsyan, "Spectral Efficiency Improvement in Nonlinear Wireless Systems", Proceedings of "Microwave and THz Technologies, Photonics and Wireless Communications IRPhE'2016", pp. 19-23, 2016.
- [5] E. G. Larsson, O. Edfors, F. Tufvesson, T. L. Marzetta, B. Labs, and A. Lucent, "Massive MIMO for next generation wireless systems," *IEEE Communications Magazine*, vol. 52, issue 2, pp. 186–195, 2014.

OFDM Radar Signal Processing

(Proceedings of the Int. Conference on “Microwave and THz Technologies and Wireless comm.”)

G. Mkrtchyan^{1,2}, A. Hakhoumian¹, D. Nersisyan^{1,2}, T. Manukyan^{1,2}

¹ Institute of Radio physics and Electronics, Alikhanian Brothers str. 1, 0203 Ashtarak, Armenia

² YEA Engineering LLC, Engineering City, 21/1 Bagrevand str., Nor Nork, 0062 Yerevan, Armenia

Received 15 November 2018

Abstract: OFDM in radar systems gives as an opportunity to generate all desired signals. It can overcome the problem of ambiguity function for distance and velocity of target, has an ability to detect multiple targets simultaneously and insert identification (IFF) bits for distinguish enemy targets.

Keywords: OFDM radar, identification bits, multi-frequency radar signal.

1. Introduction

As we already know, the Orthogonal Frequency Division Multiplexing (OFDM) method is widely used in 4G and 5G communication systems. There are some publications, which describes the usage of OFDM in Radar applications: “Multi-frequency radar signals [1], Multi-frequency complementary phase-coded radar signal [2], OFDM signal constellation processing on Radar applications [3]. Some work have been done for target detection and tracking [4] [5], as well as direction of arrival estimation [6]. The research proves that the OFDM is ideal for both data transmission and radar sensing [7]. The research have also been done in automotive radar applications and an OFDM joint radar and communication system have been created [8][9]. Most of this research work defines the Doppler and range separately.

Why we are using OFDM for radar applications?

1. Universality
2. It overcomes the problem of ambiguity function for velocity and distance.
3. Detects multiple targets simultaneously.
4. Identification (IFF) bits can be inserted in a frame of OFDM.Theory

The OFDM is a universal method as already noticed in introduction. All radar signals can be generated using OFDM block. All is needed to do to make a FFT of this signals which will create complex coefficients for OFDM subcarriers and send these to OFDM block (figure 1).

In the output desired signal will be generated.

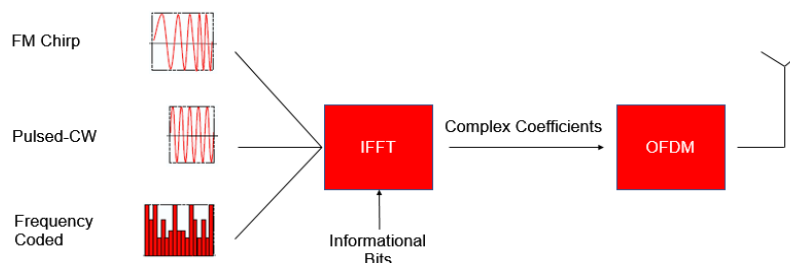


Figure 1. Universality of OFDM

The OFDM radar has an ability to include informational bits in a frame of signal, for example identification bits. The avionic radars require IFF signals to distinguish wanted targets. This means, that one module should be inserted into radar system 2), which will be responsible for this feature. In contrast, the OFDM radars can cope with without external module. These IFF signal bits can be inserted into the frame in certain pre-defined positions (figure 2). And only the own targets or objects can detect these bits and send reply message.

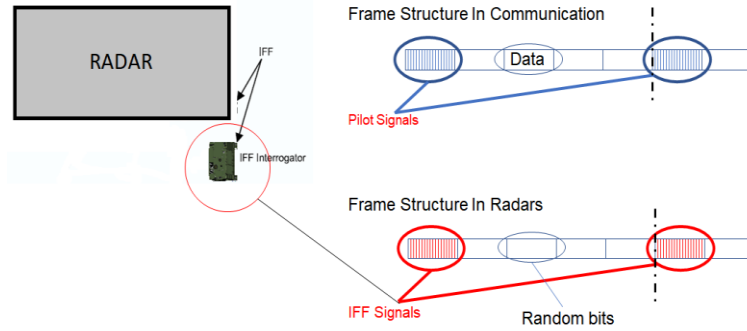


Figure 2. Avionic radar and OFDM frame with IFF bits

The radar application require high power signals. On the other hand, the OFDM require strong linearity. In that reason, the reference bits which will be generated are created by specified random method which will decrease the Peak to Average Power Ratio (PAPR). The generated signal has following structure (figure 3)

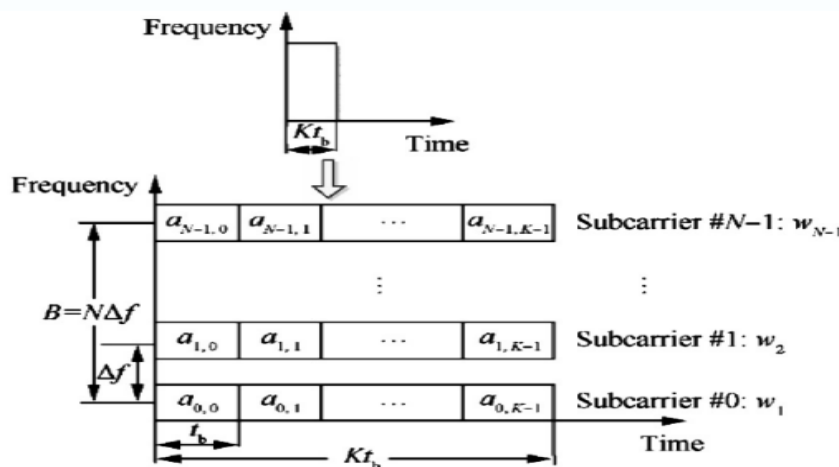


Figure 3. OFDM signal Structure In radars

In order to get appropriate OFDM parameters, we need to link them with radar parameters (Figure 4).

Radar parameters		OFDM parameters	
• Range Resolution	$\Delta R_{max} = \frac{c}{2B}$	• Bandwidth	$B = \frac{c}{2\Delta R_{max}}$
• Maximum Velocity	$V_{max}, f_d = \frac{V_{max}}{c} \cdot f_c$	• Subcarrier Spacing	$\Delta f \gg f_d$
• Carrier Frequency	f_c	• Number of Subcarriers	$N = \frac{B}{\Delta f}$
• Maximum Range	R_{max}	• Cyclic Prefix or Guard Interval	$T_a = \frac{2R_{max}}{c}$

Figure 4. Link between Radar and OFDM signal Parameters

The received OFDM radar signal is represented by this equation

$$r(p, k) = \rho e^{-j2\pi f_0} \sum_{n=0}^{N-1} w_n a_{n,k} e^{j2\pi n p / N} e^{-j2\pi f_d t_b} e^{-2\pi n \Delta f \tau_0}, \quad (1)$$

Where $e^{-j2\pi f_d t_b}$ is the Doppler information and $e^{-2\pi n \Delta f \tau_0}$ is the range information. The equation (1) can be represented in matrix form (Figure 5) [10].

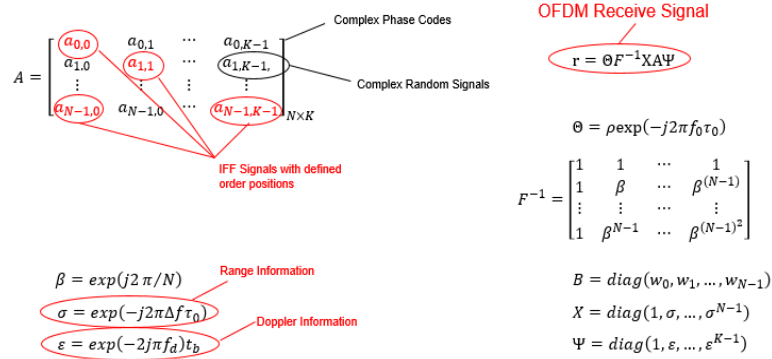


Figure 5. Matrix representation of OFDM Radar received signal

After receiving radar signal we need to do radar signal processing. The processing consists of following steps:

1. Multiplying the received signal with DFT matrix F

$$Fr = \Theta F^{-1} B X A \Psi \quad (2)$$

2. Multiplying both sides by B^{-1}

$$B^{-1} Fr = \Theta X A \Psi \quad (3)$$

3. Let $D = \Theta X A \Psi$

$$[D]_{n,k} = \rho a_{n,k} e^{-j2\pi f_0 \tau_0} e^{-j2\pi f_d k t_b} e^{-2\pi n \Delta f \tau_0} \quad (4)$$

4. Taking element-wise division

$$[T]_{n,k} = \frac{[D]_{n,k}}{[A]_{n,k}} = \rho e^{-j2\pi f_0 \tau_0} e^{-j2\pi f_d k t_b} e^{-j2\pi n \Delta f \tau_0} \quad (5)$$

5. Applying 2D-DFT with $N_r \times N_d$ points on T

The algorithm of generating and receiving OFDM signal p is created in LabVIEW environment. Figure 6 demonstrate OFDM radar operation model which was realized on real OFDM radar prototype.

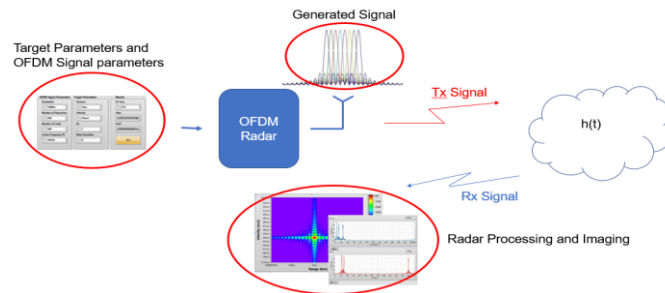


Figure 6. OFDM Radar operating model

The maximum number of simultaneously detected targets depends on number of OFDM subcarriers. The following figures demonstrate multi targets scenarios without noise (Figure 7. a) and with noise (Figure 7. b)

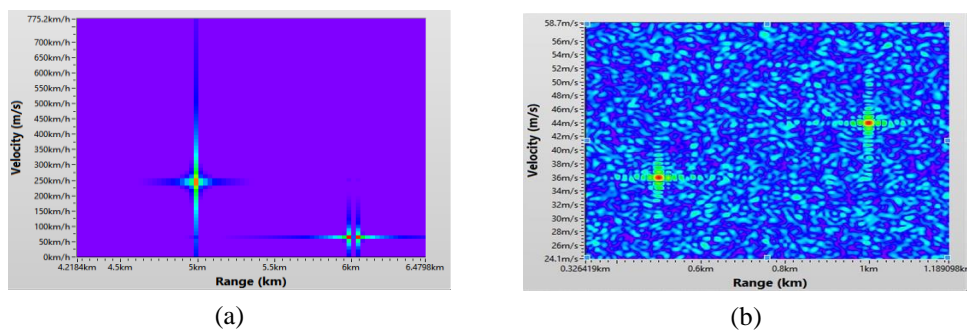


Figure 7. Multi target scenarios in OFDM radar without noise (a), with noise (b).

References

- [1] Levanon N. Multifrequency radar signals. Proceedings of IEEE 2000 international radar conference; 2000 May 7–12; Alexandria, VA, USA. Piscataway, NJ: IEEE Press; 2000. p. 683–8.
- [2] Levanon N. Multifrequency complementary phase-coded radar signal. IEEE Proc Radar Sonar Navigation 2000;147(6):276–84
- [3] Kh. Tovmasyan OFDM signal constellation processing on Radar applications. Armenian Journal of Physics, 2013, vol. 6, issue 4, pp. 204-208
- [4] Sen S, Nehorai A. Adaptive OFDM radar for target detection in multipath scenarios. IEEE Trans Signal Process 2011; 59(1):78–90.
- [5] Sen S, Nehorai A. OFDM MIMO radar with mutual-Information waveform design for low-grazing angle tracking. IEEE Trans Signal Process 2010; 58(6):3152–62.
- [6] Wu XH, Kishk AA, Glisson AW. MIMO-OFDM radar for direction estimation. IET Radar Sonar Navig 2010; 4(1):28–36.
- [7] Sturm C, Wiesbeck W. Waveform design and signal processing aspects for fusion of wireless communications and radar sensing. Proc IEEE 2011; 99(7):1236–59.
- [8] Sturm C, Braun M, Zwick T, Wiesbeck W. A multiple target Doppler estimation algorithm for OFDM based intelligent radar systems. Proceedings of the 2010 European radar conference (EuRAD); 2010 Sep 30–Oct 1, Paris, France. Piscataway, NJ: IEEE Press; 2010. p. 73–6.
- [9] Braun M, Sturm C, Niethammer A, Jondral F. Parametrization of joint OFDM-based radar and communication systems for vehicular applications. Proceedings of the 20th international symposium on personal, indoor and mobile radio communications (PIMRC); 2009 Sep 13–16; Tokyo, Japan. Piscataway, NJ: IEEE Press; 2009. p. 3020–4.
- [10] Tigrek, R. F., De Heij, W. J. A., & Van Genderen, P. (2012). OFDM Signals as the Radar Waveform to Solve Doppler Ambiguity. IEEE Transactions on Aerospace and Electronic Systems, 48(1), 130–143

Novel Approach to Wireless Communications Software Development Performance and Productivity Measurement – SAFe Based

(Proceedings of the Int. Conference on “ Microwave and THz Technologies and Wireless comm.”)

F. Muhammad¹, C. Cilliers¹

¹ *VIAVI Solutions, Wireless, Longacres House, Six Hills Way, Stevenage, SG1 2AN, United Kingdom*

Received 15 November 2018

Abstract: This paper gives an overview of a method that can be used to measure the productivity of software/hardware development teams. The approach is based on currently utilised Key Performance Indicator (KPI) in a product development programme as part of VIAVI's Wireless R&D organisation. The method with all associated processes and their applications are presented here. The outcome of the KPI is used to further improve the productivity of the team and ensure adequate Return on Investment (ROI) as well as to initiate Root Cause Analysis (RCA), where necessary. With this KPI, performance benchmarks can be set for Individual Cross Functional Teams (XFT) and the overall Agile Release Train(s) (ART) where productivity can be monitored over any time granularity. Other secondary benefits of this KPI is to facilitate management decisions which include; but is not restricted to; which site to use for R&D assignments, where to scale up/down, what work allocation to which team, true cost comparison between different geographical locations etc.

Keywords: Key performance indicator, wireless communication.

1. Introduction

Most R&D teams adopt some sort of KPIs as part of their development management whether Agile or Waterfall. These KPIs provide the necessary data which can be used to make informed decisions that positively impact engineering departments as well as the business as a whole.

The literature [2] suggests scores of different engineering KPIs but the actual value of their use depends on how a particular KPI is implemented and used in an R&D organisation. Collectively these KPIs complement each other to give management the full team performance picture across all teams in all locations in order to support overall business objectives.

Successful R&D teams adopt development processes, associated KPIs and analyses that are fit for purpose to support their business objectives. Analysing results help improve performance, identify and mitigate risks and issues, plan programmes and business evaluation.

Furthermore, these KPIs can improve resource allocation, planning, monitor progress, decision making and improves cost forecasting and gives a true productivity comparison between different teams in different locations operating on different cost bases.

This paper presents an overview of the Productivity Measurement process in software development on a particular product development. Associated KPIs and processes will also be discussed.

Introduction

Most R&D teams adopt some sort of KPIs as part of their development management whether Agile or Waterfall. These KPIs provide the necessary data which can be used to make informed decisions that positively impact engineering departments as well as the business as a whole.

The literature [2] suggests scores of different engineering KPIs but the actual value of their use depends on how a particular KPI is implemented and used in an R&D organisation. Collectively these KPIs complement each other to give management the full team performance picture across all teams in all locations in order to support overall business objectives.

Successful R&D teams adopt development processes, associated KPIs and analyses that are fit for purpose to support their business objectives. Analysing results help improve performance, identify and mitigate risks and issues, plan programmes and business evaluation.

Furthermore, these KPIs can improve resource allocation, planning, monitor progress, decision making and improves cost forecasting and gives a true productivity comparison

between different teams in different locations operating on different cost bases.

This paper presents an overview of the Productivity Measurement process in software development on a particular product development. Associated KPIs and processes will also be discussed.

2. Overall development flow

Most R&D organisations implement conventional homogeneous workflows based on a unified organisation with a single Way of Working (WoW). This is then with its supportive processes are applied to all areas of the organisation at all stages of product development. In this paper we are presenting a progressive method specifically applied to organisations where Time to Market (TTM) is critical, good quality on legacy and high stability is maintained throughout. These market requirements seem to be conflicting if approached by a single product development process, hence TTM-influenced development process initially and Time-In-Market TIM-influenced development process later.

With the above in mind we have devised a three-stage development process; Proof-of-Concept (PoC) stage, Rapid-Development (RD) stage and Product-Development (PD). These three stages will demand their own WoW, processes, team structures and supporting KPIs. In the following sections we will briefly describe the last two stages with emphasis on the product development stage. The productivity KPI is most applicable to the third stage. As illustrated in Figure (1) after the initial business and technical feasibility is carried out, the development method is decided according to its TTM criticality.

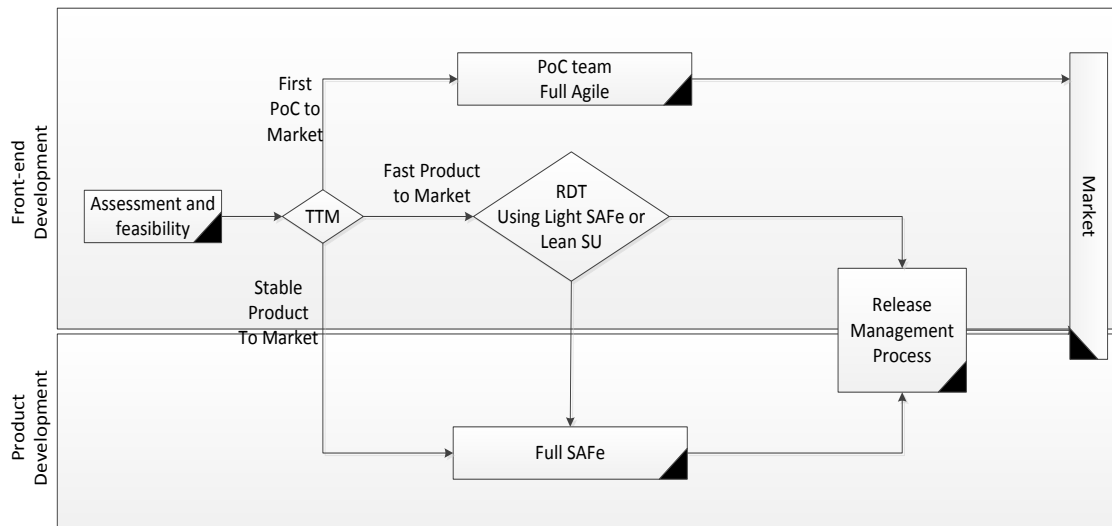


Figure (1)

a) PoC Stage:

At this stage, the team delivers any useful shippable software that helps the client progress their development. This team performs best in full Agile/Kanban, smallest planning and delivery increments, lightest processes, and most-relaxed quality gates approach. Nevertheless, release traceability and governance need to be maintained. Forward reusability is preferable but not mandatory to ensure TTM is met.

b) *RD Stage:*

At this stage, the foundations of the product are established. Features are developed in accordance with the Minimum Viable as TTM is still a major factor. Continuous Integration (CI) processes are used and short-lived temporary release branches are allowed when absolutely necessary. These teams work in an Agile Framework, e.g. customised SAFe, where faster cadence is required, in addition to shorter planning intervals, lighter processes, and relaxed quality gated for new features as new feature stability is still not a factor. Legacy feature quality must always be maintained. Co-located teams are necessary and closer collaboration with the support teams is vital.

c) *PD:*

This is the final development stage where prolonging TIM is key, which builds on the RD foundation and any initial prototypes developed. This stage is responsible for developing a resilient, scalable, stable and long-lasting product hence must follow a strict New Product Development (NPD) and quality control process. For this SAFe, CI and full quality gating are adhered to.

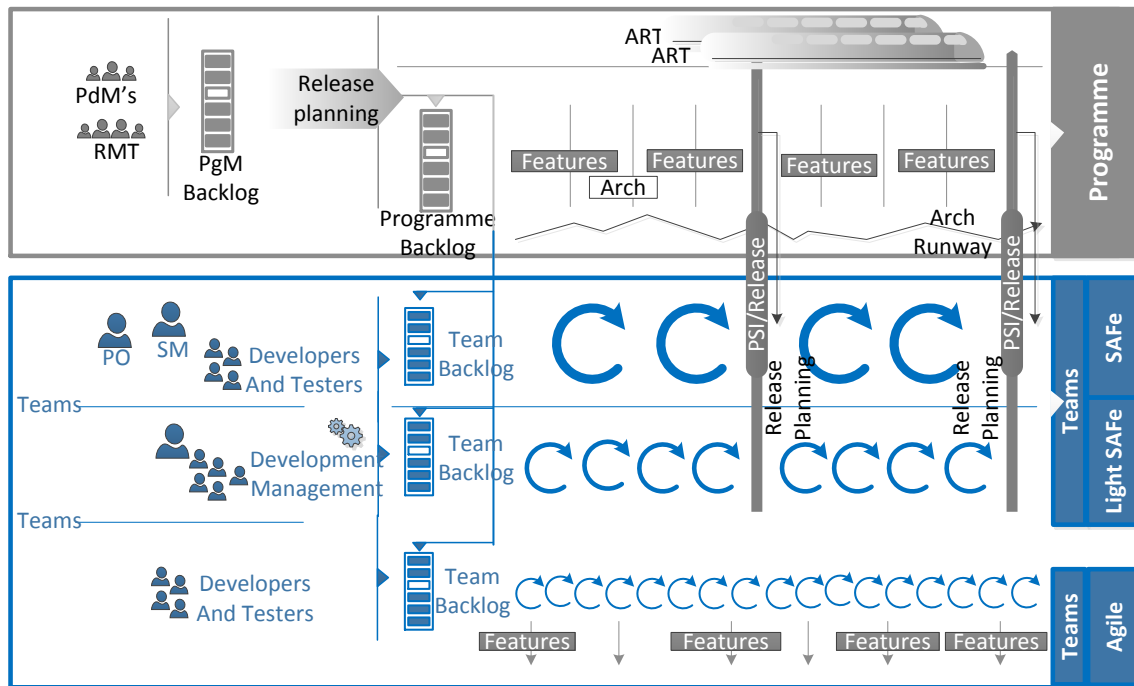


Figure (2)

3. Hybrid approach

Due to the aforementioned TTM and TIM reasons, different approaches to development are required at different stages. Hence it is recommended to adopt a hybrid Waterfall/Agile approach. At the initial stage of feature assessment, the development approach is decided, i.e. full Agile, Lean Start-up, or full SAFe, see Figure (2). Support and dependency teams, e.g. VHDL, Hardware, Platform, Quality Control, Algorithms teams, etc are common and shared across all development stages, i.e. PoC, RD and PD.

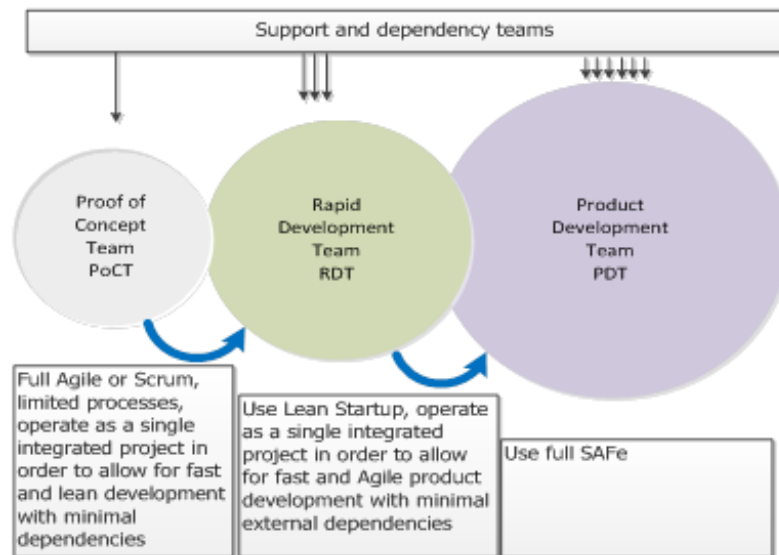


Figure (3)

4. Safe and capacity allocations

Team capacity allocation to plannable, non-plannable and interruptions depends on the type of product development. Typical allocation is as illustrated in the below Figure (4).

It is relatively easy to allocate capacity to plannable items, i.e. most of the 70% which is consumed with software development, design and code reviews and some plannable low priority defects. The 10% IP Sprint is taken up by technical refinement, upcoming PI planning, tasks that end up taking longer than first estimated, tasks that are looked over or missed during the PI planning event, and finally any time spent on new ideas and innovation. Teams often, experience a challenge in allocating capacity to the interruptive work and high priority defects. As such, 20% is typically reserved for these types of unpredictable tasks. These may include other tasks as illustrated in Figure (4).

5. How to deal with interruptions

There are many ways to deal with interruptions;

- a) *Stick to the Scrum Rules, the rules are clear, if its not part of the Sprint plan, then it shouldn't be done. This is not recommended as it is too strict and not interruption-friendly.*
- b) *Short Iterations which is shorter than interruption frequency. In this method, choose your iteration length to be so short that you can always start work on urgent interruptions. This is not recommended as well as it can be exhausting, but it is one ways to get the team and the organization to understand the large toll that these interruptions take.*
- c) *Handle interruptions on case-by-case bases, which requires constant change and crisis management and is highly unpredictable, [1].*

It is recommended to allocate a portion of time to interruptions based on Commitment Velocity where possible. After each sprint, consider how well the unplanned time allocation against that needed ended up for the sprint and adjust. This is something the XFT will improve

over time. Instead, it's a game of averages. The team needs to save the right amount of time for unplanned tasks on average. Some sprints will have more unplanned tasks occurring and some sprints will have fewer. When fewer occur, the team should get ahead on their stretched work, so that they're better prepared for when unplanned tasks occur further down the line.

The preceding advice works well for most SAFe teams where the level of interrupts is moderate. Some teams, however, are highly interrupted and therefore should have a different WoW, e.g. KANBAN approach. Hence another good approach is to create a dedicated team to deal with interruptions.

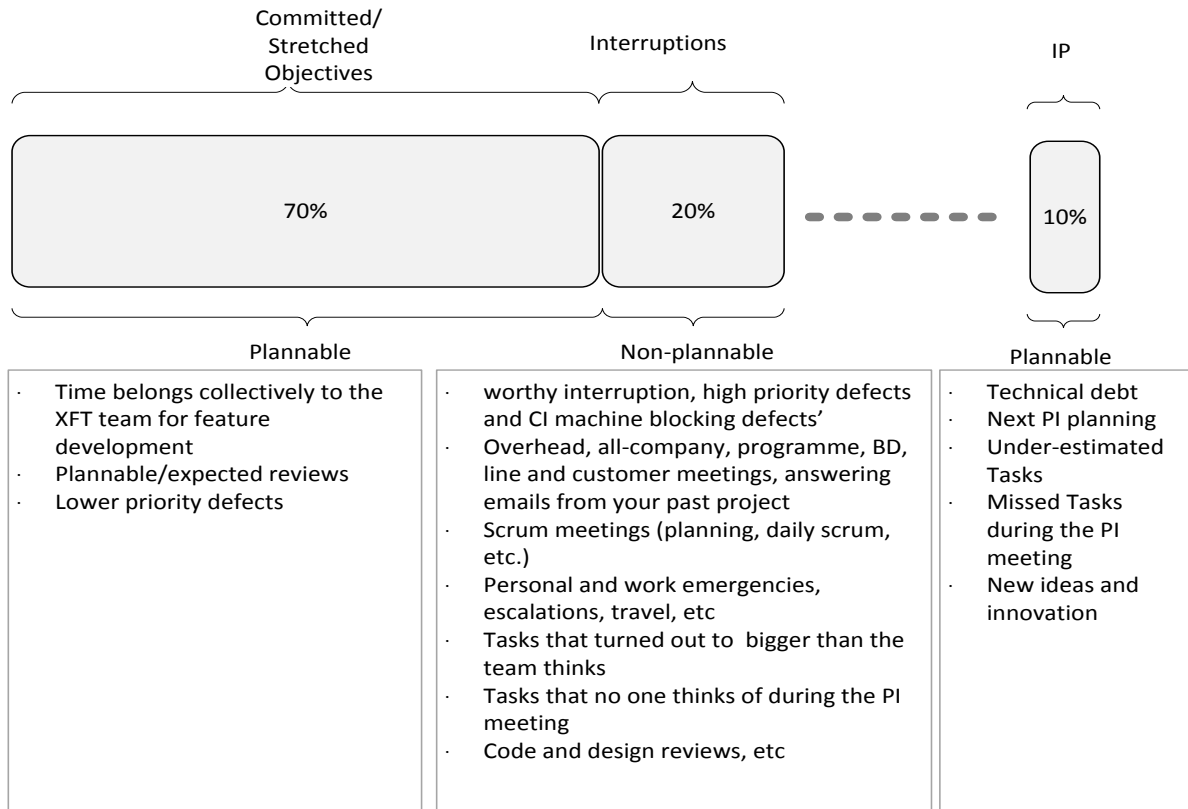


Figure (4)

In conclusion, no magic percentage exists but must be larger for the area of 'unplanned time' in Figure (4). These highly-interrupted SAFe teams still need to include space in their sprints for unplanned time.

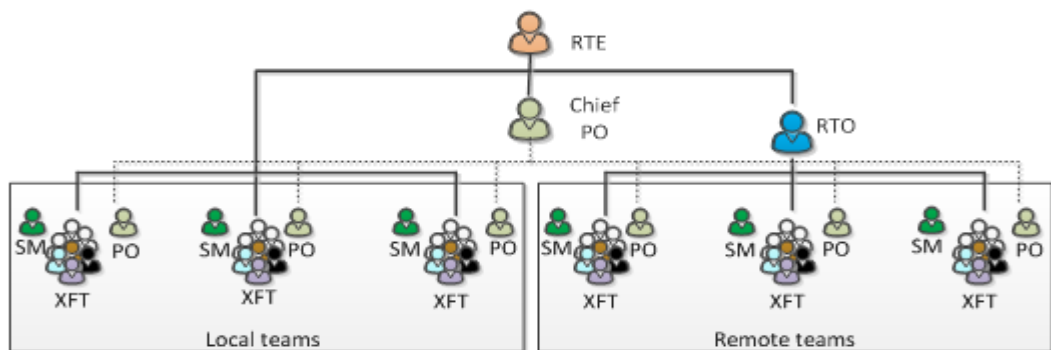


Figure (5)

6. Team structure

The below simplified Figure (5) illustrates a team structure for a single train consisting of local teams as well as remote teams. Each team consists of Agile team members, Scrum Master (SM) and Product Owner (PO). These teams interface directly to the Release Train Engineer (RTE). In case of the remote teams they interface to the RTE via Remote Team Owner (RTO) who is local to the RTE. Teams' POs are co-located with their teams; a single PO can be associated with more than one XFT and all POs are technically co-ordinated by the Chief PO although they are accountable to the RTE.

Each ART (or multiple ARTs) are supported by a number of Dependency Teams, which includes but is not limited to; Defect Triage Team, Architecture Team, Quality validation team, System Validation Team, VHDL team, Algorithms Team, HW Team etc. as illustrated in Figure (6).

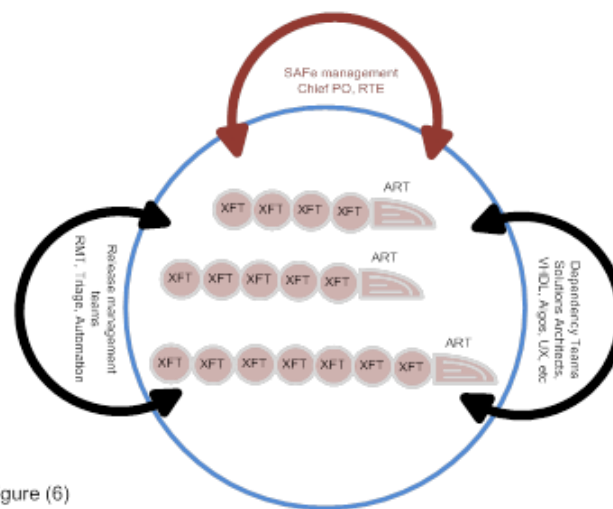


Figure (6)

7. Team and Art productivity evaluation

The performance of the team is measured using productivity, a novel approach which has been devised and implemented. This is a relative measurement (unit-less) and is based on a common reference and comparable currency, i.e. Complexity Value (CV), as the CV is related to the estimated feature development effort. It became apparent that just counting the number of features/work items delivered by a team is not a good measure, as features vary in size.

This KPI is used to measure productivity rather than efficiency. Efficiency and Productivity are often confused, yet the two have vastly different meanings when it comes to getting your work done. Being efficient, means you are working in a well-organised environment (work flow) while being productive means you are successful in producing the desired results. More on the definition of efficiency, productivity and effectiveness in a later section.

The starting point is to estimate the size of a feature by using a reference, i.e. the already known size of an implemented feature. The Modified Fibonacci sequence is used to determine the relative size of a feature as recommended by SAFe. Feature size is not connected to any specific unit of measurement. The size (effort) of each story is estimated relative to the smallest story, which is arbitrarily assigned a size of 1. SAFe applies the modified Fibonacci sequence (1, 2, 3, 5, 8, 13, 20, 40, 100) to reflect the inherent uncertainty in estimations, especially large numbers (e.g. 20, 40, 100, etc.).



Figure (7)

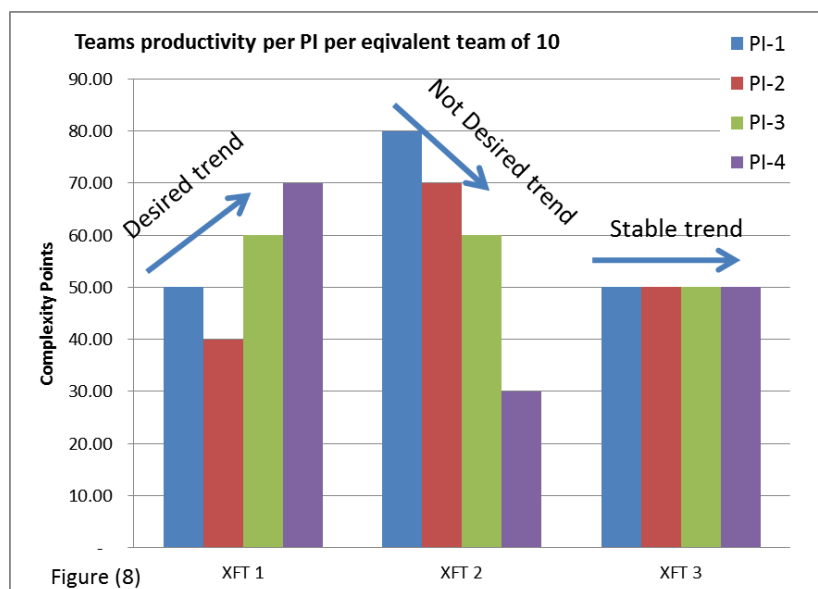


Figure (8)

Feature size to Effort Unit (can be days, weeks, etc) is based on past experience. A practical example can be found below.

For example, according to the below mapping, if a known feature size 1 is a two-month effort, then a size 10 feature is 20-week effort.

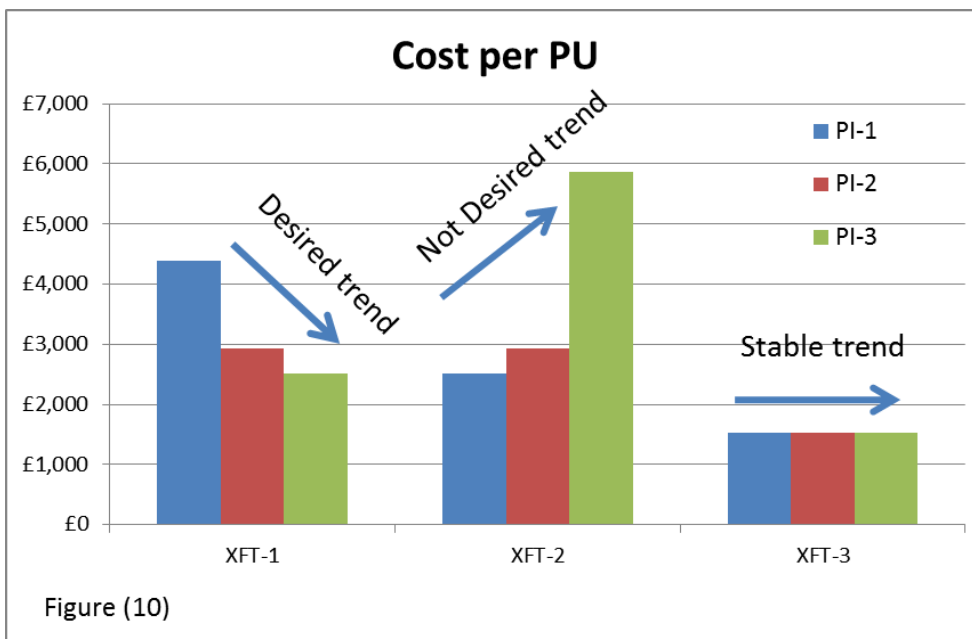
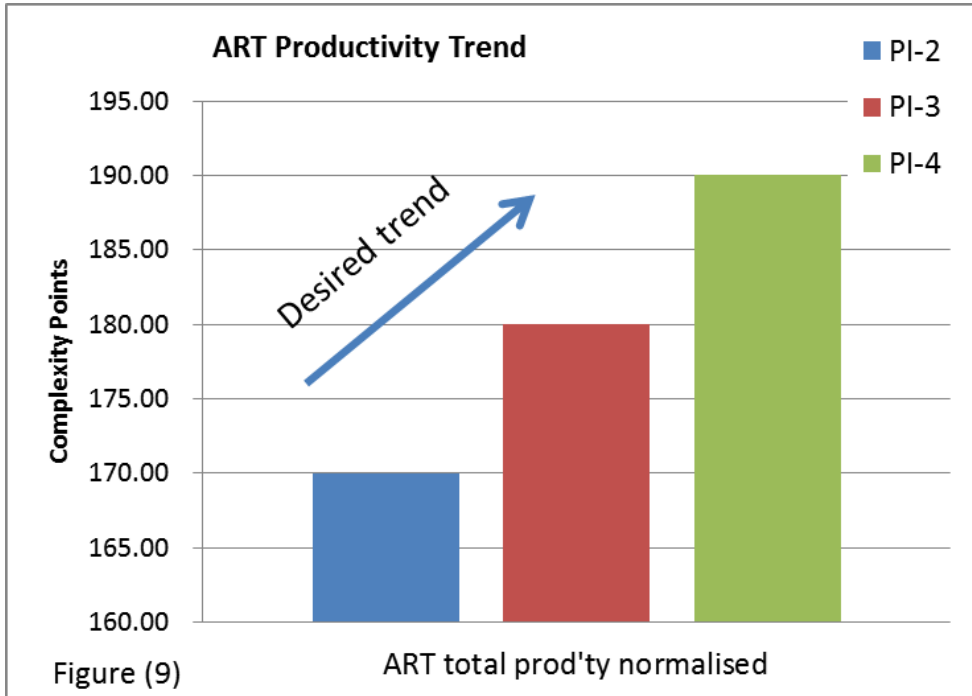
- Size 0 = negligible
- Size 1 = 2 effort units
- Size 2 = 4 effort units
- Size 3 = 6 effort units
- Size 5 = 10 effort units
- Size 8 = 16 effort units
- Size 13 = 26 effort units
- Size 20 = 40 effort units
- Size 40 = 80 effort units
- Size 100 = 200 effort units

For the Productivity KPI to be meaningful and in order to use it to compare different teams, estimates (feature sizing) have to be centralised and independent of the XFT, i.e. done by same person or same forum. Also the delivered Complexity Points by a team have to be normalised to a constant team size and fixed time-period, e.g. an XFT size of 10 members and PI of 10 weeks. Normalised to a team of 10, the total delivered Complexity Units for a team is;

$$CP = \frac{TCP}{TS} \times 10$$

where CP is the total normalised delivered Complexity Points by a team, TCP is the true Team Complexity Points delivered, and TS is the true Team Size. This can then be used to plot the total output per team over a given period (PI in this case), see Figure (8). This is agnostic of location, cost base or supplier.

Summed and normalised (to the total number of teams), the delivered Complexity Points gives you the overall ART productivity trend as illustrated in Figure (9). This can be used to measure the productivity increase.



8. Team and Art ROI evaluation

It is important is to determine the returned value on your investment (ROI). It is calculated below and example trends are illustrated in Figure (10).

$$CpCp = \frac{CpPpEU \times PIP \times TS}{CP}$$

Where $CpCP$ is Cost per Complexity Points, $CpPpEU$ Cost per Person per Effort Unit and PIP are the Programme Interval Period.

This KPI can be common to different teams' cost, e.g. Local or Offshore, permanent or contractor. It can also be measured over any period, i.e. week, month, PI, etc. This allows us to measure ROI taking into account different cost bases in different geographical locations.

9. The relationship between efficiency, effectiveness and production

Often, we demand improvement by focusing exclusively on efficiency. There a limit to how much improvement you can make at the input (efficiency) side. Does it still make sense to try to reduce the team or the supplier cost further? By managing solely by keeping the cost price down, you may run a large risk of saving pennies on the expense of quality. We look less often at the output side – the effectiveness – of the team [3].

Efficiency is determined by the number of resources (time, money, and effort) that are necessary to produce the committed CVs. To meet the committed objectives, we commit a specific resource. For example, if we can meet the committed CVs with less resources we have operated more efficiently.

Productivity is determined by looking at the number of output CVs (effectiveness) versus the invested resources in order to achieve the output CVs (efficiency); in other words, if we can achieve more CVs with the same or less resources, productivity increases.

Effectiveness is determined by comparing what a team can produce with what they actually produce; therefore, effectiveness does not tell anything about the efficiency – the amount of resources that have to be committed to obtain that output CVs. If we are successful in producing more CVs in the same time period with the same resources, effectiveness will increase. See Figure 11 for understanding the relationship between the three parameters.

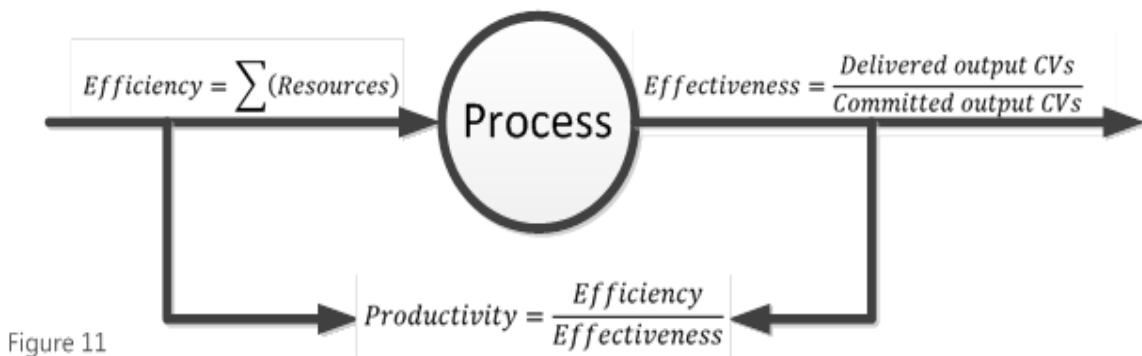
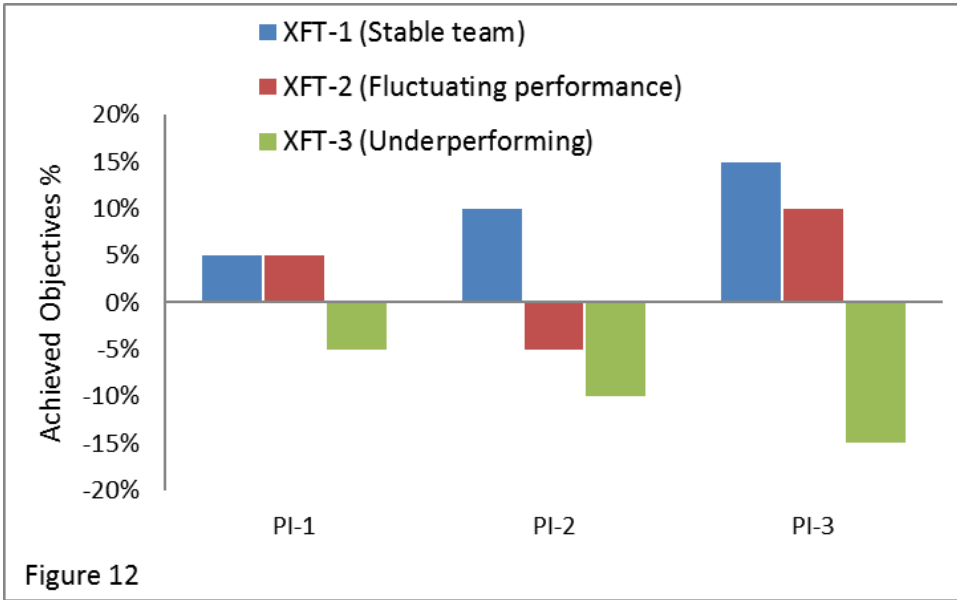


Figure 11

10. Team effectiveness

Team ‘effectiveness’ in other word is the actual achievement vs the theoretical commitment. During the PI event each team commits to “Committed” and “Stretch” Objectives, this KPI measures the “Effectiveness” of each team. Some teams deliver more than what is committed and some underachieve, as we can see in the example in Figure (12). This example presents the percentage of missed objectives (from committed objectives) that could not be delivered at the end of that PI, to the total number of objectives (in CP units). This gives an indicator of productivity, estimation accuracy, quality of deliverables etc. As a result, this may trigger an RCA.



11. Conclusion

There are many methods to govern and manage software development, we found SAFe as the most appropriate for VIAVI’s needs. R&D teams need to select and adopt development processes, associated KPIs and analyses that are fit for purpose to support their business objectives. Results help improve performance, identify and mitigate risks and issues, plan programmes and business evaluation. In this paper we presented a progressive method specifically applied to organisations where Time to Market (TTM) is critical, good quality on legacy and high stability is maintained throughout. We have devised a three-stage development process; Proof-of-Concept (PoC) stage, Rapid-Development (RD) stage and Product-Development (PD). Due to the TTM and TIM reasons, we recommend to adopt a hybrid Waterfall/Agile approach.

The above development approach is supported by a novel productivity KPI and other KPIs mentioned in this paper that can be used to measure the productivity of software and/or hardware development team.

Also, we concluded that there is no magic allocation percentage to cover for interruptions but has to be based on previous experience. This works for most SAFe teams where the level of interruptions is moderate, and if include sufficient space in their sprints for unplanned time. Some teams however, are highly interrupted and therefore should have a different WoW.

References

- [1] Agileadvicecom. 2012. Agile Advice. [Online]. [2 September 2018]. Available from: <http://www.agileadvice.com/2012/01/08/scrumxplean/seven-options-for-handling-interruptions-in-scrum-and-other-agile-methods/>
- [2] Pandian, C.R. 2015. Software Quality Metrics Overview. In: Pandian, C.R & Kumar, M eds. Simple Statistical Methods for Software Engineering: Data and Patterns. : CRC Press, pp. 85-126
- [3] Oeecoachcom. 2012. OEE Coach. [Online]. [4 September 2018]. Available from: <http://oeecoach.com/efficiency-effectiveness-productivity/>

Content-Aware Cross Layer Optimisation for IMT-Advanced Systems

(Proceedings of the Int. Conference on “ Microwave and THz Technologies and Wireless comm.”)

M. S. Johal¹, G. Markarian², A. Awang Md Isa¹, Y. Dasril¹

¹ Centre for Telecommunication Research and Innovation, Faculty of Electronics and Computer Engineering, Universiti Teknikal Malaysia Melaka, 76100 Durian Tunggal, Melaka, Malaysia

² School of Computing and Communications, InfoLab21, Lancaster University, Lancaster United Kingdom LA1 4WA

Received 15 November 2018

Abstract: Radio Resource Management (RRM) is crucial to properly handle the delivery of quality-of-service (QoS) in LTE systems. One of the techniques used for RRM in IMT-Advanced is cross layer optimisation (CLO) which normally involves the interaction between PHY and MAC layers before proper resource scheduling can be decided [1]. As the IMT-Advanced standard [2] only defines the PHY and MAC layers [3, 4], the effect of CLO is limited as the nature of the transmitted information is not taken into account.

Keywords: Radio resource management, cross layer optimization.

1. Introduction

Recently, some initiatives have been taken to include the application (APP) layer as part of the CLO techniques for RRM in LTE networks. By having this type of cross-layer design architecture, the LTE/LTE-Advanced can achieve multitude objectives such as improving spectrum efficiency, multi-layer diversity gain, adapting to wireless channel and satisfy users with different traffic classes [5]. Most of the APP and MAC/PHY cross layer architecture are targeted for data hungry services such as video streaming applications where high quality video frames will be adjusted which are then scheduled appropriately to particular user(s) whilst taking into account the channel state information (CSI) for each individual user as demonstrated by [6-9]. In these methods, the video frames or the encoding parameters are dynamically adjusted to suit the channel conditions for all users. However, the studies on the performance parameters, such as system throughput, packet loss ratio and delay for a certain time, are not clearly stated in those papers. Furthermore, compatibility with the legacy systems and standards is not considered as one of the major criteria for design. In this article, we are proposing a new technique which employs the CLO concept, namely “CONTENT AWARE RADIO RESOURCE MANAGEMENT”. This CLO concept will be expanded from the PHY layer up to the APP layer and will utilise specific properties of the data and overhead transmitted over the network to ensure backward compatibility with the legacy standards and systems.

2. LTE simulation model

In addressing the problems mentioned in the previous section, initially, we establish a classical or baseline LTE simulation model which exhibits basic RRM only. The importance of this baseline simulation model is reflected by its conformity to the 3GPP Release 8 standard, and thus, is considered a normal performing LTE platform. In fact, it will serve as the benchmark for our proposed content-aware RRM model. The LTE topology. The design of the LTE topology begins with a Remote Host connected to a SGW/PGW Gateway which is then linked together with an eNodeB before finally acquiring a wireless interface with four UEs. The

purpose of having four UEs is to represent four types of applications or services, namely web browsing, file transfer, voice-over-IP and video conferencing as shown in Fig. 1 [10]. The simulations are repeated for various distances between the UEs and the eNodeB and the output performance parameters such as the throughput, packet loss ratio, average delay and SINR values for a specific UE having video rate of 4 Mbps are also recorded. In this paper, only the throughput versus SINR graphs are plotted for both uplink and downlink transmissions as indicated in Fig. 2. Those results are expected due to the link adaptation performed by the eNodeB which result in various AMC schemes in both transmissions producing staircase-like pattern.

3. Cross layer optimization of RRM model

Based on Figs. 2 (a) and (b), we can draw the correlation between the Throughput and SINR and thus, recommending the suitable video packet generation rate at the sources for both uplink and downlink transmissions. Based on that observation, we want to introduce a new concept in radio resource management system which can dynamically adjust the transmitted data rate depending on the UE or eNodeB SINR performance in order to minimise the packet loss.

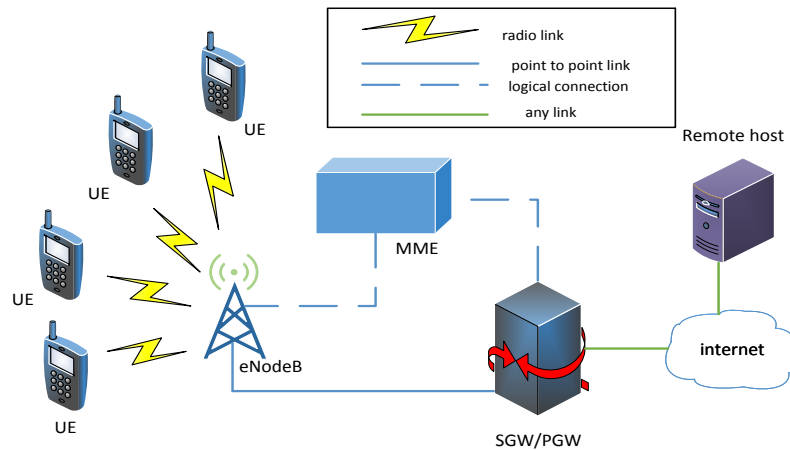


Fig. 1 Single eNodeB LTE – EPC simulation topology [10].

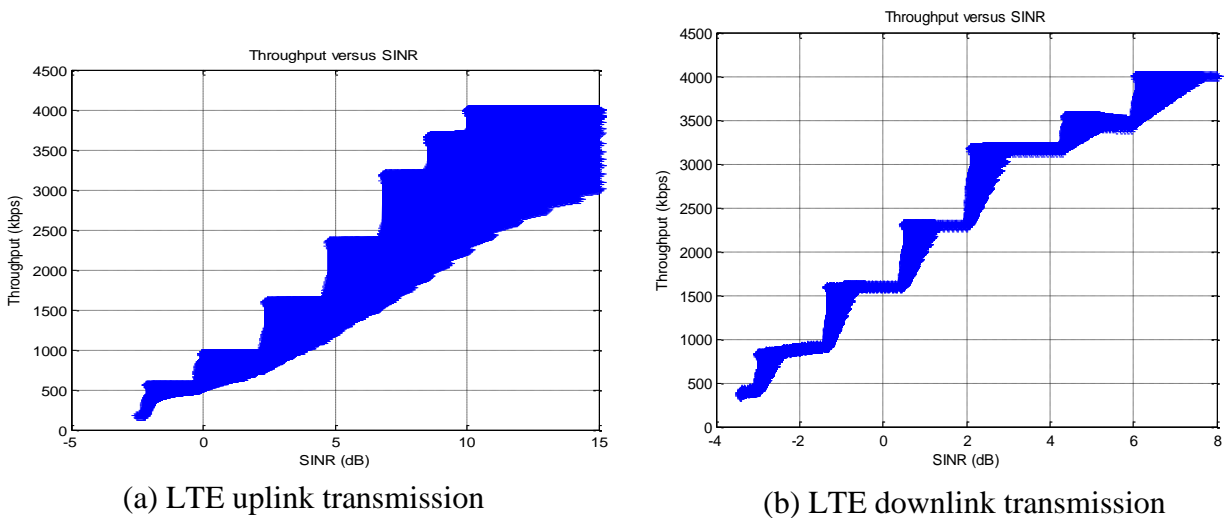


Fig. 2 Throughput against SINR plot for video rate, R = 4 Mbps.

This concept, which involves the cross-layer optimization approach, is called the content-aware RRM model or sometimes it is also called joint source and channel coding. In order to realise this, we propose a cross-layer look-up table that sets up the matching rules between the specific UE SINR and the assigned data rate for delivering video packets through the protocol suite for both uplink and downlink transmissions as shown in Table 1 (a) and (b). Both tables are derived from the Fig. 2 respectively.

Table 1: Proposed look-up table for content-aware RRM model.

(a) Uplink		(b) Downlink	
Proposed Data Rate, R (Mbit/s)	SINR (dB)	Proposed Data Rate, R (Mbit/s)	SINR (dB)
0.20	< -2.19	0.415	< -3.03
0.6	-2.19 – -0.2	0.875	-3.03 – -2.0
1	-0.2 – 2.29	0.92	-2.0 – -1.4
1.650	2.29 – 4.63	1.625	-1.4 – 0.41
2.450	4.63 – 6.77	2.33	0.41 – 2.0
3.250	6.77 – 8.33	3.21	2.0 – 4.26
3.750	8.33 – 10	3.5	4.26 – 6
4	> 10	4	> 6

4. Simulation results

For evaluation purposes, a new set of comparison parameters has been established in order to compare the performance of the proposed model and that of the baseline model. The new parameters are defined as follows:

$$\varphi_T = \int_0^t \text{Throughput} dt, \tag{1}$$

$$\varphi_P = \int_0^t \text{PLR} dt, \tag{2}$$

$$\varphi_D = \int_0^t \text{Delay} dt, \tag{3}$$

where φ_T is the total received data or area under the curve for throughput, φ_P is the area under the curve for packet loss ratio and φ_D is the area under the curve for average end-to-end delay. Practically, all the abovementioned parameters represent the areas under the curves calculated with respect to total simulation time for all the three output performance parameters; namely throughput, packet loss ratio and average end-to-end delay. Improvements can only take place if φ_T for one system is greater while φ_P and φ_D are smaller than those of its counterpart.

Fig. 3 shows output performance of the uplink video delivery over the course of 10 minutes, when one UE transmits video packets to the Remote Host via the eNodeB, while moving towards the eNodeB from the edge of the cell at 50km/h . In Figure 3 (b), the content-aware model outperforms the baseline model in terms of packet loss ratio by a staggering 95.32%

improvement. For the same amount of data transmitted in both models as reflected in Fig. 3 (a), the total number of packets lost during the transmission in the channel is huge in the baseline model, thus resulting in the wastage of bandwidth. As a matter of fact, the content-aware model also experiences much less average delay with 7.27% improvement as shown in Fig. 3 (c) and, this means QoS for the video streaming application can be preserved.

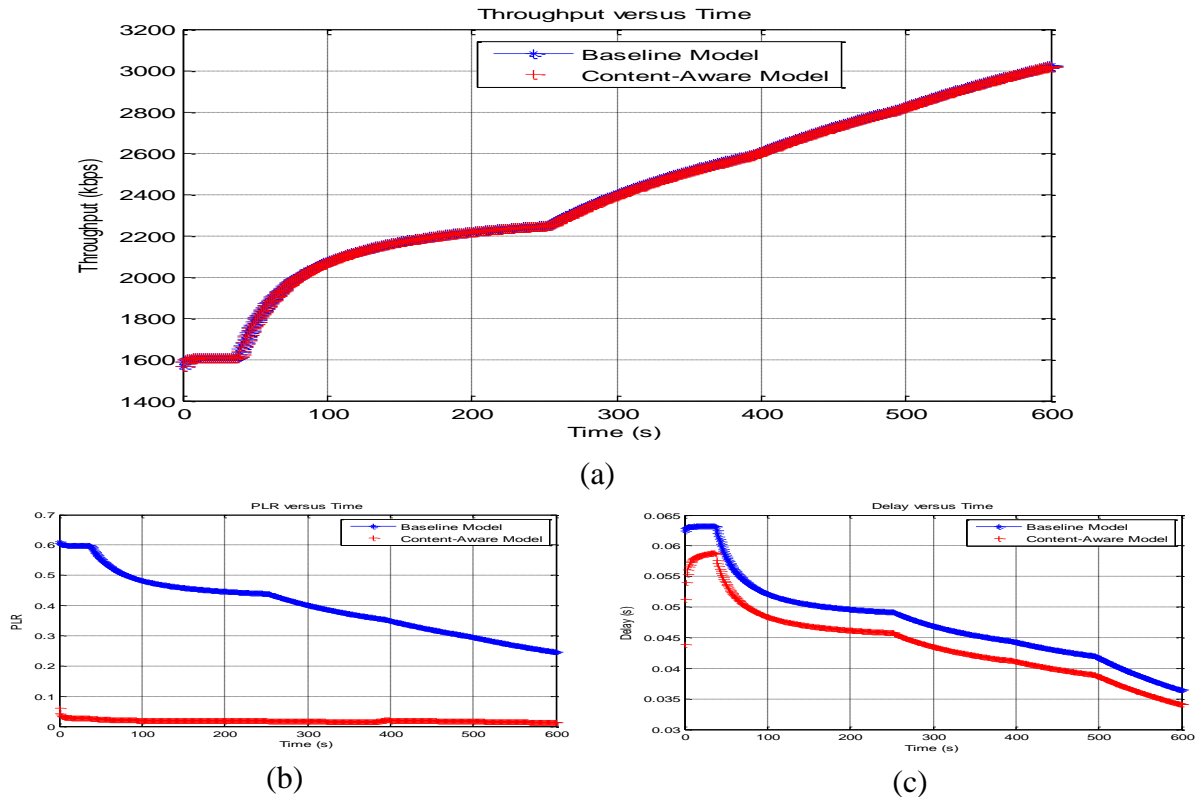


Fig. 3 Output performance for uplink video delivery at UE velocity of 50 km/h. (a) Throughput against time (b) Packet loss ratio against time (c) Average delay against time

Again, the much better performance of the content-aware model in the uplink video delivery is further supported by the same content-aware model in the downlink video transmission as indicated in Fig. 4. Over the 10-minute simulation and for the same amount of throughput, the content-aware model totally outperforms its counterpart, the baseline model with a 87.9% improvement in packet loss ratio and a significant 4.4% gain in average delay. This means that by employing content-aware model, we can avoid a great deal of bandwidth wastage and also preserve the QoS of the video streaming application, as opposed to the baseline model where the QoS could be effectively compromised. In short, it can be summarized that the Content-Aware RRM model produces much better performance than the Baseline Model in either the uplink or downlink video transmission.

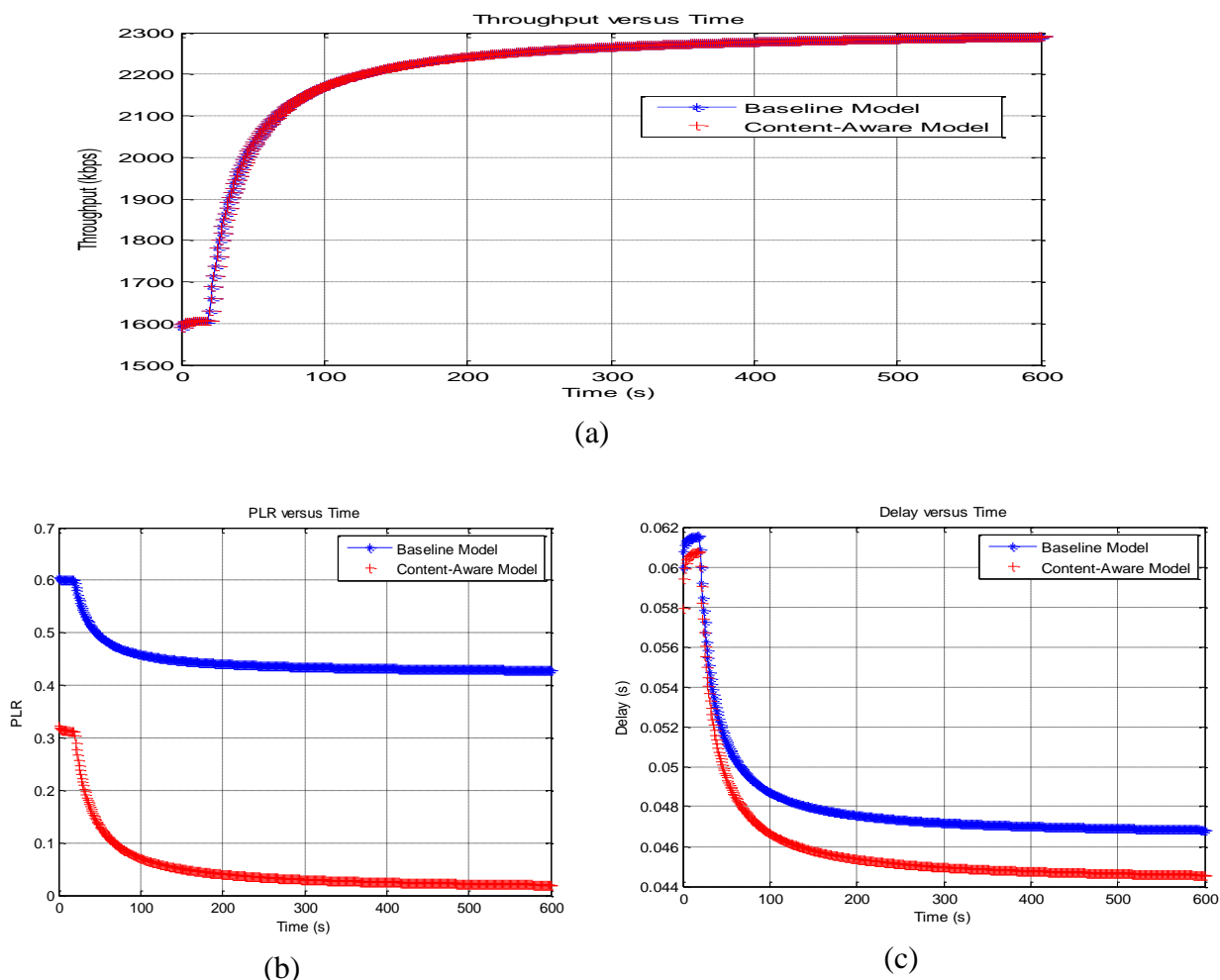


Fig. 4 Output performance for downlink video delivery at UE velocity of 50 km/h. (a) Throughput against time (b) Packet loss ratio against time (c) Average delay against time

5. Conclusion

In conclusion, a content-aware RRM model by employing cross layer optimization with the proposed look-up tables for single cell LTE system is proposed for both downlink and uplink video packet transmissions. The results have indicated that for the same amount of throughput, the proposed content-aware RRM model has vastly outperformed the LTE baseline model in terms of packet loss ratio, as well as providing significant gain in terms of average delay. Thus, the proposed model is highly recommended to be used in the current LTE-Advanced system to further improve video delivery performance.

Acknowledgments

The author would like to thank Universiti Teknikal Malaysia Melaka for sponsoring his PhD study.

References

- [1] K. I. Pedersen, T. E. Kolding, F. Frederiksen, I. Z. Kovacs, D. Laselva, and P. E. Mogensen, "An overview of downlink radio resource management for UTRAN long-term evolution," *IEEE Communications Magazine*, 2009, pp. 86–93.
- [2] 3GPP RAN Workshop on IMT-Advanced, Shenzhen, China, 07-08 April 2008, available at ftp://ftp.3gpp.org/workshop/2008-04-07_RAN_IMT_Advanced/Docs/.
- [3] S. Kumar and N. Marchetti, "IMT-Advanced: Technological requirements and solution components," *Second International Workshop on Cognitive Radio and Advanced Spectrum Management*, 2009, pp. 1-5.
- [4] S. Parkvall and D. Astely, "The Evolution of LTE towards IMT-Advanced," *Journal of Communications*, Vol. 4, No. 3, 2009, pp. 146-154.
- [5] M. K. Ismail, M. S. Johal and A. Awang Md Isa, "Current Developments in LTE-ADVANCED: Radio Resource Management Review," *Proceedings of IEEE Student Conference on Research and Development (SCoReD 2014)*, 2014.
- [6] R. Radhakrishnan, B. Tirouvengadam, and A. Nayak, "Cross Layer Design for Efficient Video Streaming over LTE Using Scalable Video Coding," *Network Protocols and Algorithm*, Vol. 4, No. 4, 2012, pp. 6509-6513.
- [7] H. Luo, S. Ci, D. Wu, J. Wu, and H. Tang, "Quality-Driven Cross-Layer Optimized Video Delivery over LTE," *IEEE Communications Magazine*, 2010, pp. 102–109.
- [8] S. Karachontzitis, T. Dagiuklas, and L. Dounis, "Novel Cross-Layer Scheme for Video Transmission over LTE-Based Wireless Systems," *IEEE International Conference on Multimedia and Expo (ICME 2011)*, 2011.
- [9] D. Wang, V. S. Somayazulu, and J. R. Foerster, "Efficient Cross-layer Resource Allocation for H.264/SVC Video Transmission over Downlink of an LTE System," *IEEE International Symposium on a World of Wireless, Mobile and Multimedia Networks (WoWMMoM)*, 2012.
- [10] M. S. Johal, G. Markarian, A. Awang Md Isa, and Y. Dasril, "Content-Aware Radio Resource Management for IMT-Advanced", *Journal of Telecommunication, Electronic and Computer Engineering (JTEC)*, Vol. 9, Issue 2, 2017, pp. 125-131.

Analysis of BE and rtPS QoS in WiFi Network

(Proceedings of the Int. Conference on “ Microwave and THz Technologies and Wireless comm.”)

Juwita Mohd Sultan^{1,*}, Garik Markarian^{2,*}, Philip Benachour³

¹ Centre for Telecommunication Research & Innovation (CeTRI), Fakulti Kejuruteraan Elektronik & Kejuruteraan Komputer (FKEKK), Universiti Teknikal Malaysia Melaka (UTeM), Malaysia.

^{2,3} InfoLab21, School of Computing and Communications, Lancaster University, Lancashire, United Kingdom.
E-mail:**) g.markarian,p.benachour@lancaster.ac.uk; *) juwita@utem.edu.my

Received 15 November 2018

Abstract: Quality of Service (QoS) in networking is defined as the assurance or as a guarantee factor that the information is perfectly delivered in a communication link. As one of the promising novel in the next communication architecture is to have a coherence quality of service in a wireless hybrid network. However, these heterogeneous networks have various levels of QoS classes. WiFi, for example, has two classes of QoS, five classes in WiMAX while nine classes are in LTE. Since each system has a particular level of QoS classes, the motivation to have a persistent communication is a challenging task. In this paper, we investigate on details of the QoS in WiFi network first before proceed to the hybrid network. The QoS involve are real time polling service (rtPS) and Best Effort (BE). Thus, in this paper, we propose QoS table for WiFi network with the consideration of the user’s application. We will evaluate the traffic outputs based on the application assigned to the end users. The propose structure will be analyzed using Opnet modeler simulation tool with the essential parameters which are throughput, delay and packet loss. The motive of this research is to have an optimize throughput, minimum amount of delay as well as zero tolerance on the packet loss. Therefore, a hybrid communication system benefited to all, especially for future user applications will be the significant from this research.

Keywords: Quality of Service; WiFi; real time polling service; Best Effort.

1. Introduction

QoS is an important factor in a communication system since its’ determine the traffic and service prerequisite would be satisfied in terms of packet loss, delay, throughput and jitter. The original version of the IEEE 802.11 WLAN standard is designed to operate only with the best effort services; which means there is no QoS allocate on the assigned applications [1] [2]. However, a new protocol has been developed by the IEEE 802.11e for the allocation of QoS over priority mechanism which are the HCF Controlled Channel Access and Enhanced Distributed Channel Access. The applications are categorized into two QoS classes which based on guarantee bit rate or otherwise [3]. Details are shown in Table 1. Based on the characteristics and the similarity of the applications, the four applications have been categorized into 2 QoS classes; Voice and Video in the rtPS QoS meanwhile Web browsing and FTP in the BE QoS classes [4].

Table 1: WiFi QoS Classes [5]

Application	Description	QoS Classes
Voice	Bidirectional Voice calls with 64Kbps at 20ms. Talk spurt and silence spurt exponential with mean 0.35 seconds and 0.65 seconds.	Real Time Polling Service (rtPS)
Video	Downlink VBR stream with an average rate of 1Mbps and a peak rate of 5Mbps.	
Web	Inter-page request time exponentially distributed of mean 15 seconds.	Best Effort (BE)
FTP	FTP download of a 20MB file	

2. Simulation environment

In this network, we analyze the effect of the QoS classes and the effect in terms number of users and distance [6]. The two QoS classes involved are rtPS and BE. Using OPNET as the simulation tool, we investigate the QoS parameters; throughput, delay and data dropped involving different numbers of QoS users in the network [7] - [9]. We start with a small number of users and next we increase the distance to study the effect on the WiFi network [10], [11]. The simulation starts for 15 meter distance from the access point to the users. The users are assigned with the same QoS and later on we have a look the effect when the QoS is change. The applications appoint to the QoS; video conference to the rtPS QoS and web browsing to the BE QoS.

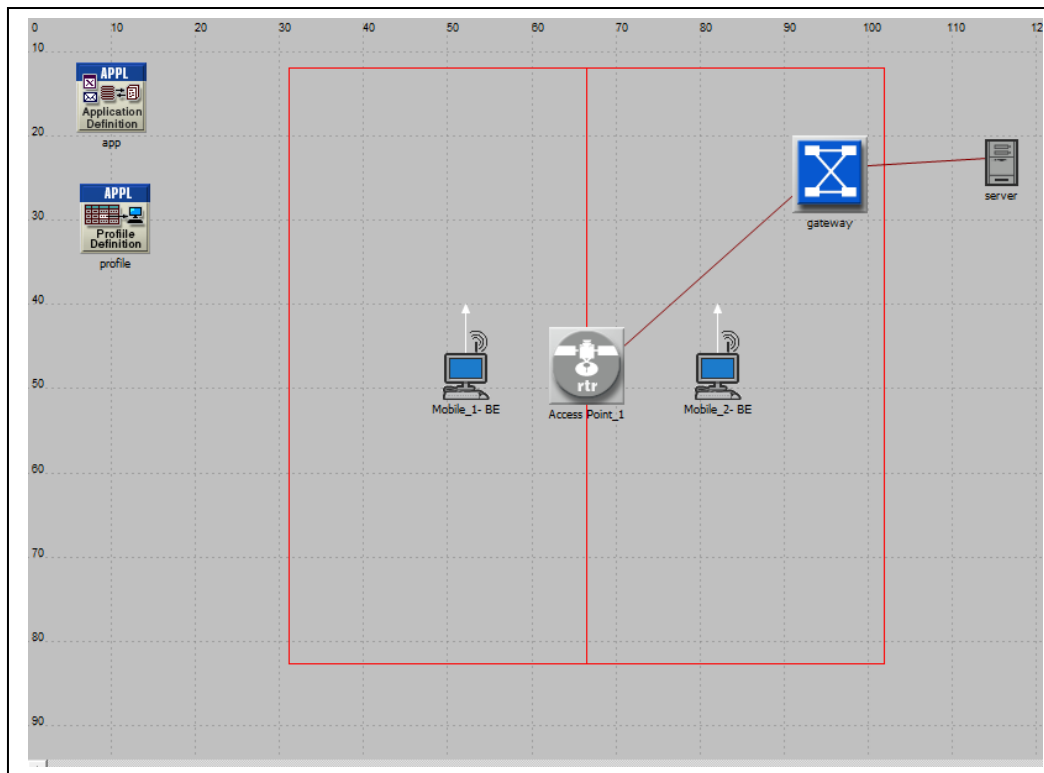


Fig.1 Network Model

The network model is the main staging region for creating a network simulation in which user can construct a network model the usage of fashions from the usual library, pick records about the community, run a simulation, and examine the results [12]. Except that, consumers can also create node and process models, build packet formats, and create filters and parameters, the usage of specialized editors that may be accessed from the assignment Editor.

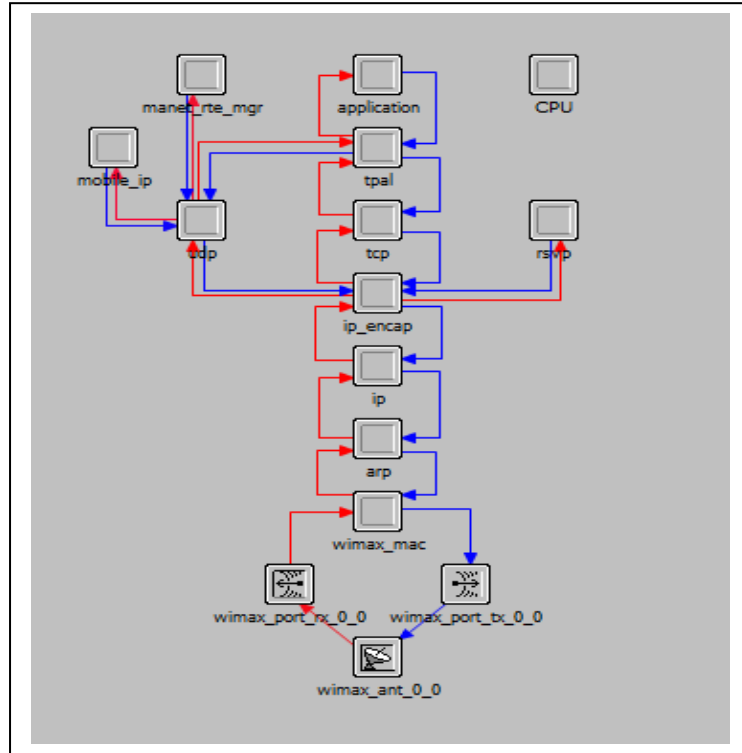


Fig.2 Node Model

The Node model is to define the action of every network object. The action is described using distinct modules, each of which defines some internal component of node action, for example data formation, data storage, and others. Modules are connected through packet streams or statistic wires. A network object is typically made up of a couple of modules that outline its behaviour [13]-[15].

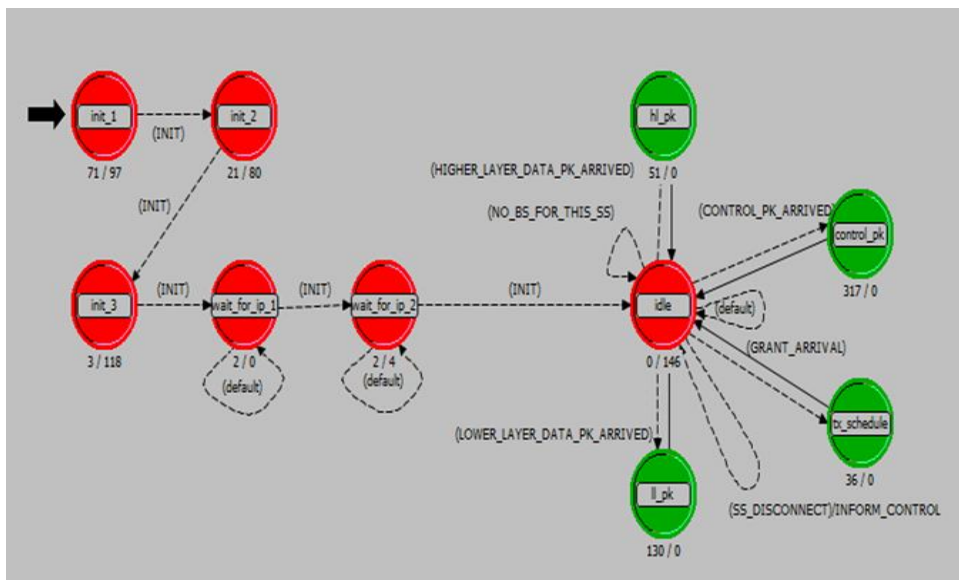


Fig.3 Process Model

The process model is used to create method fashions, which manage the underlying capability of the node fashions created within the Node Editor. Procedural models are represented via finite kingdom machines (FSMs), and are created with icons that constitute states and features that constitute transitions between states. Operations executed in every state or, for a transition are defined in embedded C or C++ code blocks.

3. Results and discussion

We conduct a few simulation scenarios to evaluate the proposed method. In this scenario, both users are set as BE QoS with the distance of 15 meters from the access point. Fig.4 shows the throughput for both users that shows almost the same reading. Throughput for user 1 and 2 are fluctuating with the highest point is between 6kbit/s and 8kbits/s since the application assigned to both users is web browsing. The signal will rise only when the user starts to browse a website and falls back when there is no activities.

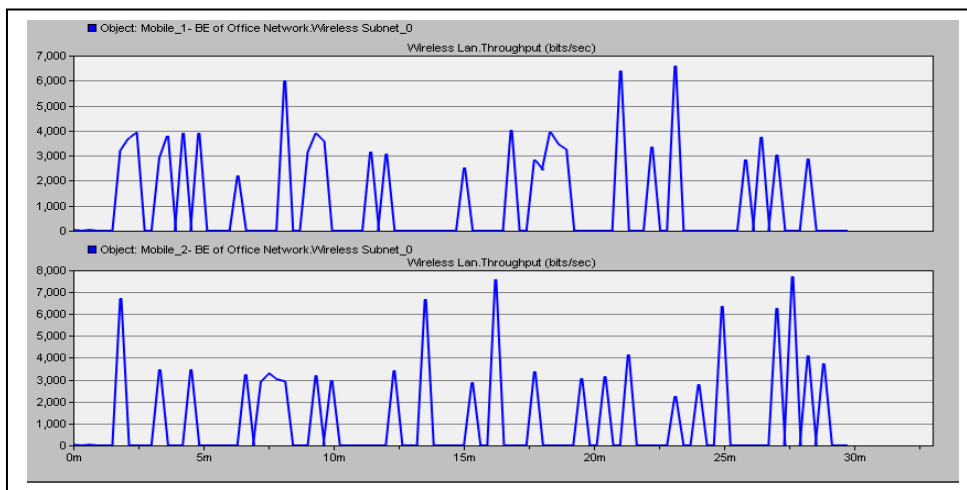


Fig.4 Throughput of BE user for 15 meter distance

In order to deeply understand the behavior of WiFi QoS, next we evaluate the delay and data dropped parameters. Fig. 5 demonstrates the average delay BE QoS for 2 users. There is not much difference between the users due to the same application settings.

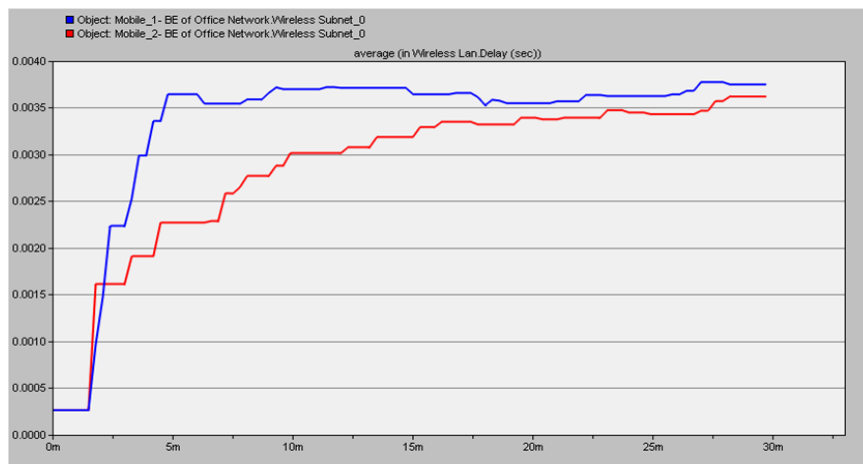


Fig.5 Average delay of BE user for 15 meter distance

Even though there is a delay reading, the data dropped for both BE QoS users are zero. This means that there is no data loss in the network. For both users, all the information is successfully transmitted and received as shown in Fig. 6.

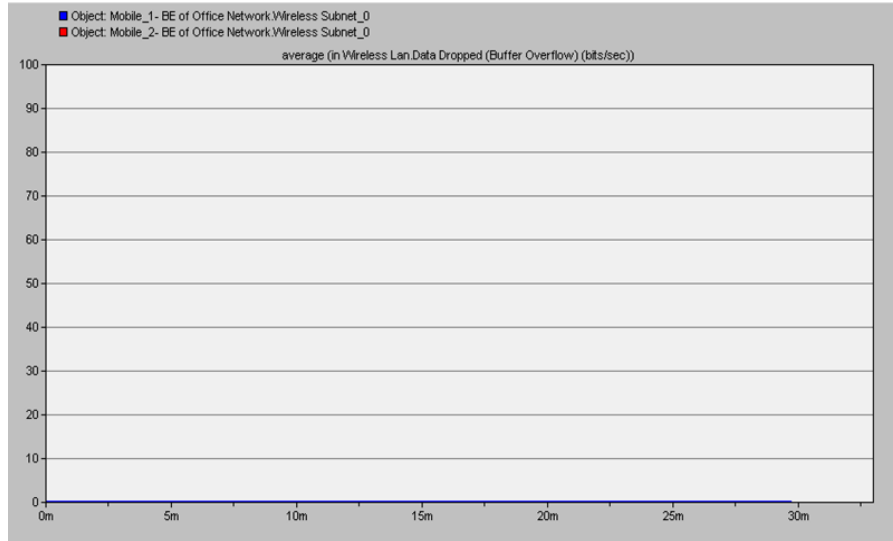


Fig. 6 Average data dropped of BE user for 15 meter distance

In this scenario, we changed the QoS to rtPS with video conferencing as the application. Fig.7, Fig.8 and Fig.9 explain the details based on the simulation outcomes. Throughput for both users remain stable till the end of the simulation time between 800 kbps and 1Mbps. However, delay for both users are utterly high that contributes to data dropped reading which is higher as well. Based on results, it shows that the rtPS QoS is truly sensitive even though it is a guaranteed bit rate QoS.

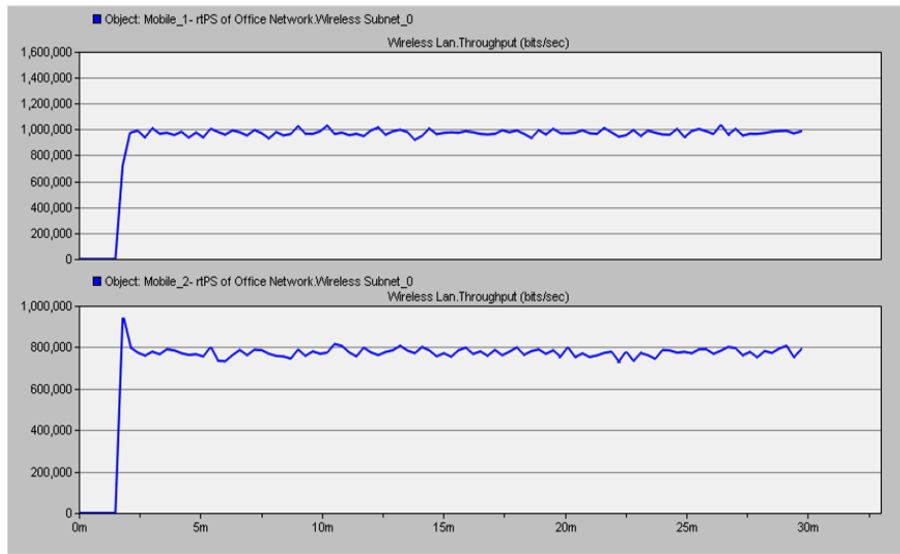


Fig.7 Throughput of rtPS user for 15 meter distance

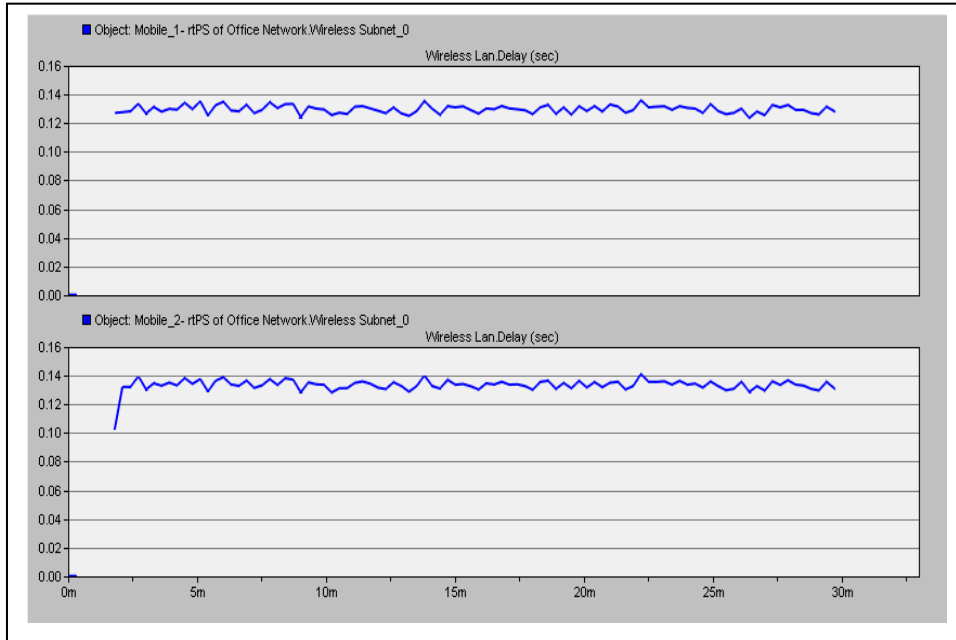


Fig.8 Average delay of rtPS user for 15 meter distance

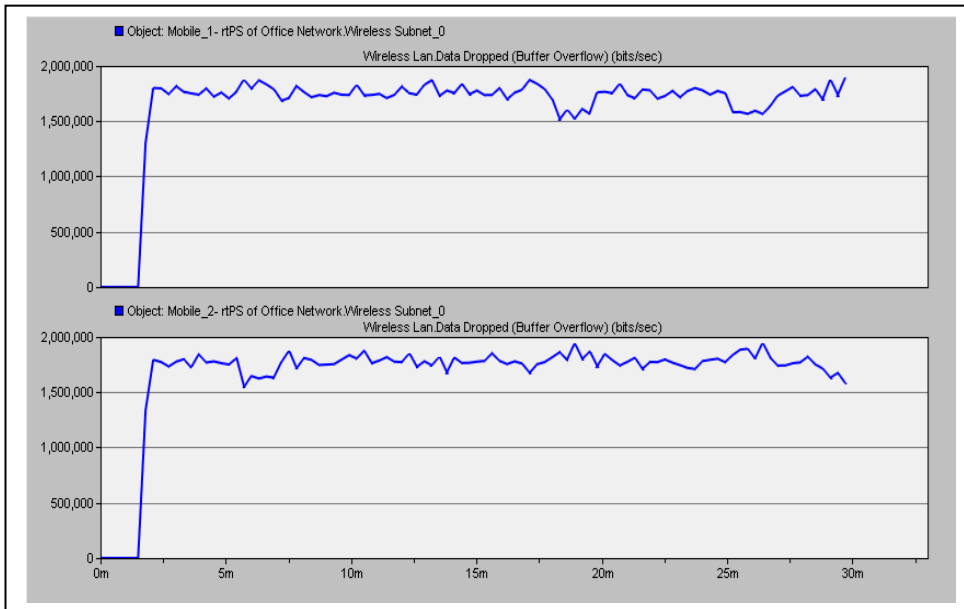


Fig.9 Data dropped of rtPS user for 15 meter distance

As for the further understanding, we assigned different QoS for each different user. User 1 is assigned with rtPS QoS and user 2 with the BE QoS. Fig.10, Fig.11 and Fig.12 demonstrates the simulation results. Both users produce throughput that is applicable to the application assigned which is 3 Mbps for the rtPS QoS and 8 kbps for the BE QoS. Delay for both users are showing the same reading at the end of the simulation time, which is lower than 0.06 seconds as illustrate in Fig. 11. The rtPS user shows a remarkably an increasing delay starting from the first point which affect the loss information. Fig 12 explains that there is a data dropped for the rtPS user compared to zero data dropped for the BE user.

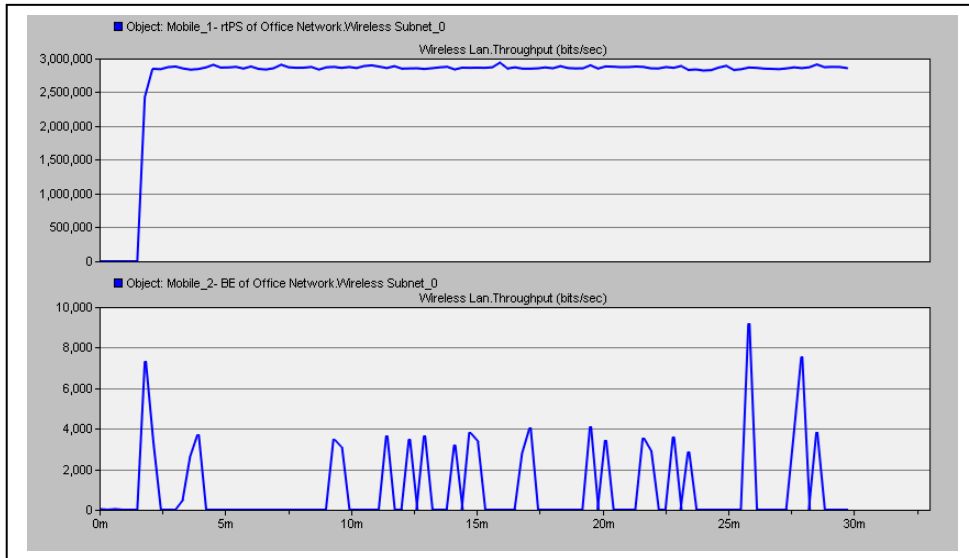


Fig.10 Throughput of rtPS and BE user for 15 meter distance

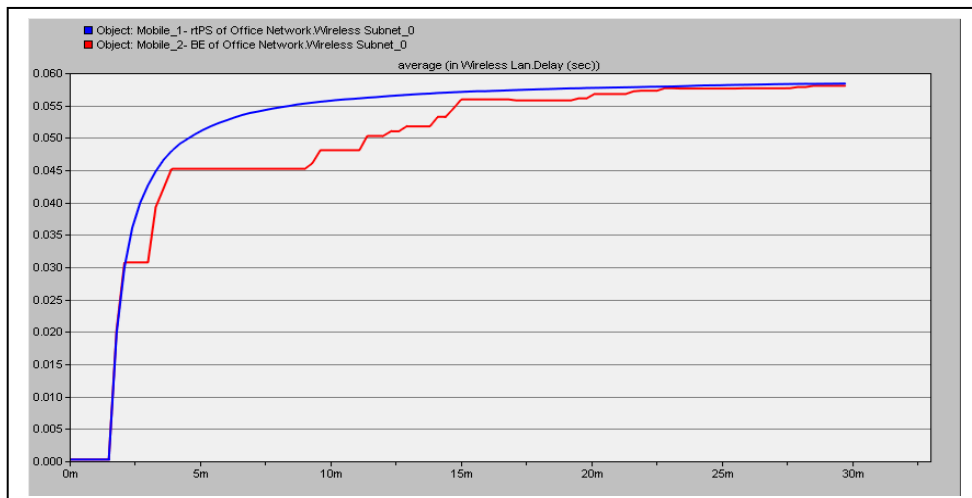


Fig.11 Average delay of rtPS and BE user for 15 meter distance

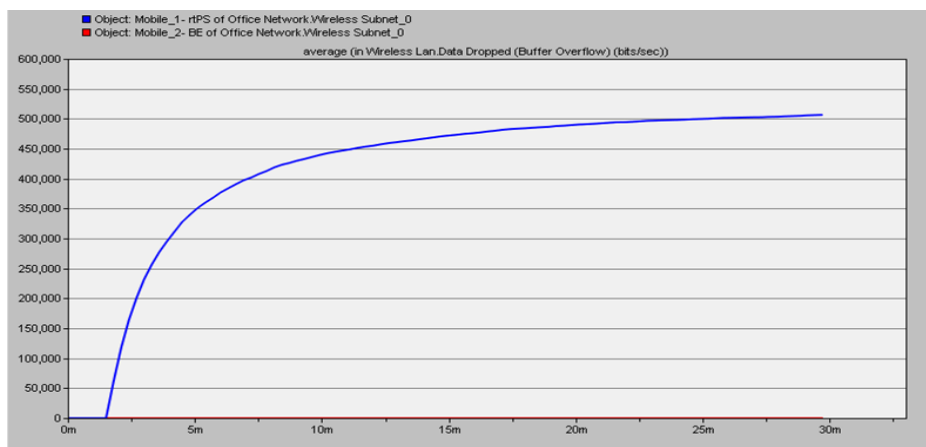


Fig.12 Data dropped of rtPS and BE user for 15 meter distance

4. Part B: Scenario 2

In this part, we expand the simulation environment into further detail to investigate the effect of QoS in WiFi network. We increase the number of WiFi users up to 20 and increase the distance up to 30 meters. The classes of QoS in WiFi network are still the same as previous settings. Also the QoS parameters such as throughput, delay and data dropped are the characteristics that determine the network performance are evaluated in this scenario. Fig. 13 shows the simulation setup in OPNET environment.

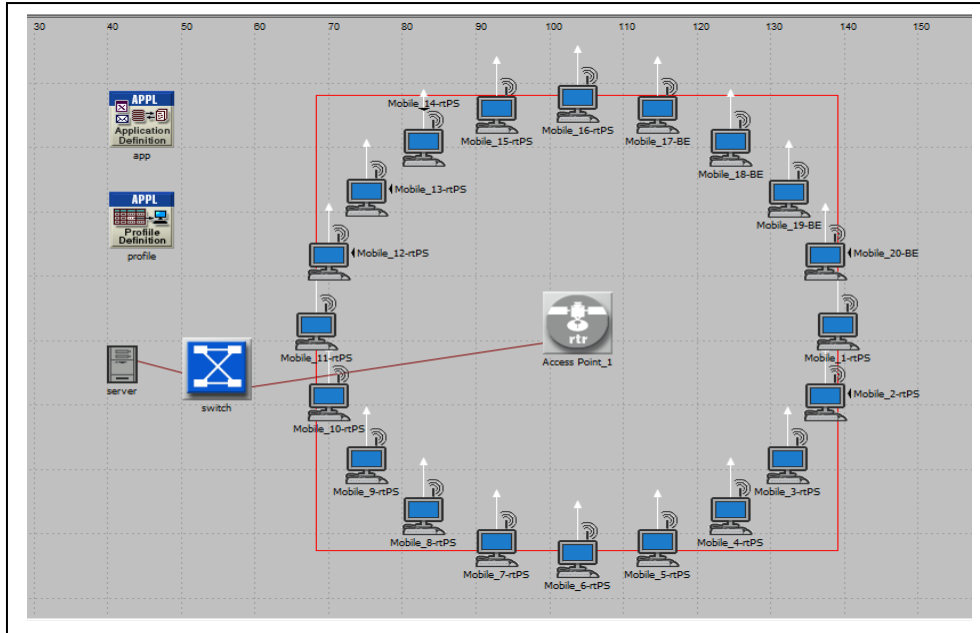


Fig.13: WiFi topology of 20 users for 30 meter distance

Fig.14, Fig.15 and Fig.16 reveal the simulation results when both the number of users are increasing and also the distances between the users and the access point. The users are all set with BE QoS and web browsing as the application. The throughput graph indicates that all 20 BE users are gaining throughput, however in a low range which is in between 400 kbps-160 Mbps. The throughput is all remain stable until the end of the simulation time. The average delay shows almost a same reading for all users, whereas zero data dropped for all the BE users. This explains that the QoS performance for all BE users are stable and all the users are producing throughput even though the quantity is limited.

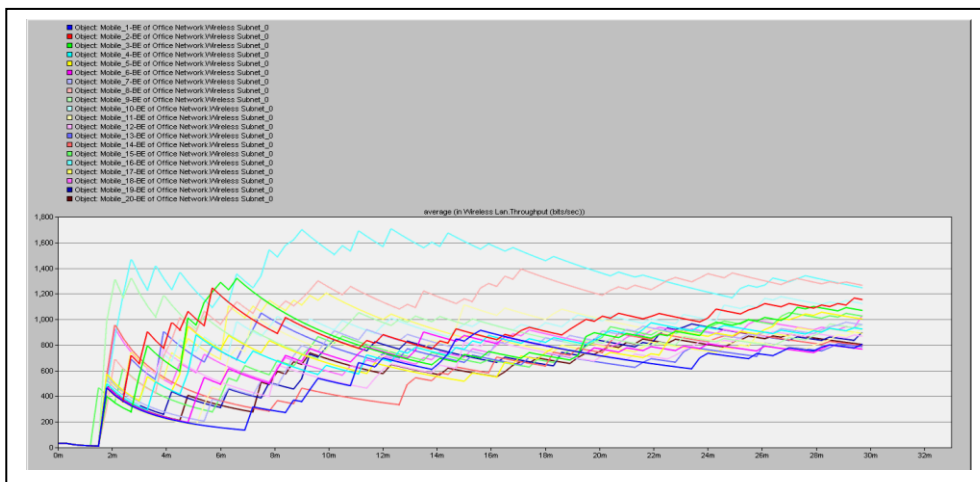


Fig.14 Throughput of 20 BE users for 30 meter distance

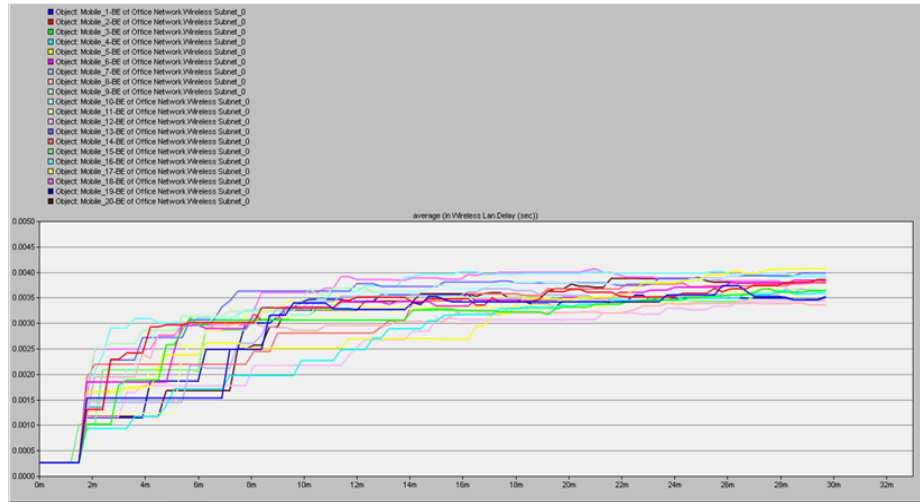


Fig.15 Average delay of 20 BE users for 30 meter distance

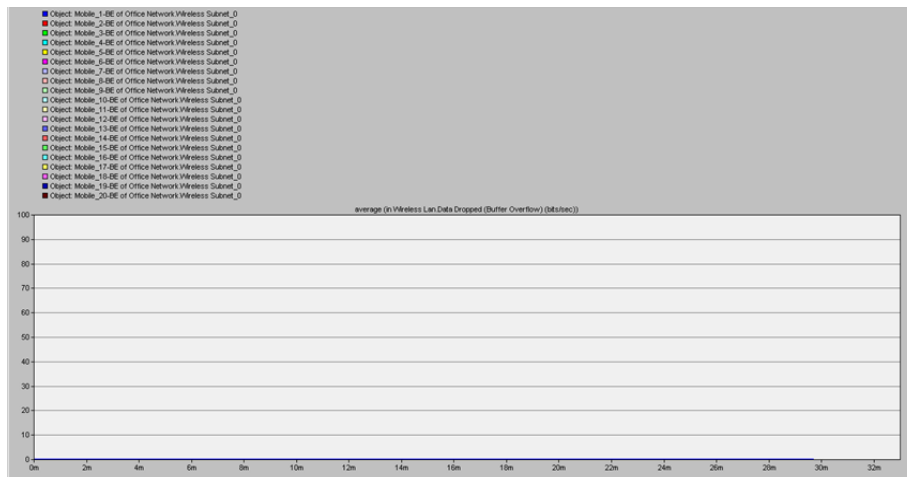


Fig.16 Data dropped of 20 BE users for 30 meter distance

Fig. 17 shows the average throughput for 20 rtPS users. It shows that the throughput falls drastically from the starting point which then remain stable in a low range scale. The highest throughput will be around 15 kbps meanwhile the lowest is 5 kbps.

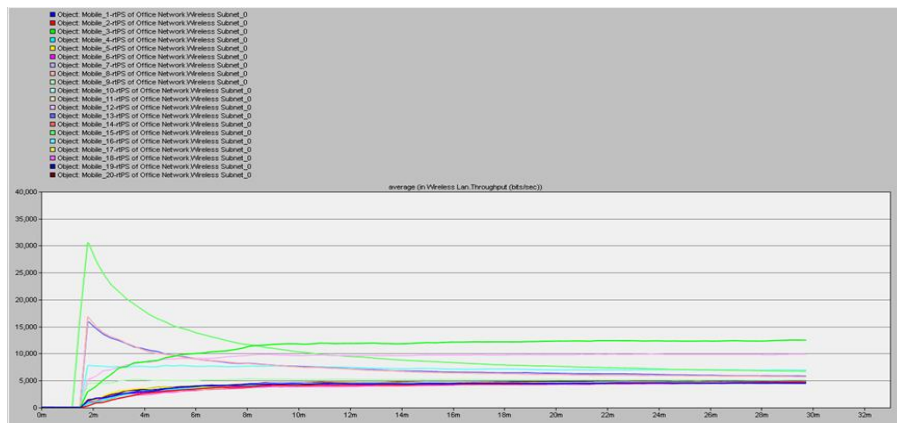


Fig.17 Throughput of 20 rtPS users for 30 meter distance

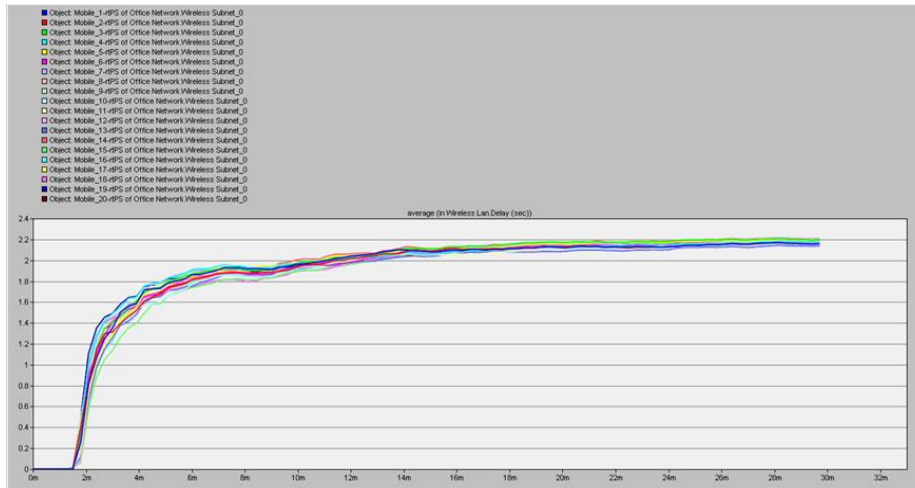


Fig.18 Average delay of 20 rtPS users for 30 meter distance

The delay measured in this scenario recaps a huge rising for this users with the video conferencing. The reading that shows a range in between 2 and 2.2 seconds, which classify as very high delay is degrading the cohesiveness of the video application. This eventually affected the data dropped performance as well. Fig. 19 shows the consequences of data dropped for the rtPS users, which is very high and summarize as unacceptable data loss ranges. The data dropped obtained from the simulation for all 20 users are 3.6 Mbps.

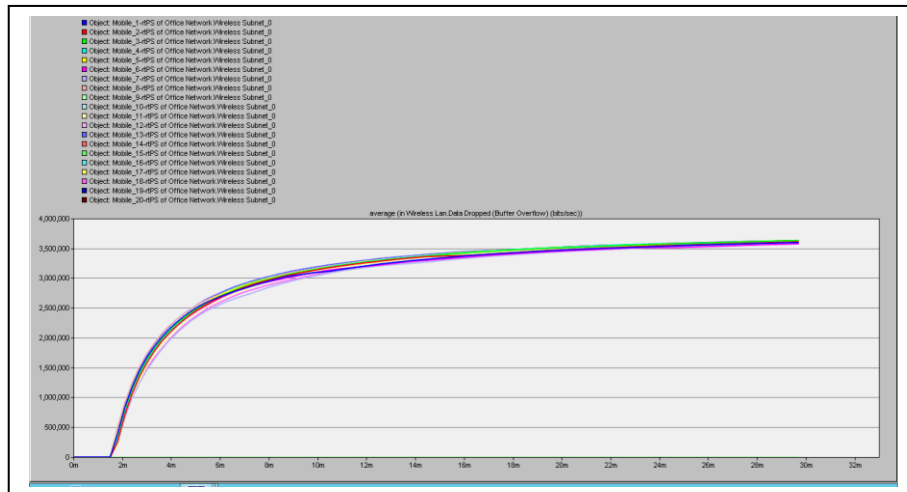


Fig. 19 Data dropped of 20 rtPS users for 30 meter distance

Next we investigate the output when the number of QoS users is equal. In this situation, we analyze the impact when the available bandwidth is given to a balance QoS number. Therefore, we set 10 users with BE QoS and remaining 10 users with the rtPS QoS users. Fig. 20 demonstrates that all the users in the network produce throughput even though some are in the low range and others in the higher range. Despite the limited bandwidth, all users still gaining throughput.

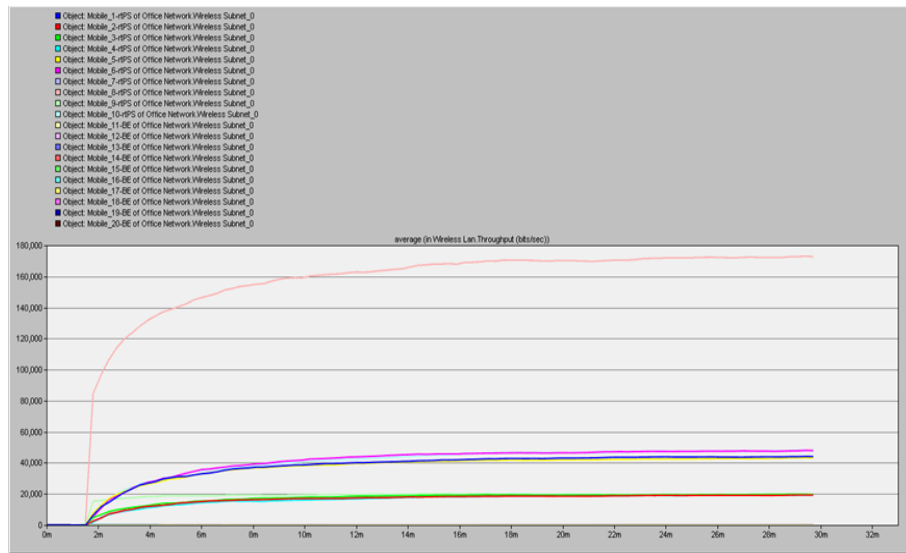


Fig.20 Throughput of 10 rtPS users and 10 BE users for 30 meter distance

In spite of that, delays for all users are considerably as high compare to the previous results. The average delay for the rtPS and BE QoS users' ranges from 0.48 seconds to 0.57 seconds. There is not much different between the rtps QoS and BE QoS since the number of users are equal.

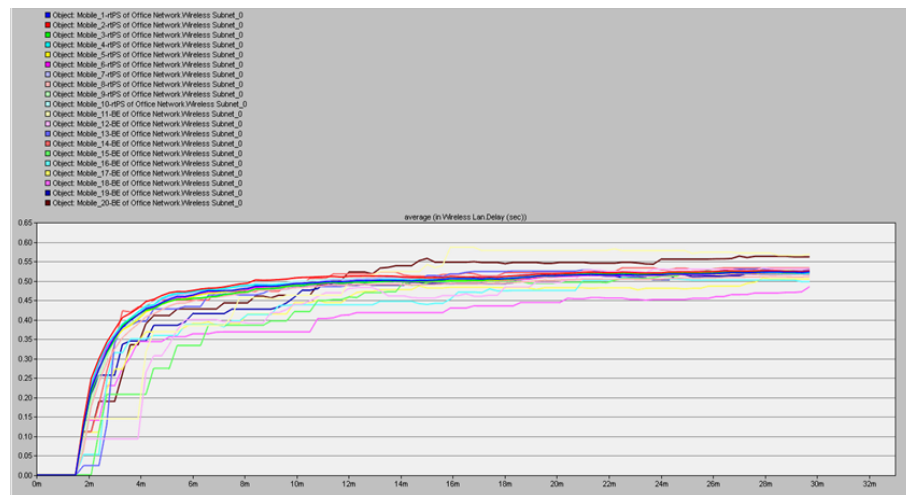


Fig.21: Average delay of 10 rtPS users and 10 BE users for 30 meter distance

Fig.22 shows the data dropped results indicates that there is no data loss for the BE QoS users, however rtPS users experienced a high data dropped which is around 3 Mbps.

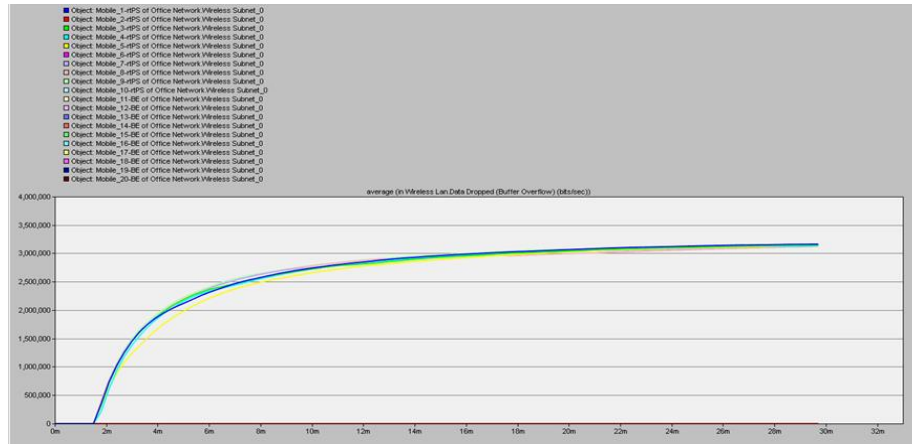


Fig.22: Data dropped of 10 rtPS users and 10 BE users for 30 meter distance

5. Conclusion

The table shows the summary based on the results obtained. Commonly known that BE QoS is the best available QoS which means the total bandwidth will be divided fairly among the users in the network. All the BE users will gain a throughput, with a slight delay, however no data loss. The Throughput for each BE users are quite small and likely the same which is the range of 8-9 kbps. When we changed the QoS of the users from BE to rtPS, total throughput for both users increasingly high. A higher data gain will make the users satisfied, however, it also causes the delay and data dropped reading to intensely high. Even though rtPS QoS is in the guarantee bit rate QoS classes, based on these results the data dropped value is outweigh the data achieved by the user. To discover the optimum result, we include the same number of QoS as an effort to a balanced output. Based on simulation results, total throughput in the network, increasing thoroughly which produces the highest throughput compared to the previous QoS allocation. For each QoS user, the throughput gain is adequate for the application assigned. For example, throughput 3 Mbps for video conferencing application and 9 kbps for web browsing that is sufficiently accepted. Delay for both users show almost the same reading and showing a raise value, however, it is still on a small-scale and under the acceptable delay for each application. For the rtPS user, there is still showing data loss during the transmission nonetheless it is very low because of the delay factor. As for the BE user, the data dropped shows a zero reading.

Table 2. Summarization of WiFi QoS

WiFi QoS	Parameter		
	Throughput	Delay	Data Dropped
All BE	Total : 15 kbit/s	0.004 s	0
All rtPS	Total : 1.8Mbit/s	0.14 s	2Mbit/s
BE=rtPS	Total : 3.8Mbit/s	0.055 s	500 kbit/s

When we include more users in the network, there is not much difference in the QoS behavior. The performance of each scenario is almost the same as before. Therefore the investigate reveals that the distance between the users and the access point does not affect much on the QoS

parameter in WiFi network. However, the network performance of WiFi is degrading based on the fragmentation of the QoS in the network itself. This new discovery played an important factor in designing the optimization of WiFi network in terms of QoS parameter which are throughput, delay and data dropped.

Acknowledgments

The main author would like to acknowledge Universiti Teknikal Malaysia Melaka (UTeM), Centre for Telecommunication Research & Innovation (CeTRI) and Lancaster University for all the supports given during this research.

References

- [1] Prinima, P. Joythi, "Evolution of Mobile Communication Network; 1G to 5G", International Journal of Innovative Research in Computer and Communication Engineering, vol.4, 2016.
- [2] B. Ramia, B. Amin, A. Osman, "A Comparison between IEEE 802.11 a, b, g, n and ac Standards", International of Computer Engineering, vol.7, Issues 5, 2015.
- [3] S. Surendra Tambe, "Wireless Technology in Networks", International Journal of Scientific and Research Publications, vol.5, Issues 7, pp 1-3, 2015.
- [4] D. Zvikhachevskiy, J. M Sultan, K. Dimiyati "Quality of Service Mapping Over WiFi+WiMAX and WiFi+LTE Networks," Journal of Telecommunication, Electronic and Computer Engineering, vol.5, no. 2, pp. 1-10, 2013.
- [5] D. Camps-Mur, et al, "Leveraging 802.11n frame aggregation to enhance QoS and power consumption in Wi-Fi networks," Computer Networks, vol. 56, no. 12, pp. 2896-2911, 2012.
- [6] M. Meeran, P. Annus, M. Alam et al., "Evaluation of VoIP QoS Performance in Wireless Mesh Networks", vol.8, Issues 3, pp 1-26, 2017.
- [7] (2016) Measuring Delay, Jitter, and Packet Loss with Cisco IOS SAA and RTTMON - Cisco. [Online]. Available: <http://www.cisco.com>
- [8] (2014). Jitter. [Online]. Available: <http://www.wikipedia.com>.
- [9] M.A Alawi, R.A. Alsaqour, E. Sundarajan and M. Ismail, "Prediction Model for Offloading in Vehicular Wi-Fi Network," International Journal on Advanced Science Engineering Information Technology, vol.6, No. 6, ISSN 2088-5534, 2016.
- [10] E. Khaili, "Science & Technology WiFi and WiMAX QoS Performance Analysis on High-Level- Traffic using OPNET Modeler", Journal Science and Technology, vol. 25, issues 4, pp 1343-1356, 2017.
- [11] (2014) Opnet Modeler. [Online]. Available: <http://www.mil3.com>.
- [12] J.M Sultan, G. Markarian, J. Jackson, "Hybrid WiFi and WiMAX in Disaster Management for PPDR Services", Journal of Telecommunication and Computer Engineering, vol. 9, No 3, 2017.
- [13] J.M. Sultan, G. Markarian, P. Benachour, "Integration of WiFi and WiMAX Services: Bandwidth Optimization and Traffic Combination", International Journal Web Applications, vol.7, 95-108, 2015.
- [14] W. Jiang., "OPNET-based WLAN Modeling and its Performance Testing", Chemical Transaction, vol. 51, pp 361-366, 2016.
- [15] V. Singh, D. Rai, "Simulation of Network with Cloud Servers Using OPNET Modeler", International Journal of Advance Research and Innovation, vol. 5, pp 315-319, 2017.